CRANFIELD UNIVERSITY

Adisorn Sirikham

Three-Dimensional Subsurface Defect Reconstruction for Industrial
Components using Pulsed Thermography

School of Aerospace, Transport and Manufacturing
PhD in Manufacturing

PhD Degree
Academic Year: 2015 - 2019

Supervisor: Dr Yifan Zhao
Associate Supervisor: Professor Jorn Mehnen
May 2020

CRANFIELD UNIVERSITY

School of Aerospace, Transport and Manufacturing
PhD in Manufacturing

PhD Degree

Academic Year 2015 - 2019

Adisorn Sirikham

Three-Dimensional Subsurface Defect Reconstruction Industrial
Components using Pulsed Thermography

Supervisor: Dr Yifan Zhao
Associate Supervisor: Professor Jorn Mehnen
May 2020

This thesis is submitted in partial fulfilment of the requirements for
the degree of PhD
*(NB. This section can be removed if the award of the degree is
based solely on examination of the thesis)*

ABSTRACT

Pulsed thermography is a promising method for detecting subsurface defects, but most pulsed thermographic inspection results are represented in the form of 2D images. Such a representation can limit the understanding of where the defects initiate and how they grow by time, which is a key to predict the remaining use of life of component and feedback to the design to avoid such defects. Three-dimensional subsurface defect visualisation is a solution that can unlock this limitation. A straightforward approach to reconstruct 3D subsurface defect is conducting two inspections on both front and rear sides. However, the deployment of this approach can be limited because 1) one side of the inspected component could be inaccessible; 2) the accuracy of measurement could be compromised if the defect thickness is very thin due to extreme closed values of defect depths from two inspections; and 3) if the defect is too deep for one side, the defect could be missed. Addressing the challenge of 3D subsurface defect reconstruction and visualisation, this thesis proposes a novel technique to measure defect depth and estimate defect thickness simultaneously through estimating the thermal wave reflection coefficient value achieved by introducing a modified heat transfer model based on a single-side inspection method.

The proposed method is validated through model simulations, experimental studies, and a use case. Four composite samples with different defect types, sizes, depths and thicknesses, are used for experimental studies; a steel sample with a 's' shape triangular air-gap inside is used for a use case. The simulation results show that under the noise level of 25 dB, the percentage error of the developed depth measurement method is 0.25% whilst the minimum error of the best existing method is 2.25%. From the experimental study results, the averaged percentage error of the defect thickness estimation is less than 10% if the defect thickness is no more than 3 mm. For the use case, the reconstructed defect shape is similar to the X-ray image.

Keywords:

ACKNOWLEDGEMENTS

TABLE OF CONTENTS

LIST OF FIGURES

LIST OF TABLES

LIST OF EQUATIONS

LIST OF ABBREVIATIONS

APST	Absolute Peak Slope Time
CCD	Charge-Coupled Device
CFRP	Carbon Fibre Reinforced Polymer
DPT	Dye Penetrant Testing
ECLT	Eddy Current Lock-in Thermography
ECPT	Eddy Current Pulsed Thermography
ECT	Eddy Current Thermography
ET	Electromagnetic Testing
FEM	Finite Element Method
IR	Infrared
IRT	Infrared and Thermal Testing
LED	Light Emitting Diode
LSD	Logarithmic Second Derivative
LSF	Least-Squares Fitting
LT	Lock-in Thermography
LWIR	Long-Wavelength Infrared
MPT	Magnetic Particle Testing
MWIR	Mid-Wavelength Infrared
NDT	Non-Destructive Testing
NFIR	Nonlinear Finite Impulse Response
NLSF	New Least-Squares Fitting
NSI	Nonlinear System Identification
OLS	Orthogonal Least Squares
PCC	Pearson Correlation Coefficient
PCT	Peak Contrast Time
PST	Peak Slope Time
PT	Pulsed Thermography
QNDE	Quantitative Non-Destructive Evaluation
ROI	Region of Interest
RT	Radiographic Testing
SNR	Signal-to-Noise Ratio
TC	Temperature Contrast

TSR	Thermal Signal Reconstruction
UT	Ultrasonic Testing
VOT	Visual and Optical Testing
VT	Vibro-Thermography

LIST OF PUBLICATIONS

1. **A. Sirikham**, Y. Zhao, H. Liu, Y. Xu, S. Williams, and J. Mehnen, "Three-dimensional subsurface defect shape reconstruction and visualisation by pulsed thermography," *Journal of Infrared Physics & Technology*. vol. 104, pp. 1–10, 2020.

2. **A. Sirikham**, Y. Zhao, H. Y. Nezhad, W. Du, and R. Roy, "Estimation of damage thickness in fiber-reinforced composites using pulsed thermography," *Journal of IEEE Transactions on Industrial Informatics*, vol. 15, no. 1, pp. 445–453, 2019.

3. **A. Sirikham**, Y. Zhao, and J. Mehnen, "Determination of thermal wave reflection coefficient to better estimate defect depth using pulsed thermography," *Journal of Infrared Physics & Technology*, vol. 86, pp. 1–10, 2017.

4. Y. Zhao, S. Addepalli, **A. Sirikham**, and R. Roy, "A confidence map based damage assessment approach using pulsed thermographic inspection," *Journal of NDT and E International*, vol. 93, pp. 86–97, 2018.

5. Y. Zhao, J. Mehnen, **A. Sirikham**, and R. Roy, "A novel defect depth measurement method based on Nonlinear System Identification for pulsed thermographic inspection," *Journal of Mechanical System and Signal Processing*, vol. 85, pp. 382–395, 2017

1 INTRODUCTION

1.1 Background

Nowadays, it is possible to extend the service life of vital infrastructural elements through the use of Non-Destructive Testing (NDT). The advantage of NDT is that it allows a structure to be examined without causing any adverse effect to that structure [1]. The technology is considered to offer a safe approach to detect both surface and subsurface faults without actually altering the properties, characteristics or operation of the structure or equipment itself [1], [2], [3]. This technique has been applied over the past three decades in a broad range of industries, including aviation, manufacturing, rail transport, agriculture, power plants, civil structures, manufacturing, the environment, art, medicine, and the automotive industry [4]. The methods used in NDT are diverse, encompassing techniques such as electromagnetic testing [5], ultrasonic testing [6], acoustic emission testing [7], radiographic testing [8], liquid penetrant testing [9], magnetic particle testing [10], and infrared thermography testing [11].

As a highly efficient and powerful NDT technique, pulsed thermography (PT) is contact-free and offers a rapid inspection while covering a large area within a short time frame [12] and thus readily adaptable to in-situ monitoring applications [13]. The technique is both quick and economical because it can be performed on-site, avoiding the need to first transport the object to a laboratory for the inspection [14], [15], [16]. It can detect various types of defect such as impact damage and cracks. Pulsed thermography can be used with a range of materials including concrete [17], [18], [19], high-density polyethylene [20], composite materials used in aviation [21], [22], wood and wood-based materials [23], and also adhesive bond evaluation [24], [25]. Other thermography technique-based NDTs, such as microwave thermography, eddy current thermography, ultrasound thermography, and lock-in thermography, take several measurements using signals of different frequencies to gain information about different depth; however, they require a longer inspection time. Pulsed thermography is more straightforward and faster because the flash time is a well-defined instant for time reference. Quantitative characterisation of defects by extracting shape, size and

depth, and estimation of thermal properties have been proven to be effective in pulsed thermography [14], [26]. Consequently, this technology has been successfully applied to a wide range of areas such as civil engineering, medicine and biology as well as agriculture, aerospace, automotive and manufacturing industries.

Although many quantitative analysis approaches have been developed to characterise defects, the characterisation results of subsurface defects (e.g. size and depth) are usually presented and visualised in the form of 2D images. In general, the form of 3D images performs better in displaying depth information of defects rather than 2D images. Moreover, realistic 3D visualisation is essential in studying the mechanism of defect propagation.

Currently, there are very limited reports about 3D subsurface defect reconstruction and visualisation using the pulsed thermography method. Most works in pulsed thermographic inspection focus on defect detection, sizing defect, and defect depth measurement. To reconstruct defect to the form of 3D images, the defect thickness is also required. However, there are very limited reports about defect thickness estimation.

This thesis addresses the challenge to reconstruct and visualise the subsurface defect in the form of 3D images based on the pulsed thermography technique, as demonstrated in Figure 1-1. To achieve this target, this thesis will primarily focus on developing new experimental setups and corresponding data analysis algorithms to improve the accuracy of depth measurement, measure the defect thickness, reconstruct and visualise the volume image of defects.
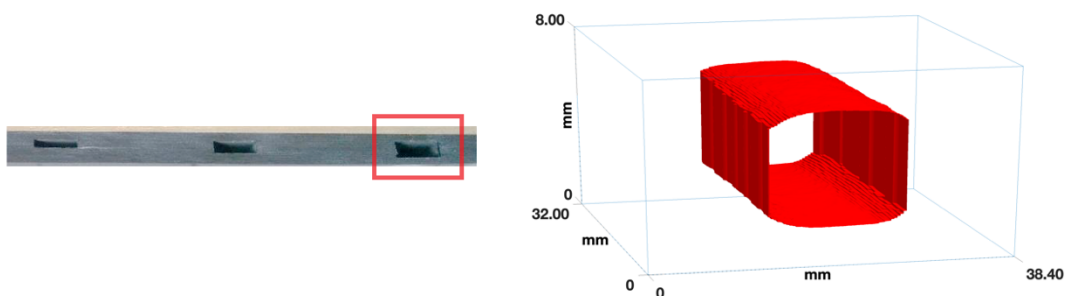
Figure 1-1 An example of 3D subsurface defect visualisation

1.2 Research Motivation

The pulsed thermographic inspection, which is a technique of NDT, is a pragmatic and effective approach. Its applications are well understood and extensively applied to inspect, analyse and evaluate defects of a wide range of industrial parts.

This thesis used PT because this method provides several advantages over other NDT methods. For example, in term of inspection time, PT offers a rapid inspection through covering a large area within a short period time. This method can also perform with contactless where the equipment (e.g., infrared (IR) camera and flash lamps) do not need to contact with the sample. In term of flexibility, PT can perform off-site inspections where the sample does not need to be transported to a laboratory. This method can also adapt to in-situ inspection applications. Furthermore, PT is a hazard-free method. IR camera is used for recording the thermal data and it does not emit any radiation. In addition, quantitative characterisation of defects by extracting shape, size and depth has been proven to be effective in PT.

However, most PT results are represented in the form of 2D images. The representation in the form of 2D images can limit the analysing of the type of the defect and limit the understanding of the origin of the defect (where the defect initiates and how it grows by time). These are important information to predict the remaining use of life of the components and feedback to the design to prevent some problems such defects.

Most inspectors have a desire to deskill the analysis of defect type and better understand the occurrence of the hidden defect. Three-dimensional representation of the inspected subsurface defect is a solution and could be a desirable tool for those inspectors because it facilitates to solve and unlock the abovementioned limitations. The 3D representation of subsurface defects is easier to understand for both experienced and non-experienced inspectors. The capability of 3D subsurface defect representation is not only able to visualise the defect dimension (size and thickness), but also helps the inspectors better

3

understand the mechanism of how the defect grows and where it starts from, including evaluating the defect volume.

From the facts that the 3D subsurface defect representation provides several significant benefits over 2D subsurface defect representation and several abovementioned reasons, the motivations of this thesis are:

- to make a valuable tool/algorithm/software to deskill the data analysis and monitor the subsurface defect of industrial components,
- to reduce several limitations of the inspection and expand the ability to evaluate the size, depth, thickness, and volume of the defect,
- to characterise the defects in a more comprehensive way,
- to save the cost of inspection (in term of using an inexpensive device to represent the 3D defect images),
- to save the operation time of inspection,
- to help inspectors better understand the origin of the defect and the mechanism of the defect propagation,
- to help inspectors better evaluate and predict the remaining use of life of the object,
- and to decrease workload and improve the quality of life for the inspectors.

It is expected that a wide range of people and industries can benefit from the outcomes of this research.

1.3 Research Aim and Objectives

1.3.1 Research Aim

The overall scientific aim of this thesis is to develop a three-dimensional subsurface defect reconstruction and visualisation approach based on the pulsed thermography method with a single-side inspection.

1.3.2 Research Objectives

The aim of this thesis is achieved through meeting the following objectives:

Objective 1. Identification of appropriate technique for three-dimensional subsurface defect reconstruction and visualisation for industrial components

Objective 2. Investigation of experimental setup and routine to capture data for three-dimensional subsurface defect reconstruction and visualisation

Objective 3. Development of novel methods to estimate subsurface defect depth and thickness for three-dimensional subsurface defect reconstruction and visualisation

Objective 4. Development of three-dimensional subsurface defect reconstruction and visualisation algorithms

Objective 5. Validation of the results by using model simulations, experimental studies, and a use case

1.4 Thesis Structure

This thesis is divided into seven chapters, the structure of which is illustrated in Figure 1-2.

Chapter 1 provides an introduction and a general overview of the NDT. This chapter also discusses the research motivation, aim and objectives of the research.

Chapter 2 provides a review of the literature and identifies the research gap. This review includes the overview of NDT techniques, thermographic inspection, defects depth measurement based on pulsed thermography, and defects visualisation methods.

Chapter 3 describes the strategy of research, research methods by addressing each objective.

Chapter 4 proposes two novel methods of subsurface defect depth measurement, compares and discusses the results from the developed method and the state-of-the-art methods in both model simulation and experimental study.

Chapter 5 proposes a novel method of subsurface defect thickness estimation by further developing the method proposed in Chapter 4.

Chapter 6 presents a framework to reconstruct and visualise the subsurface defect in a form of 3D images by utilising the developed method from Chapter 4 and Chapter 5.

Chapter 7 concludes the research findings of the thesis, discusses the advantages and limitations of the proposed solution, and describes future work.

Chapter 1
Introduction

Review & Method

Chapter 2
Literature Review

Chapter 3
Research Methodology

Algorithm Development

Chapter 4
Defect Depth Measurement

Chapter 5
Defect Thickness Estimation

Chapter 6
3D Defect Reconstruction

Chapter 7
Conclusion
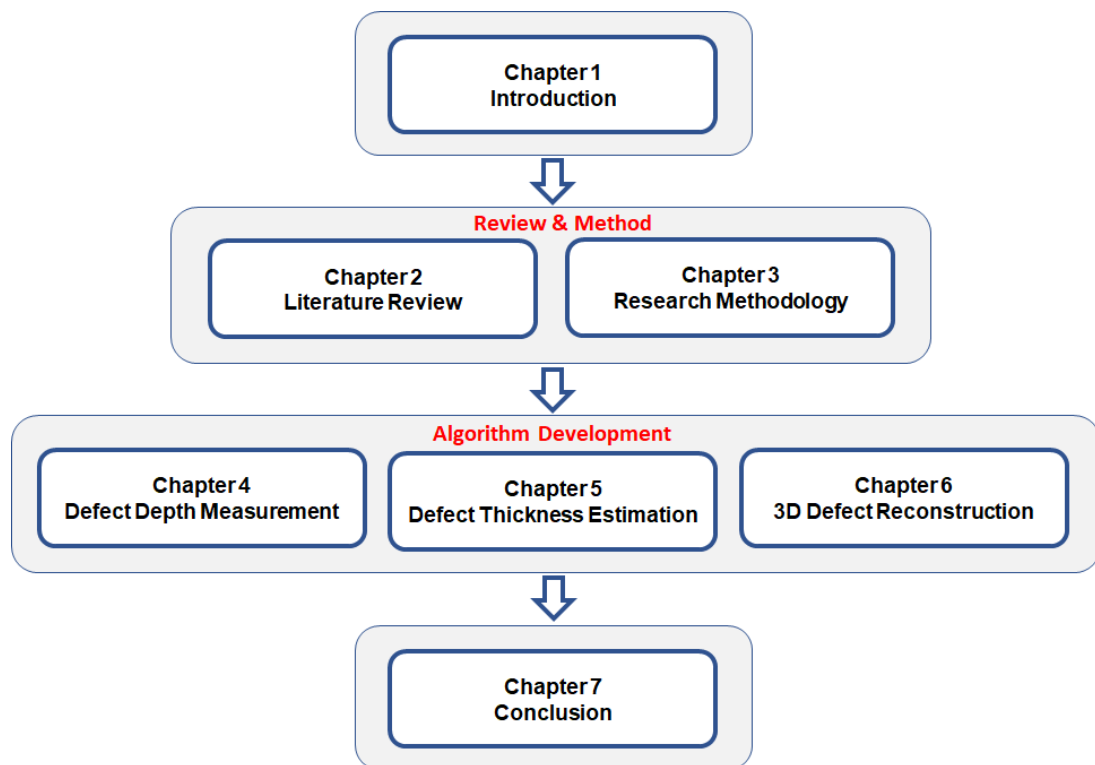
Figure 1-2 Thesis structure

2 LITERATURE REVIEW

2.1 Introduction

Inspection and evaluation of material flaws can be divided into two main types that are destructive testing and non-destructive testing (NDT). Destructive testing is often used to test the physical properties of materials such as impact resistance, toughness, ductility, and tensile strength. In contrast to destructive testing, NDT is a procedure of investigating, detecting, or assessing characteristics differences of components without destroying the inspected object [27]. NDT can be used to control manufacturing processes, to maintain the quality level, and to ensure integrity and reliability of products. It has been applied in various areas such as manufacturing, automotive, aerospace, and fabrication.

The literature review is organised into four main sections: the overview of NDT techniques, the thermographic inspection techniques, the defect detection and depth measurement method, and the three-dimensional defect visualisation. The purpose of the first section, the overview of NDT techniques, is to study and understand the advantage and disadvantage of each common NDT technique and select the most suitable technique to do in this thesis. The purpose of the second section is to study the process of the subsurface defect inspection based on the thermography method. The purpose of the third section is to study the evolution of the defect detection and depth measurement method based on pulsed thermography. The purpose of the fourth section is to review subsurface defect visualisation in the form of 3D images based on pulsed thermography. After that, the research gaps are described in the next section. The outline of this chapter is illustrated in Figure 2-1.
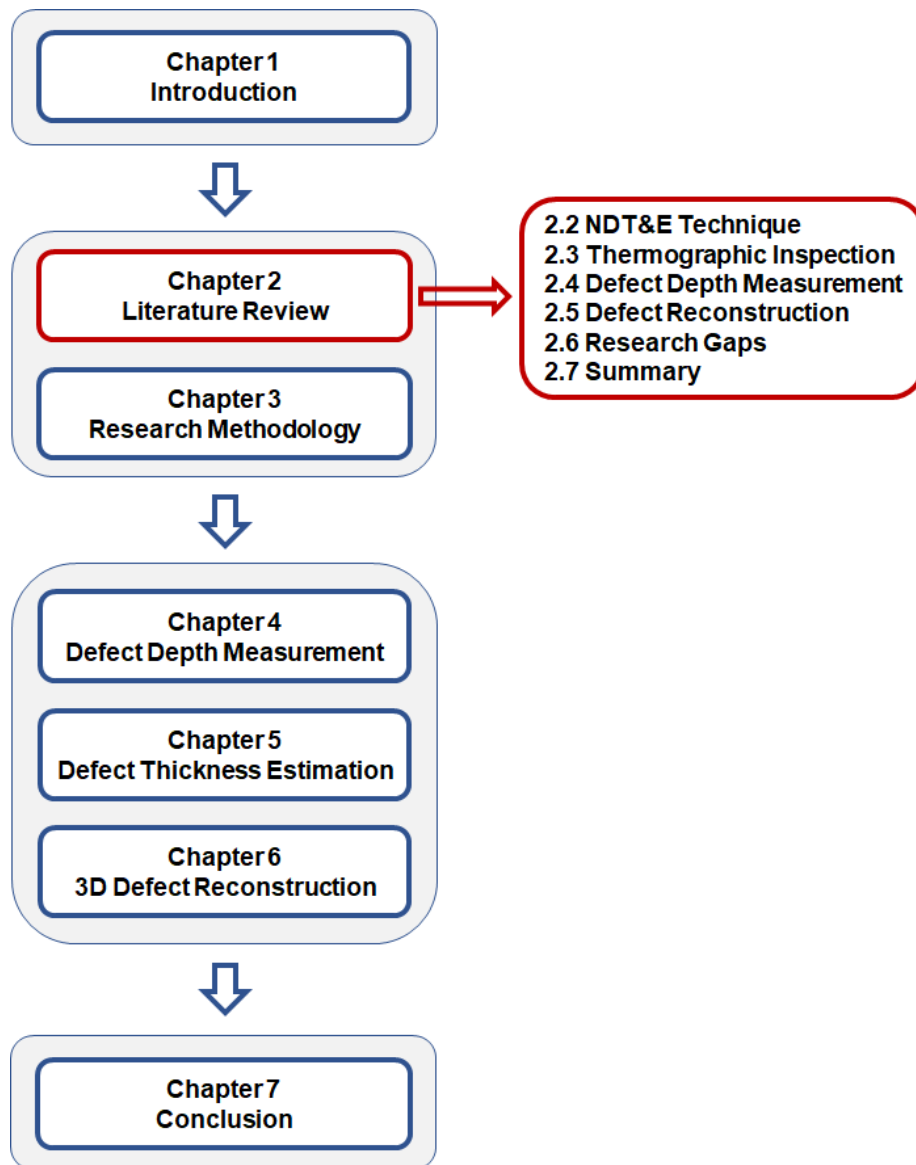
Figure 2-1 The outline of Chapter 2

2.2 Non-Destructive Testing Techniques

There are various NDT techniques used in different applications, depending on criteria such as type of materials, type of defects, size of defects, and location of defects. Commonly used NDT techniques include visual and optical testing, dye penetrant testing, magnetic particle testing, electromagnetic testing, radiographic testing, ultrasonic testing, and infrared and thermal testing, the details of which are introduced below.

2.2.1 Visual and Optical Testing

Visual and optical testing is the most common NDT method. It concerns the visual observation of the tested item's surface to assess flaws [14]. This investigation can direct watching or can be enhanced by using optical tools such as magnifying glasses, mirrors, borescopes, and charge-coupled devices (CCDs). This method can only detect abnormalities on the exterior surface of the object, the internal defect cannot be detected by this method. Figure 2-2 shows examples of tool in visual and optical inspection.
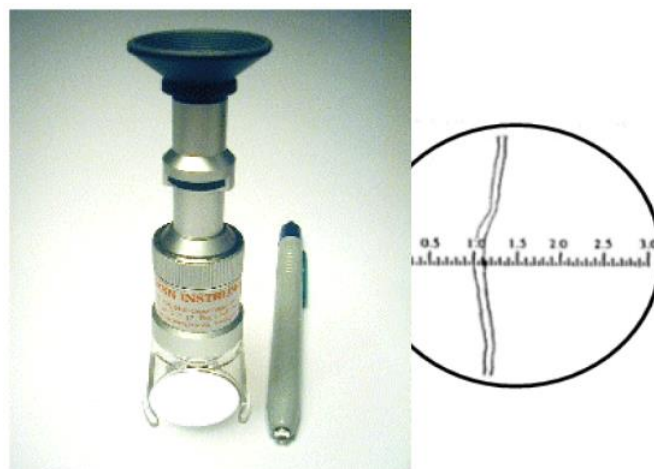
Figure 2-2 Crack microscope [28]

2.2.2 Dye Penetrant Testing

Dye penetrant testing, known as liquid penetrant inspection, are simple and are generally used for the detection of surface-breaking discontinuities, porosity, laps, fractures, and particularly cracks. The test object is coated with a visible or fluorescent dye solution. The dye solution seeps into any imperfect surface openings (defects). The abundance dye is removed from the surface, and a developer which deeds as a blotter is applied to draw penetrant out of the defects. In case of using a visible dye solution, the clear shading contrast between the penetrant and the developer is utilised. For using a fluorescent dye solution, an ultraviolet lamp is used to make the glow from the dye solution for observing the defect clearly. Dye penetrant method is suitable for inspecting the surface-

9

breaking cracks in non-ferromagnetic materials [9], [14], [29]. Figure 2-3 shows an example of testing by the dye penetrant method.

Figure 2-3 Example of testing by dye penetrant method [30]

2.2.3 Magnetic Particle Testing

Magnetic particle testing relies on the collection of magnetic particles (indicating particles) where the magnetic flux leakage on the object [10], [14]. The magnetic particles usually are iron oxide which can be made in a form of dry powder, liquid solution, or fluorescent substance. This technique utilises one or more magnetic fields to detect surface and near-surface discontinuities in the targeted object. The magnetic field can be generated from a permanent magnet or an electromagnet. When the magnetic field confronts a horizontal crack to the magnetic field direction, a magnetic flux leakage field will be produced by their flux lines. Because magnetic flux line travels through the air poorly, when magnetic particles are applied on the object's surface, they will be drawn into the discontinuity and making visible sign on the object's surface, as shown in Figure 2-4. Magnetic particle method is mainly used to detect surface-breaking cracks in ferromagnetic materials such as steel. However, it is restricted to the surface or only near-surface defects.
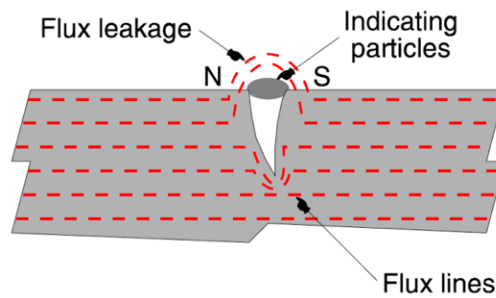
Figure 2-4 Example of Magnetic flux leakage on an object [31]

2.2.4 Electromagnetic Testing

Electromagnetic testing, particularly Eddy current testing, is normally used to examine conductive materials [31]. Eddy current techniques use alternating currents adapt to a conducting coil stand near the tested object [5], [14], as shown in Figure 2-5. Accordingly, the test object produces eddy currents to resist the rotating current in the coil. The eddy currents are then detected by magnetic field sensors. The change of the induced eddy currents relates to the cracks inside the object. The Eddy current testing techniques usually perform well for evaluating cracks beneath the surface of metallic materials. However, the depth of penetration is an important problem in eddy current testing due to the penetration of eddy current is limited by the skin effect.
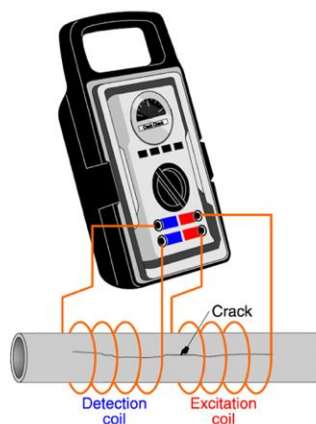
Figure 2-5 An illustration of Eddy current testing equipment [31]

2.2.5 Radiographic Testing

The tested object is placed between the source of radiation and the film, as shown in Figure 2-6. The X-rays go through the object and the amount of penetrating radiation after absorbed by material are captured on a film or a digital device. The different intensity of the radiation image on the film can be used to identify defects inside the object [31]. This technique can be used with various materials such as steel, composite materials, both metal and non-metal materials. However, both sides of the tested object should be accessible and accurately orientation between the radiation beam and the two-dimensional defects is required. The radiation of X-rays may be harmful to health.
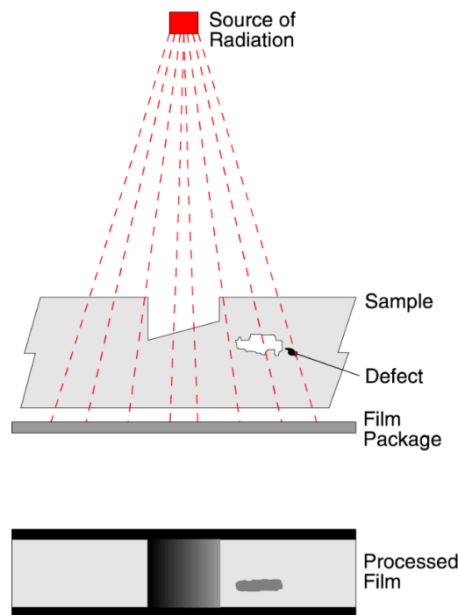
Figure 2-6 An illustration of radiography [31]

2.2.6 Ultrasonic Testing

Ultrasonic testing utilises high-frequency sound waves to identify flaws or changes in characteristics inside materials [6], [14], as shown in Figure 2-7. Most ultrasonic methods use frequencies in the range of 1 MHz to 10 MHz. In general, there is a couplant inserted between the probe and the object for better transmit the sound wave. The velocity of ultrasonic waves going through the object is a

basic function of density and modulus of the object. Ultrasonic methods can be used to estimate the thickness and detect crack of both non-metallic and metallic materials. However, it cannot detect defect which is parallel to the sound beam. It is not suitable to inspect very thin parts. The roughness surface can also be an issue for inspection.
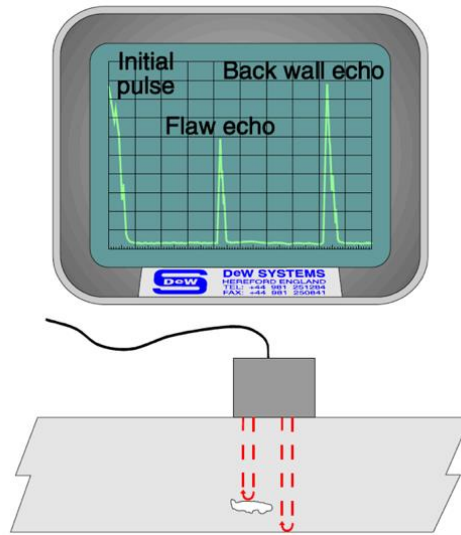
Figure 2-7 Ultrasonic detection of slag in a material using a normal probe [31]

2.2.7 Infrared and Thermal Testing

The infrared and thermal testing method analyses heat flow in the object which is a function of material properties [11], [14]. Thermal cameras are the most widely used sensors to capture thermal profiles on the tested object's surface. Thermal imaging can be employed to identify defects or cracks in materials. For example, passive imaging can be utilised to detect hot or cold spots which indicate the problems. Figure 2-8 shows infrared thermal imaging of some flaws (cold spots) under roof. Infrared and thermal testing method can apply to inspect both surface and subsurface defect in various material such as composite materials, metal and non-metal, plastic, etc. It is also a rapid and onsite inspection method, and is widely used in various industrial areas. In addition, the infrared thermographic camera/video is hazard-free. It only records the infrared radiation emitted from the inspected object and does not emit any hazard radiation.

13

Infrared and thermal testing is focused on this thesis because it provides several advantages as mentioned above. The details of this method are described below.
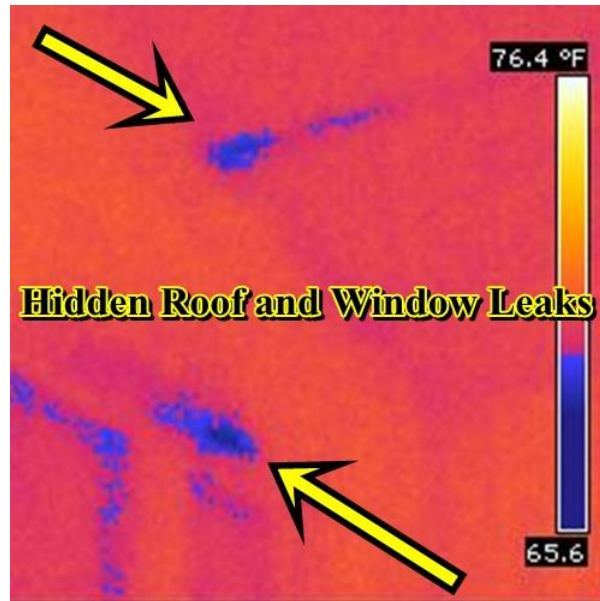
Figure 2-8 Example of infrared thermal imaging of some flaws under roof [32]

2.3 Thermographic Inspection

The thermographic inspection involves observing abnormally cold or hot spots on the object's surface. Thermographic inspection in term of NDT is detecting, inspecting, analysing, and evaluating the hidden defects inside the object from the information of thermal image/video. Thermal image/video can be acquired from a thermal imaging camera/video or infrared camera/video. Thermographic cameras (infrared radiometer) regularly detect radiation in the wavelengths of the electromagnetic spectrum between 3 μm to 5 μm (mid-wave infrared bands) or 8 μm to 14 μm (long-wave infrared bands) [33] and generate images of the radiation, called "thermograms" [34]. The infrared radiation bands in the electromagnetic spectrum are shown in Figure 2-9, the mid-wave (3 – 5 μm) and the long-wave (8 – 14 μm) of the electromagnetic spectrum are denoted as MWIR and LWIR, respectively.
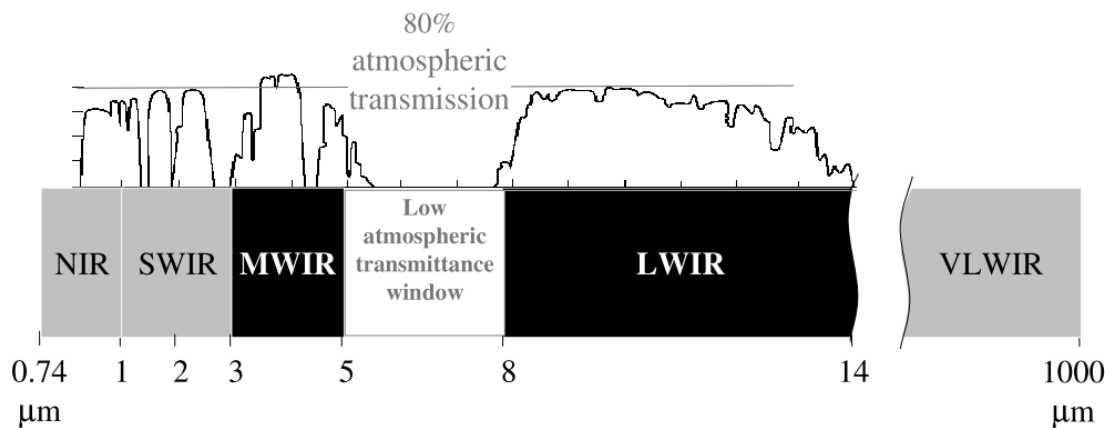
Figure 2-9 The infrared bands in the electromagnetic spectrum [33]

The energy fallen on the object can be dissipated in three ways: absorption, reflection, and transmission [35]. In 1860, Gustav Robert Kirchhoff defined a blackbody as a surface that does not have both reflection and transmission of the incident radiation [36]. Instead, the blackbody has only absorption of all incident radiation in all direction and wavelength. In physics, a blackbody is a theoretical object which emits electromagnetic radiation at its temperature. The electromagnetic radiation emitted from a blackbody is a function of wavelength and temperature. The radiation intensity from a blackbody can be calculated by Planck's law, expressed as

$$E_{\lambda b}(\lambda, T) = \frac{C_1 \lambda^{-5}}{e^{\frac{C_2}{\lambda T}} - 1} \tag{2-1}$$

where $E_{\lambda b}(\lambda, T)$ is the radiation intensity which is the function of wavelength and temperature emitted from the blackbody; λ [m] is the wavelength; T [K] is the temperature; C_1 and C_2 are radiation constants: $C_1 = 3.742 \cdot 10^8$ W μm⁴/m², $C_2 = 1.4389 \cdot 10^4$ μm·K.

In order to obtain the total radiation intensity of a blackbody, Equation (2-1) is integrated over all wavelengths from zero to infinity, expressed as

$$E_b = k_B T^4 \tag{2-2}$$

where E_b is the total radiation intensity emitted from the blackbody; k_B is the Boltzmann constant, $k_B = 567 \cdot 10^{-8}$ W/m²·K⁴.

The emissivity of a body defined for a specified wavelength (ε_λ) is the ratio of the radiation intensity emitted by the body at the wavelength (E_λ) to the radiation intensity emitted by a blackbody at the wavelength ($E_{\lambda b}$) at the same temperature, written as

$$\varepsilon_\lambda = \frac{E_\lambda}{E_{\lambda b}} \tag{2-3}$$

A real body emits only a fraction of the thermal energy emitted by a blackbody at the same temperature (E). The body will be considered as a graybody if the emissivity is constant and independent of the wavelength. The emissivity of real body (ε) can be calculated as

$$\varepsilon = \frac{E}{E_b} = \frac{E_\lambda}{E_{\lambda b}} = \varepsilon_\lambda \tag{2-4}$$

At a steady temperature, all of the energy absorbed must be emitted. A real blackbody is a perfect absorber and a perfect radiator. Therefore, the emissivity of real blackbody would be one. The emissivity of graybody could be less than one.

Infrared radiation is the energy radiated by the object's surface whose temperature equals to or above absolute zero ($T \geq 0$ K) [37]. The emitted radiation is a function of the object's temperature, the higher temperature is greater radiate the intensity of the infrared radiation. Based on the principle of infrared radiation, thermographic inspection/infrared thermography can be classified into two categories: passive thermography and active thermography [33], [38], [39], [40], [41].

Passive thermography investigates the features of interest which are naturally at a different temperature than the ambient [14]. The passive thermography is used when the object of interest has enough thermal contrast with respect to the background in order to be detected with an infrared sensor. Typical applications

include surveillance, people tracking, humidity assessment in buildings, liquid levels in storage tanks, insulation problems, and electrical components.

Opposite to the passive thermography, active thermography [16], [17] requires external energy to induce a thermal contrast between the feature of interest and the background (defective area and non-defective area). Figure 2-10 shows the main classical methods and excitations used in the active thermography. There are three common types of energy source: optical excitation, mechanical excitation, and inductive excitation. Under the optical excitation, the energy is transmitted to the object by means of optical devices such as flash lamps and halogen lamps. The light is transformed into heat and then delivered to the surface of the object. The defects are stimulated externally. Under the mechanical excitation, the energy is transmitted to the object by means of mechanical oscillation such as using ultrasonic transducer. The defects are stimulated internally. Under the inductive excitation, the energy is transmitted to the object by the inductance such as using the eddy current.

Many methods have been developed for active thermography. The selected evaluation method depends on the applications. The active thermography can be main sub-classified based on the source of excitation: pulsed thermography (PT), lock-in thermography (LT), ultrasound thermography (vibro-thermography (VT) [33], [42]), and eddy current thermography. The common methods using external excitation are pulsed thermography [43] and lock-in thermography [14], [44]. Base on the location of the external excitation source, it can be divided into two modes: reflection mode and transmission mode. The reflection mode refers to the position of the excitation source and the image acquisition camera is collocated on the same side, shown in Figure 2-11(a), whereas the transmission mode, the excitation source and the image acquisition are collocated in the opposite side, shown in Figure 2-11(b). Generally, the reflection mode is suitable for detect defects which located close to the heated surface while the transmission mode may be used to detect defects which located closer to the rear surface. It should be noted that in some cases only one side of surface is accessible, which means only the reflection mode is practicable.
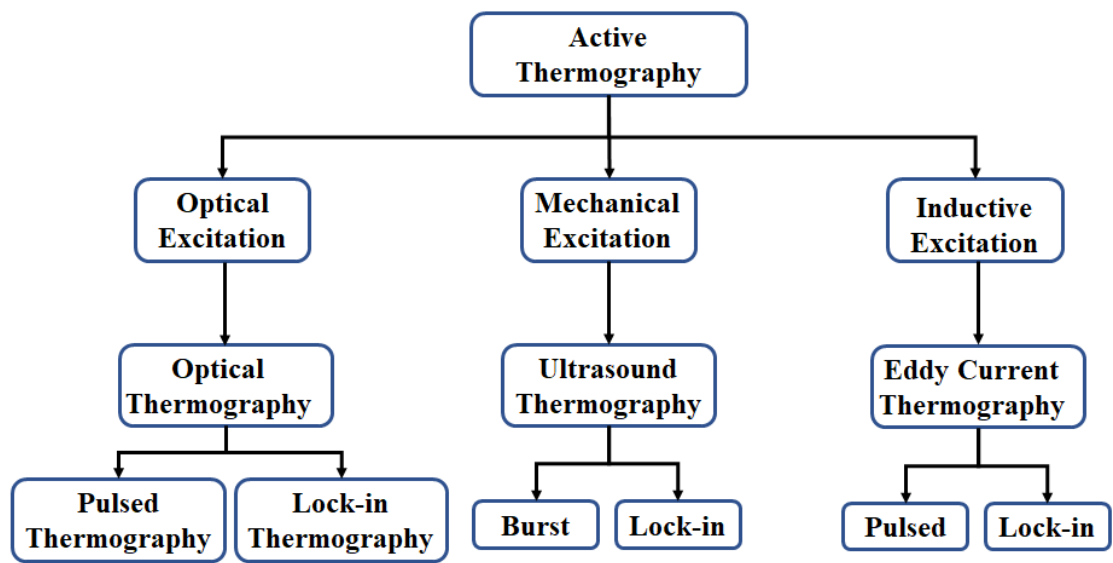
Figure 2-10 A list of active thermography approaches

(a)

(b)
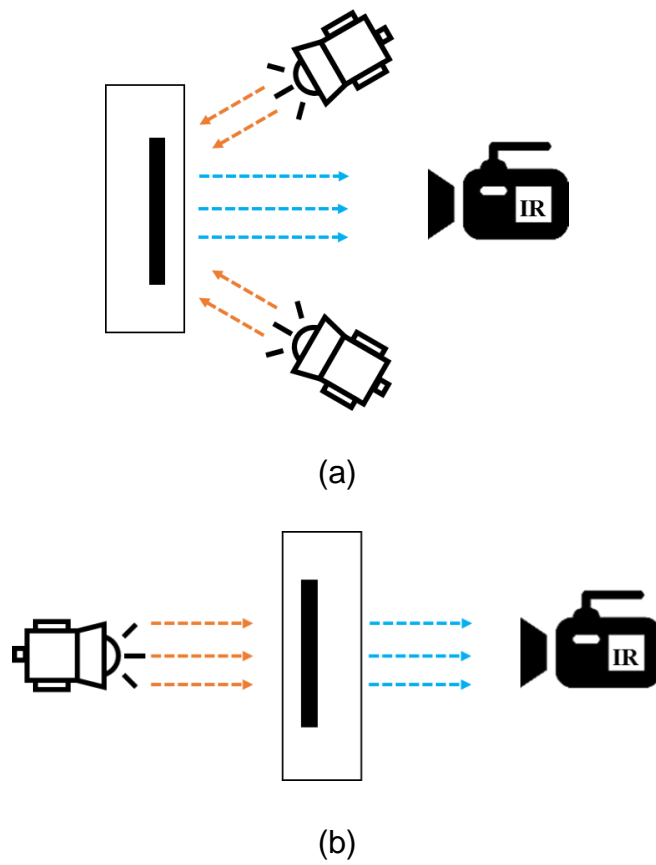
Figure 2-11 Thermographic inspection under the (a) the reflection mode (b) the transmission mode

2.3.1 Pulsed Thermography

Typical set-up of pulsed thermography is shown in Figure 2-12. In pulsed thermography (high power short pulse), a Dirac heat pulse is ideally transient waveform used to excite the specimen. The duration of the heat pulse may vary from a few milliseconds to several milliseconds (approximately 2 - 15 ms) depending on thermal properties of materials and defects. The excitation source normally uses flash lamps or photographic flashes. In long pulse thermography [45], which is similar to pulsed thermography, but the duration of heat pulse is longer from a few seconds to several minutes (e.g., 7 seconds [46]). This technique does not need a high power of stimulation. The excitation source commonly uses halogen lamps. The temperature on the surface is generally recorded by an infrared camera. After the specimen's surface is heated by excitation sources, the thermal propagates from the surface through the specimen and the cooling process is then diagnosed.

Pulsed thermography is more suitable for examining thin layers with shallow defects whilst long pulse thermography is more suitable for investigate a low conductivity material with a large structure which can be evaluated and imaged in a single shot [36].
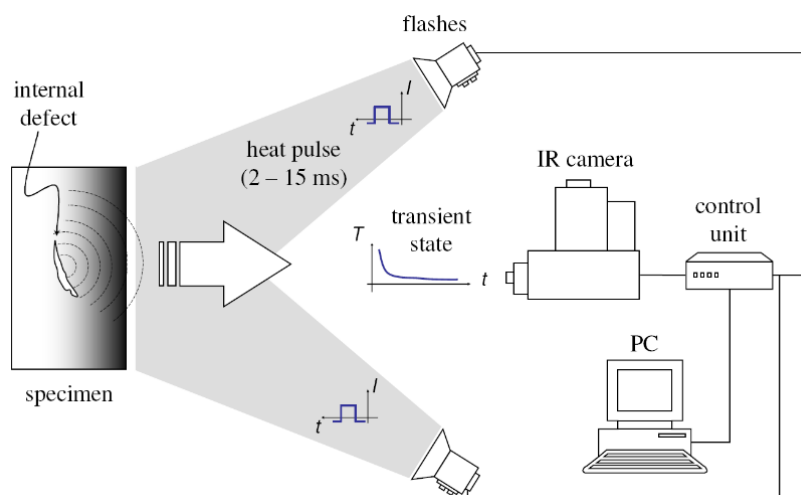
Figure 2-12 A typical set-up of pulsed thermography [33]

Figure 2-13 shows the comparison between the temperature decay curve on the non-defective area and the defective area. The black curve shows an observed temperature decay curve in a non-defective area. If the energy from the excitation source travels through a non-defective area, the observed temperature on the specimen's surface will decrease uniformly until the heat from excitation is gone. On the other hand, the red curve shows the observed temperature in a defective area. If the energy travels through an internal defective area, the observed temperature on the specimen's surface will drop abnormally and different pattern from the black curve because of the effect of the heat deviation. Although the 3D heat diffusion is a complex problem, many qualitative and quantitative techniques have been developed by using the relationship between time and defect depth, which is simplified by Equation (2-9). The advantages of this approach are the speed and straightforward inspection.
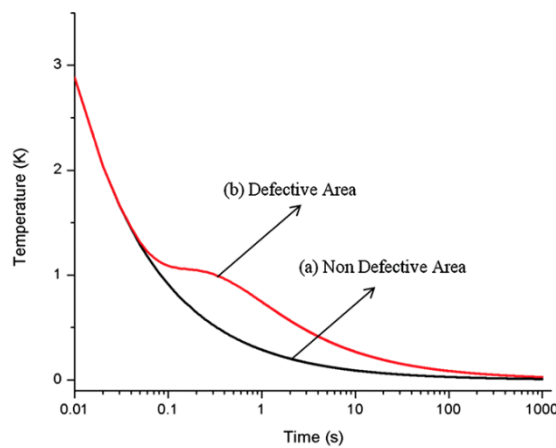
Figure 2-13 A temperature decay curve [47]

When the surface of solid material is heated by thermal energy, then some of the incident energy will be absorbed and diffused through the material, which can be described by Fourier's partial differential equation [48] as

$$Q = \rho \cdot C_p \frac{\partial T}{\partial t} + \nabla \cdot (-k \cdot \nabla T) \qquad \textbf{(2-5)}$$

20

where T [K] is the temperature, t [s] is the sampling time, Q [J/m²] is the pulse energy absorbed by the surface, ρ [kg/m³] is the mass density, C_p [J/(kg·K)] is the specific heat capacity, k [W/(m·K)] is the thermal conductivity of the material.

The heat diffusion through isotropic solid is a complex 3D problem that can be simplified by Fourier's law of heat diffusion [33], [39], [48] which can be expressed as

$$\nabla^2 T - \frac{1}{\alpha} \cdot \frac{\partial T}{\partial t} = 0$$

(2-6)

The one-dimensional solution of Fourier equation for the propagation of a Dirac heat pulse in a semi-infinite isotropic solid [33], [36], [39], [48] can be expressed as

$$T(L, t) = T_i + \frac{Q}{\sqrt{\rho C_p k \pi t}} \exp\left(-\frac{L^2}{4\alpha t}\right)$$

(2-7)

where $T(L, t)$ means the temperature at time t and depth L, L [m] is the depth from the heated surface, T_i [K] is the initial temperature, and $\alpha = \frac{k}{\rho C_p}$ [m²/s] is the thermal diffusivity. Equation (2-7) can be rewritten as

$$T(L, t) = T_i + \frac{Q}{e\sqrt{\pi t}} \exp\left(-\frac{L^2}{4\alpha t}\right)$$

(2-8)

where $e = \sqrt{\rho C_p k}$ is thermal effusivity of the material (J/(s^{1/2}·m²·K)). At the surface (L = 0 mm), Equation (2-8) can be rewritten as

$$T(0, t) = T_i + \frac{Q}{e\sqrt{\pi t}}$$

(2-9)

2.3.2 Lock-in Thermography

Lock-in thermography is a periodic excitation method. It is also known as modulated thermography [33], [39], [42], [49], [50]. The one-dimensional solution

of the Fourier's law for a periodic thermal wave through a semi-infinite homogeneous material [33], [39], [51] can be expressed as

$$T(L,t) = T_i \exp\left(-\frac{L}{\mu}\right) \cos\left(\frac{2\pi L}{\lambda} - \omega t\right) \tag{2-10}$$

$$\mu = \sqrt{\frac{2 \cdot \alpha}{\omega}} \tag{2-11}$$

or

$$\mu = \sqrt{\frac{\alpha}{\pi \cdot f}} \tag{2-12}$$

where $T(L,t)$ is the temperature at time t and depth L, t [s] is sampling time, L [m] is the depth from the heated surface, T_i [°C] is the initial temperature change produced by the heat source, $\omega = 2\pi f$ [rad/s] is the modulation frequency, f [Hz] is the thermal wave frequency, $\lambda = 2\pi\mu$ [m] is the thermal wavelength, μ [m] is the thermal diffusion length, and α [m²/s] is the thermal diffusivity. The surface temperature in the time domain [52] can be expressed as

$$T(0,t) = q_0 \sqrt{RE^2 + IM^2} \sin\left[\omega t + \tan^{-1}\left(\frac{IM}{RE}\right)\right] \tag{2-13}$$

the real part is expressed as:

$$RE = \frac{1}{2k\beta}\left[\frac{1 - \exp(-4\beta L) + 2\exp(-2\beta L)\sin(-2\beta L)}{1 + \exp(-4\beta L) - 2\exp(-2\beta L)\cos(-2\beta L)}\right] \tag{2-14}$$

the imaginary part is expressed as

$$IM = \frac{-1}{2k\beta}\left[\frac{1 - \exp(-4\beta L) + 2\exp(-2\beta L)\sin(-2\beta L)}{1 + \exp(-4\beta L) - 2\exp(-2\beta L)\cos(-2\beta L)}\right] \tag{2-15}$$

where q_0 [W/m²] is the incident peak heat flux intensity, k [W/(m·K)] is the thermal conductivity.

$$\beta = \frac{1}{\mu} \tag{2-16}$$

The real and imaginary parts of the complex transform are used to estimate the amplitude and phase. The amplitude (A) [33] can be derived as

$$A = \sqrt{RE^2 + IM^2}$$

(2-17)

the difference of phase angle (φ) between the surface temperature and reference excitation modulation heat flux [52] can be derived as

$$\varphi = \tan^{-1}\left(\frac{IM}{RE}\right)$$

(2-18)

when RE and IM in Equation (2-18) are replaced with Equation (2-14) and Equation (2-15), Equation (2-18) can be rewritten as

$$\varphi = \tan^{-1}\left[-\frac{1 - \exp(-4\beta L) - 2\exp(-2\beta L)\sin(-2\beta L)}{1 - \exp(-4\beta L) + 2\exp(-2\beta L)\sin(-2\beta L)}\right]$$

(2-19)

Empirical expressions of direct relationship between the defect depth and the thermal diffusion length have been proposed [16], [53]. The relationship is given as

$$L = C_1 \cdot \mu$$

(2-20)

Equation (2-20) can be rewritten as

$$L = C_1 \cdot \sqrt{\frac{\alpha}{\pi \cdot f_b}}$$

(2-21)

where f_b [Hz] is the blind frequency [54], C_1 is an empirical constant that is usually in the range of 1.5 to 2, such as $C_1 = 1.82$ [16], [53].

Sinusoidal waves are typically used as a modulated periodic source, and the common excitation sources are halogen lamps or LED lamps. The periodic thermal wave from the excitation source propagates through the air and heat on the surface of the specimen. The heat propagates into the material and blocked by the internal defect, which produces the change of the amplitude and phase of the response signal at the surface of the specimen. Internal defects can be

23

evaluated from the phase shift and the amplitude of the measured signal. Typical set-up of lock-in thermography is shown in Figure 2-14.

The lock-in thermography is suitable for analysing materials which have low thermal diffusivity and large surface. However, this approach is in general slower than other approaches such as pulsed thermography.
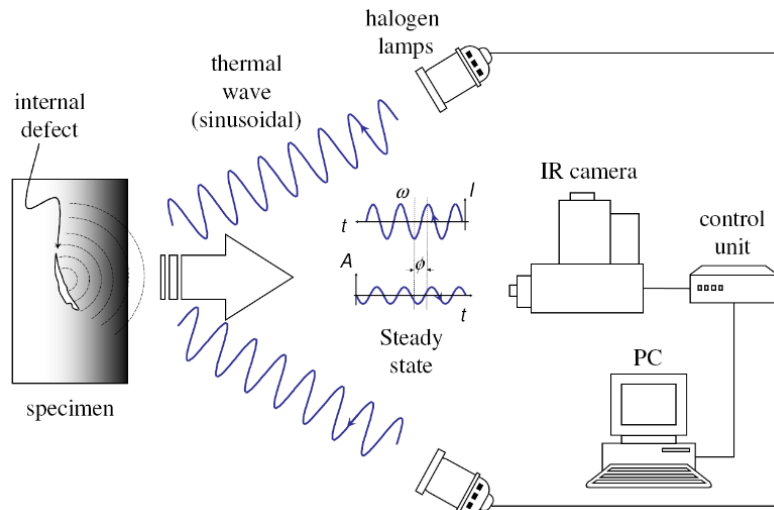
Figure 2-14 A typical set-up of lock-in thermography [33]

2.3.3 Ultrasound Thermography

Ultrasound thermography is also well known as vibro-thermography (VT) [55] or thermosonic [56]. Typical set-up of ultrasound thermography is shown in Figure 2-15. There are basically two configurations in ultrasound thermography: lock-in approach and burst approach, shown in Figure 2-15(a) and Figure 2-15(b), respectively. These two configurations can be considered as optical methods such as LT and PT. The lock-in approach is similar to LT and the burst approach is similar to PT. The specimen is stimulated internally by a mechanical excitation source. Normally, ultrasound wave, frequency between 15 kHz to 40 kHz, is applied into the specimen by using a transducer, which is connected to the specimen. Usually, coupling material, inserted between the transducer and the specimen, is used to avoid damage of the specimen and correct misalignment [33], [39]. The mechanical energy is transmitted into the specimen, is converted

to thermal energy and spread surround inside the material in the form of heatwave, then dissipates through the internal defect and travels to the specimen's surface and is detected by an infrared camera.

(a)

(b)
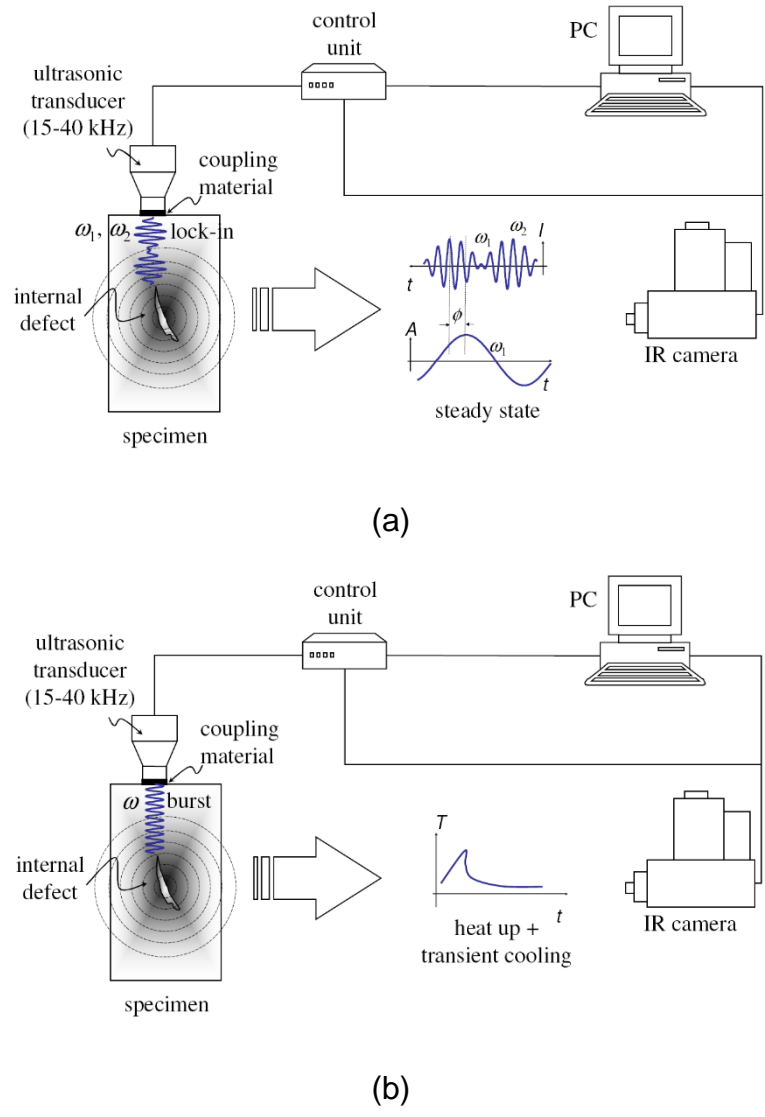
Figure 2-15 A typical set-up of ultrasound thermography (a) lock-in ultrasound thermography approach (b) burst ultrasound thermography approach [33]

2.3.4 Eddy Current Thermography

Eddy current thermography (ECT) is an induction thermography which compounds the advantages of eddy current testing and thermography. Based on the stimulation method, it can be divided into two main configurations: pulsed approach (eddy current pulsed thermography, ECPT) and lock-in approach (eddy

current lock-in thermography, ECLT) [57]. The basic configuration of eddy current thermography is shown in Figure 2-16.
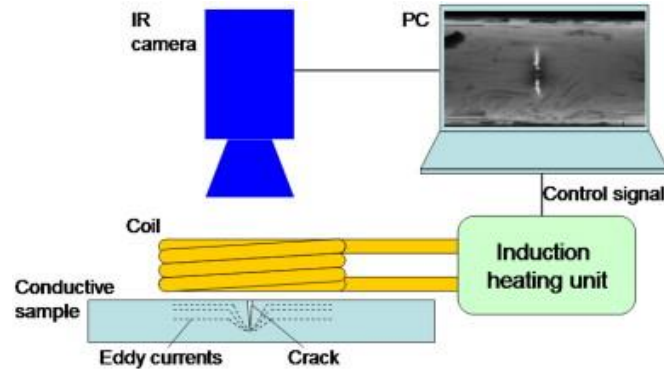
Figure 2-16 Basic configuration of eddy current thermography system [58]

The sample is heated by eddy currents induced by electric currents in the coil produced from the induction heating unit. Then, the heat resistance in the conductive sample is generated. The change of the induced eddy current flow is used to detect defects through monitoring the temperature distribution on the sample's surface which is captured by an IR camera and recorded in a PC [59].

The depth of the induction current flow can be described by the electromagnetic skin depth or penetration depth (δ) [60], [61], [62], expressed as

$$\delta = \frac{1}{\sqrt{\pi f \sigma \mu}} \qquad \text{(2-22)}$$

where f [Hz] is the electromagnetic frequency of the excitation (typically 50 – 500 kHz), μ [H/m] is the magnetic permeability of the material, and σ [S/m] is the electrical conductivity of the material.

The flows of eddy current in the sample generate the resistive heat (Q), known as Joule heating, which is proportional to the square of the eddy current density (J_s),

$$Q = \frac{1}{\sigma}|J_s|^2 \qquad \text{(2-23)}$$

or which is proportional to the square of the electric field intensity (E),

$$Q = \frac{1}{\sigma}|\sigma E|^2 \qquad \text{(2-24)}$$

The heat conduction of the sample caused by Joule heating can be given by

$$Q = \rho C_p \frac{\partial T}{\partial t} - \nabla \cdot k\nabla T \qquad \text{(2-25)}$$

where k [W/m·K] is the thermal conductivity of the material, ρ [kg/m³] is the density of the material, C_p [J/kg·K] is the specific heat capacity of the material. The thermal diffusion process is given by

$$\frac{\partial T}{\partial t} = \frac{k}{\rho C_p}\left(\frac{\partial^2 T}{\partial x^2} + \frac{\partial^2 T}{\partial y^2} + \frac{\partial^2 T}{\partial z^2}\right) + \frac{1}{\rho C_p} q(x,y,z,t) \qquad \text{(2-26)}$$

where $T = T(x,y,z,t)$ is the temperature distribution, $q(x,y,z,t)$ is the internal heat generation function per unit volume and unit time.

In addition, the defect depth can be quantified from the heat waves (caused by a Joule heating) propagated within the material [63]. In pulsed approach, the depth of the thermal propagation at observation time t_{obs}, the penetration depth (μ_T) is given by

$$\mu_T = 2\sqrt{\alpha t_{obs}} \qquad \text{(2-27)}$$

In lock-in approach, the depth of the thermal propagation at modulation frequency f_{mod}, the penetration depth (μ_T) is given by

$$\mu_T = \sqrt{\frac{\alpha}{\pi f_{mod}}} \qquad \text{(2-28)}$$

where α is thermal diffusivity of the material (m²/s),

$$\alpha = \frac{k}{\rho C_p} \qquad \text{(2-29)}$$

2.3.5 Comparison of Thermographic Inspection Method

Each thermographic inspection method has advantages and limitations. Table 2-1 compares the capability of inspection between optical thermography, ultrasound thermography and eddy current thermography. From the table, it is found that all methods can detect voids subsurface defect with various types of excitation waveform (e.g., pulse and lock-in), while optical thermography and eddy current thermography can also detect delamination defect. When considering the method of excitation, only optical thermography and eddy current thermography are non-contact method. In terms of the capability of the application for non-conductive materials between optical thermography and eddy current thermography, it is found that optical thermography is more suitable than eddy current thermography.

Table 2-1 The comparison of capability between optical thermography, ultrasound thermography and eddy current thermography

Capability of Inspection	Optical Thermography	Ultrasound Thermography	Eddy Current Thermography
Contactless of excitation source	✓		✓
Various excitation waveform	✓	✓	✓
Suitable for voids subsurface defect	✓	✓	✓
Suitable for delamination defect	✓		✓
Suitable for surface-breaking cracks			✓
Suitable for non-conductive materials	✓	✓	

Considering the aim of this thesis, pulsed thermography is selected because this technique offers the most rapid inspection, and also is proven as a high performance technique to quantify subsurface defect size and depths, which is crucial for 3D defect reconstruction.

2.4 Defect Depth Measurement based on Pulsed Thermography

Many methods of defect detection and depth measurement in pulsed thermography have been presented in the last 20 years. Raw data for analysis may be stored in the form of a 3D matrix, as shown in Figure 2-17(a). The temperature decay on the surface by time was normally used to analyse the defect, as shown in Figure 2-17(b). The cooling behaviour between t^* to t^{**} is associated with the size, the depth, and the thickness of the defect. Most defect depth measurement methods relied on the relationship between defect depth and the temperature deviation time (t^*). Various methods evaluate the defect depth from the thermal contrast or the peak time of the first or the second derivative of the temperature decay curve. For example, the peak slope time (PST) method [64] is corresponding to the peak time of the first derivative of thermal contrast. It was found that PST is approximately proportional to the square of the defect depth. The logarithmic second derivative (LSD) method [40] uses the peak time of the second derivative of temperature decay in the logarithmic scale to determine defect depth. Most methods start with heating to the surface of the specimen. The surface then absorbs the heat and its temperature increases immediately. After that, the thermal wave propagates inside the specimen causing diminution on the surface's temperature.

(a)   (b)
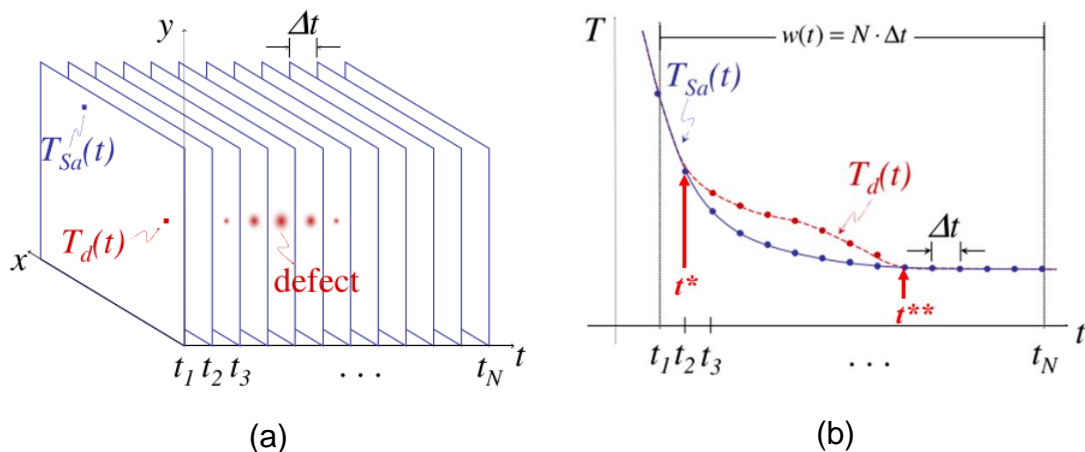
Figure 2-17 Temperature evolution (a) data3D matrix (b) temperature profile for a non-defect point (T_{Sa}, blue curve) and defect point (T_d, red curve) [33]

The emissivity and reflectivity of the material's surface can have strong effect on the measurement [65]. The performance of measurement based on optical thermography can be strongly influenced by uneven emissivity of the surface [66]. The level of emissivity can be influenced by several causes such as condition of surface, type of material, etc. Many works (e.g., [67], [68], [69], [70], [71], [72]) have attempted to reduce the influence of emissivity. For example, a classic and straightforward method is painting the matt black or non-reflective black on the sample's surface to reduce the reflective light, increase the thermal absorption, and increase the uniform distribution of surface emissivity.

2.4.1 Temperature Contrast Method

At the early period, the temperature contrast method (TC) [14] was mainly used for the defect detection purpose. There are four common temperature contrast techniques including absolute contrast, running contrast, normalised contrast, and standard contrast. The basic definition of temperature contrast is the "Absolute Temperature Contrast", which measures the dissimilarity in temperature between a faulty region and a non-faulty region [14]. A typical temperature contrast curve is shown in Figure 2-18. The absolute temperature contrast [14] method is defined as

$$TC_{abs}(t) = T_{def}(t) - T_{snd}(t) \tag{2-30}$$

where $T_{def}(t)$ is temperature over defect area and $T_{snd}(t)$ is temperature over a sound area (non-defect area). Elevated $TC_{abs}(t)$ means higher visibility for the defect. The contrast of the temperature over a defective area is not constant. There is a divergence, with initial elevation followed by eventual diminishment.

The running temperature contrast technique was developed to reduce the effects of emissivity different in surface, defined as

$$TC_{run} = \frac{T_{def}(t) - T_{snd}(t)}{T_{snd}(t)} \tag{2-31}$$

The normalised temperature contrast technique is computed in the proportion of the temperature at the end time of the thermal process, t_{end}, (the temperature at the last frame) or the time of maximum temperature, t_{max}, (the temperature at the first frame), defined as

$$TC_{nor} = \frac{T_{def}(t)}{T_{def}(t_n)} - \frac{T_{snd}(t)}{T_{snd}(t_n)} \qquad \textbf{(2-32)}$$

where t_n is either t_{end} or t_{max}.

The standard temperature contrast technique was developed to dispose of contributions of the surrounding environment by subtracting with the temperature at pre-flash time, t_p, defined as

$$TC_{std} = \frac{T_{def}(t) - T_{def}(t_p)}{T_{snd}(t) - T_{snd}(t_p)} \qquad \textbf{(2-33)}$$

Temperature contrast relates to the depth of the defect, such an example in Figure 2-18. Defect depth can be estimated by the peak contrast time determined by the plot of temperature contrast and time. The peak contrast time (t_{PCT}) refers the time at the maximum value of the temperature contrast. The peak contrast time increases follow the increase of defect depth, and it is also a function of defect size and shape [47].
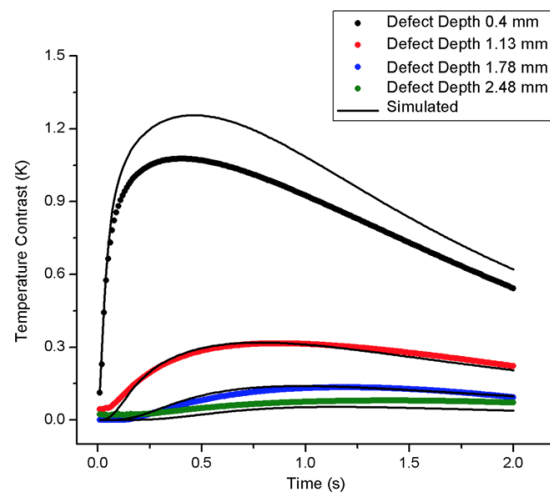
Figure 2-18 A temperature contrast curve [47]

31

2.4.2 Peak Slope Time Method

The peak slope time (PST) method is corresponding to the peak time of the first derivative of temperature contrast. Defect depth can be estimated by the time at the peak slope. The peak slope time (t_{PST}) is introduced as a peak contrast derivative time [64] and provided by

$$t_{PST} = \frac{3.64L^2}{\pi^2\alpha} \qquad \text{(2-34)}$$

alternatively, if the peak time is obtained, defect depth can be computed as

$$L = \sqrt{\frac{\pi^2\alpha \cdot t_{PST}}{3.64}} \qquad \text{(2-35)}$$

where L [m] is defect depth, α [m²/s] is thermal diffusivity. It was found that the contrast derivative method is also approximately proportional to the square of the defect depth, and the proportionality coefficient does not depend on defect size [73]. The major problem of this method is to determine a reference point from the sound area. Harry *et al.* [64] suggested a method to use the average temperature of the entire surface as the reference temperature.

2.4.3 Logarithmic Second Derivative Method

Shepard *et al.* [40] proposed that the time at the peak slope of the second derivative of temperature on the surface in a logarithmic domain can be used to determine defect depth. Temperature variation on the surface [74] is given by

$$T(t) = \frac{Q}{\sqrt{\pi\rho C_p kt}} \qquad \text{(2-36)}$$

where $T(t)$ is the temperature variation of the surface at time t, Q [J/m²] is the energy deposited on the surface of the material, ρ [kg/m³] is the density of the material, C_p [J/kg·K] is the specific heat capacity of the material, k [W/m·K] is thermal conductivity of the material, and t [s] is the observed time.

The temperature in the logarithmic domain [47] can be express below:

$$ln\big(T(t)\big) = ln\left(\frac{Q}{\sqrt{\pi\rho C_p k}}\right) - \frac{1}{2} ln\,(t) \qquad \textbf{(2-37)}$$

or

$$ln\big(T(t)\big) = ln\left(\frac{Q}{e\sqrt{\pi}}\right) - \frac{1}{2} ln\,(t) \qquad \textbf{(2-38)}$$

where e [m] is thermal effusivity ($e = \sqrt{\rho C_p k}$). It is found that the temperature and time curve in the logarithmic domain has a linear relationship with slope -0.5 [75]. Deviation from the linear response is related to the temperature response of a defective area. The peak time can be computed directly from the temperature decay curve (without the need of a reference point) by taking the second derivative of both log temperature and log time. The time at the peak slope of the second derivative [76] is given below:

$$t_{LSD} = \frac{L^2}{\pi\alpha} \qquad \textbf{(2-39)}$$

where α is thermal diffusivity ($\alpha = \frac{k}{\rho c}$) and L is defect depth. Alternatively, if the peak time is obtained, defect depth can be computed as

$$L = \sqrt{\pi\alpha \cdot t_{LSD}} \qquad \textbf{(2-40)}$$

The peak time of the logarithmic second derivative method (LSD), t_{LSD}, is less than that of the temperature contrast derivative method, t_{PST}, which means the peak second derivative time appears earlier, and has less affected by three-dimensional heat diffusion.

However, finding the peak time with the second derivative method is quite sensitive to noise. Shepard [75] proposed a Thermal Signal Reconstruction (TSR) method to reduce temporal noise using a high order polynomial model to fit the raw temperature decay curve. The model is written as

$$ln\big(T(t)\big) = \sum_{n=0}^{N} a_n(ln(t))^n \qquad \text{(2-41)}$$

where N is the order of the polynomial function, a_n are coefficients to be estimated from the polynomial function. The unknown coefficients a_n can be estimated by the least square method. The raw temperature can be replaced by the reconstructed thermal data. The first derivative of $ln\big(T(t)\big)$ can be direct computed by

$$\frac{d\,ln\big(T(t)\big)}{d\,ln(t)} = \sum_{n=1}^{N} a_n \cdot n \cdot (ln(t))^{n-1} \qquad \text{(2-42)}$$

and the second derivative can be computed by

$$\frac{d^2\,ln\big(T(t)\big)}{d\,ln^2(t)} = \sum_{n=2}^{N} a_n \cdot n \cdot (n-1) \cdot (ln(t))^{n-2} \qquad \text{(2-43)}$$

There are some advantages of using TSR data over raw thermal data, for example, increased signal to noise ratio (SNR), saving storage, etc.

2.4.4 Absolute Peak Slope Time Method

Zeng *et al.* [77] proposed a defect depth measurement based on the analysis of a theoretical one-dimensional solution of pulsed thermography [78], [79] given by

$$\Delta T(t) = \frac{Q}{e\sqrt{\pi t}} \left[1 + 2 \sum_{n=1}^{\infty} exp\left(-\frac{n^2 L^2}{\alpha t}\right) \right] \qquad \text{(2-44)}$$

where L is defect depth or sample thickness, α is the thermal diffusivity, e is thermal effusivity, Q is the energy.

The Absolute Peak Slope Time (APST) method was developed from the concept of the PST method. PST method needs a reference point to estimate defect depth, but APST method does not need a reference point. In order to get a specific characteristic time with does not need a reference point, both sides of

34

Equation (2-44) are initially multiplied with $\sqrt{t}$ and the new time-dependent function $f(t)$ can be characterised as

$$f(t) = \Delta T(t) \cdot \sqrt{t} = \frac{Q}{e\sqrt{\pi}} \left[1 + 2 \sum_{n=1}^{\infty} exp\left(-\frac{n^2 L^2}{\alpha t}\right) \right] \tag{2-45}$$

To find the absolute peak slope time, the first derivative of Equation (2-45) is taken as below:

$$f'(t) = \frac{2Q}{e\sqrt{\pi}} \left[1 + 2 \sum_{n=1}^{\infty} exp\left(-\frac{n^2 L^2}{\alpha t}\right) \cdot \frac{n^2 L^2}{\alpha t^2} \right] \tag{2-46}$$

the second derivative of Equation (2-45) is expressed as

$$f''(t) = \frac{2Q}{e\sqrt{\pi}} \left[1 + 2 \sum_{n=1}^{\infty} exp\left(-\frac{n^2 L^2}{\alpha t}\right) \cdot \frac{n^2 L^2}{\alpha t^3} \cdot \left(\frac{n^2 L^2}{\alpha t} - 2\right) \right] \tag{2-47}$$

The absolute peak slope time (t_{APST}) is corresponding time that the second derivative of $f(t)$ equals to zero, Equation (2-47) equals zero $(f''(t) = 0)$:

$$t_{APST} = \frac{L^2}{2\alpha} \tag{2-48}$$

The defect depth can be computed as

$$L = \sqrt{2\alpha \cdot t_{APST}} \tag{2-49}$$

2.4.5 Least-Squares Fitting Method

Sun [76], [80] proposed a defect depth prediction based on a least-squares fitting method. Commonly, the curve fitting methods, including the least-squares fitting method, are not sensitive to noise. This method applies a theoretical heat transfer model to fit the temperature decay curve at each point on the surface. The proposed analytical model for the time period $0 < t < t_b$ is approximately expressed as

$$T(t) \approx A\left[1 + 2\sum_{n=1}^{\infty} exp\left(-\frac{n^2\pi^2}{L^2}\alpha t\right)\right] - st \tag{2-50}$$

where T is temperature on the surface, A is an amplitude, α is thermal diffusivity, t is sampling duration, L is defect depth if the point on the defect area (point 1 in Figure 2-19(a)) or sample's thickness if the point is on the sound area (point 2 in Figure 2-19(a)), and s is slope which determined by a linear fitting in the time period $t_a < t < t_b$ (see in Figure 2-19(b)), by using various calculations from the experiment, time instants t_a and t_b were optimised and selected as

$$t_a = \frac{L^2}{2\alpha} \tag{2-51}$$

and

$$t_b = 3t_a \tag{2-52}$$

Typically, the slope s is small and zero for the inspected point which is on the sound area of uniform thickness. It is observed that the time instant t_a coincides to the t_{APST} of absolute peak slope time method [77].

(a)   (b)
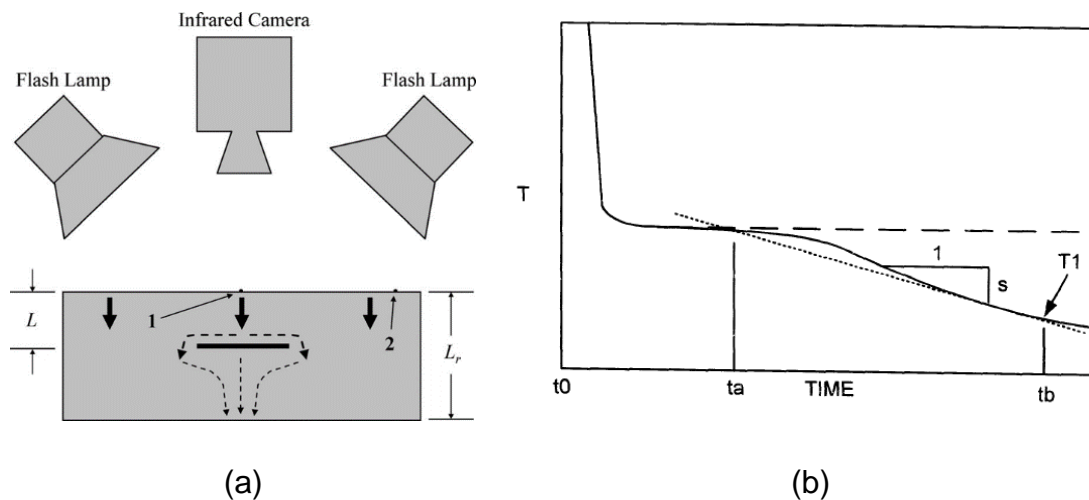
Figure 2-19 (a) Heat conduction through and around lateral crack at point 1 (b) Surface temperature decay curve at point 1 [76], [80]

2.5 Defect Reconstruction

In inversion quantitative non-destructive evaluation (QNDE), defects can be analysed and reconstructed based on methods of inverse problem and forward problem. The inverse problem refers to the reconstruction of the unknown defect information (e.g., defect shape, defect size, defect depth, and defect thickness) from the inspection data (e.g., temperature sequences on the surface's sample), which can be evaluated by inverse methods such as mathematical optimisation method and stochastic optimisation method (e.g., genetic algorithm and neural network). In contrast, the forward problem refers to the analysis of the acquiring inspection data from the known properties of sample and defect information, which can be performed by forward methods such as simulation methods. Figure 2-20 illustrates the category of defect reconstruction methods and different data analysis between the inverse problem and the forward problem is compared in Table 2-2.

Figure 2-21 illustrates the typical workflow of defect reconstruction by inversion analysis. The workflow starts with the establishing of the defect model (defect parameterisation) and forward problem simulation method. The residual error between the simulated data and the inspection data is then calculated. To calculate the residual error, an inverse problem approach (e.g., optimisation technique) is applied to compute the optimal defect parameters by iteratively updating the defect parameters until the residual error is less than the criterion.
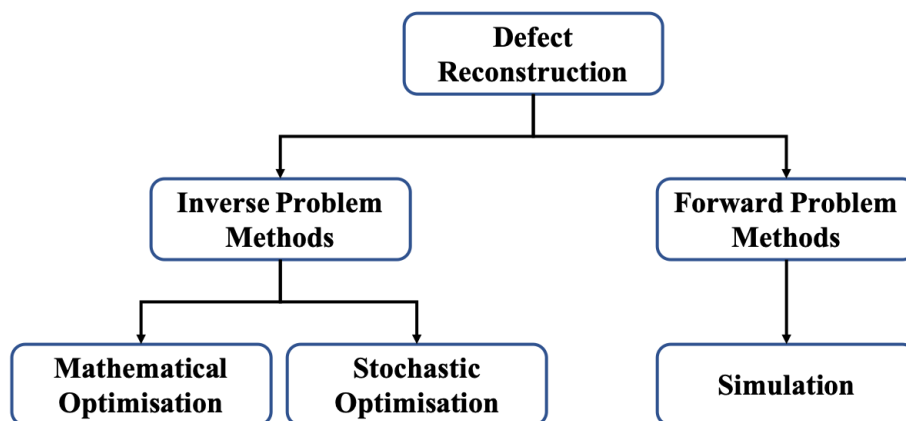
Figure 2-20 The category of defect reconstruction methods

Table 2-2 The comparison of the different analysis between inverse problem and forward problem

Model Type	Known input	Prediction
Inverse problem	Inspection data: temperature decay on the surface's sample	Defect information: defect shape, defect size, defect depth, defect thickness, and defect location.
Forward problem	Properties of the sample and defect: thermal conductivity, specific heat capacity, mass density, dimension of the sample and defect, and location of the defect	Inspection data: temperature profile occurred or changed of the sample
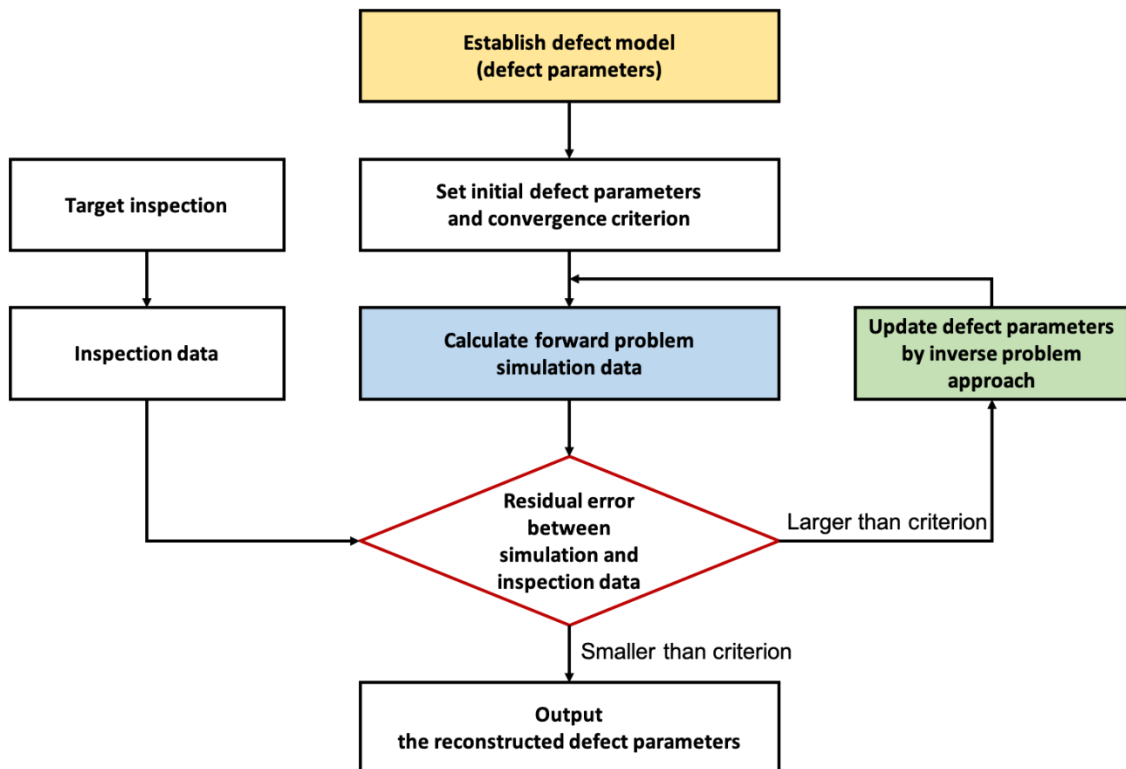
Figure 2-21 Typical workflow of defect reconstruction by inversion analysis [81]

In inversion QNDE, three main components: defect model (defect parameters), forward problem simulation, and inverse problem approach have been studied in different application areas. Several studies have presented applications of inversion analysis based on techniques for reconstruction of various types of defect information, including wall-thinning depth [82] and material thermal property [83]. In infrared thermography NDE, the inversion reconstruction approach has been proven to be effective in measurement of corrosion depth and delamination size and depth [84].

Liu *et al.* [81] proposed a strategy based on Fourier series fitting radiative radius of defect parameterisation and fast forward simulation, shown in Figure 2-22, to evaluate and reconstruct delamination defects in multi-layered structures, shown in Figure 2-23.
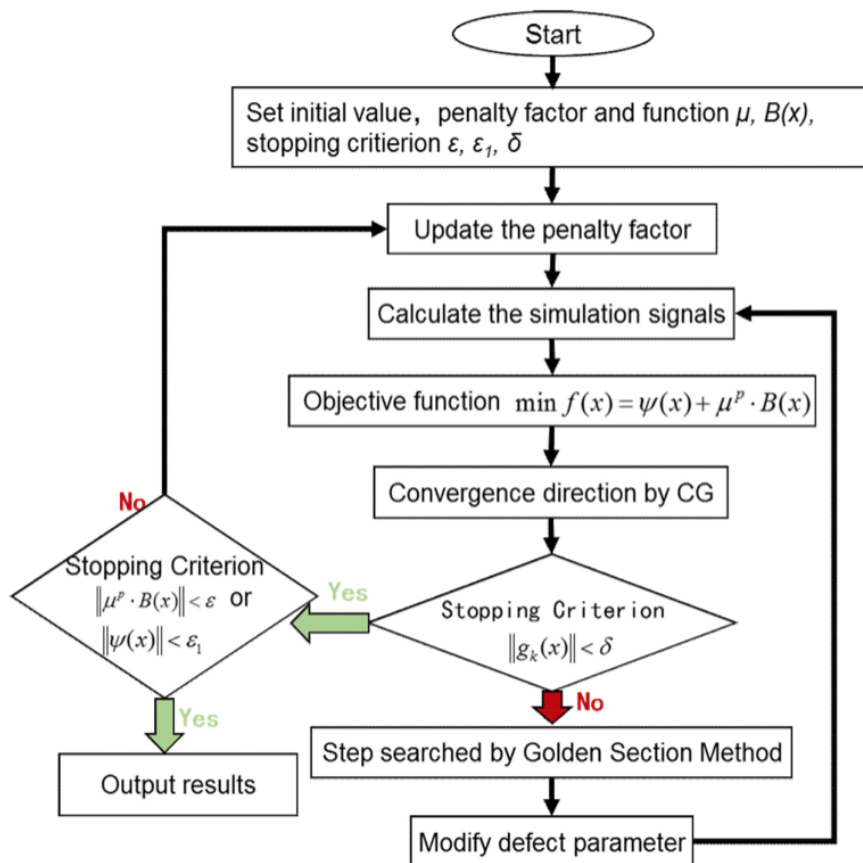
Figure 2-22 The defect profile reconstruction method proposed by Liu *et al.* [81]
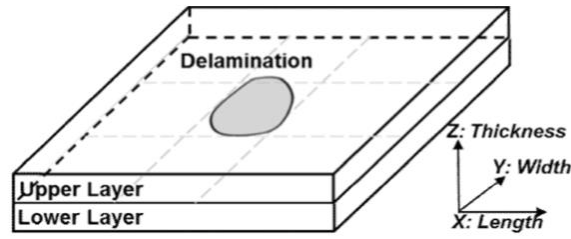
Figure 2-23 Delamination defects in multi-layered structures [81]
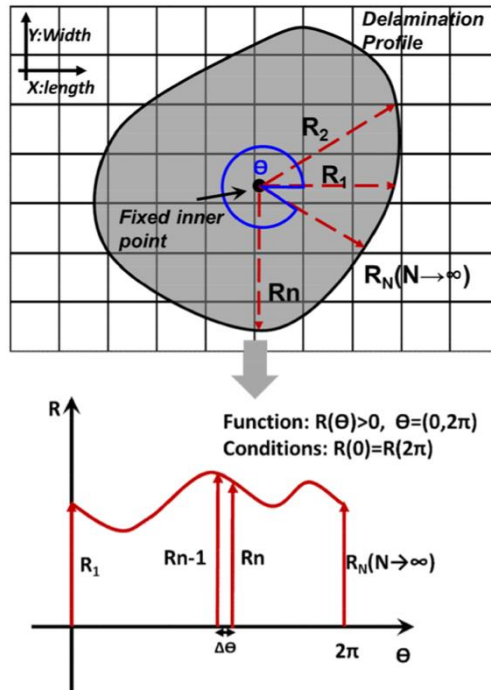
Figure 2-24 Defect parameterisation proposed by Liu *et al.* [81]

The defect shape is described by polynomial model based on Fourier series fitting radiative radius, $R(x, \theta)$. R_1 to R_n are the length of the variable sweeping radius, as shown in Figure 2-24.

$$R(x, \theta) = \frac{1}{2}x_0 + x_n \sum_{n=1}^{N} \cos(n\theta) + \varepsilon(\theta) \tag{2-53}$$

where x is the vector of defect parameters; θ is the angle of radius sweep from the X-axis which the value of θ is between 0 to 2π; N is the polynomial model order; $\varepsilon(\theta)$ is the high order noise, and x_0 and x_n are Fourier series coefficients representing the $R(x, \theta)$.

The objective function is constructed to compute residual error, expressed as

$$\min f(x) = \psi(x) + \mu^p \cdot B(x) \tag{2-54}$$

where x is the defect parameter vector, $\psi(x)$ is the residual between simulated feature data and experimental observed feature data, μ^p is the penalty factor, and $B(x)$ is the interior penalty function, Equation (2-54) is rewritten as

$$\min f(x) = \sum_{n=1}^{M} |T_n^{cal}(x) - T_n^{obs}|^2 + \sum_{j=1}^{NR} \left(\frac{\mu^p}{R_j(x)} + \frac{\mu^p}{R_{max} - R_j(x)} \right) \tag{2-55}$$

where R is the length of the variable sweeping radius, R_{max} is the maximum radius length of suspect region that contains the delamination used in the fast forward simulation, T_n^{cal} is the simulated feature data, T_n^{obs} is the experimental observed feature data, M is the number of feature data, NR is the number of radius used for defect parameterisation. The defect parameter is updated by the conjunction gradient (CG) algorithm, the updating direction (d_k) is written as

$$d_k = \begin{cases} -g_k & (if \ k = 1) \\ -g_k + \beta_k d_{k-1} & (if \ k \geq 2) \end{cases}, \qquad \beta_k^{FR} = \frac{\|g_k\|^2}{\|g_{k-1}\|^2} \tag{2-56}$$

where β_k is the updating direction coefficient in CG, β_k^{FR} is the updating direction strategy used in the Fletcher–Reeves nonlinear CG method, and k is the iteration step. The gradient is calculated by

$$g_k(x_i) = \frac{\partial f(x)}{\partial(x_i)} \tag{2-57}$$

Equation (2-57) is rewritten as

$$g_k(x_i) = 2 \sum_{n=1}^{M} \left((T_n^{cal} - T_n^{obs}) \cdot \frac{\partial T_n^{cal}(x)}{\partial x_i} \right)$$
$$+ \mu^p \cdot \sum_{j=1}^{NR} \left(\frac{1}{(R_{max} - R_j(x_i))^2} - \frac{1}{(R_j(x_i))^2} \right) \cdot \frac{\partial R_j(x)}{\partial(x_i)} \tag{2-58}$$

where $\frac{\partial T_n^{cal}(x)}{\partial x_i}$ and $\frac{\partial R_j(x)}{\partial(x_i)}$ are calculated by the differential derivative method. The residual and defect parameter are iteratively computed and updated until the value of $\|g_k(x)\|$, $\|\psi(x)\|$, and $\|\mu^p \cdot B(x)\|$ are smaller than the criterion.

Richter *et al.* [85] proposed Levenberg-Marquardt with echo defect shape method to reconstruct back wall geometry by means of active thermography. The reconstruction procedure is shown in Figure 2-25.
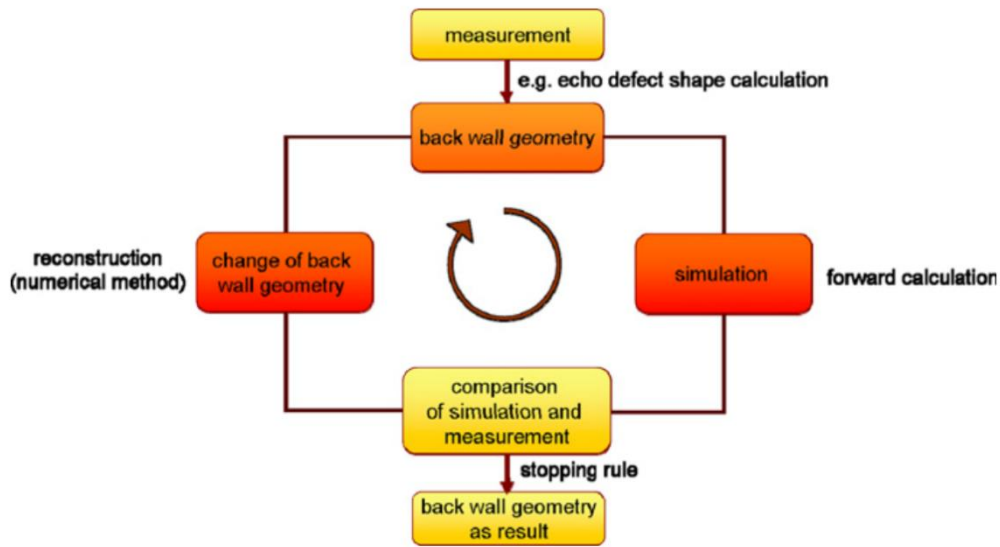
Figure 2-25 Inversion procedure used for back wall geometry reconstruction by Richter *et al.* [85]

The first procedure starts with initialling the back wall geometry by echo defect shape method [86]. The back wall geometry is yielded by the experimental data. The temperature on the sample's surface is measured. The relative contrast with respect to a reference area is expressed as

$$C_{rel}(t) = \frac{T_{defect}(t) - T_{reference}(t)}{T_{reference}(t)} \qquad \textbf{(2-59)}$$

where $C_{rel}(t)$ is the relative contrast at time t, $T_{defect}(t)$ is the temperature above the defective area at time t, $T_{reference}(t)$ is the temperature above the non-defective reference area at time t, the remaining thickness of the sample can be evaluated by

$$y = \sqrt{-\frac{kt}{\rho c} \cdot (\ln (C_{rel}(t)))} \qquad \textbf{(2-60)}$$

where k is the thermal conductivity, ρ is the mass density, c is the specific heat capacity, and t is the time elapsed after the delta pulse heating. Richter *et al.* defined the $C_{rel}(t)$ as 0.07 to evaluate the thickness/back wall geometry, the echo defect shape is applied as

$$y = \sqrt{-\frac{kt}{\rho c} \cdot (\ln (0.07))} \qquad \textbf{(2-61)}$$

The second procedure is simulation (forward calculation). The temperature devolution is simulated by using finite element method (FEM). COMSOL Multiphysics, FEM software, is used to solve the transient heat equation for temperature-dependent material coefficients. The properties of the material (e.g., thermal diffusivity) are needed to know for the simulation.

The third procedure is reconstruction which means reversing the forward problem. The back wall geometry y relatives to the temperature devolution T, $F(y) = T$, if the temperature is measured by the experiment, the inverse function can be written as $F^{-1}(T) = y$. The Levenberg-Marquardt method [87] is applied to reconstruct the back wall geometry, expressed as

$$y_{k+1} = y_k + [F'(y_k)^T \cdot F'(y_k) + \alpha \cdot I]^{-1} \cdot F'(y_k)^T \cdot (T - F(y_k)) \qquad \textbf{(2-62)}$$

where y_{k+1} is the new back wall geometry, y_k is the guess of back wall geometry, T is the experimental data, $F(y_k)$ is the simulation data, $F'(y_k)$ is the derivative of $F(y_k)$, $F'(y_k)^T$ is the transpose matrix of the derivative of $F(y_k)$, I is the identity matrix, α is a regularisation parameter adjusted to the signal-to-noise ratio, and subscript k is iteration step.

The last procedure, comparing the experimental data and the simulated results, and change/update the back wall geometry by reconstruction method (Levenberg-Marquardt method). This procedure is done iteratively until the difference between the experimental data and the simulated data reaches the

certain value. This standard method is called discrepancy method. The certain value is set as 0.017 K, expressed as

$$\sqrt{\sum_{i=1}^{475 \cdot 591} \frac{(T_i - F_i(y_k))^2}{475 \cdot 591}} \leq 0.017 \qquad \textbf{(2-63)}$$

It is noted that, the interesting data are 475 pixels at the time interval of [10, 600] seconds.

Lugin and Netzelmann [86] proposed a method to reconstruct the defect shape from pulsed thermography data with known thermal properties. The method consists of two main units: defect shape correction unit and simulation unit. The structure of the proposed algorithm is shown in Figure 2-26. The defect shape correction unit is performed for extracting and refining the defect shape sequentially. The simulation unit is performed for simulating the process of thermal distribution in the tested sample (the thermal properties and the geometrical size are known).
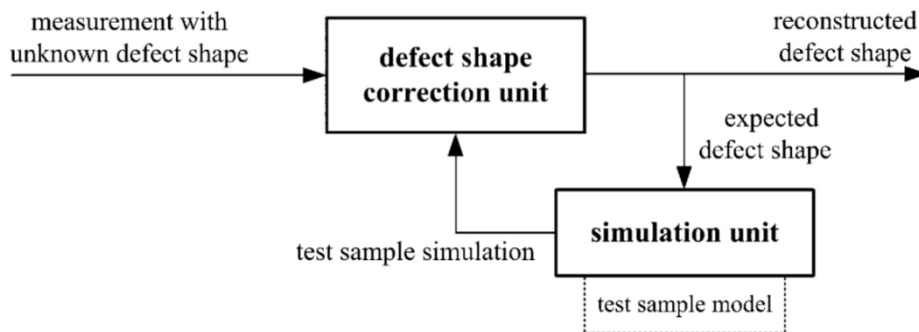
Figure 2-26 The algorithm structure of defect shape reconstruction proposed by Lugin and Netzelmann [86]

The algorithm starts with expecting the unknown defect shape by the defect shape correction unit, and transmits it to the simulation unit. The first unknown defect shape is computed by the echo defect shape method, the echo defect depth (D_{EDS}) is computed as

$$D_{EDS} = \sqrt{-\frac{\lambda t_k}{\rho c} \log\left(|T_{rel-incr}(t_k)|\right)} \qquad \textbf{(2-64)}$$

where λ is thermal conductivity of the sample, ρ is density of the sample, c is specific that capacity of the sample, $T_{rel-incr}(t_k)$ is the relative temperature contrast at time t_k. The extracted time t_k is shown in Figure 2-27, and the recommended value of $T_{rel-cont}$ is about 0.025.
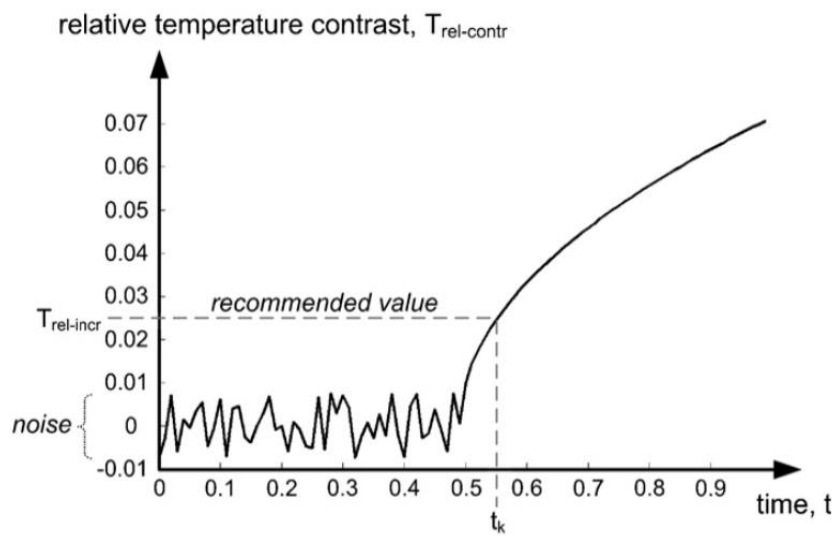
Figure 2-27 Extraction of the time t_k proposed by Lugin and Netzelmann [86]

The relative temperature contrast curve is computed by

$$T_{rel-cont}(t) = \frac{T_s(t) - T_{defect-free}(t)}{T_{defect-free}(t)} \qquad \textbf{(2-65)}$$

where $T_s(t)$ is the temperature curve on the analysed point, $T_{defect-free}(t)$ is the temperature curve on the defect-free point.

Then, the expected defect shape is transmitted to the simulation unit. The simulation unit simulates the thermal distribution from the expected defect shape, and returns the data to the defect shape correction unit. To simulate the thermal distribution, the thermal properties (e.g., thermal conductivity, density, and

specific heat capacity) and geometrical dimensions of the tested sample are pre-known. A commercial FEM software is used in this simulation.

Then, the defect shape correction unit is received the data from the simulation unit. The thermal distribution from the source measurement and the simulation is analysed and compared. The defect shape is refined and reconstructed by

$$DS_{S+1} = DS_S + (EDS_M - EDS_S)$$ **(2-66)**

where DS_{S+1} is the refined defect shape used for the next simulation $(S+1)$ or the output reconstructed defect shape, DS_S is the defect shape used in the last simulation, EDS_M is the echo defect shape computed from the measurement, and EDS_S is the echo defect shape computed from the simulation. After that, the refined defect shape is sent to the simulation unit again.

The process of the defect shape correction unit and simulation unit is repeated in the same order. The defect shape is refined iteratively until the simulation converges to the measurement. The reconstructed defect shape is produced after some iteration cycles.

Rodriguez and Nicolau [88] proposed a method based on inverse heat transfer approach to estimate thermal conductivity and defect depth. The inverse problem of the estimation of thermal conductivity and defect, a general ill-posed problem, is solved by conjugate gradient method (CGM) [89] and numerical sensitivity analysis method [90]. Figure 2-28 shows the implementation methodology for the estimation of thermal conductivity and defect depth.
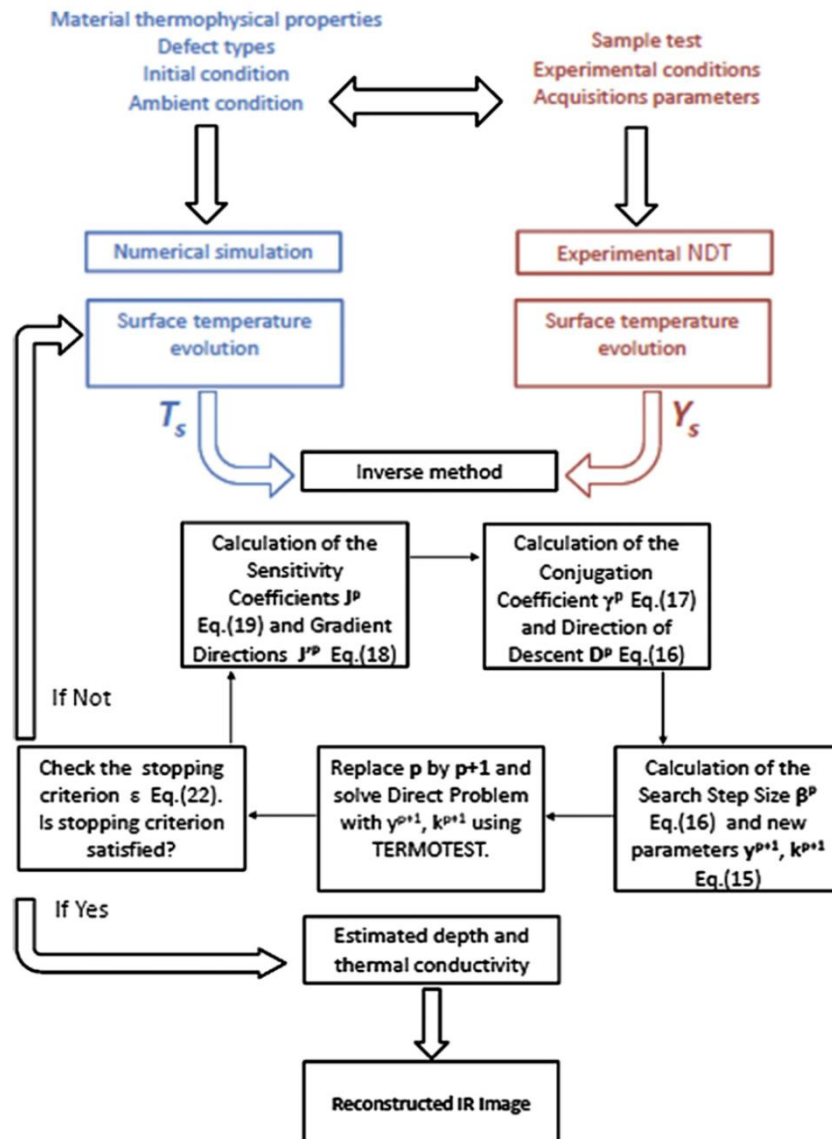
Figure 2-28 The implemented methodology for the estimation of defect depth and thermal conductivity proposed by Rodriguez and Nicolau [88]

The methodology is implemented through five main steps, as described below:

Step 1: Compute the sensitivity coefficients of thermal conductivity (J_k), the sensitivity coefficients of defect depth (J_y), the gradient direction of thermal conductivity at iteration p (J'^p_k), and the gradient direction of defect depth at iteration p (J'^p_y), defined by Equation (2-67) to (2-70), respectively.

$$J_k = \sum_{m=1}^{M} \frac{\partial T_s(x_m, t)}{\partial k} \tag{2-67}$$

$$J_y = \sum_{m=1}^{M} \frac{\partial T_s(x_m, t)}{\partial y} \tag{2-68}$$

$$J'^p_k = -2 \sum_{m=1}^{M} \int_{t=0}^{t_f} \frac{\partial T_s(x_m, t)^p}{\partial k} [Y_m(t) - T_s(x_m, t; k^p)] dt \tag{2-69}$$

$$J'^p_y = -2 \sum_{m=1}^{M} \int_{t=0}^{t_f} \frac{\partial T_s(x_m, t)^p}{\partial y} [Y_m(t) - T_s(x_m, t; y^p)] dt \tag{2-70}$$

where k is the thermal conductivity, y is the defect depth, t is time, $T_s(x_m, t)$ is the simulated temperature at position m, $Y_m(t)$ is the experimental temperature, superscript p is iteration level or time step, M is the total number of measured positions, and t_f is final time of the experiment. The partial derivatives $\frac{\partial T_s}{\partial k}$ and $\frac{\partial T_s}{\partial y}$ are computed by Equation (2-71) and (2-72), respectively.

$$\frac{\partial T_s}{\partial k} = \frac{T_s(k + \Delta k) - T_s(k)}{\Delta k} \tag{2-71}$$

$$\frac{\partial T_s}{\partial y} = \frac{T_s(y + \Delta y) - T_s(y)}{\Delta y} \tag{2-72}$$

where Δk is the perturbation of thermal conductivity and Δy is the perturbations of defect depth.

Step 2: Compute the conjugation coefficients of thermal conductivity (γ_k^p), the conjugation coefficients of depth (γ_y^p), the direction of descent of thermal conductivity (D_k^p), and the direction of descent of defect depth (γ_y^p), defined by Equation (2-73) to (2-76), respectively.

$$\gamma_k^p = \sum_{m=1}^{M} \int_{t=0}^{t_f} \frac{(J'^p_k)^2}{(J'^{p-1}_k)^2} dt \tag{2-73}$$

$$\gamma_y^p = \sum_{m=1}^{M} \int_{t=0}^{t_f} \frac{(J'^p_y)^2}{(J'^{p-1}_y)^2} dt \tag{2-74}$$

$$D_k^p = J'^p_k - \gamma_k^p D_k^{p-1} \tag{2-75}$$

$$D_y^p = J'^p_y - \gamma_y^p D_y^{p-1} \tag{2-76}$$

where superscript $p-1$ denotes the previous iteration.

Step 3: Calculate the search step size of thermal conductivity (β_k^p) and the search step size of defect depth (β_y^p) from Equation (2-77) and (2-78), respectively.

$$\beta_k^p = \sum_{m=1}^{M} \int_{t=0}^{tf} \frac{[Y_m(t) - T_s(x_m, t)][[J_k]^T D_k^p]}{\{[J_k]^T D_k^p\}^2} dt \tag{2-77}$$

$$\beta_y^p = \sum_{m=1}^{M} \int_{t=0}^{tf} \frac{[Y_m(t) - T_s(x_m, t)][[J_y]^T D_y^p]}{\{[J_y]^T D_y^p\}^2} dt \tag{2-78}$$

With the initial parameter of thermal conductivity k^p and the initial parameter of defect depth y^p, calculate the new estimated parameter of thermal conductivity (k^{p+1}) and the new estimated parameter of defect depth (y^{p+1}) from Equation (2-79) and (2-80), respectively.

$$k^{p+1} = k^p - \beta_k^p D_k^p \tag{2-79}$$

$$y^{p+1} = y^p - \beta_y^p D_y^p \tag{2-80}$$

Step 4: Replace p with $p+1$ and solve the direct problem (Thermal NDT Model) by using the computation algorithm *TermoTest*® in order to receive the temperature evolution map $T_s(i, k, t)$, as shown in Figure 2-29. The used numerical solver is based on finite volume method (FVM). The energy balance for an element volume is shown in Figure 2-30. The discrete energy balance for internal volume is expressed as

$$\frac{\rho C_p \Delta x \Delta y \Delta z}{\Delta t}\left(T_{(i,j,k)}^{p+1} - T_{(i,j,k)}^{p}\right)$$

$$= \frac{k}{\Delta x}\left(T_{(i-1,j,k)}^{p+1} - T_{(i,j,k)}^{p}\right)\Delta y \Delta z$$

$$+ \frac{k}{\Delta x}\left(T_{(i+1,j,k)}^{p+1} - T_{(i,j,k)}^{p}\right)\Delta y \Delta z$$

$$+ \frac{k}{\Delta y}\left(T_{(i,j-1,k)}^{p+1} - T_{(i,j,k)}^{p}\right)\Delta x \Delta z \qquad \textbf{(2-81)}$$

$$+ \frac{k}{\Delta y}\left(T_{(i,j+1,k)}^{p+1} - T_{(i,j,k)}^{p}\right)\Delta x \Delta z$$

$$+ \frac{k}{\Delta z}\left(T_{(i,j,k-1)}^{p+1} - T_{(i,j,k)}^{p}\right)\Delta x \Delta y$$

$$+ \frac{k}{\Delta z}\left(T_{(i,j,k+1)}^{p+1} - T_{(i,j,k)}^{p}\right)\Delta x \Delta y$$

where k is the thermal conductivity, ρ is the density, is C_p is the specific heat capacity, T is temperature, t is time, (i,j,k) is the grind points, and superscript p is the time step.
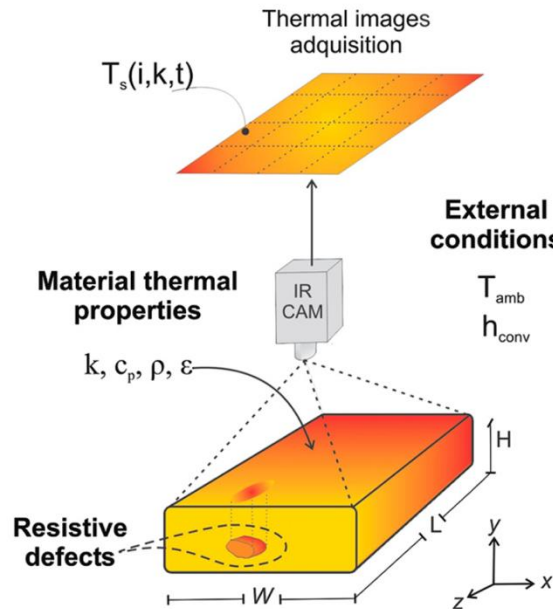
Figure 2-29 The thermal NDT model with the temperature evolution map $T_s(i,k,t)$ proposed by Rodriguez and Nicolau [88]
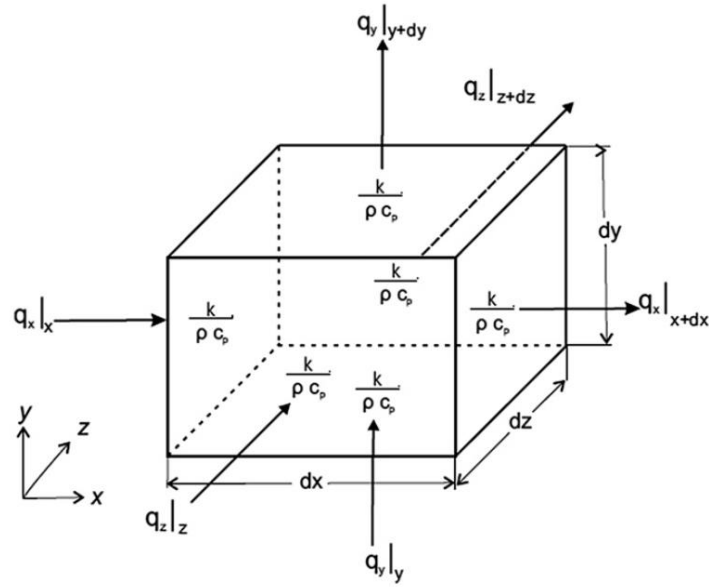
Figure 2-30 The energy balance for an element volume proposed by Rodriguez and Nicolau [88]

Step 5: Check the stopping criterion, if it is satisfied, return the estimated thermal conductivity and defect depth; if it is not satisfied, return to Step 1. The stopping criterion is given by

$$J^{p+1} < \varepsilon \tag{2-82}$$

$$\varepsilon = \sum_{m=1}^{M} \sigma_m t_f \tag{2-83}$$

$$\sigma_m \approx |Y_m(t) - T_s(x_m, t)| \tag{2-84}$$

where J^{p+1} is the sensitivity matrix or Jacobian, ε is the value of the tolerance, σ_m is the standard deviation of the measurement error at each instant time.

Elhassnaoui and Sahnoun [91] proposed a method for 3D reconstruction of a geometry defect located on the inaccessible surface of homogeneous materials without the need for thermal properties such as thermal diffusivity. Based on thermal distribution, this method analyses the thermal response on the sample's surface and computes defect distance (defect depth and sample thickness). It modifies the APST method [77], to evaluate defect distance of the sample

(distance from the sample's surface). They eliminated thermal diffusivity (α), which is a material's property, by dividing arbitrary two points from the sample surface. It can be written as

$$\frac{L_i}{L_j} = \sqrt{\frac{t_{APST_i}}{t_{APST_j}}}$$
(2-85)

Equation (2-85) can be rewritten as

$$L_i = \sqrt{\frac{t_{APST_i}}{t_{APST_j}}} \cdot L_j$$
(2-86)

where L_i is the defect depths at any point in the front of the surface, L_j is the sample thickness of the reference point which is chosen from the non-defect region. The 3D defect image is reconstructed from the values of L_i and L_j. The plate of steel and aluminium are simulated for the experiment. Each type of material is simulated with two defect shapes on the surface, an elliptical and a triangular shape, as shown in Figure 2-31(a) and Figure 2-31(b), respectively. The inspected side is shown in Figure 2-32. The examples of 3D reconstruction of the defect shapes are shown in Figure 2-33 and Figure 2-34. However, this method can only be applied to the characterisation of surface defects.
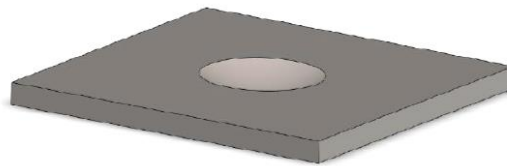
(a)
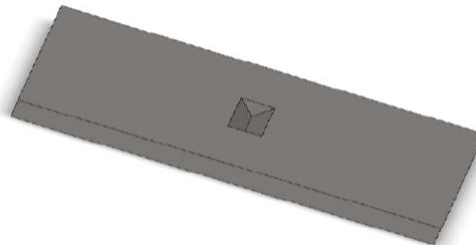
(b)

Figure 2-31 The simulated samples (a) elliptical defect (b) triangular defect [91]
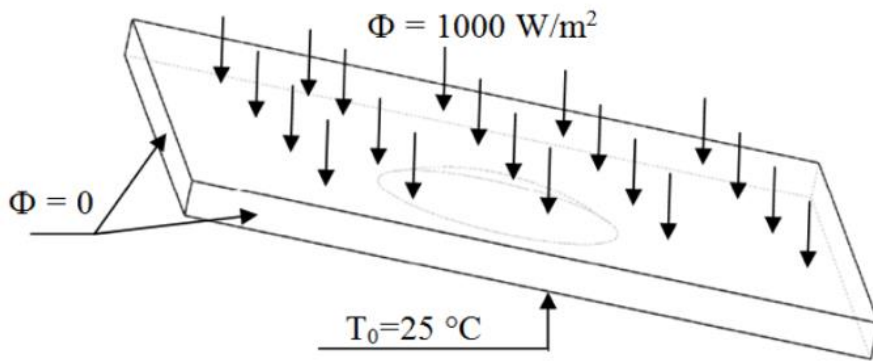
Figure 2-32 The inspected side of the simulated sample [91]
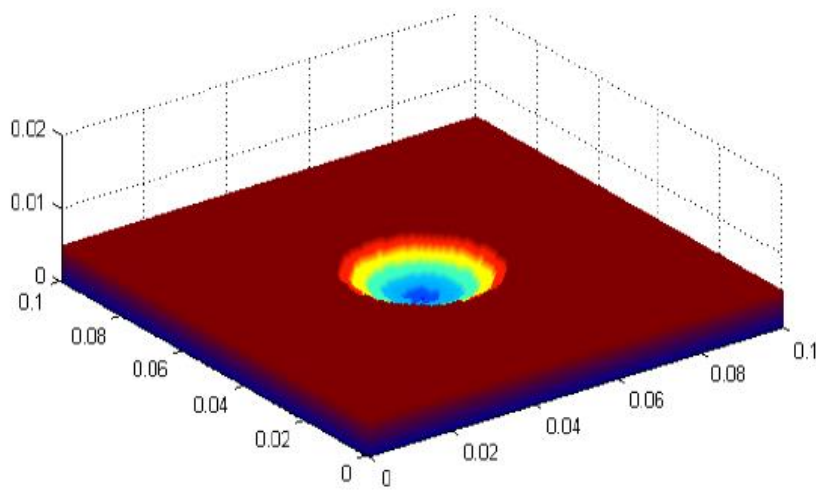
(a)
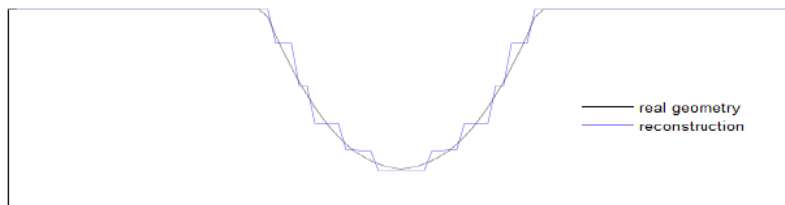
(b)

Figure 2-33 (a) 3D reconstruction of the triangular defect of the simulated steel sample (b) the corresponding section along the plane at the side view [91]
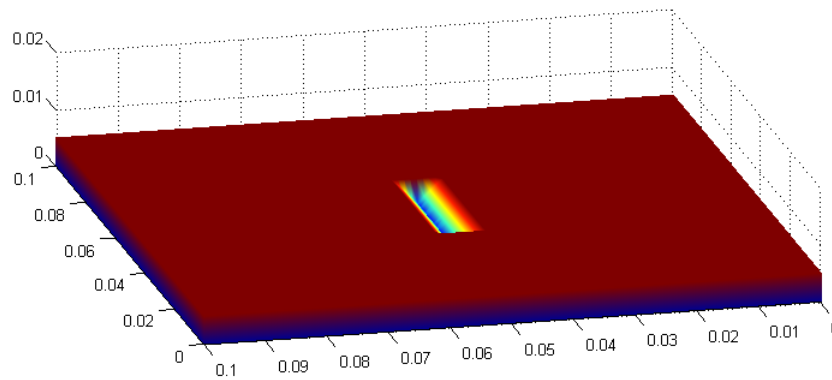
(a)
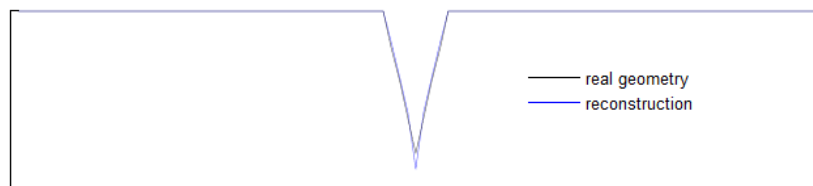
(b)

Figure 2-34 (a) 3D reconstruction of the triangular defect of the simulated aluminium sample (b) the corresponding section along the plane at the side view [91]

Ramirez-Granados *et al.* [92] proposed a 3D subsurface defect reconstruction method by using the finite-difference model. Firstly, a non-defect nodal network with the same geometry, structure, properties, and characteristics as the tested sample is established for performing the detection of internal defects, as shown in Figure 2-35. As can be seen in Figure 2-35, Δx, Δy, and Δz are the length of the node size, the spatial coordinates take multiples of the node-side lengths, including discretization of time, t takes multiples of the time increment (Δt); the discrete values are given by $x = l\Delta x$, $y = m\Delta y$, $z = n\Delta x$, and $t = p\Delta t$, where l, m, n, and p are positive integer. The finite difference equation [92] can be written as

$$\nabla^2 T(x, y, z, t) = \frac{1}{\alpha} \frac{\partial T(x, y, z, t)}{\partial t}$$

(2-87)

where $\alpha = \dfrac{k}{\rho C_p}$ [m²/s] is thermal diffusivity, surface, ρ [kg/m³] is the mass density, k [W/(m·K)] is the thermal conductivity of the material, and C_p [J/(kg·K)] is the specific heat capacity.
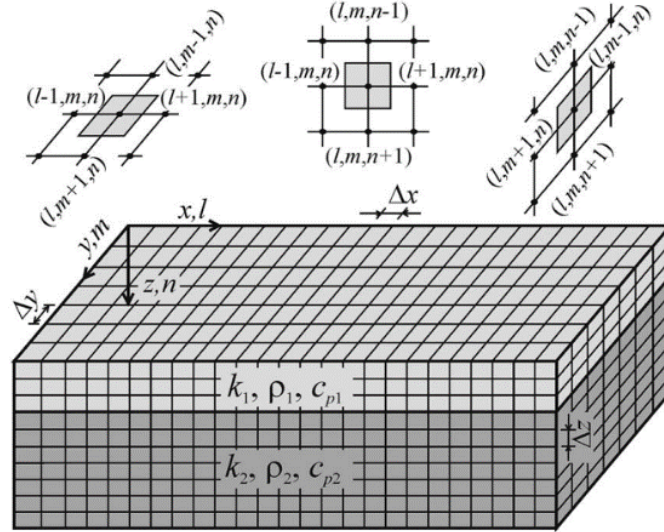
Figure 2-35 A nodal network is generated for the finite difference modelling [92]

Then, detecting the internal defects by analysing the difference of temperature between the temperature evolution of the inspected object surface and the established non-defect finite-difference model with a threshold. If the computed different temperature is more than the threshold value, it will be considered as an internal defect. The temperature difference threshold (ΔT_{th}) is set as 25 mK. The finite-difference equation in the explicit form used to describe the temperature evolution of the internal node as a function of time is derived from Equation (2-87), expressed as

$$
\begin{aligned}
T_{l,m,n}^{p+1} = {} & \frac{\alpha\Delta t}{(\Delta x)^2}\left(T_{l+1,m,n}^{p} + T_{l-1,m,n}^{p}\right) + \frac{\alpha\Delta t}{(\Delta y)^2}\left(T_{l,m+1,n}^{p} + T_{l,m-1,n}^{p}\right) \\
& + \frac{\alpha\Delta t}{(\Delta z)^2}\left(T_{l,m,n+1}^{p} + T_{l,m,n-1}^{p}\right) + \left(1 - 2\frac{\alpha\Delta t}{(\Delta x)^2} - 2\frac{\alpha\Delta t}{(\Delta y)^2}\right. \\
& \left. - 2\frac{\alpha\Delta t}{(\Delta z)^2}\right)T_{l,m,n}^{p}
\end{aligned}
\qquad \textbf{(2-88)}
$$

And the finite difference equation in explicit form applied a balance of energy to any surface node ($n = 0$). Its temperature along time can be expressed as

$$T_{l,m,0}^{p+1} = 2\frac{\alpha\Delta t}{(\Delta x)^2}\left(T_{l+1,m,0}^{p} + T_{l-1,m,0}^{p}\right) + 2\frac{\alpha\Delta t}{(\Delta y)^2}\left(T_{l,m+1,0}^{p} + T_{l,m-1,0}^{p}\right)$$

$$+ 2\frac{\alpha\Delta t}{(\Delta x)^2}T_{l,m,1}^{p} + \left(1 - 4\frac{\alpha\Delta t}{(\Delta x)^2} - 4\frac{\alpha\Delta t}{(\Delta y)^2} - 2\frac{\alpha\Delta t}{(\Delta z)^2}\right)T_{l,m,0}^{p} \quad \textbf{(2-89)}$$

$$+ 2\frac{\alpha\Delta t}{(\Delta z)^2})\frac{h\Delta z}{k}T_{\infty}$$

where T_{∞} [K] is the room temperature environment (normally 300 K) with average convection coefficient h.

After that, adjust the depth $d(l,m)$ and thickness $e(l,m)$ of the detected internal defects in the nodal network (see in Figure 2-36) by minimising the cost function (Equation (2-90)) with an iterative algorithm method and then replace the non-defect node by the adjusted defect nodes. Defect detection and defect depth and thickness adjustment algorithm are shown in Figure 2-37.

$$Q^p = \sum_{l=0}^{L-1}\sum_{m=0}^{M-1}\left|Tr_{l,m,0}^{p} - Ts_{l,m,0}^{p}\right|\Delta T \quad \textbf{(2-90)}$$

where Q^p [K·s] is the value of the cost function at time p, L and M are the total numbers of columns and rows on the surface of the nodal network, respectively, Tr [K] is the temperature distributions of the real inspected object, and Ts [K] is the temperature distributions of the nodal network.
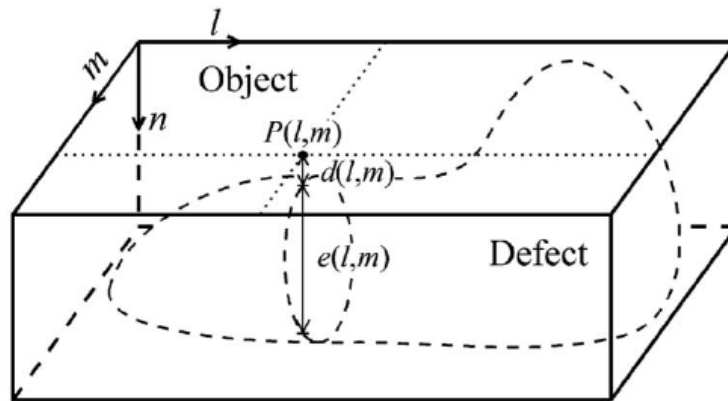
Figure 2-36 Internal defect in three-dimensional with a depth $d(m,l)$ and a thickness $e(m,l)$ [92]
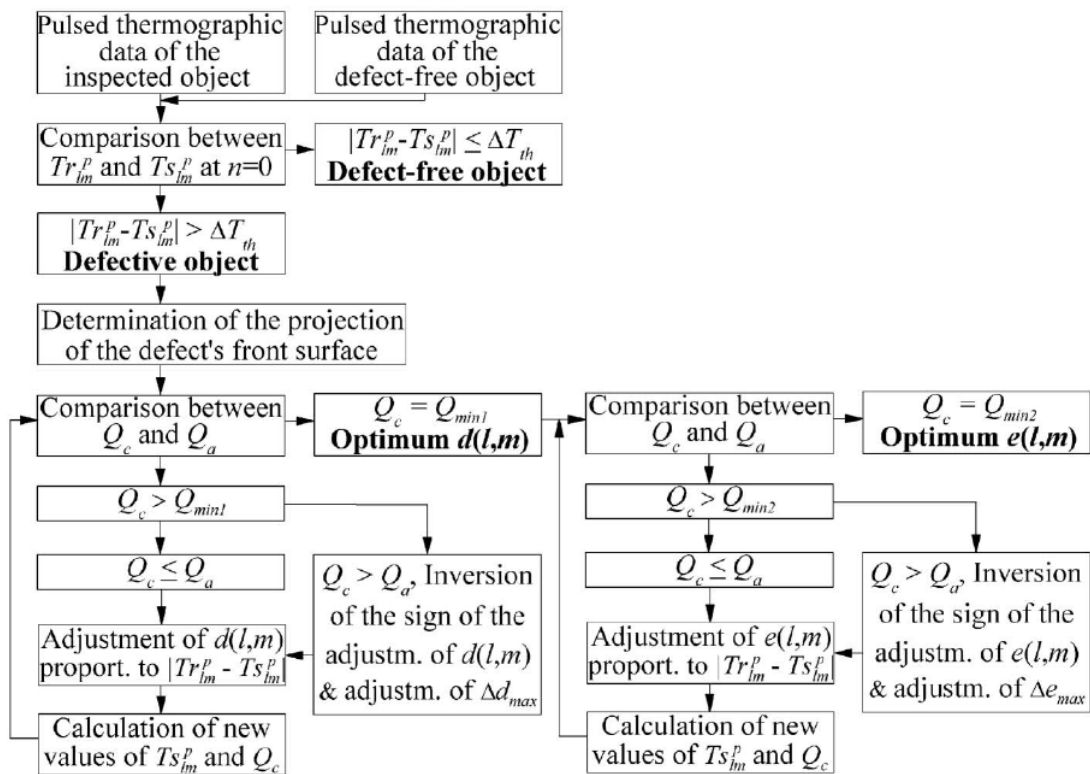
Figure 2-37 Flow chart of the algorithm to detect internal defects and to determine the defect depth and thickness [92]

Finally, creating a mesh graph of the nodal network to display the 3D shape, location, size, depth, and thickness of the internal defects. The dimensions of the modelled sample, the modelled internal defect, and the reconstructed internal defect are shown in Figure 2-38, Figure 2-39(a), and Figure 2-39(b), respectively.
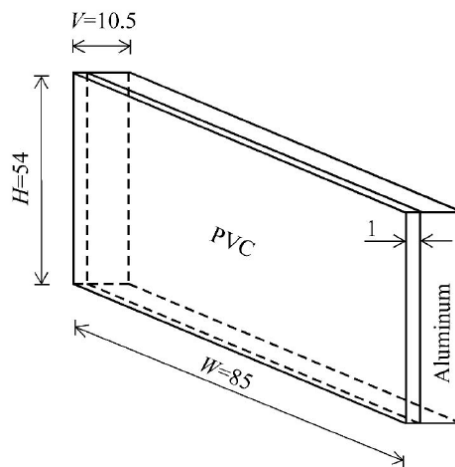
Figure 2-38 The dimension in millimetres of the modelled sample [92]
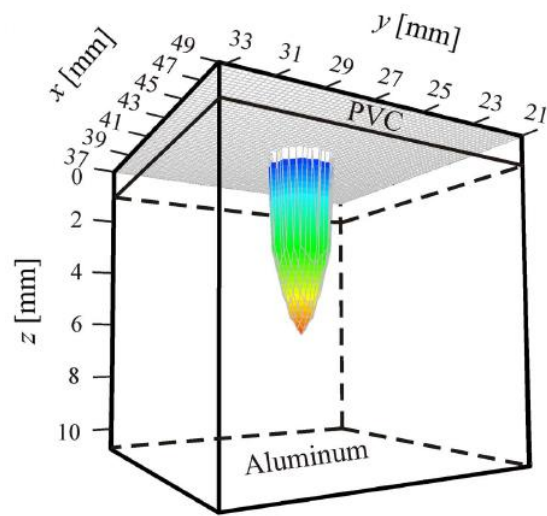
(a)
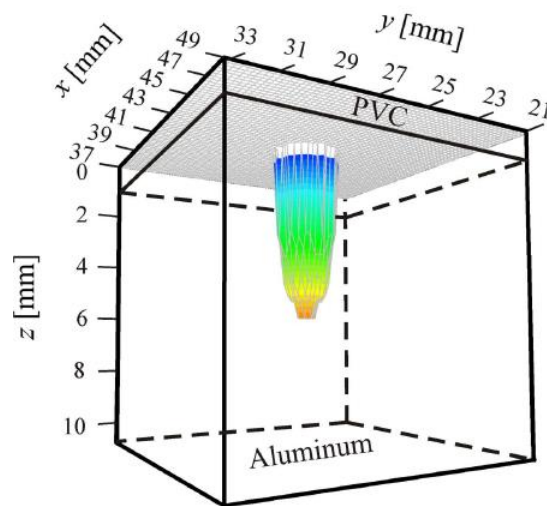
(b)

Figure 2-39 The 3D internal defect visualisation (a) actual geometry of the defect (b) the reconstruction of the detected defect [92]

The final step of the inspection is to visualise the testing results such as the location and size of the defects. These results can be reconstructed and visualised in the form of either 2D images or 3D images. If 3D visualisation is realised, the location and size of the defect inside the specimen can be presented more directly, clearly, and understand easily. Three-dimensional defect visualisation in the field of infrared and thermal testing has attracted a few studies.

Plotnikov and Winfree [93] visualised different depths of the defect in the form of 3D tomograms. Pulsed phase thermography technique is used to detect defect area and defect depth. To detect the defect areas, defect maps are extracted with the thermal contrast and phase distribution method, then multiply the two extracted maps together. Different depths of the defect are constructed by using reversed time of the peak slope. A used sample in the experiment (the aluminium plate with three artificial defects) is shown in Figure 2-40(a), the binary image of the defect reconstructed from the contrast distribution is shown in Figure 2-40(b), the binary image of the defect reconstructed from the phase distribution is shown in Figure 2-40(c), and the binary image of the defect multiplied by Figure 2-40(b) and Figure 2-40(c) is shown in Figure 2-40(d). The 3D thermogram of the defects in different depth is shown in Figure 2-41. However, the quantitative values of defect depth are not computed. It shows only different depths.
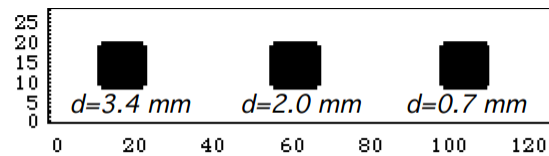
(a)

(b)

(c)

(d)

Figure 2-40 Binary image of the defects [93]
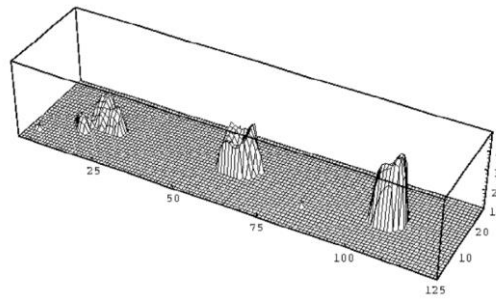
Figure 2-41 3D tomogram of the aluminium plate having three voids [93]

Soldan *et al.* [94] proposed to mapping the 3D model with its thermal information. The thermal 3D model is reconstructed by using three main tools: a motion tracking system, a handheld 3D scanner, and an infrared camera. The motion tracking system and markers are used for referencing the position of the 3D image and the thermal image. The geometry of the object with complex shape (surface data) is modelled by the 3D scanner. The subsurface data of the object are captured by the infrared camera, analysed, mapped onto the geometry model of the object. The sample of 3D reconstruction of this method is shown in Figure 2-42. The thermal data is mapped on the 3D structure model, consequently, where it is easy to observe the abnormal point. However, this method does not have any defects characterisation such as defect depth.

Figure 2-42 The sample of 3D images by mapping the geometry of the object with the thermal [94]

Akhloufi *et al.* [95] proposed a framework to fuse the 3D image of the object with thermal images, and visualise the measured defect depth overlay to the 3D model. The framework is shown in Figure 2-43. The 3D images of the object are

captured by a 3D camera, and the thermal images are captured by an infrared camera under an active thermography configuration. The 3D images captured by the 3D camera are represented in the form of a heightmap or a point cloud. Both images from the 3D camera the infrared camera are extracted their features to project the infrared images in the 3D data space. Pulsed thermography technique is used to detect defect and estimate defect depth. The warping transform technique is used to produce 3D mesh by projecting the thermal images with a texture map of the captured data in 3D space. Example of a virtual 3D image and their depth estimation is shown in Figure 2-44. The colour-coded display represents defect depth. However, only defect depth information is overlaid in the 3D model. The defect thickness is not mentioned.
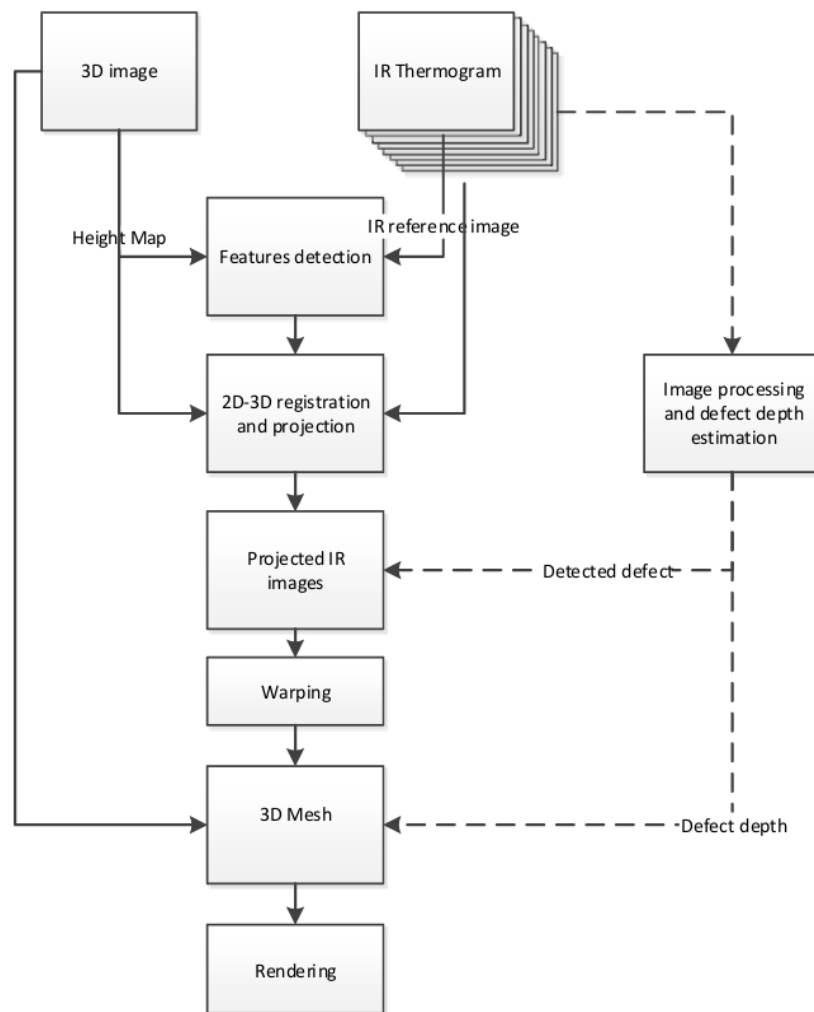
Figure 2-43 The multimodal fusion framework [95]
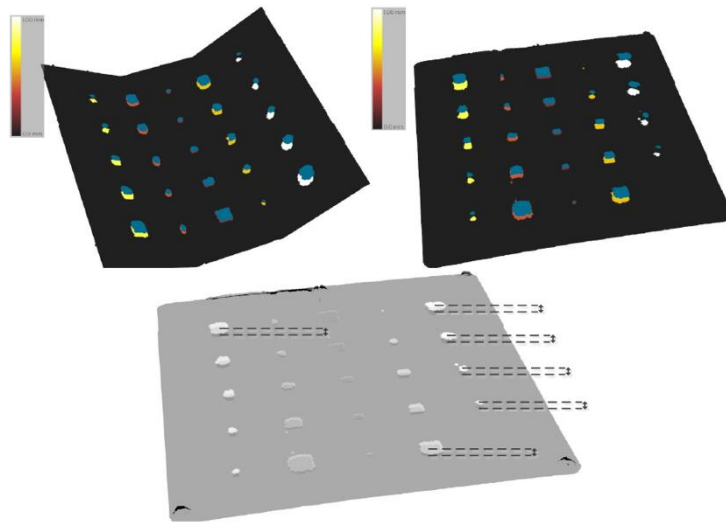
Figure 2-44 Example of virtual 3D image and their depth estimation [95]

2.6 Research Gaps

The pulsed thermographic inspection, as one of typical NDTs, is commonly used in the wide range of laboratory and practical industry. Because this method has many advantages, for example, it can fast scan large areas without contacting and destroying the sample during testing and can detect various types of defects (e.g., impact damage and cracks).

Considerable methods have been developed on defect detection and defect depth evaluation. The relationship between the decay of temperature on the inspected surface and time is a widely-used tool to measure defect depth, denoted by d in Figure 2-45. Majority of pulsed thermography works focus on measuring the location and sizes of damages, but very limited studies on the characterisation of their damage thickness, denoted by h in Figure 2-45. To evaluate the thickness of a subsurface defect, most of the existing techniques need to inspect from two sides (front and rear side) of the object. A target of this thesis is to address the challenge to measure the defect thickness based on a single-side inspection using pulsed thermography under the reflection mode. Such an approach is attractive because, in some situations, some industrial

components are accessible only on one surface, where measuring the defect depth from both sides to estimate h is not applicable. Furthermore, even both surfaces are accessible, the defect could be too deep to be detected from one surface.

In addition, currently, 3D visualisation is playing a paramount role and widely used to analyse problems in several areas. For example, in the field of medical, the X-ray and MRI images of the brain are reconstructed and visualised in the form of 3D to help doctors better understand the position of the abnormal point in the brain. For another instance, in the area of manufacturing, 3D image from CT scanner is used to help specialists analyse the types of porosity defects occurred in the materials from castings. However, the visualisation of defects/damage of most software of pulsed thermographic inspection is limited to the form of 2D images. For the pulsed thermographic inspection, 2D visualisation could limit the understanding of where the defects initiate and how they grow by time, which is the key to predict the remaining use of life of components and feedback to design to avoid such defects. Evaluation and visualisation of defects in 3D can unlock this limitation. In several cases, 3D images provide significant benefits over 2D images. The visualisation of the defect in the 3D form can display both of defect size and defect thickness, and evaluate the volume of defects. It can help better understand the mechanism of how the defects grow. It can also reduce operational time and improve quality control of production in the industry.

Characterisation of subsurface defects from 2D to 3D is a big step increment of degradation assessment. To represent a subsurface defect in the 3D form, the dimensions of the defect (width and length), defect depth and defect thickness are required.

Considering the abovementioned problems, subsurface defect thickness estimation and 3D subsurface defect reconstruction and visualisation are very important. This thesis aims to reduce the identified gap in these problems. This thesis proposes a novel method to estimate the thickness of subsurface defect with single-side inspection by using pulsed thermography technique, included reconstructing and visualising the subsurface defect in the form of 3D images.
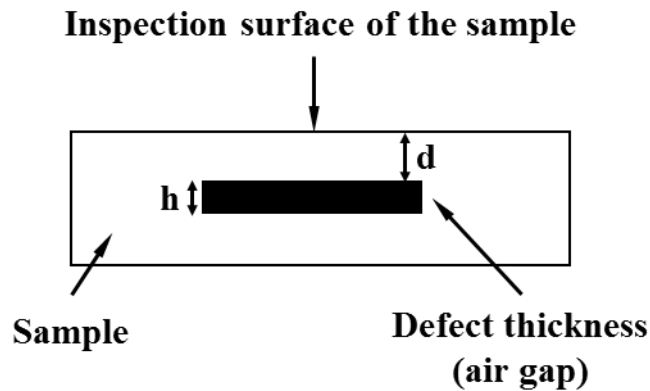
Figure 2-45 Position and dimension of defects

2.7 Summary

Non-destructive testing and evaluation (NDT&E), particularly infrared thermography method, can be used to inspect, detect, and evaluate the location, depth, and size of defects without contacting the sample.

In infrared thermography, a thermographic inspection, many inversion quantitative non-destructive evaluation (QNDE) methods have been developed to reconstruct subsurface defect such using finite element method (FEM). There are very few works which report three-dimensional subsurface defect reconstruction based on unknown thermal properties of the test sample. Most works need to know thermal properties of the test sample and the hidden defect to reconstruct the subsurface defect which could be a huge problem in several applications of inspection.

In pulsed thermography, a subsurface defect evaluation approach based infrared thermography, some defect detection and depth measurement methods need a reference point such as temperature contrast method (TC) and peak slope time method (PST). To eliminate the need of reference point, logarithmic second derivative method (LSD), absolute peak slope time method (APST), least-squares fitting method (LSF) were developed. The state-of-the-art methods of defect depth measurement based on pulsed thermography are summarised in

64

Table 2-3. After the testing process is finished, most results are displayed in the form of coded colour 2D images or 3D tomograms.

Table 2-3 Summary of the reviewed methods of defect depth measurement

Method	Reference Point Requirement	Key Equation
Absolute Temperature Contrast (TC) [14]	Yes	$TC_{abs} = T_{def} - T_{snd}$
Peak Slope Time (PST) [64]	Yes	$t_{PST} = \dfrac{3.64L^2}{\pi^2 \alpha}$
Logarithmic Second Derivative (LSD) [40]	No	$t_{LSD} = \dfrac{L^2}{\pi \alpha}$
Absolute Peak Slope Time (APST) [77]	No	$t_{APST} = \dfrac{L^2}{2\alpha}$
Least-Squares Fitting (LSF) [80]	No	$T(t) \approx A\left[1 + 2\sum_{n=1}^{\infty} exp\,(-\dfrac{n^2\pi^2}{L^2}\alpha t)\right] - st$

From the reviews, it is found that:

(1) There are very limited studies on subsurface defect thickness estimation by using single-side inspection method. Most works focus on the evaluation of defect size and defect depth.

(2) There are very few reports on three-dimensional subsurface defect thickness reconstruction and visualisation by using pulsed thermography without the needing to know thermal properties of the subsurface defect. Most results are represented in the form of 2D image.

The next chapter will provide approaches and methods to achieve the aim of this thesis.

3 RESEARCH METHODOLOGY

3.1 Introduction

This chapter presents the research methodology. The first section describes the overview of the research approach. The second section describes the research method follow each objective. The last section summaries the chapter. The outline of this chapter is illustrated in Figure 3-1.
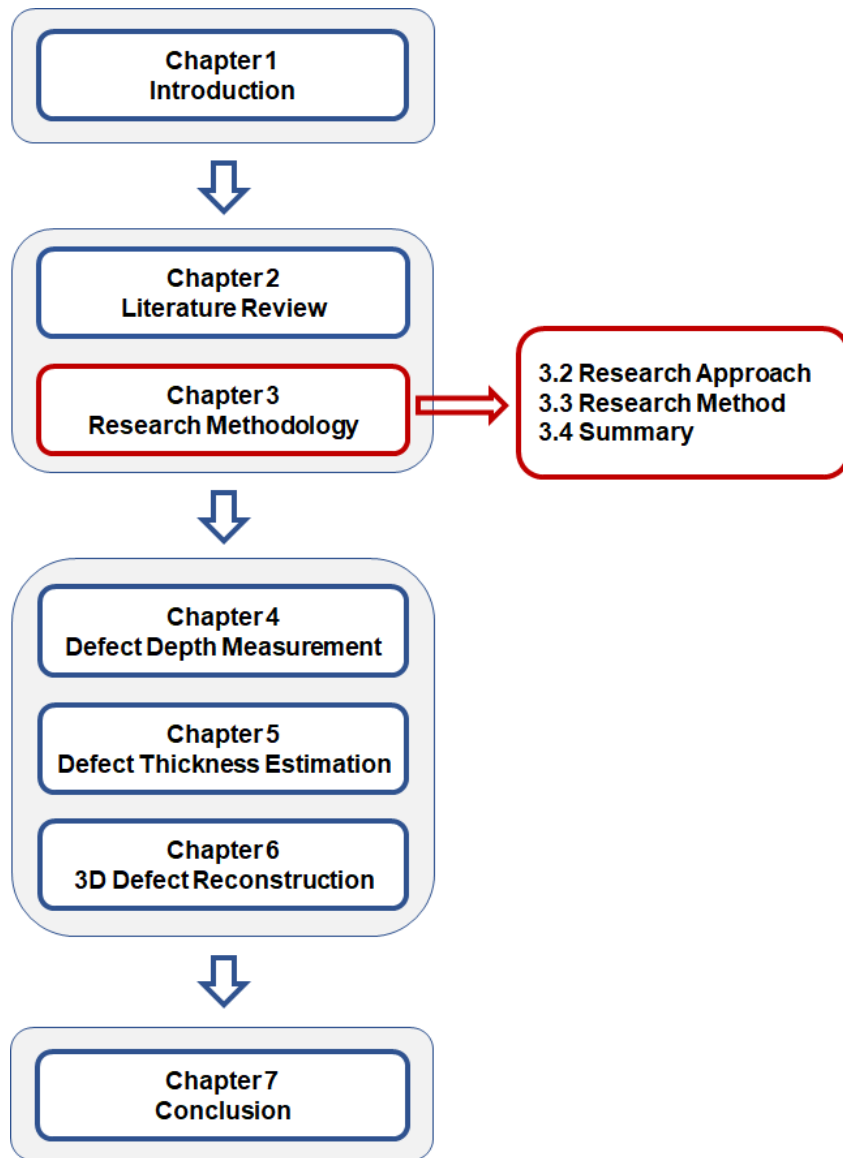
Figure 3-1 The outline of Chapter 3

3.2 Research Approach

The research is divided into three phases: literature reviews, algorithm development, and validation. The research approach is illustrated in Figure 3-2.

The first phase is literature reviews, which covers non-destructive testing and evaluation (NDT&E) techniques with a specific focus on thermographic inspection, defect depth measurement, and defect reconstruction. The purpose of this literature review is to identify an appropriate NDT&E method for reconstructing the subsurface defect in the form of 3D images.

The second phase is algorithm development. The main target of this phase is to develop a solution to reconstruct and represent the defect in a 3D form. This phase involves the improvement of the accuracy of depth measurement and estimation of the defect thickness. This phase is subdivided into three steps. The first step is defect depth measurement, proposed in Chapter 4. Due to the defect depth is essential for the three-dimensional subsurface defect reconstruction, the performance of the state-of-the-art methods is compared with the developed method to identify the best method in terms of the accuracy of depth measurement. The second step is defect thickness estimation, proposed in Chapter 5. This step involves studying the relationship between defect thickness, defect depth, defect size and thermal reflection coefficient. And the last step is three-dimensional defect reconstruction and visualisation, proposed in Chapter 6. The data from the first step (defect depth measurement) and the second step (defect thickness estimation) will be used to reconstruct 3D defect model. The surface information (size and dimension of the inspected sample) and the subsurface defect information (depth, thickness, location, size and dimension of the defect) will be merged together and visualised in a form of 3D images (volume image).

The final phase is validation. The developed method and the results will be tested with model simulation, experimental studies, and a use case. Firstly, the performance of the developed method and the state-of-the-art methods will be compared by testing the data from the model simulation. Then, the quantitative results from the experimental studies will be compared with the ground truth of

the designed samples. And lastly, the developed method will be tested with a use case (an industrial component) and the results will be compared with X-ray image.
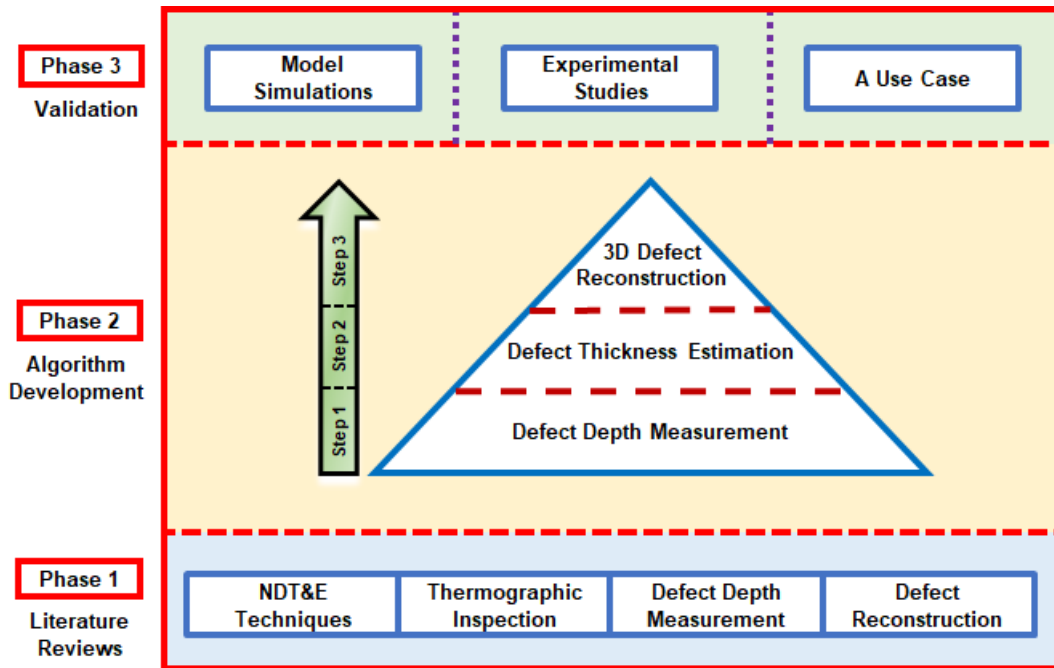
Figure 3-2 Research approach diagram

3.3 Research Methods

The approach of research is implemented through the following five research objectives.

3.3.1 Identification of Appropriate Technique for 3D Subsurface Defect Reconstruction and Visualisation for Industrial Components

To identify appropriate imaging technique for 3D subsurface defect reconstruction, various types of NDT&E technique have been reviewed such as ultrasonic testing, radiographic testing, electromagnetic testing, and infrared and thermal testing etc. The infrared thermography is specially focussed, particularly, the pulsed thermography. The review of pulsed thermography consists of the type

of thermographic inspection, defect depth measurement, and three-dimensional defect reconstruction.

Concluded from the review, the pulsed thermographic inspection under the reflection mode is selected for developing the three-dimensional subsurface defect reconstruction and visualisation approach in this thesis because of its various advantages. This technique is rapid, low-cost, non-contact and can be applied to diverse materials such as composite material, plastic, aluminium, steel, metal, and non-metal material. This technique has been widely used in a variety of industrial.

3.3.2 Investigation of Experimental Setup and Routine to Capture Data for 3D Subsurface Defect Reconstruction

The experimental setup is illustrated in Figure 3-3(a), where a short and high energy light pulse is projected onto the sample surface through two flash lamps. Heat conduction then takes place from the heated surface to the interior of the sample, leading to a continuous decrease of the surface temperature [76] (see Figure 3-3(b)). An infrared camera controlled by a computer captures the time-dependent response of the sample surface temperature. If the sample is defect-free, the time when the temperature deviation occurs can be used to estimate the sample thickness (if thermal diffusivity is known) or thermal diffusivity of local materials (if the thickness is known). For example, as shown in Figure 3-3(b), if the thermal diffusivity is known, the thickness of the point 1 and point 2 on the inspected surface can be estimated based on the time of temperature deviation, t_1 and t_2, respectively. This approach can be extended to measure defect depth by considering the first time of temperature deviation. The surface temperature due to the back-wall at depth L for a homogeneous plate [74] is given by

$$T(t) = \frac{Q}{\sqrt{\rho k C_p \pi t}} \left[1 + 2 \sum_{n=1}^{\infty} R^n \exp \left(-\frac{n^2 L^2}{\alpha t} \right) \right] \qquad \textbf{(3-1)}$$

where $T(t)$ is the temperature variation on the surface at time t, t [s] is the sampling time, Q [J/m²] is the pulse energy absorbed by the surface, ρ [kg/m³] is

the mass density, k [W/(m·K)] is the thermal conductivity of the material, C_p [J/(kg·K)] is the specific heat capacity, R is the thermal reflection coefficient of the interface with air, and α [m²/s] is the thermal diffusivity. Equation (3-1) can be rewritten as

$$T(t) = \frac{Q}{e\sqrt{\pi t}}\left[1 + 2\sum_{n=1}^{\infty} R^n \exp\left(-\frac{n^2 L^2}{\alpha t}\right)\right] \tag{3-2}$$

where $e = \sqrt{\rho k C_p}$ is the thermal effusivity of the material [J/(s$^{1/2}$·m²·K)].

(a)

(b)
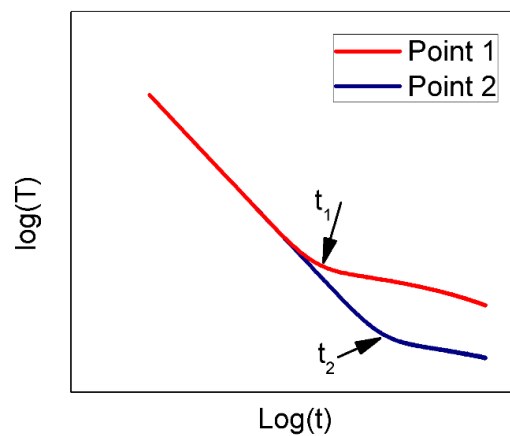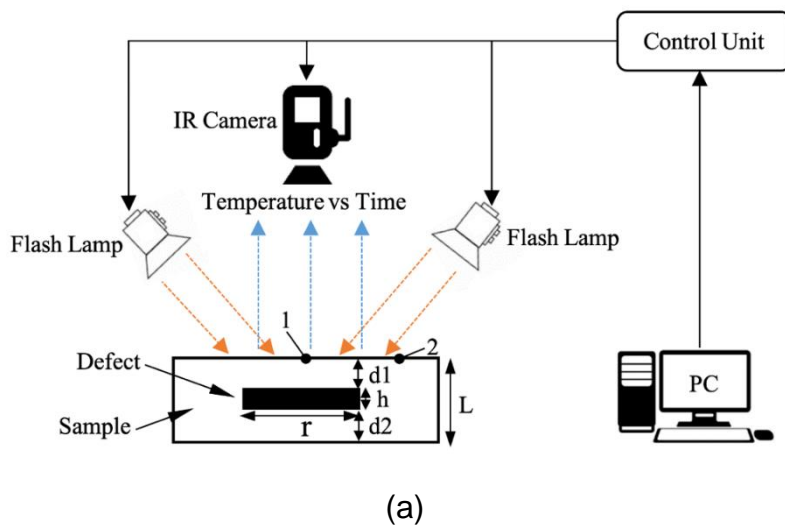
Figure 3-3 Experimental configuration of the pulsed thermographic inspection under the reflection mode, where point 1 denotes a location on the sample surface with a defect underneath and point 2 denotes a location on the sample surface with no defect underneath; (b) Typical observed time-temperature decay curves in the logarithmic domain for the point 1 and 2, respectively, where the time of t_1 and t_2 is the key to measure the defect depth of the thickness of local materials [96]

Most defect evaluation methods aim to classify the curve based on the cooling behaviour. The time when the temperature deviation occurs (t_1 in Figure 3-3(b)) is usually used to estimate defect depth.

In this thesis, although Equation (3-2) only applies to 1D heat transfer, it is proposed to approximate the 3D heat transfer in the real world to simplify the problem. Without this simplification, the model will be over complex and potential lead to over-fitting due to involving too many parameters.

The experiments in this thesis were conducted with Thermoscope® II pulsed-active thermography system that comprises of two capacitor banks powered Xenon flash lamps mounted in an internally reflective hood as shown in Figure 3-4. The thermoscope, FLIR SC7000 series infrared radiometer operating between 1.5 and 5.1 μm, has a spatial resolution of 640×512 pixels. The technical specification of the thermoscope is highlighted in Table 3-1. The workpieces are placed with their surface perpendicular to the infrared camera's line of sight at a distance of 250 mm from the lens. The applied energy is approximately 2 kJ over the inspection area of approximately 160 mm × 200 mm.

Table 3-1 Thermoscope FLIR SC7000 series technical specifications

Technical Specification	Detail
Model	FLIR SC7600
Sensor Type	InSb
Waveband	Mid-Wave
Spectral Range	1.5 to 5.1 μm
NETD (Sensitivity and noise levels)	<20 mK
Temperature Calibration Range	5 °C to 300 °C
Temperature Measurement Accuracy	±1 °C or ±1%
Pixel Pitch	15 μm
Image Size	640×512 pixels
Full Frame Rate	100 Hz
Aperture	F/3
Dynamic Range	14 bit
Size (L×W×H) (mm)	403×130×168
Weight	4.95 kg
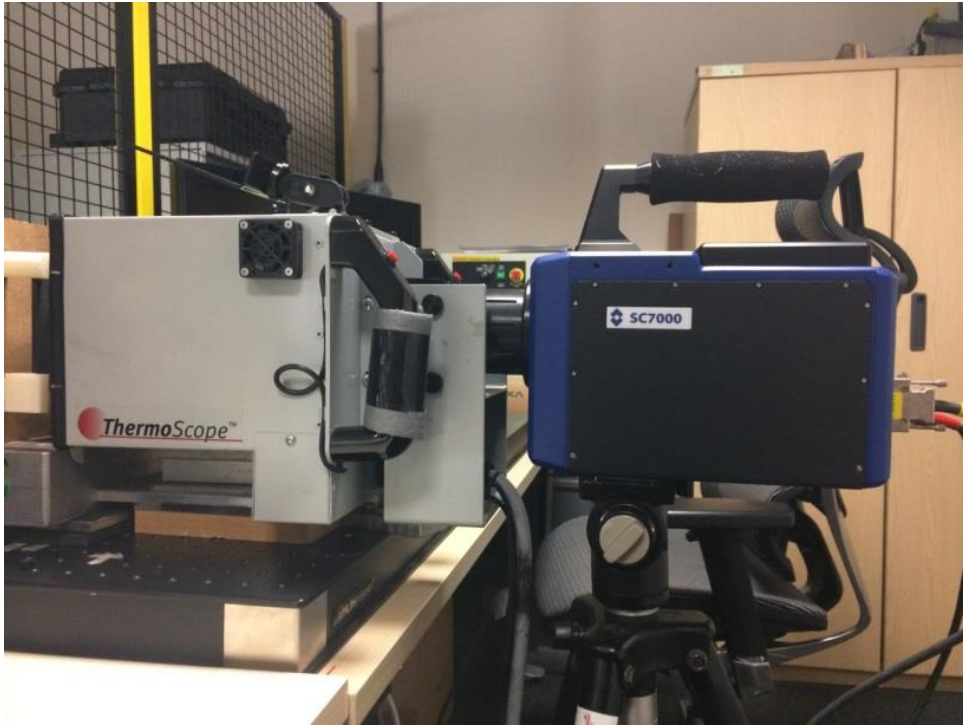
(a)

(b)

Figure 3-4 ThermoScope FLIR SC7000 series (a) the side view (b) the back view

3.3.3 Development of Novel Methods to Estimate Subsurface Defect Depth and Thickness for 3D Subsurface Defect Reconstruction

The most important step to reconstruct subsurface defect in a 3D form is the depth and thickness evaluation of defects. A novel method of subsurface defect depth and thickness measurement has been developed, named, New Least-Squares Fitting (NLSF) method. This developed method is established upon an extension of the theoretical heat transfer model. The accuracy of depth measurement under various levels of noise is tested and compared with the state-of-the-art methods. The developed NLSF method has been published in the "*Infrared Physics & Technology*" journal. The title of the published paper is "Determination of Thermal Wave Reflection Coefficient to Better Estimate Defect Depth using Pulsed Thermography" [97].

The developed NLSF method is also utilised to estimate defect thickness inside samples. The estimation of defect thickness has been published in "*IEEE Transactions on Industrial Informatics*" journal. The title of the published paper is "Estimation of Damage Thickness in Fiber-Reinforced Composites using Pulsed Thermography" [98]. The detail of the defect depth measurement and thickness estimation using the developed NLSF method is described in Chapter 4 and Chapter 5, respectively. In this thesis, the developed NLSF method has been chosen as the main method for three-dimensional subsurface defect reconstruction and visualisation because it can estimate both of defect depth and defect thickness simultaneously.

3.3.4 Development of 3D Subsurface Defect Reconstruction and Visualisation Algorithms

The 3D subsurface defect reconstruction and visualisation is a process to reconstruct the subsurface defect based on the estimated dimension (size, depth, and thickness of the defect) and visualise it in the form of 3D images. The defect depth and defect thickness can be estimated by the developed NLSF method. Two potential solutions to reconstruct defect are introduced: double-side inspection and single-side inspection. The double-side inspection method can be

mainly used in the case of both sides of the inspected object can be accessed. This inspection reconstructs the 3D structure of defects by evaluating the defect depth $d1$ and $d2$, as shown in Figure 3-3(a). The single-side inspection can be used in the scenario where only one side is accessible. This inspection reconstructs the 3D structure of the defects by evaluating the defect depth ($d1$ or $d2$) and the defect thickness (h), as shown in Figure 3-3(a).

The information of subsurface defect (defect depth and thickness from the double-side inspection or the single-side inspection) and the dimension (width, height, and deep) of the sample will be fused to construct a 3D volume image. The detail of 3D subsurface defect reconstruction and visualisation is described in Chapter 6. The method of 3D subsurface defect reconstruction and visualisation has been published in "*Infrared Physics and Technology*" journal. The title of the paper is "Three-Dimensional Subsurface Defect Shape Reconstruction and Visualisation by Pulsed Thermography" [99].

3.3.5 Validation of The Results by using Model Simulations, Experimental Studies and a Use Case

Validation is a procedure to evaluate and test the capability of the developed solution. This procedure is undertaken for data from both model simulations and experimental studies. In this thesis, model simulations were used to compare the performance of the developed NLSF method with four existing state-of-the-art methods (peak slope time [64], logarithm second derivative [40], absolute peak slope time [77], and least-squares fitting [80]) against different values of thermal wave reflection coefficient (R) and noise levels. For the experimental studies, the created specimens (carbon fibre-reinforced polymer material made from the local manufacturing) were used to test the performance and accuracy of defect depth and thickness measurement of the developed NLSF method.

The created specimens consist of several different artificial defect depths and thicknesses:

- Sample 1, a flat-bottom holes sample with same defect size but different three defect depths;

- Sample 2, a semi-close air-gaps sample with the same defect depth but five different defect thicknesses;
- Sample 3, a semi-close air-gaps sample with the same defect thickness but five different depths;
- Sample 4, a flat-bottom hole sample with four different defect depths and four different defect sizes (totally 16 different defects).

After testing the developed method with the model simulations and experimental studies, a use case (Sample 5, a steel sample with 'S' shape triangular air-gap through the sample made by the additive manufacturing), is used to test the proposed method. The defect image from the developed method is compared with the X-ray technique.

3.4 Summary

This chapter presented the research methodology. The approach of this research consists of three phases: literature reviews, algorithm development, and validation. The research approach is performed through the five research objectives. To achieve the target, three main methods are presented: defect depth measurement, defect thickness estimation, and three-dimensional defect reconstruction, which described in Chapter 4, Chapter 5 and Chapter 6, respectively. These methods are tested by model simulations, experimental studies, and a use case. There are five samples used for experiments in this thesis. Sample 1 is used for testing the defect depth measurement in Chapter 4. Sample 2, 3, and 4 are used for testing the defect thickness estimation in Chapter 5. Sample 2 and Sample 5 are used for testing the three-dimensional defect reconstruction and visualisation in Chapter 6.

4 DEFECT DEPTH MEASUREMENT

4.1 Introduction

Quantitative characterisation of defects by extracting shape, size and depth, and estimation of thermal properties have been proven to be effective in Pulsed Thermography [76], [79], [100], [101], [102], [103], [104], [105], [106]. Considerable methods have been developed on defect detection and defect depth evaluation. The relationship between the decay of temperature on the inspected surface and time is a widely-used tool to measure defect depth and most of the methods are based on frequency domain [15], [107], [108] or time domain [14], [109].

Many depth measurement methods require a reference point that defines the pre-known sound areas, such as peak contrast time method (PCT) [110], [111] and peak slope time method (PST) [73], [109]. PCT measures the peak time of the temperature contrast between the considered point and the reference point, and PST detects the peak time of the first derivative of temperature contrast. Both PCT and PST are approximately proportional to the square of the defect depth, whereas the proportionality coefficient of the PCT method depends on the size of the defect, but the proportionality coefficient of the PST method does not depend on the size of the defect [112]. In general, the reference point is manually chosen from the sound area.

Some researchers attempted to obtain the reference point automatically such as Ringermacher *et al.* [64] and Pilla *et al.* [113]. The methods without a reference point include logarithm second derivative method (LSD) [40], absolute peak slope time method (APST) [77], lease-squares fitting method (LSF) [80] and nonlinear system identification method (NSI) [96]. In LSD method, the temperature decay curve is converted to the logarithm domain, and a polynomial model is then used to fit the curve to reduce temporal noise and save storage space, where the fitting method is called as thermal signal reconstruction (TSR) [75]. The peak of the second derivative of TSR fitting is then used to estimate the defect depth. The APST method multiplies the square root of its time to temperature decay curve

and then computes the peak-time of the first derivative of the modified curve, which is used to estimate the defect depth. Similar to APST, the NSI method fits the modified temperature curve using a polynomial model but the difference is that the model order is chosen automatically for each pixel to produce more reliable depth measurement. These methods, including other recently developed fitting methods of thermal data, such as least-square fitting [114] and partial least squares regression [115], can be categorised as parametric methods where the characteristic time for depth estimation is calculated from the fitted model rather than the raw data.

A limitation of all above-mentioned methods is that they are susceptible to noise, typically large in thermography data because the fitted models are data-driven without considering the underlying physics-based models. The LSF method uses a curve fitting technique to fit the temperature decay curve based on a theoretical heat transfer model to determine the defect depth directly. This method is less susceptible to noise but it presumes that the thermal wave reflection coefficient (R) is 1, which is not true for most real situations [112]. Such an assumption can affect the accuracy of the estimated parameters of the heat transfer model using optimisation techniques. It is therefore crucial to estimate the value of R before detecting defect depth or simultaneously. Moreover, the value of R can be used to investigate thermal effusivity of the defect, which has the potential to help quantify the volume of defect or identify the material of defect (e.g., air, water or oil).

This chapter proposes a new defect depth measurement method to increase the accuracy of depth measurement against different noise levels by estimating the thermal wave reflection coefficient value based on pulsed thermography under the reflection mode, named, New Least-Squares Fitting method (NLSF) [116]. Furthermore, this chapter introduces a new method to improve the reliability and confidence level of defect depth measurement by addressing the over-fitting problem, named, Nonlinear System Identification method [96]. The outline of this chapter is illustrated in Figure 4-1.
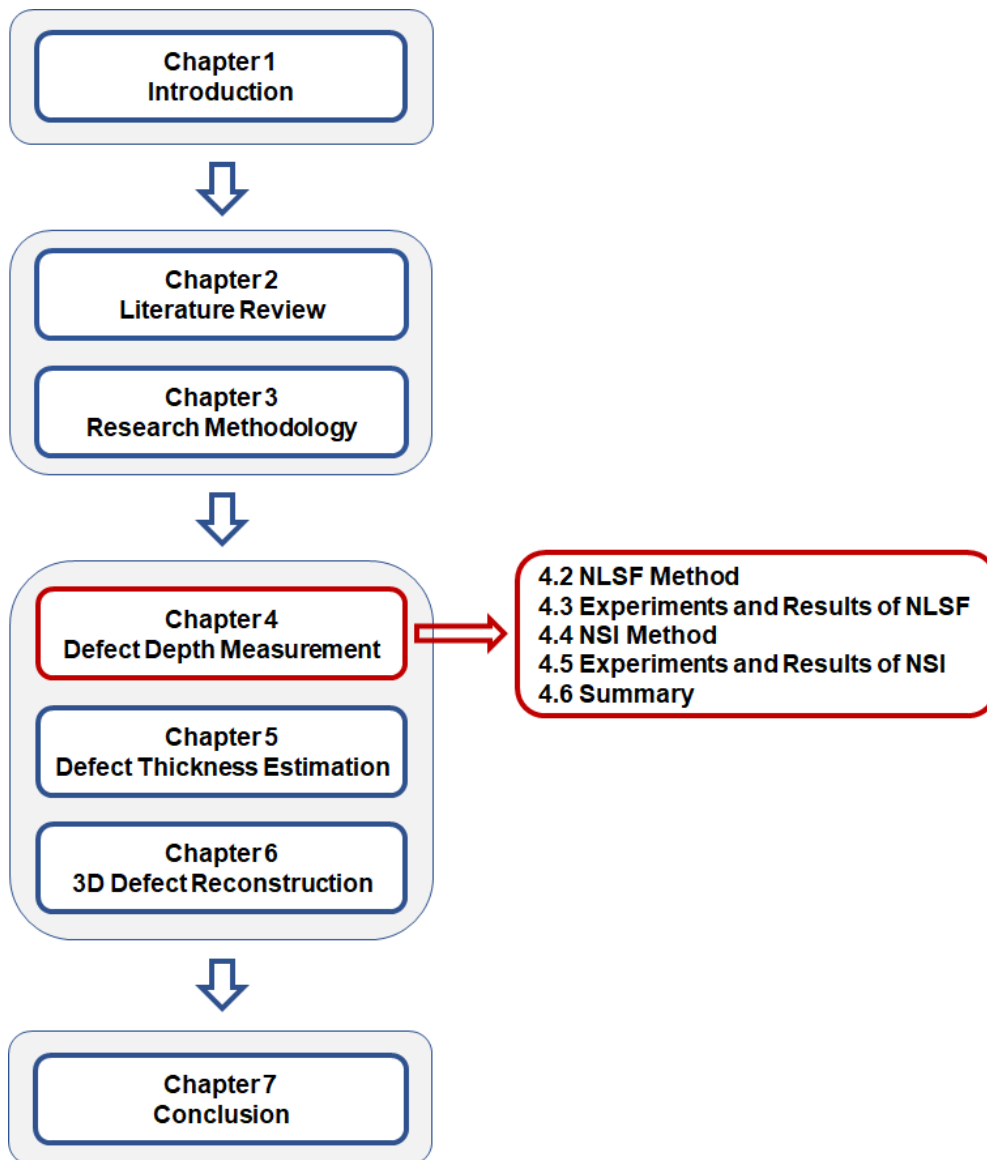
Figure 4-1 The outline of Chapter 4

4.2 The New Least-Squares Fitting Method (NLSF)

Sun [80] introduced a least-square fitting (LSF) method for the pulsed thermography using a speculative heat transfer model. This theoretical model is roughly applicable for the time period $0 < t < t_b$, expressed as Equation (2-50) in Chapter 2. One limitation of this method is that the value of R in this model is assumed to be 1, which is true when the thickness of defect (e.g., air-gap) is infinite. However, for most real applications (e.g., detecting delamination of composite), the thickness of defect is very limited and the value of R can be significantly smaller than 1. For such cases, the accuracy of the estimated defect depth is therefore compromised if R is assumed to be 1. Another limitation is that the estimation of s can be difficult due to the challenge to determine the values of t_a and t_b, unless both L and α are pre-known.

To address the above limitations, this thesis introduces a modified analytical model aiming to not only estimate the depth more accurately but also measure the thermal wave reflection coefficient. The proposed analytical model is written as

$$\tilde{T}(t, A, W, R, t_s, s) = \frac{A}{\sqrt{t + t_s}} \left[1 + 2 \sum_{n=1}^{M} R^n \exp\left(-\frac{n^2 W}{t + t_s}\right) \right] - s(t + t_s) \qquad \textbf{(4-1)}$$

where $A = \frac{Q}{\sqrt{\pi \rho c k}}$, $W = \frac{L^2}{\alpha}$, L is the defect depth or the thickness of the sample, α is the thermal diffusivity of the material, R is thermal wave reflection coefficient, t is sampling duration, t_s is the starting time of sampling, s is slope, and M is a large iteration number.

Two extra parameters are introduced, R and t_s. In practical applications, R is not always equal to 1. It depends on the thermal property of the materials between the interface, including thermal effusivity, shape, size, and depth of the defect. Some amount of the thermal energy transmit through the interface (blue arrow) while some amount of the thermal energy reflect back (red arrow) at the interface, as illustrated in Figure 4-2(a). For the interface between the material and infinite air-gap, R value could be close to 1. In contrast, for finite thin air-gap (defect), as

illustrated in Figure 4-2(b), R could be much less than 1. The thermal wave reflection coefficient can be described as a function of thermal effusivity [117] by

$$R = \frac{e_1 - e_2}{e_1 + e_2} \qquad \text{(4-2)}$$

where e_1 is thermal effusivity of the first layer of material, e_2 is thermal effusivity of the second layer of material. The introduced R can apply to real applications even without needing to know the R value to improve the performance of depth evaluation.
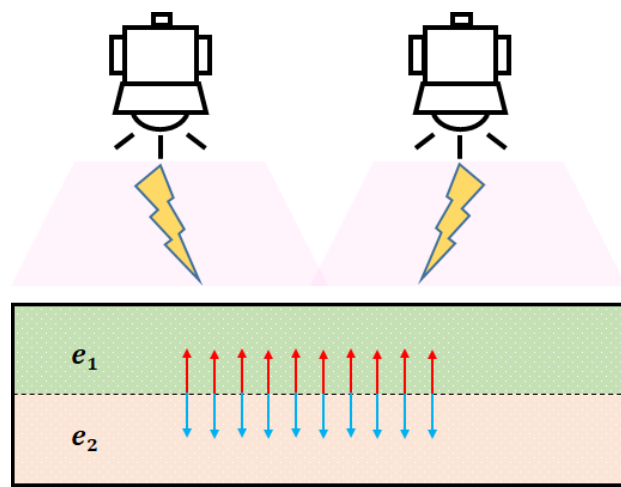
(a)
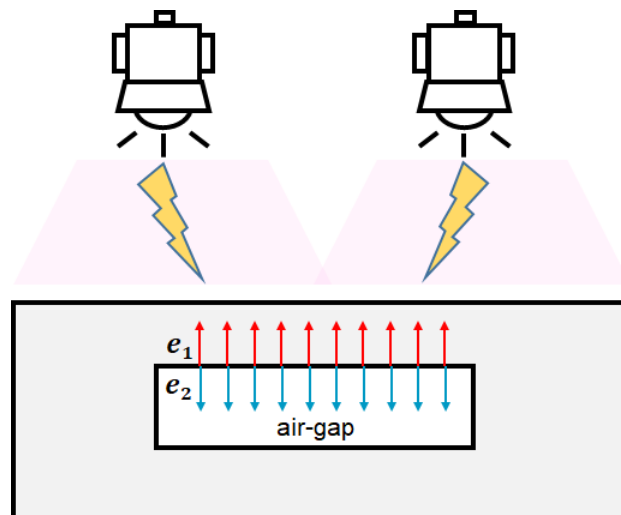
(b)

Figure 4-2 Thermal reflection between two interfaces of (a) different material (b) material and thin finite air-gap

The introduced t_s can apply to any segment of collected data without knowing the starting time. Such a feature is attractive for data with a low sampling rate where the starting time could be larger than 0 due to accumulated latency by hardware and software of data acquisition.

There are totally five parameters to be estimated including A, W, R, t_s, and s. This thesis employs a nonlinear least-squares solver in Matlab (*lsqnonlin*) to solve this five-parameters optimisation problem. Through initially setting the lower and upper bounds for each parameter, the proposed New Least-Squares Fitting method (NLSF) estimates the optimal parameters that has

$$\min_{A,WR,t_s,s} \left\| \tilde{T}(t) - T(t) \right\|$$

(4-3)

The initial value of the parameter t_s is selected as zero and the lower and upper bounds are selected as -1 and 1, respectively, because it is usually very small. The initial value of R is selected as 1 and the lower and upper bounds are selected as 0 and 1. The selection of A depends on the energy applied on the inspection surface, and the selection of W depends on the material and thickness of samples (estimated by $W = \frac{L^2}{\alpha}$). The lower and upper bounds of W and A are usually selected as 5 times lower and 5 times higher than the initial values. The lower and upper bounds of s are selected as -50 and 50, and the initial value is chosen as 0, the slope s usually is a small value and almost equal 0 when the inspected point is on a sound area. It should be noted that the computational time of this method depends on the selection of initial value and lower and upper bounds.

Once the optimal parameters are estimated, if α is known, the thickness of the sample or the defect depth can be estimated by

$$L = \sqrt{W \cdot \alpha}$$

(4-4)

Alternatively, if L is known, the thermal diffusivity can be estimated by

$$\alpha = \frac{L^2}{W}$$

(4-5)

The temperature contrast ΔT between a defect region and a sound region is dependent not only on the difference between the defect depth and the sample thickness, but also on the lateral size of the defect because of induced 3D heat conduction around the defect. Most of the existing methods, such as PST, LSD, NSI, and APST, tried to estimate the defect depth as early as possible before the three-dimensional heat conduction takes place. These methods work well when the defect size is large, but the accuracy is reduced when the defect size is small due to severe three-dimensional heat conduction, as the results shown in Sun's paper [26]. The proposed equation introduces two extra parameters R and s that consider part of the three-dimensional conduction effect. It can also incorporate the duration effect by introducing the parameter t_s. Therefore, this method can perform better when the three-dimensional conduction and the flash duration effects are present in the flash thermography data.

4.3 Experiments and Results of NLSF

4.3.1 Model Simulations

The aim of these model simulations is to compare the performance of the proposed NLSF method with other existing methods against different values of R and noise levels. Based on the one-dimension solution of the Fourier equation for a Dirac delta function when there is any subsurface defect [78], [112], [118], the temperature-time curves with noise [96], [119] were simulated by

$$T(t) = \frac{Q}{e\sqrt{\pi t}}\left[1 + 2\sum_{n=1}^{\infty} R^n \exp\left(-\frac{n^2 L^2}{\alpha t}\right)\right] + \varepsilon(t) \tag{4-6}$$

and the temperature contrast between defective areas and sound areas by the time [112] with noise was simulated by

$$\Delta T(t) = 2\frac{Q}{e\sqrt{\pi t}}\left[\sum_{n=1}^{\infty} R^n \exp\left(-\frac{n^2 L^2}{\alpha t}\right)\right] + \varepsilon(t) \tag{4-7}$$

where Q is the pulse energy (J), e is thermal effusivity (J/(s$^{1/2}$·m^2·K)), t is sampling time (s), the parameters $\frac{Q}{e\sqrt{\pi}}$ is set to 1, α was set to 4×10^{-6} m^2/s, L was set to 4×10^{-3} m, and R was varied from 0.1 to 1. The sampling rate was set as 50 Hz and the sampling duration was set as 5 s. The latency of data acquisition was set as zero. The symbol $\varepsilon(t)$ denotes a white noise sequence with a zero mean and a standard deviation of σ_ε. Assume σ_T denotes the standard deviation of a signal without noise, the signal-to-noise ratio (SNR) [96], [120], [121], representing the level of noise, is written as

$$SNR = 20\log_{10}\frac{\sigma_T}{\sigma_\varepsilon} \tag{4-8}$$

Figure 4-3 shows the plots of temperature decay in the logarithmic domain with different values of R. It can be clearly observed that the time of temperature deviation, representing the depth, is independent of the value of R. Furthermore, the value of R determines the slope of the curve after the temperature deviation. If R is 1, the slope is zero, which indicates 100% thermal wave is reflected by the defect or back-wall. If R is zero, there is no temperature deviation occurred.
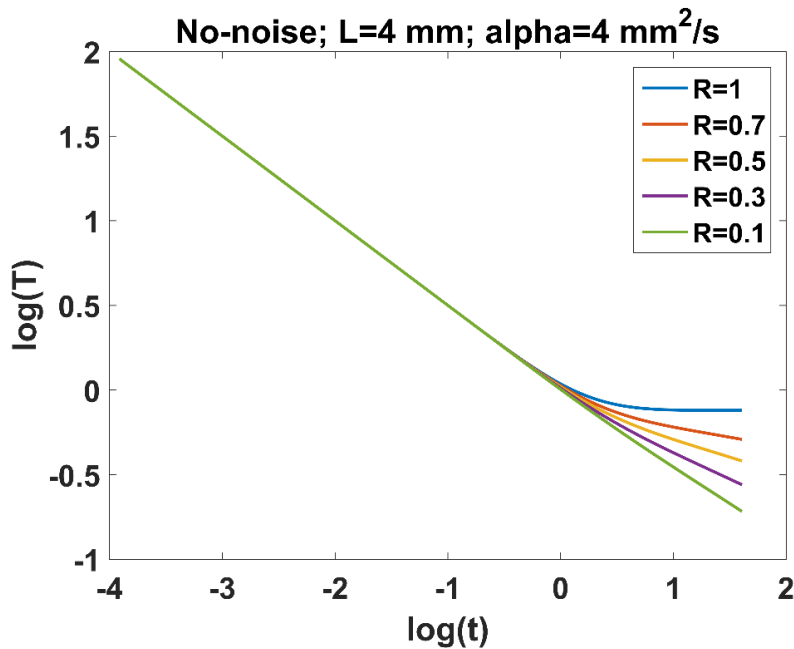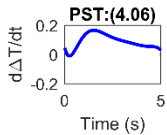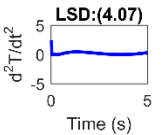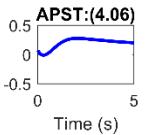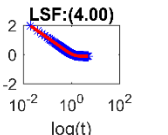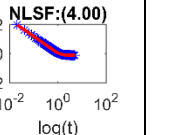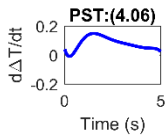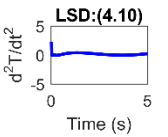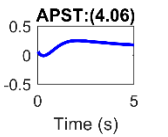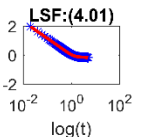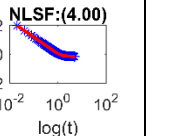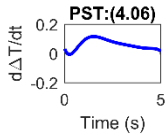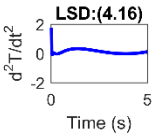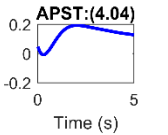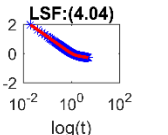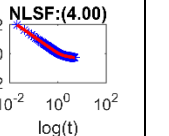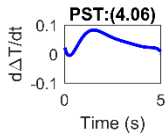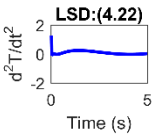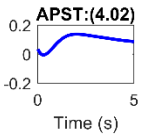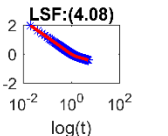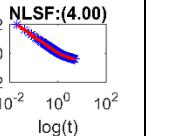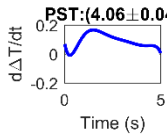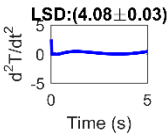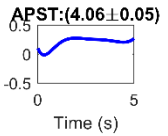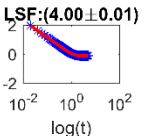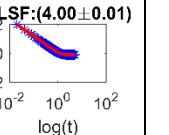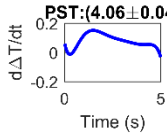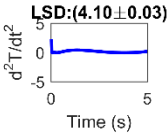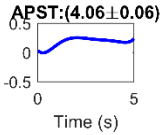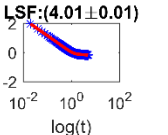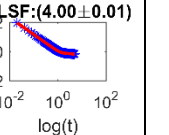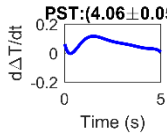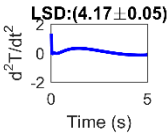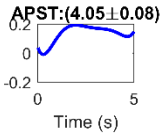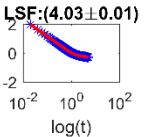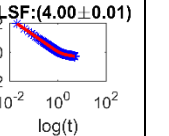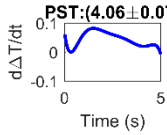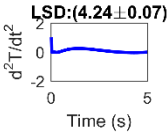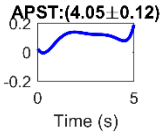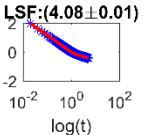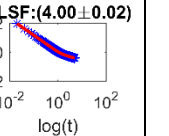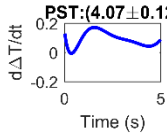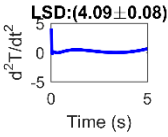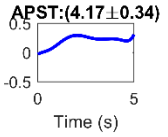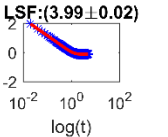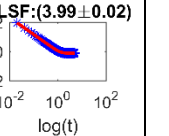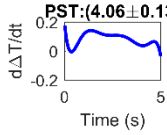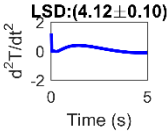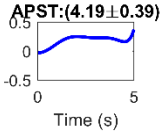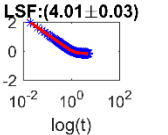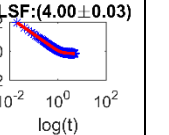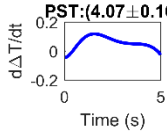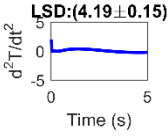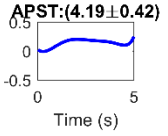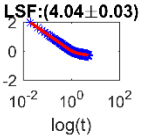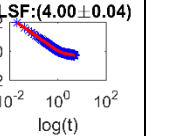
Figure 4-3 The comparison of model simulation with different values of R, where other parameters are shown on the top of the graph.

In the first test, the value of R was set as 1, 0.9, 0.7 and 0.5, respectively, and the noise level was set as 'no noise', 45 dB, 35 dB and 25 dB, respectively. The LSD, APST, LSF and NLSF methods were applied on the data produced from Equation (4-6), while the PST method (temperature contrast based) was applied on the data from Equation (4-7). The produced data for PST, LSD and APST methods were fitted by a polynomial model (8th order). For the LSF and NLSF methods, the bounds of optimisation parameters were set as $0 \leq A \leq 2000$, $0 \leq W \leq 50$, $-50 \leq s \leq 50$; for the NLSF method, two extras parameters are added with the bounds of $0 \leq R \leq 1$ and $-1 \leq t_s \leq 1$. Assuming that the value of α is pre-known, the mean and standard deviation of depth measurement are summarised in Table 4-1. The key plots of the compared methods, including the characterise time of PST, LST and APST, and the model fitting of LSF and NLSF, are shown in Table 4-2.

Table 4-1 The comparison of thickness measurement against different noise levels and R values for five selected methods, where the most accurate values are highlighted.

Noise Level (SNR)	R	Measured Thickness (mm)				
		PST	LSD	APST	LSF	NLSF
No-noise	1	4.06	4.07	4.06	4.00	**4.00**
	0.9	4.06	4.10	4.06	4.01	**4.00**
	0.7	4.06	4.16	4.04	4.04	**4.00**
	0.5	4.06	4.22	4.02	4.08	**4.00**
45 dB	1	4.06±0.04	4.08±0.03	4.06±0.05	4.00±0.01	**4.00±0.01**
	0.9	4.06±0.04	4.10±0.03	4.06±0.06	4.01±0.01	**4.00±0.01**
	0.7	4.06±0.05	4.17±0.05	4.05±0.08	4.03±0.01	**4.00±0.01**
	0.5	4.06±0.07	4.24±0.07	4.05±0.12	4.08±0.01	**4.00±0.02**
35 dB	1	4.07±0.12	4.09±0.08	4.17±0.34	3.99±0.02	**3.99±0.02**
	0.9	4.06±0.13	4.12±0.10	4.19±0.39	4.01±0.03	**4.00±0.03**
	0.7	4.07±0.16	4.19±0.15	4.19±0.42	4.04±0.03	**4.00±0.04**
	0.5	4.08±0.25	4.29±0.24	4.30±0.59	4.09±0.03	**4.01±0.05**
25 dB	1	4.14±0.48	4.14±0.34	4.74±0.82	3.97±0.05	**3.97±0.05**
	0.9	4.13±0.48	4.16±0.37	4.81±0.86	4.01±0.08	**4.00±0.08**
	0.7	4.21±0.74	4.23±0.67	4.87±0.87	4.05±0.10	**4.01±0.12**
	0.5	4.34±1.02	4.17±0.95	4.88±0.89	4.09±0.12	**4.01±0.16**

Table 4-2 The characteristic time of PST, LST and APST, and the model fitting of LSF and NLSF where the blue scatter represents the observations and the red curve represents the fitting.

SNR	*R*	Measured Thickness (mm)				
No Noise	1	PST:(4.06)	LSD:(4.07)	APST:(4.06)	LSF:(4.00)	NLSF:(4.00)
	0.9	PST:(4.06)	LSD:(4.10)	APST:(4.06)	LSF:(4.01)	NLSF:(4.00)
	0.7	PST:(4.06)	LSD:(4.16)	APST:(4.04)	LSF:(4.04)	NLSF:(4.00)
	0.5	PST:(4.06)	LSD:(4.22)	APST:(4.02)	LSF:(4.08)	NLSF:(4.00)
45 dB	1	PST:(4.06±0.04)	LSD:(4.08±0.03)	APST:(4.06±0.05)	LSF:(4.00±0.01)	NLSF:(4.00±0.01)
	0.9	PST:(4.06±0.04)	LSD:(4.10±0.03)	APST:(4.06±0.06)	LSF:(4.01±0.01)	NLSF:(4.00±0.01)
	0.7	PST:(4.06±0.05)	LSD:(4.17±0.05)	APST:(4.05±0.08)	LSF:(4.03±0.01)	NLSF:(4.00±0.01)
	0.5	PST:(4.06±0.07)	LSD:(4.24±0.07)	APST:(4.05±0.12)	LSF:(4.08±0.01)	NLSF:(4.00±0.02)
35 dB	1	PST:(4.07±0.12)	LSD:(4.09±0.08)	APST:(4.17±0.34)	LSF:(3.99±0.02)	NLSF:(3.99±0.02)
	0.9	PST:(4.06±0.13)	LSD:(4.12±0.10)	APST:(4.19±0.39)	LSF:(4.01±0.03)	NLSF:(4.00±0.03)
	0.7	PST:(4.07±0.16)	LSD:(4.19±0.15)	APST:(4.19±0.42)	LSF:(4.04±0.03)	NLSF:(4.00±0.04)

SNR	R	Measured Thickness (mm)				
	0.5	PST:(4.08±0.25)	LSD:(4.29±0.24)	APST:(4.30±0.59)	LSF:(4.09±0.03)	NLSF:(4.01±0.05)
25 dB	1	PST:(4.14±0.48)	LSD:(4.14±0.34)	APST:(4.74±0.82)	LSF:(3.97±0.05)	NLSF:(3.97±0.05)
	0.9	PST:(4.13±0.48)	LSD:(4.16±0.37)	APST:(4.81±0.86)	LSF:(4.01±0.08)	NLSF:(4.00±0.08)
	0.7	PST:(4.21±0.74)	LSD:(4.23±0.67)	APST:(4.87±0.87)	LSF:(4.05±0.10)	NLSF:(4.01±0.12)
	0.5	PST:(4.34±1.02)	LSD:(4.17±0.95)	APST:(4.88±0.89)	LSF:(4.09±0.12)	NLSF:(4.01±0.16)

Under a perfect condition, where there is no noise and R equals to 1, as shown in Table 4-1, the measured thickness of PST, LSD and APST methods is about 4.06 - 4.07 mm, within 1.5% percentage error of the ground truth (4.00 mm), and the LSF and NLSF methods produced perfect results (4.00 mm). When R decreases from 1.0 to 0.5, the measurement error of LSD increases to 0.22 mm (5.5% percentage error), whereas the PST and APST methods produced relatively good and consistent results. The error of estimated thickness of LSF increases slightly (up to 2% percentage error) following the decrease of R. The NLSF method still produced the perfect results for all four R values. Summarily, this test demonstrates that in the case of noise-free, the PST, APST, and LSF methods are less sensitive to R, whereas the LSD method is more sensitive to R. The NLSF method is not sensitive to the value of R because the proposed mode considers R as a parameter, estimation of which is a by-product of this method.

In practice, raw data are contaminated with noise and other signal degradations [14], [39]. Errors of temperature measurement with the infrared camera are typically classified into errors of the method, errors of the calibration, and errors

of the electronic part [122]. The performance of all five considered methods was analysed and evaluated by adding white Gaussian noise to the simulated signal. Three levels of noise were considered: low level of noise (45 dB), medium level of noise (35 dB), and high level of noise (25 dB). For each considered noise level, 1000 tests were repeated and the mean and standard variation of the estimated thickness was computed. The mean indicates the accuracy of measurement, and the standard deviation (std) indicates the precision of measurement. It can be observed from Table 4-1 that at the low level of noise (45 dB), the mean of measurement of each method is similar as those of no noise. The LSF and NLSF methods produced a high precision (std: 0.01-0.02 mm) than the other three methods (std: 0.07 - 0.12 mm) when R = 0.5. Considering both accuracy and precision, the proposed NLSF performs best. At the medium level of noise (35 dB), the accuracy of the PST, LSF, and NLSF methods is relatively high (< 3%) and consistent, while the accuracy of the LSD and APST method is relatively low (< 7.5%) and more sensitive to the change of R. The NLSF method has the best accuracy and the LSF method has the best precision. At the high level of noise (25 dB), the accuracy of the PST is significantly reduced (< 8.5%) and the APST method produced the largest error (< 22%). The NLSF method still has the best accuracy and almost the same level of precision as LSF. All these observations demonstrate the superior performance of the proposed method against noise.

To further evaluate the performance of LSF and NLSF, Table 4-3 shows the results for data with the very high noise level and very low R value, where the value of R changes from 0.4 to 0.1, and SNR changes from 20 dB to -10 dB. In the case of no noise, it is inferred that the estimated thickness using LSF is strongly dependent on the value of R. The error is increased from 3% to 8% when R is changed from 0.4 to 0.1. However, the results produced by the proposed NLSF method are all perfect. An example of curve fittings using the NLSF and LSF methods is illustrated by Figure 4-4 where R is chosen as 0.1 and noise level is 40 dB. Inspection shows that NLSF offers better fitting than LSF due to the introduction of the extra parameters. When the noise level is increased from 20 dB to -10 dB, the accuracy of NLSF is consistently higher than that of LSF, while there is no significant difference in precision between two methods.
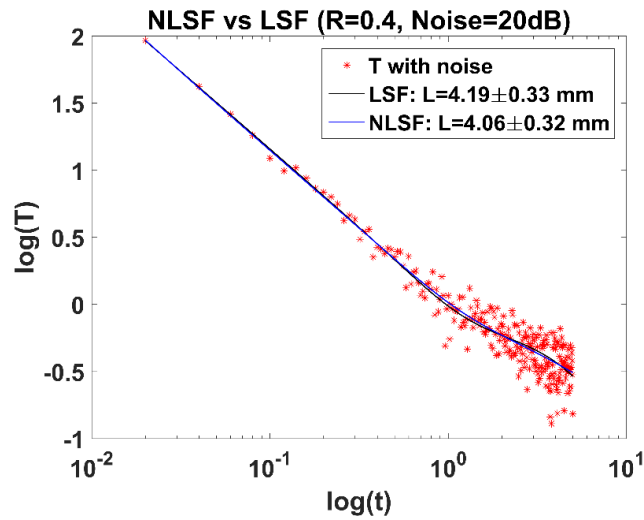
Figure 4-4 An example of curve fitting comparison between NLSF and LSF method

Table 4-3 The comparison of thickness measurement of the LSF and NLSF methods against high noise level and lower R values, where the most accurate values are highlighted.

Noise Level	R	Measured Thickness (mm)		Percentage Error (%)	
		LSF	NLSF	LSF	NLSF
No-noise	0.4	4.12	**4.00**	3.00%	**0.00%**
	0.3	4.16	**4.00**	4.00%	**0.00%**
	0.2	4.23	**4.00**	5.75%	**0.00%**
	0.1	4.32	**4.00**	8.00%	**0.00%**
20 dB	0.4	4.19±0.33	**4.06±0.32**	4.75%	**1.50%**
	0.3	4.29±0.52	**4.05±0.44**	7.25%	**1.25%**
	0.2	4.55±0.84	**4.10±0.67**	13.75%	**2.50%**
	0.1	5.14±1.42	**4.33±1.21**	28.50%	**8.25%**
10 dB	0.4	4.30±0.73	**4.03±0.85**	7.50%	**0.75%**
	0.3	4.50±0.93	**4.09±1.10**	12.50%	**2.25%**
	0.2	4.74±1.17	**4.25±1.36**	18.50%	**6.25%**
	0.1	5.01±1.56	**4.42±1.79**	25.25%	**10.50%**
0 dB	0.4	4.19±1.14	**4.04±1.50**	4.75%	**1.00%**
	0.3	4.32±1.33	**4.16±1.59**	8.00%	**4.00%**
	0.2	4.36±1.54	**4.26±1.89**	9.00%	**6.50%**
	0.1	4.44±1.56	**4.39±2.00**	11.00%	**9.75%**
-10 dB	0.4	3.59±1.58	**3.94±1.90**	10.25%	**1.50%**
	0.3	3.54±1.59	**3.97±1.94**	11.50%	**0.75%**
	0.2	3.68±1.70	**4.03±1.98**	8.00%	**0.75%**
	0.1	3.64±1.63	**4.16±1.90**	9.00%	**4.00%**

Table 4-4 shows the estimated values of R against different noise levels where R is varied from 1.0 to 0.1. For the cases without noise, the proposed method can estimate the R value perfectly. With the increase of noise level, the estimation error increases. For the noise level of less than 30 dB, the error of estimation is less than 0.02. Furthermore, the sensitivity of R estimation to noise level is dependent on the value of R. Higher the R value is, less influence from the noise.

Table 4-4 The estimated values of R against different noise levels.

R	Noise Level (SNR)							
	No-noise	45 dB	35 dB	25 dB	20 dB	10 dB	0 dB	-10 dB
1	1.00	1.00±0.00	1.00±0.01	0.99±0.02	0.98±0.04	0.95±0.09	0.90±0.19	0.96±0.13
0.9	0.90	0.91±0.01	0.92±0.03	0.94±0.05	0.94±0.07	0.92±0.13	0.92±0.19	0.96±0.14
0.8	0.80	0.81±0.01	0.82±0.03	0.86±0.08	0.87±0.11	0.89±0.16	0.89±0.21	0.96±0.14
0.7	0.70	0.71±0.01	0.72±0.03	0.76±0.09	0.80±0.13	0.85±0.20	0.88±0.23	0.95±0.14
0.6	0.60	0.61±0.01	0.62±0.03	0.67±0.11	0.71±0.15	0.80±0.24	0.86±0.25	0.95±0.14
0.5	0.50	0.51±0.01	0.52±0.03	0.57±0.10	0.63±0.17	0.76±0.27	0.84±0.27	0.96±0.14
0.4	0.40	0.41±0.01	0.42±0.03	0.47±0.11	0.53±0.18	0.70±0.31	0.84±0.27	0.95±0.18
0.3	0.30	0.31±0.01	0.32±0.03	0.37±0.11	0.43±0.18	0.66±0.32	0.86±0.27	0.95±0.17
0.2	0.20	0.21±0.01	0.22±0.03	0.27±0.10	0.36±0.19	0.64±0.35	0.84±0.28	0.95±0.16
0.1	0.10	0.11±0.01	0.12±0.03	0.19±0.12	0.30±0.22	0.63±0.37	0.85±0.28	0.95±0.17

Another benefit of the proposed method is the introduction of the parameter t_s, which measures the potential latency of the sampled timestamp of thermal data. This time shift could be caused by the latency of data acquisition or data storage. Similar to the impact of the estimation of R, the estimation of t_s aims to further improve the accuracy of depth measurement. This feature is particularly important for data collected using a slow sampling rate. Considering the sample rate as 50 Hz, the potential latency was in the range from 0 to 0.02 seconds. To evaluate the influence of the latency on the depth measurement, Table 4-5 shows the results of estimation using the proposed method with and without estimation of t_s, where the noise level was set as 30 dB and R was set as 0.4. Inspection of the result shows that the proposed method can successfully estimate the value of t_s, which is not achievable for the characteristic time-based methods such as PST, APST and LSD due to the neglect of the physical model. The value of L was estimated with an error of less than 1%. However, if the parameter t_s is not

considered in the model (4-1), the error of L measurement increases dramatically following the increase of t_s, which suggests the key role of this parameter. It should be noted that in the real applications the ground truth of t_s is unknown. Providing a capability to estimate t_s will increase the reliability of measurement.

Based on above observations, it can be concluded that the proposed NLSF method has significantly improved the robustness and accuracy of depth measurement, particularly when the value of R is significantly lower than 1 or the noise level is high. Meanwhile, the value of R can be effectively estimated. Furthermore, the accuracy of depth measurement of NLSF is immune to the latency of data acquisition while other methods are not.

Table 4-5 Estimated errors of L using the proposed method with and without estimation of t_s, where the noise level was set as 30 dB and the R value was set as 0.4.

True t_s (s)	Estimated t_s (s)	Including t_s in the model (4)				Excluding t_s in the model (4)			
		L		R		L		R	
		Value (mm)	% Error	Value	% Error	Value (mm)	% Error	Value	% Error
0.019	0.019059	4.0185	0.46	0.4418	10.46	0.0228	99.43	0.9095	127.37
0.017	0.017094	4.0270	0.68	0.4676	16.91	0.1016	97.46	0.6345	58.62
0.015	0.015452	4.0418	1.04	0.5472	36.81	0.1781	95.55	0.4460	11.50
0.013	0.013059	4.0184	0.46	0.4418	10.45	0.2398	94.01	0.3387	15.32
0.011	0.011059	4.0177	0.44	0.4416	10.39	0.3037	92.41	0.2614	34.64
0.009	0.009056	4.0185	0.46	0.4418	10.45	0.3834	90.41	0.2018	49.56
0.007	0.007059	4.0181	0.45	0.4417	10.42	2.3247	41.88	0.2549	36.27
0.005	0.005059	4.0185	0.46	0.4418	10.45	3.0314	24.22	0.3093	22.68
0.003	0.003059	4.0186	0.46	0.4418	10.46	3.4899	12.75	0.3494	12.64
0.001	0.001059	4.0185	0.46	0.4418	10.46	3.8543	3.64	0.3874	3.15

4.3.2 Experimental Study

A flat plate of carbon fibre reinforced polymer (CFRP) material was used in this experiment. The size of the composite sample is 153 mm × 102 mm × 4 mm. The plate was made of unidirectional Toray 800 carbon fibres pre-impregnated with Hexcel M21 epoxy resin and manufactured in a traditional autoclaving process to a quasi-isotropic layup. Three flat-bottom holes were drilled with the same diameter of 6 mm at different depths (1 mm, 2 mm and 3 mm, respectively), as illustrated in Figure 4-5. The distance between the holes is 25 mm. The scheme of the experimental set-up is illustrated by Figure 3-3(a) in Chapter 3. Thermographic images were captured by FLIR SC7600, as shown in Figure 3-4. Considering the thickness of the sample and its low thermal diffusivity, a sampling rate of 25 Hz was used, and totally 1000 frames, equally 40 seconds data length, were captured and analysed.
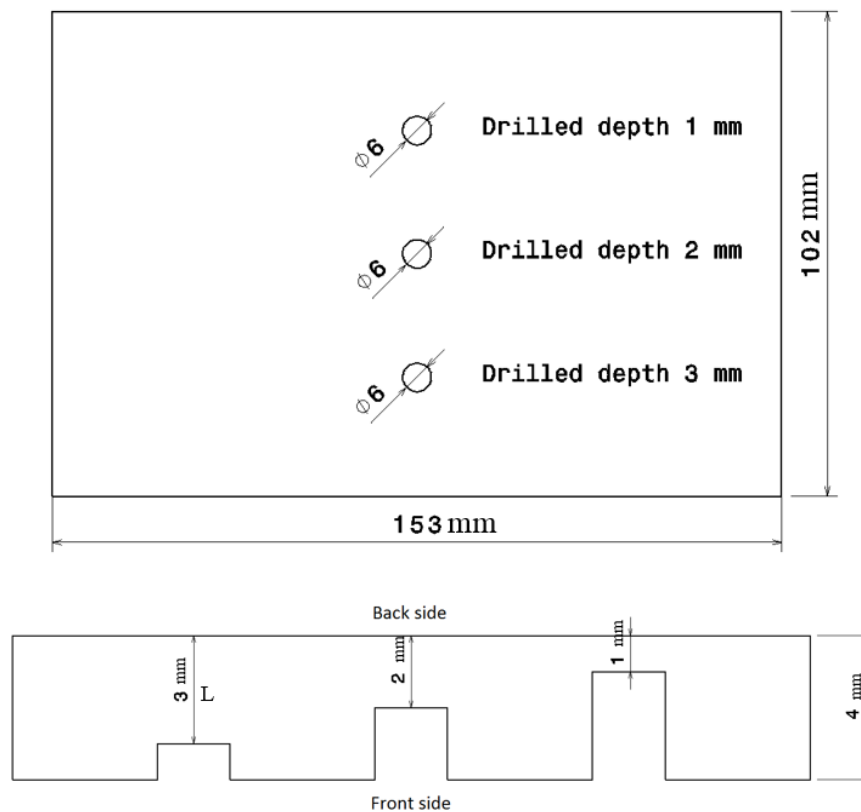
Figure 4-5 The composite material sample with drilled in various depth

Frame at time: 8.00 s

(a)

Raw Temperature

Point1 (Defect:L=1mm)
Point2 (Defect:L=2mm)
Point3 (Sound:L=4mm)

(b)

Temperature Contrast

Point1 (L=1mm)
Point2 (L=2mm)

(c)
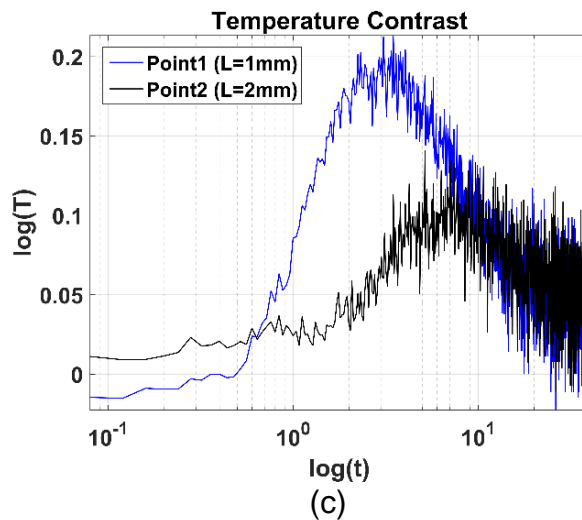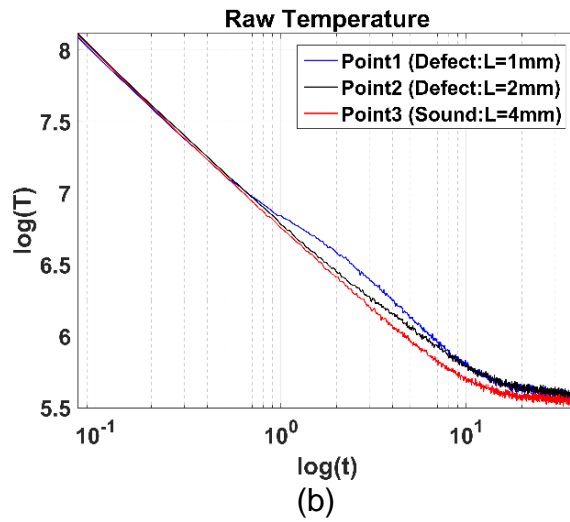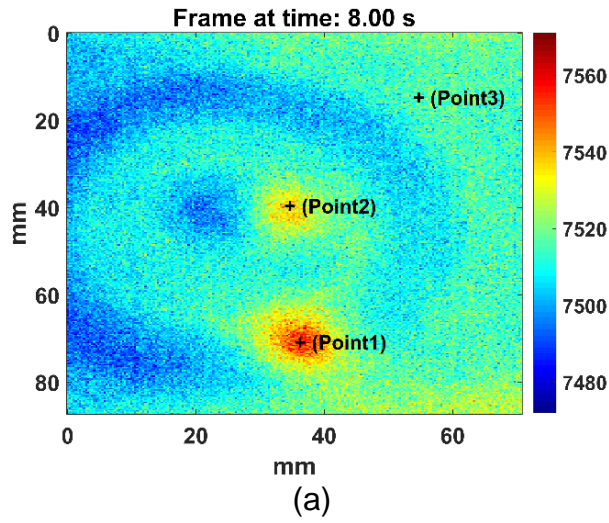
Figure 4-6 (a) Raw thermal image at the time of 8 sec where three points are sampled from the sound area, middle hole and bottom hole, respectively; (b) Temperature decay curve of the selected three points in logarithmic domain and (c) Temperature contrast of point 1 and point 2

Figure 4-6(a) shows a snapshot of the captured thermal image at the time of 8 seconds, where the middle and bottom holes can be clearly seen. However, the top hole is not detectable in this experiment due to the close distance to the back surface. To further inspect the thermal behaviour, Figure 4-6(b) shows the plots of raw temperature curve of three selected pixels overtime on the sound area, the middle hole and the bottom hole, respectively, the positions of which are marked in Figure 4-6(a). The temperature deviation of defective pixels (Point 1 and Point 2) can be clearly observed at different times while the difference of slope after this deviation is difficult to be distinguished visually. It can be seen that the temperature deviation of the defective points (Point 1 and Point 2) and the non-defective point (Point 3) in Figure 4-6(b) matches the theory of heat transfer shown in Figure 3-3(b). The time of temperature deviation on the defective points (which have thinner thickness/depth) happens before the non-defective point (which has thicker thickness) [76]. The value of estimated defect depth is dependent on the selection of sample data, which is a common issue for all depth measurement methods. If the thermal diffusivity and defect depth are known, this selection is straightforward, as suggested by Sun [22]. This thesis proposes to use the time when the maximal temperature contrast between the considered defective pixel and the reference pixel from the sound area is achieved as the end of sampling. Figure 4-6(c) shows the temperature contrast Point 1 and Point 2, where two peak time t_1 and t_2 are detected.

In this proposed method, the data segments of $[0, t_1]$ and $[0, t_2]$ were sampled for the bottom and middle holes, respectively. For the sound pixels, the full data length is sampled. To reduce the measurement error of defect depth (L) and thermal wave reflection coefficient (R), ten pixels on the sound region, the middle hole and bottom hole were manually selected and the estimated parameters were averaged. The used thermal diffusivity (α) in this experiment is 0.55×10^{-6} m^2/s. This value was calculated from Equation (4-5) on the sound area by considering the thickness of the sample as 4 mm.

Both LSF and NLSF methods were applied and the results are shown in Table 4-6. The averaged estimated depth of NLSF on the sound area is 3.98 mm and

the standard deviation, as an indicator of precision, is 0.04 mm, which is more accurate than those of LSF (3.67±0.05 mm). The measured defect depths of the middle and bottom holes are 2.05 mm and 1.03 mm, respectively, which is closer to the ground truth than those of LSF (1.90 mm and 1.06 mm, respectively). However, the LSF method produced less standard deviation (0.01 mm and 0.03 mm, respectively) than the NLSF method (0.04 mm and 0.06 mm, respectively). This observation could be caused by the introduction of two extra parameters. The estimated R value on the sound area is 0.84, which is close to 1, while the s value is 0. The estimated R values for the middle hole and the bottom hole are much smaller (0.18 and 0.25, respectively) and the s values are much larger (0.87 and 16.46, respectively).

Table 4-6 The measurement of the experimental data using the LSF and NLSF methods.

Position	Ground Truth (mm)	Estimated Depth (mm)		Estimated R (NLSF)	Estimated s (NLSF)	Estimated t_s (NLSF)
		LSF	NLSF			
Sound area	4.00	3.67±0.05	3.98±0.04	0.84±0.04	0.00±0.00	0.0226±0.0023
The middle hole	2.00	1.90±0.01	2.05±0.04	0.18±0.02	0.87±0.43	0.0256±0.0011
The bottom hole	1.00	1.06±0.03	1.03±0.06	0.25±0.02	16.46±2.22	0.0269±0.0012
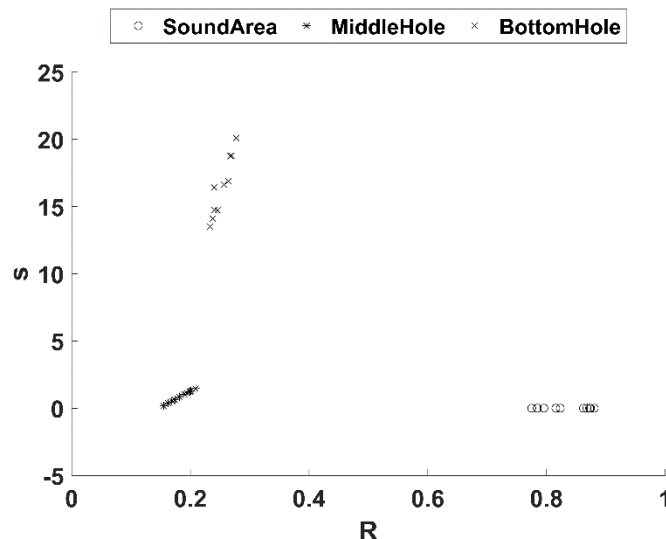
Figure 4-7 Scatter chart of the estimated R and s parameters, which shows ten pixels for each of the three sampled regions

To further inspect the estimated parameters on difference positions, Figure 4-7 plots the scatter of the estimated values of R and s, where ten pixels for each of the three regions were sampled. It can be observed that for each region the estimated parameters are relatively consistent while for different regions they are significantly different. Therefore, the clustering of these two parameters can be a potential approach to effectively classify the pixels.

For further analysis, the estimated R and and s values from the NLSF method in Table 4-6 are plotted in Figure 4-7, where three groups can be clearly observed. The value of R in sound area is naturally higher and close to 1 and the value of s in sound area is usually small and close to 0 [80]. R value also varies following the depth of the defect. Larger defect depth provides lower R value.

The proposed method can estimate both the thickness and defect depth effectively. The error of estimation of the proposed method in the sound area is less than 1% while the LSF method has error up to 7%. For the defective region, the LSF method produced higher error than the NLSF method around 2%. It should be noted that Equation (3-1) is valid only for a homogeneous plate. The composites are non-homogeneous materials. In previous Zhao's work [45], the measured thermal diffusivity of CFRP is about 0.47±0.03 m^2/s, which also depends on the lay-up configuration of the sample. As far as we are concerned, there is no heat diffusion models for non-homogeneous materials, so the assumption that the thermal diffusivity of the tested composite sample is uniform was applied in this research.

4.4 Nonlinear System Identification Method (NSI)

This thesis also proposes a new method to improve the reliability of defect depth measurement based on the pulsed thermographic inspection by addressing the over-fitting problem. Different from existing methods using a fixed model structure for all pixels, the proposed method adaptively detects the optimal model structure for each pixel thus targeting to achieve better model fitting while using fewer model terms. Fitting a heat transfer model as shown in Equation (2-45) is

challenging because in most real-world scenarios too many parameters are unknown. Without considering any physical parameters, a polynomial model can be used to represent complex thermal behaviour. This can be expressed as

$$f(t) = \sum_{n=0}^{N} a_n \cdot t^n + \varepsilon(t) \qquad \text{(4-9)}$$

where N is the model order, $\varepsilon(t)$ is the noise and a_n are coefficients to be estimated. LSD uses such a model to fit the time-temperature dependency in the logarithmic domain [75]. The challenge is how to automatically select the model order N. This value should be large enough to ensure a good fit to the observed data. However, N should also not be too large as it will cause overfitting problems [123]. There is very limited literature to report how to select the model order for fitting time-temperature dependence of active thermographic inspections or discuss the challenge.

Initially, consider the linear-in-the-parameters model [124]

$$f(t) = \sum_{m=1}^{B} \theta_m p_m(t) + \varepsilon(t) \qquad \text{(4-10)}$$

where p_m are candidate model terms, B denotes the number of all candidate model terms, and θ_m are model coefficients. Let

$$F = [f(1), f(2), \cdots, f(M)]^T \qquad \text{(4-11)}$$

be a vector of measured data with a total number of M, and

$$P_m = [p_m(1), p_m(2), \cdots, p_m(M)]^T \qquad \text{(4-12)}$$

be a vector formed the mth candidate model term. Let

$$D = \{P_1, P_2, \cdots, P_B\} \qquad \text{(4-13)}$$

be a dictionary compost of the B candidate bases. The finite-dimensional set D is usually redundant. The model term selection problem is equivalent to find a subset of $N(N \leq B)$ bases,

$$D_N = \{\emptyset_1, \emptyset_2, \cdots, \emptyset_N\} = \{P_{j_1}, P_{j_2}, \cdots, P_{j_N}\} \qquad \text{(4-14)}$$

from the dictionary D, where $\emptyset_i = P_{j_i}$, $j_i \in \{1,2,\cdots,N\}$, so that F can be satisfactorily approximated using a linear combination of $\emptyset_m$ as below:

$$F = \theta_1 \emptyset_1 + \theta_2 \emptyset_2 + \cdots + \theta_N \emptyset_N + \varepsilon \qquad \text{(4-15)}$$

The first step of the search starts with the initial full model (4-10) and the initial full dictionary $D = \{P_1, P_2, \cdots, P_B\} = \{1, t, t^2, \cdots, t^{B-1}\}$. Note that the candidate term is not necessary to be $t^j (j \in \mathbb{Z})$. It can be any linear or nonlinear relationship, such as $e^{j \cdot t}, \sin(j \cdot t)$, where $j \in \mathbb{R}$. Since the polynomial fitting has been well accepted in this application, the selection of D is straightforward. For applications where the prior knowledge is limited, some methods have been proposed [125], [126], such as bootstrap based structure detection algorithm [127], which is not the research scope of this thesis. For $m = 1,2,\cdots,B$, let $q_m = \emptyset_m$ and $\sigma = F^T F$, calculate

$$g_m^{(1)} = \frac{F^T q_m}{q_m^T q_m} \qquad \text{(4-16)}$$

$$ERR_m^{(1)} = \frac{\left(g_m^{(1)}\right)^2 q_m^T q_m}{\sigma} \qquad \text{(4-17)}$$

Let

$$l_1 = arg \max_{1 \leq m \leq B} \left\{ ERR_m^{(1)} \right\} \qquad \text{(4-18)}$$

The first significant term can be selected as $\emptyset_1 = P_{l_1}$, and the first associated orthogonal vector can be chosen as $q_1 = P_{l_1}$.

Assume that a subset D_{s-1}, consisting of $(s-1)$ significant terms $\emptyset_1, \emptyset_2, \cdots, \emptyset_{s-1}$, has been determined at the $(s-1)$th step. In the sth step, for $m = 1,2,\cdots,B$ where $m \notin \{l_1, l_{2,} \cdots l_{s-1}\}$, calculate

$$q_m^{(s)} = \emptyset_m - \sum_{r=1}^{s-1} \frac{\emptyset_m^T q_r}{q_r^T q_r} q_r, \emptyset_m \in D - D_{s-1} \tag{4-19}$$

$$g_m^{(s)} = \frac{F^T q_m^{(s)}}{q_m^{(s)T} q_m^{(s)}} \tag{4-20}$$

$$ERR_m^{(s)} = \frac{\left(g_m^{(s)}\right)^2 \left[q_m^{(s)T} q_m^{(s)}\right]}{\sigma} \tag{4-21}$$

Let

$$l_s = arg \max_{1 \le m \le B} \left\{ERR_m^{(s)}\right\} \tag{4-22}$$

The sth significant terms can then be chosen as $\emptyset_s = P_{l_s}$, $EER_m = ERR_m^{(ls)}$ and the sth associated orthogonal vector can be chosen as $q_s = q_{l_s}^{(s)}$. At each step, the term with the strongest capability to represent the output is selected. The significance of each selected model term is measured by an index, called the Error Reduction Ratio (ERR), which indicates how much of the variance change in the system response, in percentage terms, can be accounted for by including the relevant model terms. Values of ERR range from 0% to 100%. The larger ERR of a term, the higher the dependence is between this term and the output.

To stop the search procedure and determine the number of significant terms N, a criterion called Penalised Error-to-Signal Ratio (PESR) is introduced [128]. It can be written as

$$PESR_n = \frac{1}{\left(1 - \frac{\lambda n}{M}\right)^2} (1 - \sum_{i=1}^{n} ERR_i) \tag{4-23}$$

This term was introduced to monitor the search procedure, where n denotes the index of the selected terms. The search procedure stops when $PESR_n$ arrives at the first valley. The effect of the adjustable parameter λ on the results is discussed in [128], which suggested that λ should be chosen between 5 and 10.

PESR has been used to monitor the search of model structure for various application [129], [130], [131].

Once the model structure is determined, the unknown parameters θ_i in Equation (4-15) can then be estimated using the least square method. The temperature decay curve can be reconstructed by

$$\hat{T}(t) = \frac{\hat{f}(t)}{\sqrt{t}} = \frac{\theta_1 \emptyset_1(t) + \theta_2 \emptyset_2(t) + \cdots + \theta_N \emptyset_N(t)}{\sqrt{t}} \tag{4-24}$$

The first derivative of $\hat{f}(t)$ can be calculated by

$$\hat{f}'(t) = \theta_1 \emptyset_1'(t) + \theta_2 \emptyset_2'(t) + \cdots + \theta_N \emptyset_N'(t) \tag{4-25}$$

If α is known, the thickness can be estimated by

$$\hat{L} = \sqrt{2\alpha \cdot t_{NSI}} \tag{4-26}$$

where t_{NSI} denotes the highest peak time of $\hat{f}'(t)$. Or if L is known, the thermal diffusivity can be estimated by

$$\hat{\alpha} = \frac{L^2}{2t_{NSI}} \tag{4-27}$$

Note the examples of this thesis focus on the measurement of sample thickness and thermal diffusivity, so the coefficient of 2 was used. To inspect a defective sample, especially when the defect is small, multiple reflections should be considered by replacing the coefficient 2 in Equation (4-26) and (4-27) with 1.93.

The procedure of the proposed NSI method can be summarised:

1) Extract the temperature decay data for a pixel;

2) Define a set of candidate terms as shown in Equation (4-13). This thesis used $\{1, t, t^2, \cdots, t^{B-1}\}$ for all examples;

3) Calculate the ERR value of each candidate term, and the term with maximum ERR value is selected;

4) Calculate the PESR value after a new term is selected. The term selection

procedure stops when PESR arrives at the first valley.

5) Reconstruct the time-temperature functions $\hat{T}(t)$ and $\hat{f}(t)$ by Equation (4-24);

6) Calculate the first derivative of $\hat{f}(t)$ by Equation (4-25), and then detect the peak time;

7) Estimate the sample thickness or defect depth by Equation (4-26) or the thermal diffusivity by Equation (4-27);

8) Repeat the steps 1-7 for all pixels.

4.5 Experiments and Results of NSI

4.5.1 Model Simulation without Noise

To validate the proposed method, model simulations were produced by Equation (4-6), where the parameters Q, R and e were set to 1 and the thermal diffusivity (α) was set to 1×10^{-6} m^2/s.

Initially, simulation data without noise for the thickness value of 2 mm were produced. The proposed NSI method was then applied to these data to estimate the thickness assuming α is known. The sample rate was chosen as 100 Hz and totally 500 data points (5 s) were sampled. The principle of the proposed method can be demonstrated by Figure 4-8 and Table 4-7. The observed temperature curves $T(t)$ and $f(t)$ are plotted by the solid blue curve in Figure 4-8(a) and Figure 4-8(b), respectively. The maximum order of the candidate terms B was chosen as 15.

Table 4-7 PESR values for different numbers of selected model terms against different values of λ. The final number of model term N is chosen when the PESR arrives at the first valley.

Number of terms	λ				
	5	6	7	8	9
1	5.132E-01	5.153E-01	5.174E-01	5.195E-01	5.216E-01
2	2.322E-01	2.341E-01	2.361E-01	2.380E-01	2.400E-01
3	2.430E-03	2.460E-03	2.490E-03	2.520E-03	2.560E-03
4	8.770E-04	8.918E-04	9.070E-04	9.226E-04	9.386E-04
5	5.320E-04	5.434E-04	5.551E-04	5.672E-04	5.798E-04
6	8.755E-05	8.983E-05	9.220E-05	9.467E-05	9.723E-05
7	8.284E-05	8.540E-05	8.807E-05	9.087E-05	9.380E-05
8	7.946E-06	8.229E-06	8.529E-06	8.844E-06	9.178E-06
9	**2.387E-06**	**2.484E-06**	**2.587E-06**	**2.697E-06**	**2.814E-06**
10	2.390E-06	2.499E-06	2.617E-06	2.743E-06	2.879E-06
11	1.624E-06	1.708E-06	1.798E-06	1.895E-06	2.000E-06
12	3.571E-07	3.774E-07	3.995E-07	4.236E-07	4.499E-07
13	5.997E-07	6.372E-07	6.783E-07	7.236E-07	7.736E-07
14	1.544E-06	1.650E-06	1.767E-06	1.897E-06	2.042E-06
15	2.502E-06	2.688E-06	2.897E-06	3.130E-06	3.392E-06

Table 4-7 shows the values of PESR with different numbers of terms against the selection of the parameter λ. It can be observed that the PESR arrives at the first valley when the number of terms is 9, which is therefore selected as the final number of model terms N. Furthermore, it is inferred that the selection of λ is not sensitive to the selection of N due to the fact that N is chosen as 9 for all considered values of λ. In this thesis, λ was chosen as 6 for all examples. The reconstructed $T(t)$ and $f(t)$ can then be produced using Equation (4-24), and they are plotted by the dash red curve in Figure 4-8(a) and Figure 4-8(b), respectively. Inspection shows that the reconstructed signals fit the observed signals very well, which is also confirmed by inspection of the fitting error between $f(t)$ and $\hat{f}(t)$, shown in Figure 4-8(c). The first derivatives of $\hat{f}(t)$ was then calculated by Equation (4-25) and the result is illustrated by Figure 4-8(d). The peak of $\hat{f}'(t)$, marked by the arrow, was then detected at 2.04 s. If α is known, the estimated thickness based on Equation (4-26) is 2.02 mm. The error is within 1% considering the true value of 2 mm.
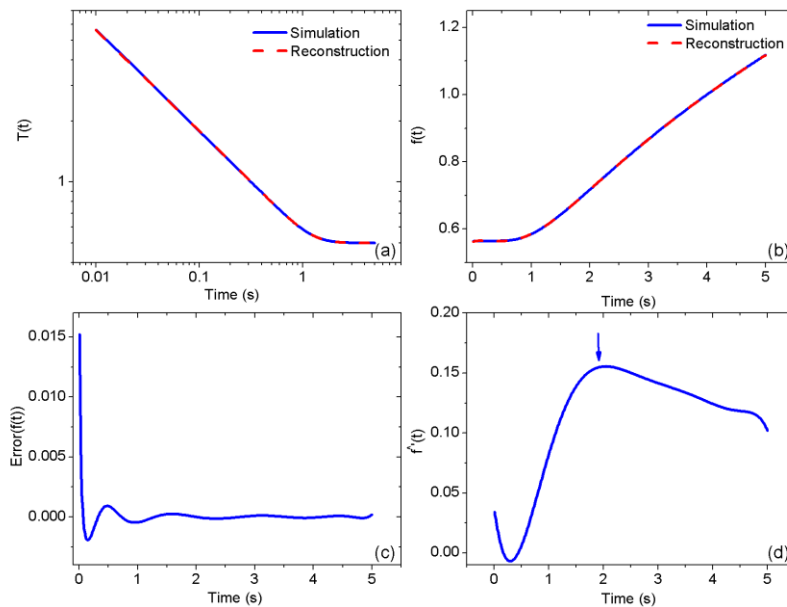
Figure 4-8 (a) The simulated temperature $T(t)$ (blue solid plot) and reconstructed temperature $\widehat{T}(t)$ (red dash plot) with a thickness of 2 mm, plotted in the logarithmic domain; (b) The simulated $f(t)$ (blue solid plot) and reconstructed $\widehat{f}(t)$ (red dash plot) temperature curves; (c) The errors between $f(t)$ and $\widehat{f}(t)$; (d) The first derivative of $\widehat{f}(t)$, where the arrow highlights the peak at the time of 2.04 s.

To assess the sensitivity of the number of the fitting model order for the LSD and APST methods, Figure 4-9(a) compares the estimated thickness using three considered methods (LSD, APST, and NSI) for simulation data without noise against the true thickness. The number of terms was chosen in the range between 5 and 20. Note that the number of terms determines the model order for the LSD and APST methods, which is not the case for the NSI method. It has been observed that, not surprising, for both LSD and APST methods, a higher number of model terms produces better results. It indicates that for data without noise a selection of a high order model of both LSD and APST methods can guarantee an accurate result.
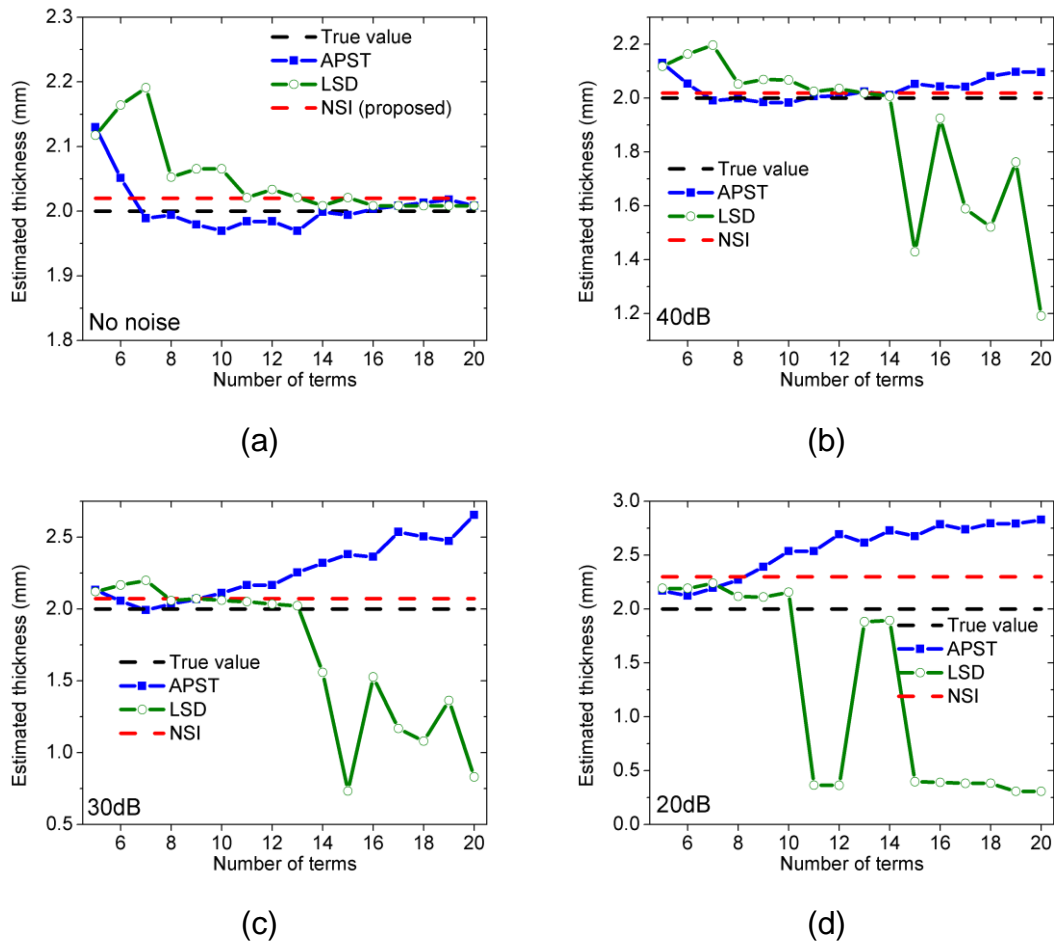
Figure 4-9 Comparison of estimated thickness using the APST method (the blue plot), the LSD method (the green plot) and the propose NSI method (the red dash line) as well as the true thickness (the black dash line). For the APST and LSD methods, different model orders, from 5 to 20, were tested. For the proposed NSI method, the number of model terms is automatically chosen. This process was applied to model simulations data with different levels of noise: (a) no noise, (b) SNR = 40 dB, (c) SNR = 30 dB, and (d) SNR = 20 dB. The results were produced by averaging 100 tests for each considered SNR.

4.5.2 Model Simulation with Noise

In practice, raw data are contaminated with noise and other signal degradations [14], [39]. Errors of temperature measurement with infrared cameras are typically classified into (a) errors of method, calibration errors and electronic path errors [122]. The level of noise is different case to case. To evaluate the performance of all three considered methods against different levels of noise, model simulations were produced and analysed with the SNR from 20 dB to 40 dB. For each considered SNR, 100 tests were repeated and the estimated thickness was

averaged. Figure 4-9(b) - (d) illustrate the results of three examples with the noise level at 40 dB, 30 dB, and 20 dB, respectively. Inspection of these figures clearly indicates that the results for both LSD and APST methods are sensitive to the selection of the model order. The LSD method produced relatively large errors of the estimated thickness when the model order is larger than 14 for the noise level at 40 dB (see Figure 4-9(b)), 13 for the noise level at 30 dB (see Figure 4-9(c)) and 10 for the noise level at 20 dB (see Figure 4-9(d)). Similar results have been observed for the APST method. Determining an optimal number of model order automatically is a challenge because it depends on the level of noise unless the noise level can be determined before applying these methods. This is usually difficult and sometimes impossible for real-world data. It can also be observed that the errors of depth measurement for all considered methods increase following the decrease of SNR. These observations are not surprising because a model with a high order will over-fit the observed signal corrupted by noise. Over-fitting generally occurs when a model is excessively complex, such as having too many parameters relative to the number of observations. The model will describe noise instead of the underlying relationship. This problem can be further amplified during the calculation of the first or second derivative of the model fitting. Figure 4-10 aims to explain this problem in more detail. A numerical simulation was produced with an SNR of 20 dB. The mode order was chosen as 13 for both LSD and APST methods. Figure 4-10(a) and (c) show the raw $T(t)$ and $f(t)$ with corresponding fitting using LSD and APST, respectively. Figure 4-10(b) shows the plot of the second derivative of $\hat{T}(t)$ in the logarithmic domain, where the red arrow marks the highest peak selected and the blue arrow marks the peak that should be selected. The over-fitting problem caused an underestimation of the detected thickness, i.e., the detected thickness is 0.22 mm based on Figure 4-10(b), which is much smaller than the true value. The plot of the first derivative of $\hat{f}(t)$ is shown in Figure 4-10(d), where the red arrow marks the highest peak and the blue arrow marks the peak that should be selected. The over-fitting problem caused in this case an overestimation, i.e., the detected thickness is 2.18 mm based on Figure 4-10(d), which is larger than the true value. However, for the proposed NSI method, the number of model terms is selected automatically

by monitoring the trade-off between the model complexity, fitting error and the number of sampling using Equation (4-23). This advantage is especially important to analyse real experimental data where the noise levels are unknown.
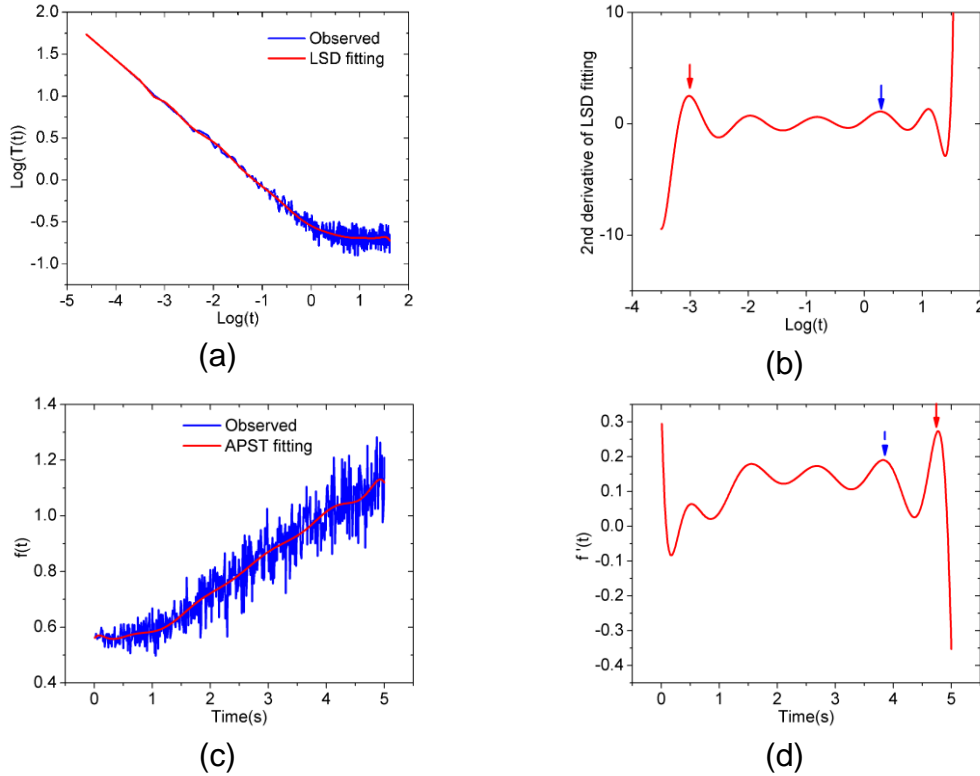
Figure 4-10 An example of the over-fitting problem where the SNR of the model simulation is 20 dB, and the model order was chosen as 13 for both LSD and APST methods. (a): The simulated temperature $T(t)$ (the blue plot) and reconstructed temperature $\widehat{T}(t)$ (the red plot) using the LSD method plotted in the logarithmic domain; (b) the second derivative of the LSD fitting where the red arrow marks the peak actually detected and the blue arrow marks the peak that should be detected; (c) The simulated $f(t)$ (the blue plot) and reconstructed $\widehat{f}(t)$ (the red plot) using the APST method; (d) the first derivative of the APST fitting where the red arrow marks the peak actually detected and the blue arrow marks the peak that should be detected.

To further evaluate the performance of the proposed technique, Figure 4-11 shows the histogram of the estimated thickness for different noise levels. With a decrease of SNR to 20 dB, it has been observed that both accuracy and precision, described by the mean and standard deviation, respectively, are reduced by inspecting that $\widehat{L} = 2.02\pm 0.02$ mm for 40 dB, $\widehat{L} = 2.07\pm0.13$ mm for 30 dB, and $\widehat{L} = 2.30\pm0.32$ mm for 20 dB.
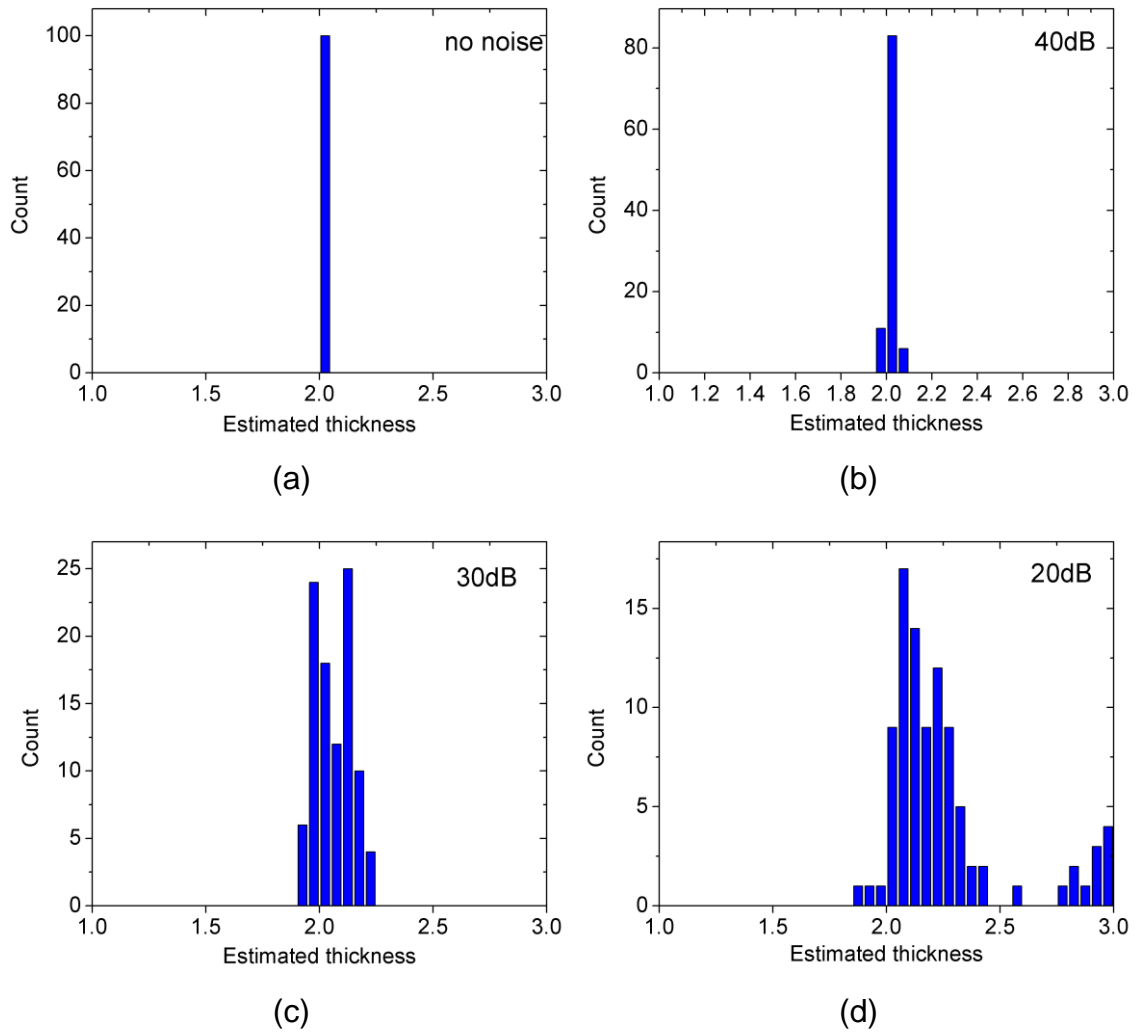
Figure 4-11 Histogram of the estimated thickness using the proposed NSI method based 100 tests for different levels of noise: (a) no noise, (b) SNR = 40 dB, (c) SNR = 30 dB, and (d) SNR = 20 dB.

To further explore the results using the proposed method in higher resolution, Figure 4-12 shows the averaged values of the selected N and estimated thickness against the value of SNR as well as corresponding standard derivatives. Figure 4-12(a) shows that the value of N was set to 8 for signals with SNR in the range from 45 dB to 30 dB. For signals with SNR larger than 45 dB, a higher number of N ($N>8$) was chosen. For signals with SNR smaller than 30 dB, a relatively small number of N ($5 \leq N \leq 8$) was chosen to avoid the over-fitting problem.

Inspection of Figure 4-12(b) shows that for signals with SNR larger than 32 dB, the error of the estimated thickness is within 0.02 mm. For signals with SNR smaller than 32 dB, the error increases almost exponentially following the decrease of SNR (increase of noise level), which is mainly due to finding the wrong peak as shown in Figure 4-10. The precision of thickness measurement, described by the standard deviation, has a similar trend as the accuracy.

(a)   (b)
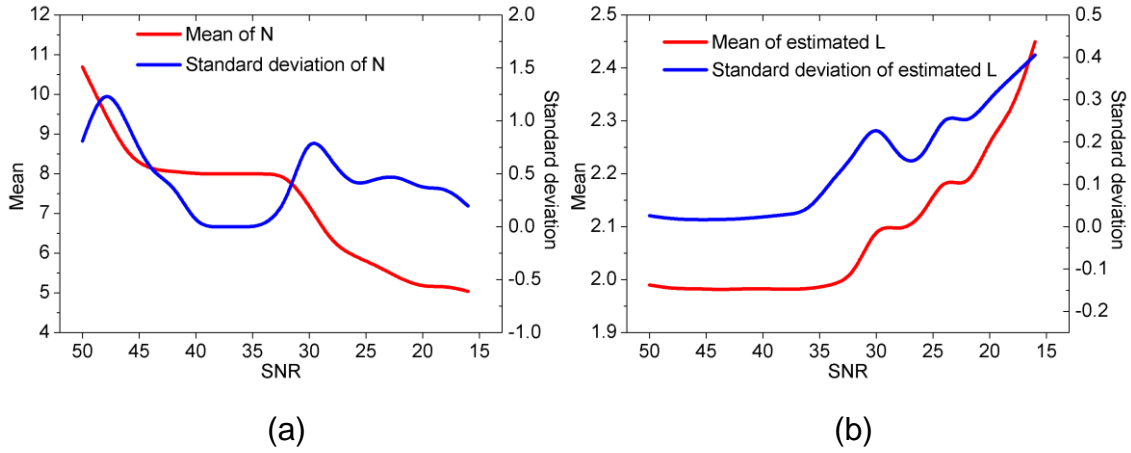
Figure 4-12 The statistical performance of the proposed NSI method for model simulations with different levels of noise. The results were calculated based on 100 tests for each considered SNR. (a) Mean and standard deviation of the selected number of terms against noise level; (b) Mean and standard deviation of the estimated thickness against noise level.

4.5.3 Selection of Sampling Parameters

This section discusses how the selection of sampling parameters affects the results. Assume that the sampled data length is expressed as M_t in the unit of time and M_p is the amount of data point. Obviously,

$$M_p = M_t \cdot f \tag{4-28}$$

where f is the sample rate. Let

$$M_t = k \cdot t_{NSI} = k \frac{L^2}{2\alpha} \tag{4-29}$$

Obviously, to ensure the peak time of $\hat{f}'(t)$ is detectable, the coefficient k must be larger than 1. Figure 4-13 shows the estimated thickness with different values

of k where M_p was fixed as 500 to ensure sufficient data for sampling. It has been observed that if k is between 1 and 1.5 the error of estimation can be up to 0.5 mm due to insufficient sampling. If k is between 1.5 and 10, the error can be up to 0.2 mm, which is within a more acceptable range. If k is more than 10, the error is significantly increased because the model primarily fits the data where the temperature is almost stable while the key segment of rapid temperature decay is fitted badly. It is inferred from these plots that the value of k is recommended to be chosen between 2 and 3.
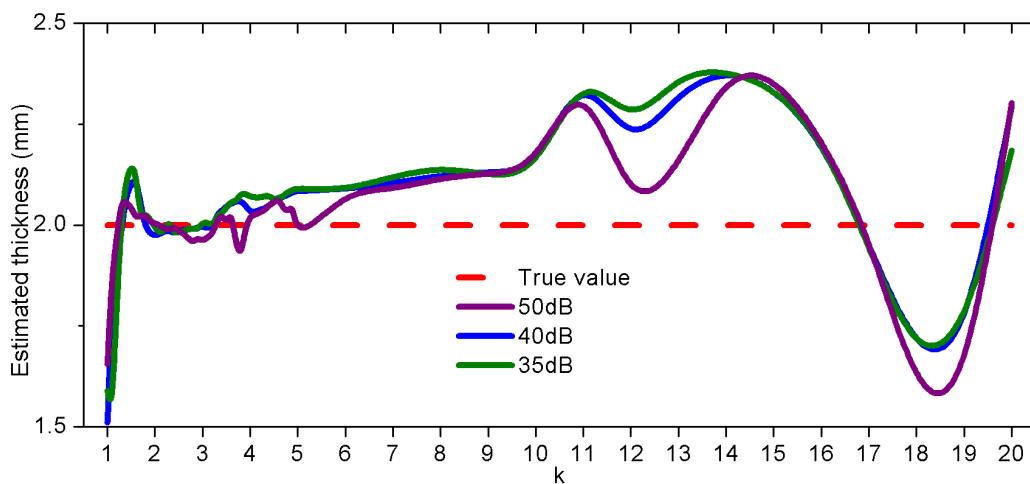
Figure 4-13 The estimated thickness against the value of ratio k for the model simulations with SNR of 50 dB, 40 dB and 35 dB, respectively.

To determine the minimum number of data points required to produce reliable results, Figure 4-14 shows the effect on the results from different values of M_t where k was chosen as 2. It has been observed that the error can be up to more than 0.5 mm when M_t is between 10 and 20. This observation is another proof of over-fitting where the number of observation is insufficient with a relatively complex model structure. When M_t is between 20 and 80, the error is significantly reduced. For example, the error is reduced from 0.3 mm to 0.02 mm at a noise level of 50 dB. If M_t is larger than 80, the variation of error is relatively small for all three cases. Hence, to ensure the reliability of results produced by the proposed method, at least 100 data points are required if the noise level is lower than 35 dB. More data points are suggested if the noise level is higher. Suggested

selections for both parameters should be applicable for other data-driven methods.
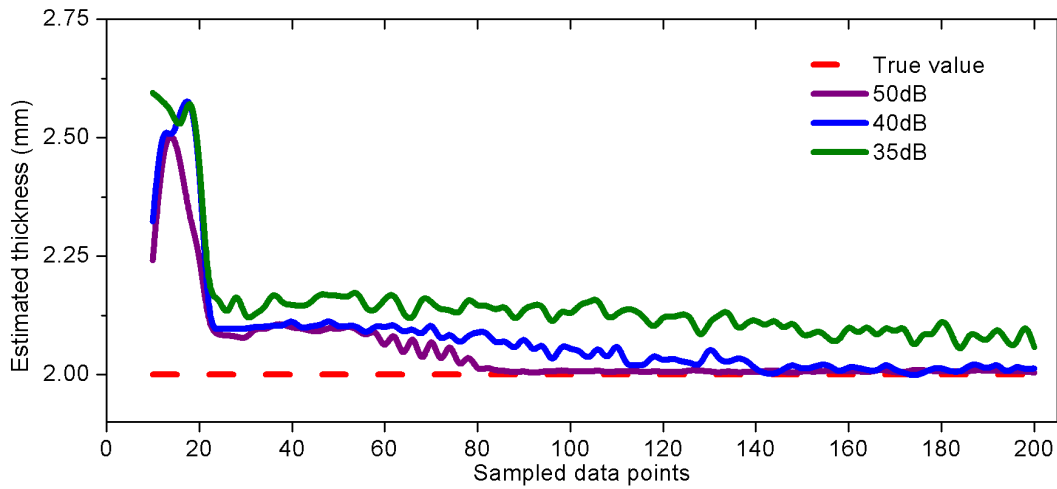
Figure 4-14 The estimated thickness against the number of sampled data for the model simulation with SNR of 50 dB, 40 dB, and 35 dB, respectively.

4.5.4 Thermal Diffusivity Measurement

A real example to use the proposed method to measure thermal diffusivity is presented in this session. A defect-free specimen was produced with the dimension of 150 mm × 100 mm × 4 mm, which was made of unidirectional Toray 800 carbon fibres pre-impregnated with Hexcel M21 epoxy resin. The sample was placed with its surface perpendicular to the camera's line of sight at a distance of 300 mm from the lens. Considering the thickness of the sample and its low thermal diffusivity, a sampling rate of 25 Hz was used, and totally 1000 frames, equally 40 seconds data length, were captured and analysed. More details can be found in [132].

Figure 4-15(a) shows the raw temperature $f(t)$ for three randomly selected pixels from the sample. Note the unit of the y axis is not Celsius but digital intensity outputted by the camera. Similar thermal behaviours for these pixels have been observed. The observed minor difference may be caused by non-uniform illumination. The value of N was automatically selected as 8 for all three pixels. Assuming the thermal decay of this experiment follows Equation (4-24), the value

of SNR for each pixel was calculated and results are 30.13 dB, 30.26 dB, and 30.27 dB, respectively. Although the selection of N was not determined directly by the noise level, the result matches the learned relationship between N and SNR from model simulations, as shown in Figure 4-12(a). The plots of the first derivative of the reconstructed $f(t)$ for three considered pixels after applying the proposed NSI method are illustrated in (b). They exhibit very similar trends from the 5th to 35th second. The peak time, t_{NSI} was then detected (17.61 s, 17.57 s, and 17.00 s, respectively) and the thermal diffusivity was calculated by Equation (4-27) (0.47 mm²/s, 0.47 mm²/s, and 0.49 mm²/s, respectively), where L was assumed to be the same across the specimen. To consider the spatial variation, a region of 100×100 pixels, equal to 33 mm × 33 mm, was selected and each pixel inside this region was analysed by the proposed NSI technique and other two methods.

Figure 4-16(a) - (c) show the thermal diffusivity maps for the selected region from LSD, APST and the proposed method respectively. The result from NSI shows more variations than those from LSD and APST. To evaluate the distribution of the estimated thermal diffusivities, Figure 4-16(d) - (e) show the histograms and the corresponding Gaussian fittings for three tested methods respectively.

(a)   (b)
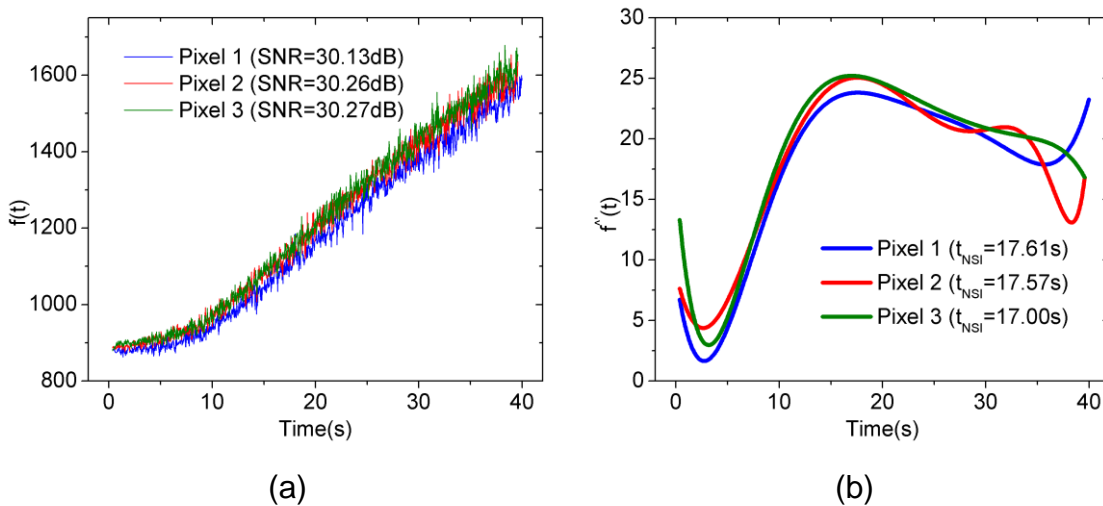
Figure 4-15 Results for three randomly selected pixels. (a) Raw values of $f(t)$; (b) the first derivative of the reconstructed $f(t)$.
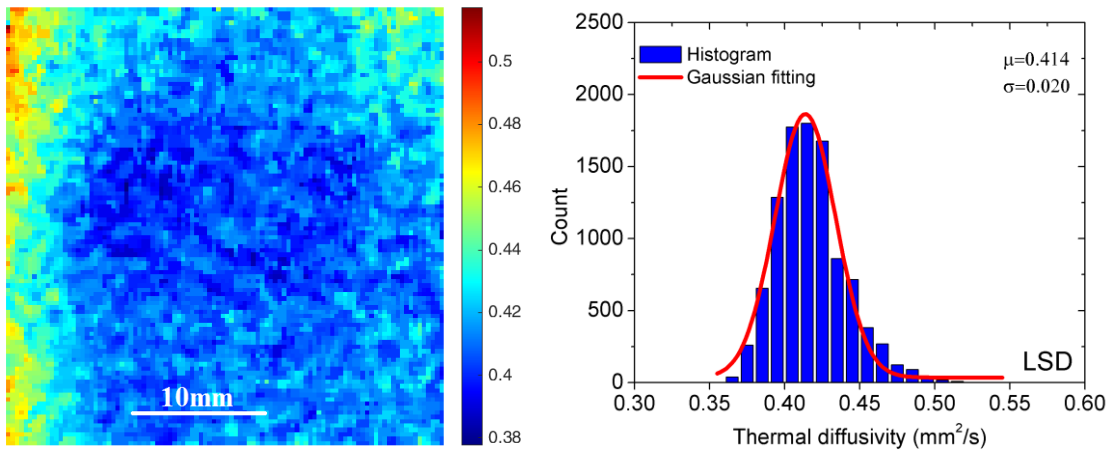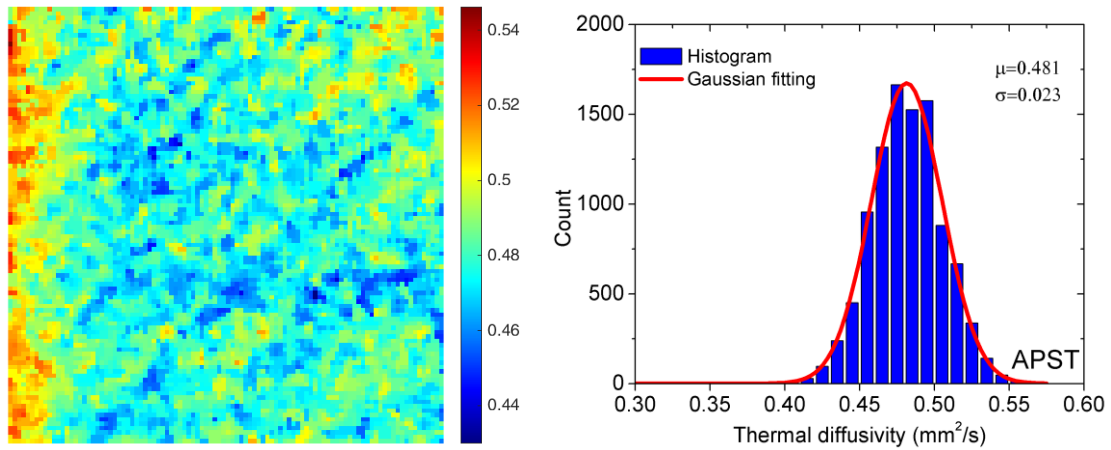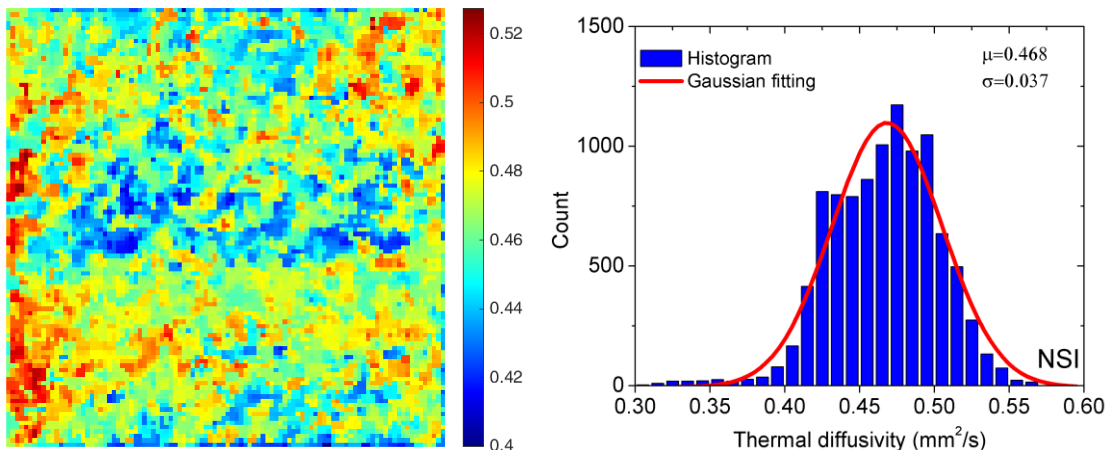
Figure 4-16 Produced thermal diffusivity map (mm^2/s) by (a) LSD, (b) APST, (c) the proposed method; histogram of the measurement with corresponding Gaussian fitting from (d) LSD, (e) APST, and (f) the proposed method.

111

It has been observed that the estimated values are located within a narrow range with an approximately Gaussian distribution. LSD produced a smaller averaged thermal diffusivity (0.41 mm^2/s) in comparison to those from APST (0.48 mm^2/s) and NSI (0.47 mm^2/s). The NSI method produced the most accurate measurement considering the thermal diffusivity reported by other papers (0.45 mm^2/s) [53]. LSD fits the curve in the logarithmic domain, which compresses the data of the later stage. If the peak time is in the later stage, the accuracy of peak time measurement will be sacrificed due to the compression, which could be the reason why the measured thermal diffusivity from LSD is not as accurate as those from other two methods. If the peak time is in the early stage, LSD should have no such an issue.

To further explore the results, Figure 4-17(a) and (b) show the maps of SNR and the selected N for the selected region. It can be clearly observed that the bottom side has relatively higher SNR than the top side. The values of N for most pixels were chosen between 6 and 8.

(a)   (b)
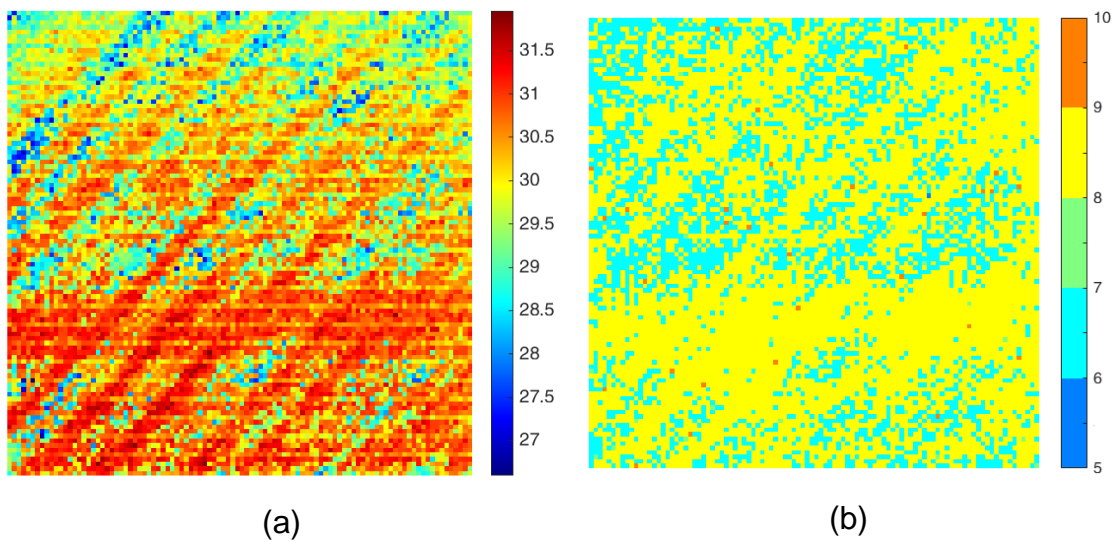
Figure 4-17 : (a) SNR map (dB) measured by the proposed method; (b) the map of the selected N.

4.6 Summary

This chapter proposed two defect depth measurement methods, NLSF and NSI methods. NLSF method aims to improve the performance of depth measurement through the determination of R value. Whilst, NSI method improves the performance of depth measurement by automatically choosing the model order of polynomial fitting. The comparison between NLSF method and NSI method is shown in Table 4-8. The summarised highlight of each method are described in Section 4.6.1 and 4.6.2.

Table 4-8 The comparison between NLSF method and NSI method

Items	NLSF	NSI
- Improving the performance of depth measurement based on	Determining R value	Automatically choosing model order of polynomial fitting pixel by pixel
- Data analysis based on	Model optimisation	Curve fitting
- Technique of optimisation or curve fitting	Nonlinear parameter optimisation based on least-squares	Polynomial fitting based on Least-squares fitting
- Number of parameters or coefficients	Fixed as 5 parameters	Not fixed, depends on the chosen model order
- Suitable sampling data length	Approximately three times of the peak time of temperature contrast	Two to three times of $\frac{L^2}{2\alpha}$
- Dimension of data analysis	One-dimensional heat diffusion model	One-dimensional heat diffusion model
- Estimation of thermal diffusivity	Yes	Yes
- Estimation of R value directly	Yes	No

4.6.1 NLSF Method

The NLSF method proposed a new method that improves the accuracy of defect depth measurement against different levels of noise through estimating the thermal wave reflection coefficient (R) based on the pulsed thermographic inspection. All previous research either neglect the R value or presume that it is pre-known, which increases the uncertainty of depth measurement. This thesis firstly provides a solution to estimate the R value directly from observed data. A modified analytical modelling with five parameters is introduced to better fit the observed temperature curve using a nonlinear optimisation technique. The results of the proposed method have been evaluated and compared with four

113

state-of-the-art methods namely PST, LST, APST and LSF based on model simulations. The main conclusions of this chapter can be summarised as below:

a. Under a noise-free condition: when $R = 1$, the proposed NLSF method and LSF methods produce perfect results for depth measurement while the other three methods have errors up to 2%. When the value of R is smaller than 1, the NLSF method still produces the perfect results while the other four methods produce different levels of imperfect results due to the neglect of R.

b. Under a noise condition: The observation of measurement accuracy is similar to the noise-free condition. The LSF and NLSF have higher precision of measurement in comparison to PST, LSD and APST method. APST method has the most sensitivity against noise level and NLSF has the least sensitivity. Such features are important because the signal-noise ratio in real applications usually is difficult to be measured and the value of R can be different at different places if the material is inhomogeneous.

c. Due to the introduction of t_s, the proposed method can be applied to any segment of observed data without knowing the start time. Such a feature is attractive for data with a low sampling rate where t_s could be larger than 0 due to accumulated latency by hardware and software of data acquisition. All other four methods neglect the potential variation of t_s, which leads to a guaranteed error, the value of which dependents on the value of t_s.

d. For the experimental studies, the performance of the proposed method was compared with LSF using the same optimisation technique. Results show that the NLSF method has higher accuracy on defect depth estimation than the LSF method for both defective area and sound area, which suggests improved reliability of measurement for real data.

One limitation the proposed method is that the accuracy of the estimation depends on data length. The depth estimation in the sound area needs more data length than the defective area. Measurement of deep defect needs more data length than shallow defect. This thesis proposes to use the time when maximal temperature contrast between the considered defective pixel and the reference pixel from the sound area is achieved to determine the sample length, and the results show that this solution works effectively. The efficiency of this method is

affected by the selection of parameters bounds before applying the optimisation technique. Limiting the parameter bounds and setting the initial values closer to ground truth based on the result of neighbours could be a solution to reduce the computational time.

The proposed method has only been applied to flat bottom holes where a defect has the same depth. This approach has been used for most of the other research. If a defect has different depths, the three-dimensional heat conduction is more complex and will have an influence on the results. However, due to the consideration of three-dimensional heat conduction by introducing two extra parameters R and s, it is expected that the proposed method will perform even better than other methods though the increased error is inevitable due to the utilisation of one-dimensional heat diffusion model. Performance evaluation for more complex defects requires further study.

4.6.2 NSI Method

The NSI method introduces a new method to improve the reliability and confidence level of defect depth measurement based on the pulsed thermographic inspection by addressing the over-fitting problem. To quantitatively measure defect depth, a polynomial model is normally used in existing methods to fit either the temperature decay in the logarithmic domain or the variation of temperature decay in the time domain. There is very limited literature reporting how the selection of model order affects the results and how to automatically determine the order. A model with a too low order cannot sufficiently fit the observed data, and consequently, depth estimation maybe not sufficiently accurate. While a model with a too high order may fit the observed data too well to model the noise rather than the underlying relationship. Such noise will be further amplified when the first or second derivative of the fitting is used to measure the depth. These problems have been demonstrated and evaluated in this thesis. This is a potential issue towards automation of the pulsed thermographic inspection.

Addressing this problem, this thesis has developed a nonlinear system identification (NSI) method to model the temperature decay. Different from other methods that build the polynomial model in a one-off manner, the NSI method searches through a relatively large set of candidate model terms to select the most significant model terms one by one. Hence, the model is built in a term-by-term manner. This search will automatically stop when the first valley of the penalized error-to-signal ratio is detected. Furthermore, this method accommodates any linear or nonlinear relationship through the set of candidate terms. The performance of the proposed method including accuracy and precision has been compared with the start-of-the-art depth measurement methods based on model simulation with different levels of noise. The impact of the selection of sampling parameters has also been discussed and recommendations have been proposed. The proposed method has been further validated through an experimental example by measuring thermal diffusivity for a composite sample. The results allow the following conclusions:

a. The NSI method is able to adaptively detect the model structure for each considered pixel which ensures a better model fitting with relatively fewer model terms. This characteristic considers the spatial variation of the model structure among pixels. Comparing with the LSD and APST methods, this more sophisticated version of model fitting can often measure the depth more accurately while reducing model complexity.

b. The number of model terms is determined automatically, which is particularly important for automation of defect/damage depth measurement. Although the model simulations in this thesis were produced by varying noise levels, in real applications, the noise level is not necessary to be pre-determined because the method itself will evaluate the relationship between the model complexity, fitting error and the number of sampling.

c. It has been observed that the number of terms was chosen as about 8 for signals with the SNR in the range from 45 dB to 30 dB. For signals with the SNR larger than 45 dB, a high number of terms (8-10) was chosen. For signals with the SNR smaller than 30 dB, a relatively small number of terms (5-8) was

chosen. This conclusion should also be applicable to the APST and LSD methods.

d. It has been observed from the results of model simulations that a sampling data length with twice to three times of $\frac{L^2}{2\alpha}$ usually produces reliable results. Model simulations also show that at least 100 data points are required if the noise level is lower than 35 dB. More data points are suggested if the noise level is higher. These conclusions will aid the practical selection of thermographic parameters such as sampling rate and integration time.

One limitation of the proposed technique is that it is a data-driven method without considering the heat diffusion model underlying the inspection process. Accurate evaluation of noise level is challenging because to achieve this the observed signal has to be clearly divided into 'true signal' and noise. The proposed method can be applied to either measure the thickness of defect-free materials or the defect depth of large defects. Further investigation is required to consider 3D heat conduction for small defects.

Another limitation is that the damage is usually assumed to be parallel to the surface, this is necessary to measure the depth using the NSI technique. Addressing these limitations, further research will focus on reconstructing a 3D representation for defect/damage, degradation volumetric measurement, and determination of the orientation of degradation.

5 DEFECT THICKNESS ESTIMATION

5.1 Introduction

Majority of NDT research focuses on measuring the location and sizes of defects or damages, but limited studies on the characterisation of their thickness. Microwave thermography has been used to study the effect of corrosion layer thickness on reinforcing steel bars [63], [133], but has not been applied on composites. Wang *et al.* proposed a microwave equiphase frequency truncation method to detect and evaluate the thickness of kissing defects in GFRP laminate [134]. Pulsed Eddy Current technique has been used in thickness evaluation of aluminium plate [135], and the ultrasonic testing has been widely used for gauging of the local thickness of a solid element [136], but very limited related research for the subsurface defect or damages. X-ray computed tomography is able to provide highly accurate 3D inspections of manufacturing defects of fibre architectures [137], however, the inspection time and equipment is relatively costly.

Pulsed Thermography is an NDT method which is contact-free and offers a rapid inspection while covering a large area within a short time frame and thus readily adaptable to in-situ monitoring applications [13]. Other thermography-based NDTs, such as microwave thermography, eddy current thermography, lock-in thermography, and ultrasonic thermography, takes several measurements using signals of different frequencies to gain information about different depths, however, it requires a longer inspection time. Pulsed thermography is more straightforward and faster because the flash time is a well-defined instant for time reference. Most of the existing pulsed thermography methods, such as Peak Slope Time [109], Logarithm Second Derivative [40], Absolute Peak Slope Time [77], Nonlinear System Identification [96], Least Square Fitting [76], and New Least Square Fitting [116], are able to estimate the defect depth (the distance from the inspected surface to the top surface of a defect) before the three-dimensional heat conduction takes place. However, currently, characterisation of defects is limited to 2-dimensional measurement, which represents a collation of all damage through-the-thickness. None of these methods is able to estimate the

defect thickness in order that the estimation can be extended to 3-dimension. A straightforward approach to tackle this challenge is conducting two inspections (two sides measurement), one of which is applied on the front side and another on the rear side. The defect thickness can then be quantified by considering the measured defect depths from both inspections and the sample thickness. This chapter aims to propose a new method to estimate defect thickness based on pulsed thermography with a single-side inspection [98]. The outline of this chapter is illustrated in Figure 5-1.
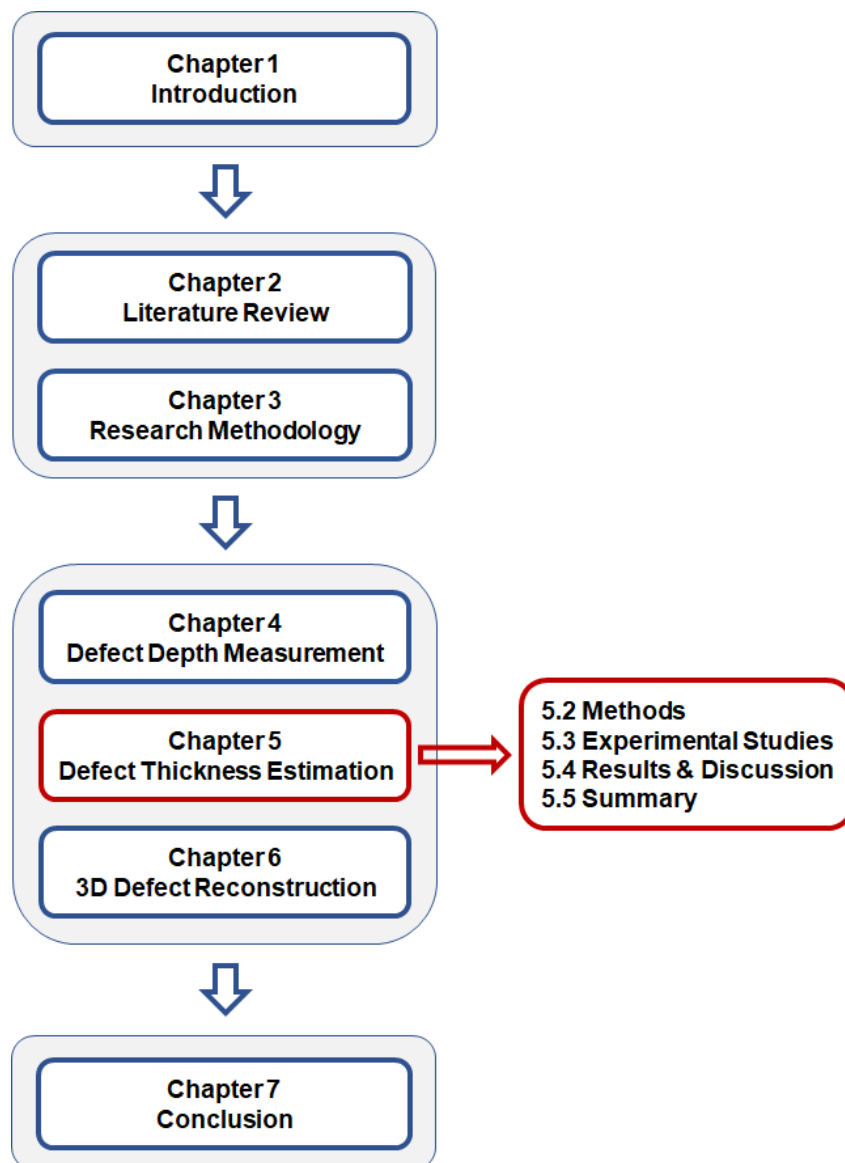
Figure 5-1 The outline of Chapter 5

5.2 Methods

Defect thickness estimation consists of three main steps: estimating of R value, estimating of defect depth, and finding the correlations, as illustrated in Figure 5-2. In the first step, the value of R is obtained by NLSF method proposed in Chapter 4. R value is an important key used to estimate defect thickness. The value of R correlates with multiple parameters such as defect depth (d), defect defect thickness (h) and defect size (r). Thus, the relationship between R and d, R and h, and R and r are studied. These relationships will be used to establish h-R model in the last step. In the second step, defect depth can be obtained by NLSF, NSI, or other methods. This thesis used NLSF method to estimate defect depth d because d can be estimated simultaneous with R value that can be used to estimate the defect thickness. The last step is to find the correlated relationship between h, R, d, and r, and establish the prediction model based on nonlinear finite impulse response (NFIR), $h = f(R, d, r)$, in a form of such as polynomial model and exponential model.
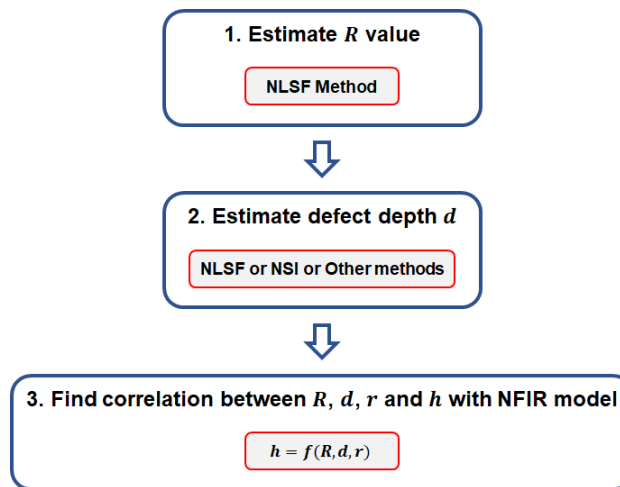
Figure 5-2 The diagram of defect thickness estimation method

5.2.1 Estimation of Thermal Wave Reflection Coefficient

In areas of the sample surface above a defect/damage (see the point 2 in Figure 5-3) the transient flow of heat from the surface into the sample bulk is wholly or

partially obstructed, thus causing a temperature deviation from the sound areas (see the point 1 in Figure 5-3. Figure 5-3(b) plots two typical observed temperature decay curves of the point 1 (blue) and point 2 (red) in the logarithmic domain. Damage detection methods aim to classify the pixels based on the cooling behaviour. The time when the temperature deviation occurs, represented by t^* in Figure 5-3(b), is usually used to estimate the defect depth d. On a sufficiently large time scale, the t^* can be viewed as a transition from one-dimensional steady state diffusion before incident heat encounters a subsurface interface to a second asymptotic steady-state [109]. We can also observe a later event t^{**} (see in Figure 5-3(b)), indicating the asymptotic return to one-dimensional diffusion. The detection of t^* and t^{**} can be achieved through detecting the peak of the second derivative of thermographic signal reconstruction (TSR) [138]. The cooling behaviour between t^* to t^{**} is associated with the size r, the depth d, the thickness h of damage and the material, as labelled in Figure 5-3(a). Estimation and understanding of the corresponding between them is the key to characterise the volume of damage and will be studied in this thesis.

(a)

(b)
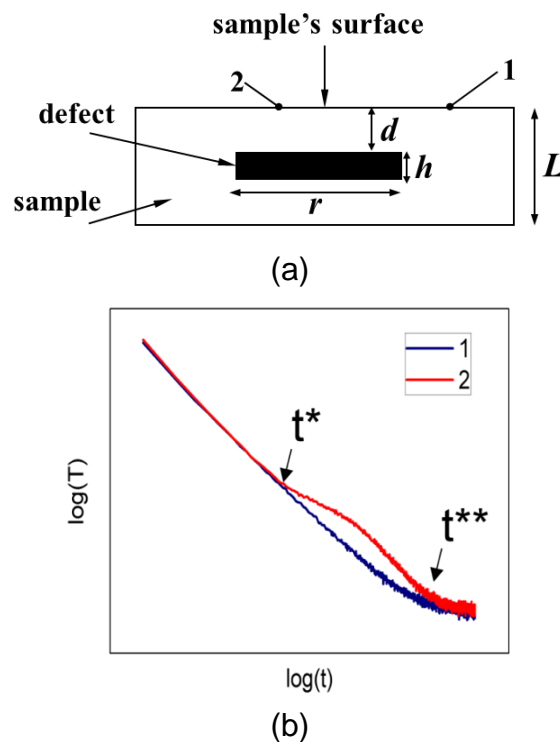
Figure 5-3 (a) Side view of the sample (b) Typical observed time-temperature decay curves in the logarithmic domain for point 1 and the point 2, respectively

The surface temperature dynamics due to the back-wall at depth L for a homogeneous plate is given by [74], expressed as Equation (3-1). For most of the research, the value of R in Equation (3-1) is assumed to be 1, which is true when the thickness or the size of damage (e.g., air-gap) is infinite, where there is no three-dimensional heat conduction takes place. However, for most of the real applications (e.g., detecting impact damage of composite), the thickness and size of damage could be very small and the heat leakage can be severe. The value of R, therefore, can be significantly smaller than 1 [116] if the whole transient lifetime is considered. By monitoring the cooling temperature during the period from the flash time to t^{**}.

This thesis proposes to characterise the damage thickness by establishing an empirical model between R and measurable geometrical parameters; and uses the new least-squares fitting method (NLSF) [116], proposed in Chapter 4, to estimate the R value directly from the observed data. The analytical model of the NLSF method written as Equation (4-1) in Chapter 4. The model also introduces two parameters R and s that consider the three-dimensional heat conduction effect. It can also incorporate the duration effect of flash by introducing the parameter t_s.

5.2.2 Correlation Analysis and Modelling

It has been mentioned above that the R value could be related to geometrical parameters including defect size, depth and thickness. This section aims to introduce an approach to quantify correlations between R and these parameters, and identify an empirical model to establish their relationship, by which means, the defect thickness can be inferred if R and other two parameters are measurable. From the system engineering point of view, to study this multiple-input single-output correlation, the simplest approach is to fix two inputs and vary the third input and then evaluate this input's influence on the output (R). The problem is now simplified to study a single-input single-output system. Least square fitting approaches, based on either linear or nonlinear models, can be employed to establish the relationship between R and the third input. This

procedure can then be repeated until the relationship between R and each geometrical parameter is studied.

To consider the compound influence of these three parameters on R, their relationship must be considered as a multi-input single-output problem. Considering a system with three inputs u_1, u_2, u_3, and an output y, to describe their relationship, this thesis proposes to use the nonlinear finite impulse response (NFIR) model, written as

$$y = f(u_1, u_2, u_3) + \varepsilon \tag{5-1}$$

where f is some unknown linear or nonlinear mapping, which links the system output to the system inputs; ε denotes the model residual.

A commonly employed model type to specify the function f in Equation (5-1) is a polynomial function [124], [139]. A second-order polynomial function can be written as

$$\begin{aligned} y = \theta_0 + \theta_1 u_1 + \theta_2 u_2 + \theta_3 u_3 + \theta_4 u_1{}^2 + \theta_5 u_2{}^2 + \theta_6 u_3{}^2 + \theta_7 u_1 u_2 + \theta_8 u_1 u_3 \\ + \theta_9 u_2 u_3 \end{aligned} \tag{5-2}$$

The next step is to estimate the parameters $\theta_m (m = 0,1, \dots ,9)$ based on the observations $\{y, u_1, u_2, u_3\}$. The procedure begins by determining the structure, or the important model terms, using the orthogonal least squares (OLS) estimation procedures. A more detailed description of this method can be found in the work of Zhao *et al.* [131].

As a feasibility study, this thesis focuses on inspecting commonly studied defects including flat-bottom holes and block defects. Considering a block-shaped defect as shown in Figure 5-3(a), the defect size r, depth d, and thickness h are considered as the system inputs, and the value of R is considered as the output. Through establishing an NFIR model, the influence of r, d, and h on R will be evaluated initially. An inverse model, written as

$$h = f(R, d, r) \tag{5-3}$$

can then be inferred to reconstruct h based on R, d, and r.

5.3 Experimental Studies

5.3.1 Sample Design

Flat plates of carbon fibre reinforced polymer (CFRP) material were used in this study. The plates were made of unidirectional Toray 800 carbon fibres pre-impregnated with Hexcel M21 epoxy resin and manufactured in a traditional autoclaving process. Based on this material, three samples were designed to simulate different types of defect. The dimension of Sample 2 is 75 mm × 230 mm × 8 mm. As illustrated by Figure 5-4(a), it includes five-block defects with a thickness (h) of 0.5 mm, 1.0 mm, 2.0 mm, 3.0 mm, and 4.0 mm, respectively. The width (r), length, and depth (d) for all defects are 10 mm, 75 mm, and 2 mm, respectively. The distance between two adjacent defects is 30 mm, which aims to reduce the influence from the adjacent defects on the thermal behaviour. A side view of the produced sample is shown in Figure 5-4(b). It should be noted that these defects are not fully closed because two sides of the defects are open. It is called as "semi-closed defect". This sample is aimed at studying the relationship between R and h when d is fixed. Sample 3 also includes five semi-closed defects, as illustrated by Figure 5-5, which have the same defect thickness h of 1.5 mm but different defect depth of 1.0 mm, 1.5 mm, 2.0 mm, 2.5 mm, and 3.0 mm, respectively. Other parameters are the same as Sample 2. This sample is aimed at evaluating the relationship between R and d when h is fixed. Sample 4, with the dimension of 155 mm × 155 mm × 8 mm, includes 16 flat-bottom holes. As illustrated by Figure 5-6(a), the holes were drilled with four groups of diameters (5 mm, 10 mm, 15 mm, and 20 mm) and four groups of thicknesses (7 mm, 6 mm, 5 mm, and 4 mm). It can be inferred that the defect depths are 1 mm, 2 mm, 3 mm, and 4 mm, respectively. The distance between the centre of two adjacent holes is 31 mm. This sample is aimed at studying the relationship between R, h, d, and r for "open defect". It should be noted that for this sample, the parameters h and d are dependent and the sum of them is a constant (8 mm).
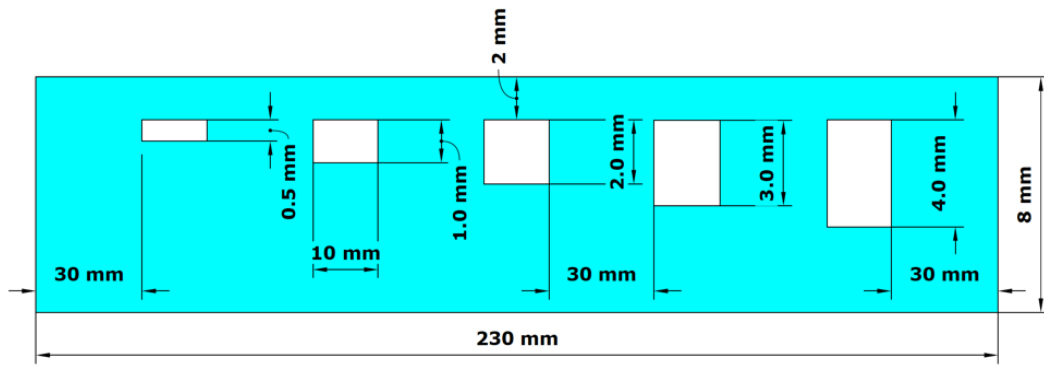
Figure 5-4 Illustration of Sample 1, where the defect size, depth and thickness are defined (a) sample design (b) side view
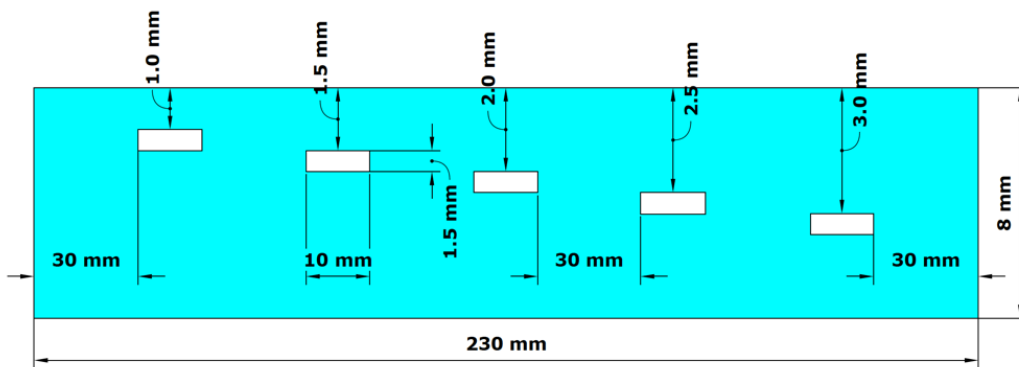
Figure 5-5 Illustration of Sample 2 (a) sample design (b) side view
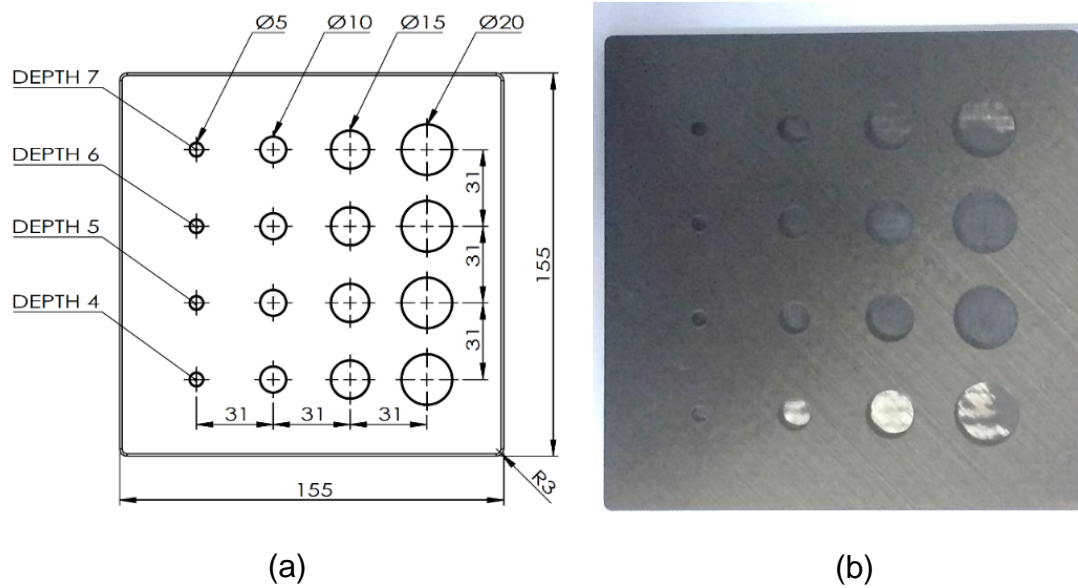
Figure 5-6 Illustration of Sample 3 (a) sample design (b) side view

5.3.2 Experimental Setup

The configuration of the experimental setup is illustrated in Figure 3-3(a) in Chapter 3. The thermographic imaging was conducted by FLIR SC7600, as shown in Figure 3-4 in Chapter 3. Sample 2 and Sample 3 were inspected from the top side. Sample 4 was inspected from the surface opposite to the drilled side. Considering the thickness of the samples and the low thermal diffusivity (α) of carbon fibre reinforced polymer (CFRP), a sampling rate of 10 Hz was used, and totally 900 frames, equally 90 seconds data length, were captured. Due to the large width of Sample 2 and Sample 3 (230 mm), the area on both left and right side of the sample is almost outside of the camera hood, as demonstrated in Figure 5-7. The defects of both samples suffer non-uniform heating for a single-side inspection, which could lead to unreliable results [140]. The non-uniform heating could be caused by the variable distance from the sample's surface to the heat source and by the radiation pattern of the heat source [86]. In this study, to reduce this effect, each sample (Sample 2 and Sample 3) has been captured for five times, where each defect was placed on the centre of the camera's view once. A region of interest of the centralised defect with the size of 160×120 pixels

for five raw data files was then cropped and merged into one file with a size of 160×600 pixels for easier analysis.
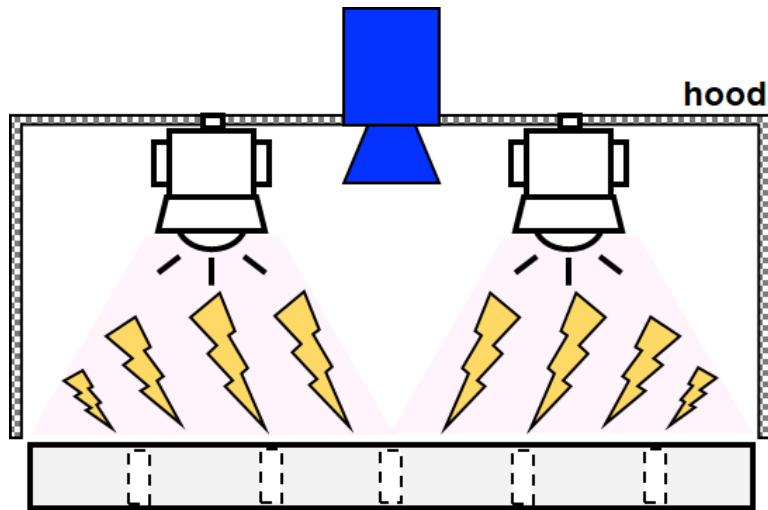
Figure 5-7 Non-uniform heating on the sample's surface

For the setting up of the five unknown parameters of the NLSF method, written as Equation (4-1) in Chapter 4, the initial value of the parameter t_s is selected as 0, and the lower and upper bounds are selected as -1 and 1, respectively, because it is usually very close to zero. The initial value of R is selected as 1, and the lower and upper bounds are selected as 0 and 1, respectively. The initial value of A is selected as 1000, and the lower and upper bounds are selected as 0 and 2000, respectively, due to the energy applied on the inspection surface around 2 kJ. The selection of W depends on the material and thickness of samples, the initial value of W is selected as 1, and the lower and upper bounds are selected as 0 and 200, respectively, because the thickness of the three samples is around 8 mm and the thermal diffusivity (α) of them is about 0.5×10^{-6} m^2/s, W can be calculated as $W = \frac{L^2}{\alpha} = \frac{8^2}{0.5} = 128$. And the initial of s is chosen as 0, and the lower and upper bounds of s are chosen as -50 and 50, respectively.

5.4 Results and Discussion

5.4.1 Results of Testing Sample 2

This sample aims to evaluate the dependence between R and h when d is fixed. Figure 5-8 shows a snapshot of the raw thermal image at time 10 seconds where the colour represents the temperature. It should be noted that the exported data of the used IR camera is in the unit of "digital intensity", which was used for the analysis below instead of temperature. To reduce the influence of the heat leaked to each opened side on results, ten pixels on the centre of each defect were sampled, as marked in Figure 5-8, and then were averaged to reduce spatial noise. The defects are labelled as "(1)", "(2)", "(3)", "(4)", and "(5)" to represent the defect thickness of 0.5 mm, 1.0 mm, 2.0 mm, 3.0 mm, and 4.0 mm, respectively, and the sampled sound area is marked as "S". Ten pixels (1×10) for each defect and the selected sound area were sampled, and the averaged temperature decays of each defect and sound area are plotted in the logarithmic domain, as illustrated in Figure 5-9.
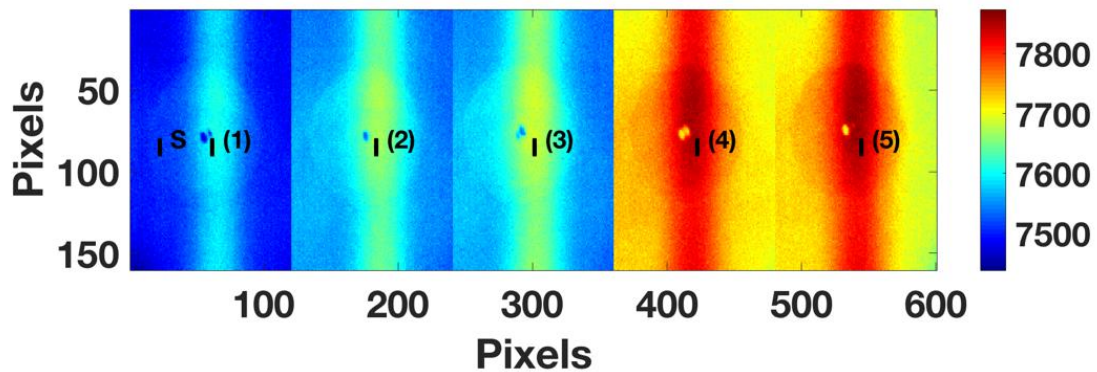
Figure 5-8 A snapshot of the captured thermal image of at time 10 seconds for Sample 2, where the unit is digital intensity, a representation of temperature
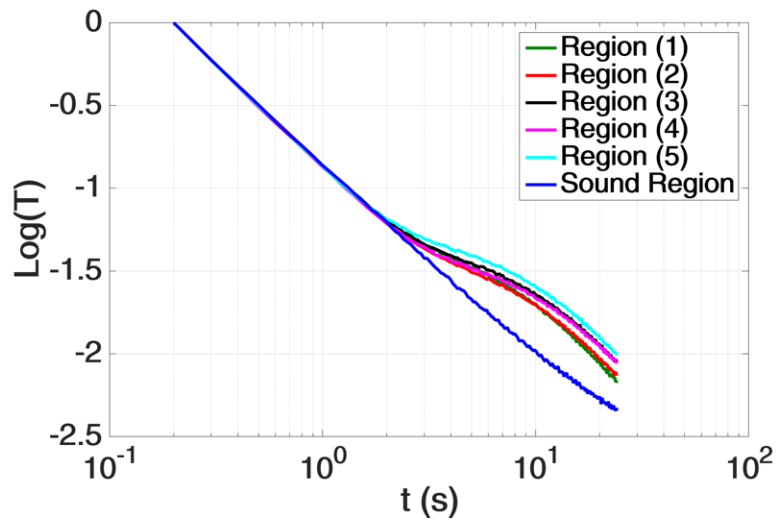
Figure 5-9 Average temperature decay, plotted in the logarithmic domain, for the sampled pixels of each defect and a sound region of Sample 2, the sampled total data length is 24 seconds

Considering that the thermal behaviour of sound area around the centre has a very limited variation for the five tests, in this thesis the sound area was selected on the first test only. It can be clearly observed that the time of the temperature deviation from the curve of the sound pixel that occurs for each defect (t^*) is similar since they have the same depth. The thermal cooling behaviours before t^* are almost identical, while after t^*, they start to exhibit a difference. Quantification of the influence of the defect thickness on thermal cooling behaviours purely based on the observation of these plots is almost impossible.

The NLSF method was then applied to each time-temperature decay data to estimate the unknown parameters. The thermal diffusivity (α) was chosen as 0.5×10^{-6} m²/s. We measure the defect depth d and R of the ten pixel (black marked shown in Figure 5-8) of each defect (Defect 1 to Defect 5), and then average the ten measured d and R of each defect. The measured values of d and R are shown in Table 5-1. It can be calculated that the average measured depth is 1.989±0.098 mm and the average percentage error is about 5% against the reference of 2 mm, which suggests a fine performance of depth estimation. Table 5-1 also shows that the value of R increases following the increase of defect thickness, although the relationship is not linear. This interesting observation is probably caused by the heat around the air-gap that is more

difficult to be leaked through the three-dimensional conduction if the volume of the air-gap is larger. The variation of R, therefore, can be considered as an indicator of the variation of the damage thickness if the diameter is the same. To further analyse the relationship between R and h, Figure 5-10 plots the scatters between them, which suggests that the relationship is not linear, but approximately exponential. Based on the observed curve, an exponential model was applied to fit the relationship between the measured R and the artificial defect thickness h in Table 5-1. The model can be described by

$$R = -0.29e^{-\frac{h}{0.93}} + 0.6$$

(5-4)

Table 5-1 Measured parameters of Sample 2

Defect Thickness (mm)	R	d (mm)
0.5	0.431	1.896
1.0	0.498	2.079
2.0	0.565	1.985
3.0	0.588	2.072
4.0	0.591	1.866
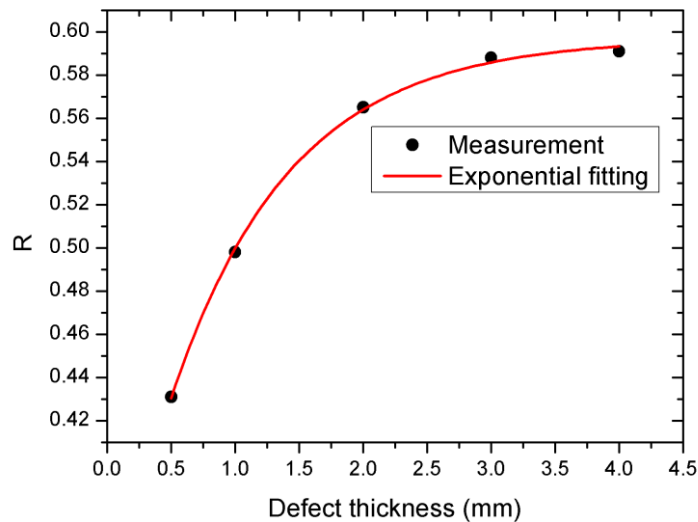
Figure 5-10 Scatter plot between the defect thickness and the measured *R* with the corresponding exponential fitting for the Sample 2

The fitting error is quantified by calculating the Pearson correlation coefficient (PCC) between the measured R and reconstructed R based on Equation (5-4) using the known h. If PCC equals to 1, it indicates a perfect fitting. The fitting curve is represented by the red plot of Figure 5-10, and the calculated PCC value is 0.999. Both observations suggest that the identified model (5-4) can well represent their relationship. To estimate the value of h using the measured R, the model (5-4) can be rewritten as

$$h = -0.93ln\frac{R - 0.6}{-0.29} \qquad \textbf{(5-5)}$$

It should be noted that the empirical model (5-5) is established only for this specified defect depth, size, and material, any change of which requires to recalculate the coefficients. However, it is expected that the model structure is similar.

5.4.2 Results of Testing Sample 3

This sample aims to evaluate the dependence between R and d when h is fixed. Figure 5-11 shows a snapshot of the raw thermal image at time 10 seconds after the flash. The defects are marked as "(1)", "(2)", "(3)", "(4)", and "(5)" to represent the defect depth d of 1.0 mm, 1.5 mm, 2.0 mm, 2.5 mm, and 3.0 mm, respectively, and the sampled sound area is marked as "S". The sampling procedure was the same as that for Sample 2. The temperature decay for each defect and selected sound region, plotted in the logarithmic domain, are shown in Figure 5-12. It is expected that the time of the temperature deviation that occurs for each defect (t^*) is different and increases following the increase of defect depth, which is caused by the difference of defect depth.
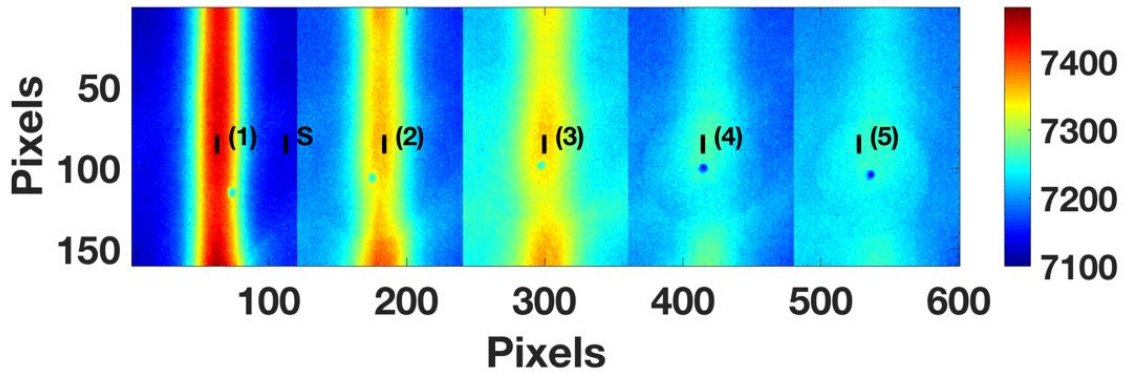
Figure 5-11 A snapshot of the captured thermal image of at time 10 seconds for Sample 3
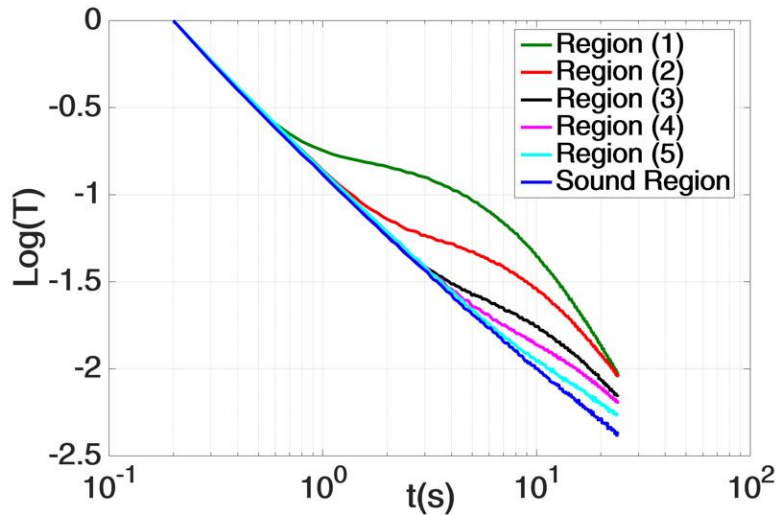
Figure 5-12 Average temperature decay, plotted in the logarithmic domain, for the sampled pixels of each defect and a sound region of Sample 3, the sampled total data length is 24 seconds

The measured values of R and d by applying the NLSF method are shown in Table 5-2. The absolute error of measured depth is 0.040±0.050 mm and the average percentage error is 2.2%. It has been observed that the value of R decreases following the increase of defect depth. Figure 5-13 plots the scatters between R and d, which suggests that the relationship is approximately linear.

132

Table 5-2 Measured parameters of Sample 3

Defect Depth (mm)	R	d (mm)
1.0	0.783	0.999
1.5	0.685	1.572
2.0	0.562	2.113
2.5	0.410	2.496
3.0	0.249	2.991
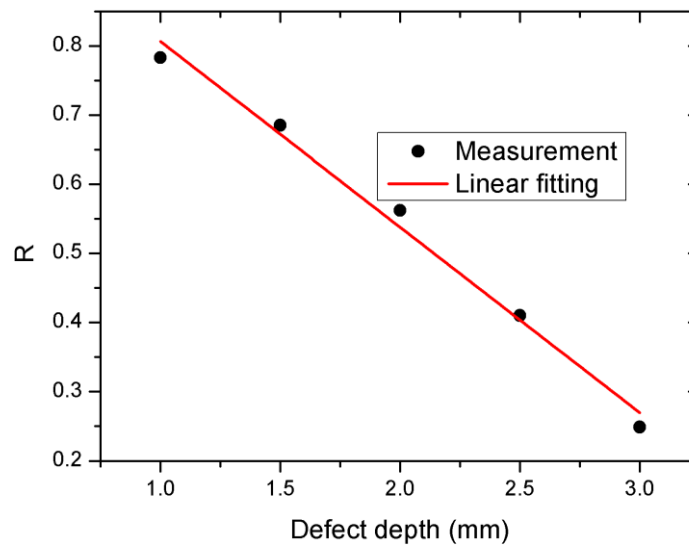
Figure 5-13 Scatter plot between the defect thickness and the measured R with the corresponding linear fitting for the Sample 3

A linear fitting process was applied to the measured data and the relationship can be written by

$$R = -0.27d + 1.07 \tag{5-6}$$

The red plot of Figure 5-13 illustrates the fitting and the PCC value is 0.993, both of which suggests the identified model (5-6) can well represent the relationship. It should be noted that the empirical model (5-6) is established only for the specified defect thickness, size, and material, any change of which requires to recalculate the coefficients. However, the linear model structure is expected.

The above results show that the value of R depends on both the defect depth and thickness. The dependence on depth is linear, and the dependence on thickness is nonlinear. The models (5-4) and (5-6) have a single input and single output,

which has limited applications due to the rigorous assumption. To analysis how d and h together affect the value of R, the NFIR model (5-1) with two inputs was employed and the data in Table 5-1 and Table 5-2 were sampled, the second-order polynomial model is used to fit these data. The identified model is written as

$$R = -0.37d + 0.07dh - 0.02h^2 + 1.11 \qquad \textbf{(5-7)}$$

with a PCC value of 0.98. This result suggests that the R value can be well explained by the defect thickness and depth. To construct a model for predicting h based on the values of R and d measured by the NLSF method, h is considered as the system output of the NFIR model and R as the system input. The results produced from both samples, presented in Table 5-1 and Table 5-2, were sampled, and the predictive model is identified as

$$h = 170.72 - 33.96R - 81.3d + 163.81R^2 + 9.44d^2 + 82.56Rd \qquad \textbf{(5-8)}$$

with a PCC value of 0.75. To validate its performance of prediction, Table 5-3 shows the predicted values of h based on model (5-8) using the measured R and d from Table 5-1 and Table 5-2, against the ground truth for the ten defects in Sample 2 and Sample 3.

Table 5-3 Defect thickness comparison of ten studied defect in Sample 2 and Sample 3 between the ground truth and estimation using the model (5-8)

Defect ID	Ground Truth (mm)	Estimation (mm)	Error (mm)	Percentage Error (%)
Sample 2-1	0.5	1.34	0.84	168.00
Sample 2-2	1.0	1.23	0.23	23.00
Sample 2-3	2.0	1.56	0.44	22.00
Sample 2-4	3.0	3.68	0.68	22.67
Sample 2-5	4.0	2.54	1.46	36.50
Sample 3-1	1.5	1.47	0.03	2.00
Sample 3-2	1.5	1.95	0.45	30.00
Sample 3-3	1.5	1.25	0.25	16.67
Sample 3-4	1.5	1.53	0.03	2.00
Sample 3-5	1.5	1.45	0.05	3.33

The experimental result from Table 5-3 indicates that, the averaged estimation error of Sample 2 is higher than Sample 3. The minimum percentage error of Sample 2 is 22.00% whilst Sample is 2.00%.

Although the estimation is not perfect, the result clearly demonstrates the potential to estimate the defect thickness using the introduced approach. There are a few potential reasons of the relatively large error: 1) the material properties of Sample 2 and Sample 3 are not identical due to the manufacturing deviation, which is usually greater for inhomogeneous materials (e.g., composites); 2) the second-order polynomial model structure cannot fully represent the mechanism; and 3) there are some other parameters apart from R and d to be included in model (5-8) to better estimate h. It is expected that the estimation performance will be further improved by including the defect size in this model.

5.4.3 Results of Testing Sample 4

This sample aims to investigate how the geometrical parameters of flat-bottom holes affect the thermal wave reflection coefficient. It should be noted that the definition of "defect thickness" for this case is slightly different than the previous two cases since the defects are open on the backside. We can consider this parameter as a representation of defect volume when the diameter is fixed, which is applicable to Sample 2 and Sample 3. A snapshot of the raw thermal image at time 10 seconds is shown in Figure 5-14, where nine holes on the top-right side can be easily spotted while the holes with 4 mm depth and 5 mm diameter cannot be clearly detected due to low diameter to depth (aspect) ratios. Beemer and Shepard [141] acknowledge the difficulty in detecting flat-bottom holes if the aspect ratio is smaller than 5. For this reason, in this experiment, only the nine marked holes in Figure 5-14 were studies.
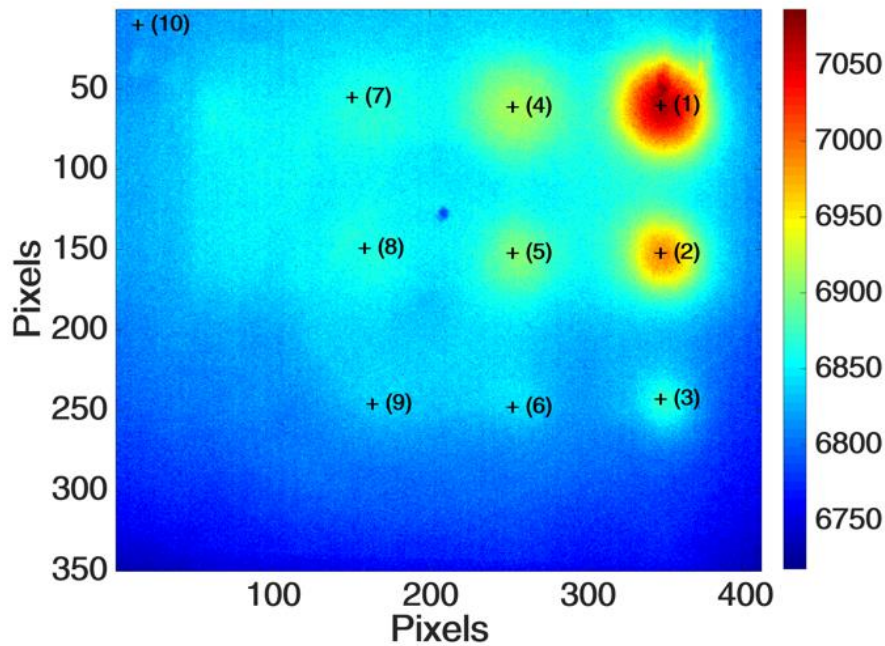
Figure 5-14 A snapshot of the captured thermal image of at time 10 seconds for Sample 4

Figure 5-15(a) plots the temperature decay of the sampled pixels "1", "2", and "3", which have the same defect depth of 1 mm, but with different defect size (20 mm, 15 mm, and 10 mm, respectively). The point "(10)" was randomly sampled from the sound region. As expected, the values of t^* for the considered three defects are similar, and the cooling behaviours between t^* and t^{**} are different due to the difference of size. Figure 5-15(b) plots the temperature decay of the sampled defects "1", "4", and "7", which have the same defect size of 20 mm, but with different defect depth (1 mm, 2 mm, and 3 mm, respectively). Both the value of t^* and the cooling behaviours of [t^*, t^{**}] are different due to the difference in size and depth.

(a)   (b)
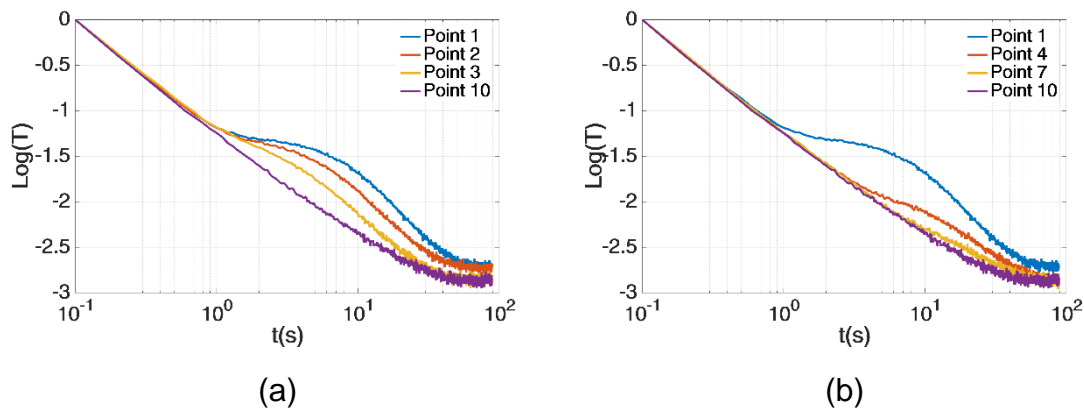
Figure 5-15 The temperature decay, plotted in the logarithmic domain, for the selected defects and sound pixel; (a) defects have the same depth, but different size (b) defects have the same size, but different depth

The measured values of R and d by applying the NLSF method are shown in Table 5-4. It can be observed that the depth can be estimated satisfactorily with an absolute error of 0.033±0.025 mm, and the average percentage error is 2.3%. It has also been observed that the larger diameter of defects leads to a higher value of R, and the deeper defect leads to the smaller value of R. This observation is similar to that of Sample 3.

Table 5-4 Estimated parameters of Sample 4

Defect Depth (mm)	r: 10 mm		r: 15 mm		r: 20 mm	
	R	d (mm)	R	d (mm)	R	d (mm)
1.0	0.224	0.926	0.512	1.011	0.792	1.072
2.0	0.214	1.974	0.396	1.991	0.666	2.029
3.0	0.210	2.968	0.359	3.005	0.487	2.962

To further understand their relationship, Figure 5-16(a) plots the R value against the defect diameter for three defect depths, where the relationship was observed as approximately linear. Figure 5-16(b) plots the R value against the defect depth for three defect diameters, where the relationship was also observed as approximately linear. This observation is very similar to that shown in Figure 5-13 for Sample 3.

(a)   (b)
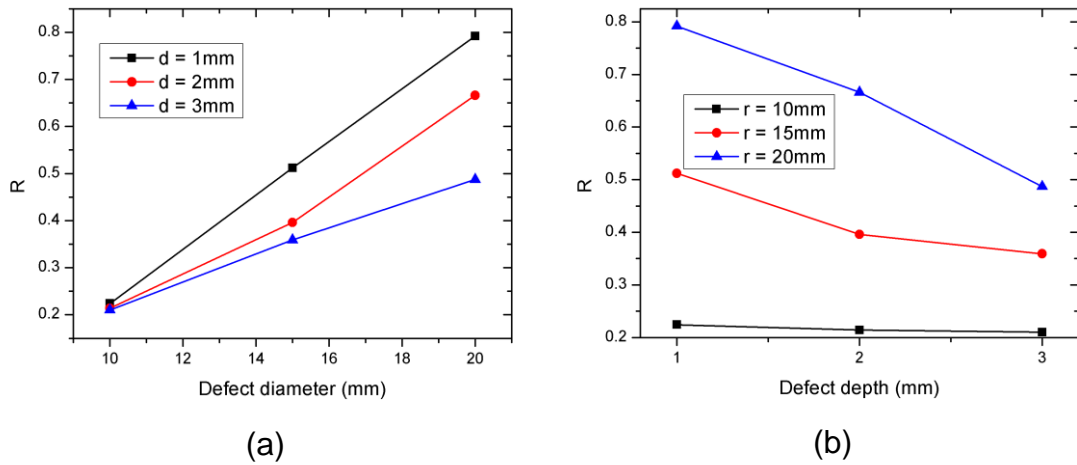
Figure 5-16 Results of Sample 4 (a) scatter plot between the defect diameter and the measured *R* (b) scatter plot between the defect depth and the measured *R*

The sensitivity of the R value on the defect depth increases following the increase of defect size. The R values are almost the same for the defects with the diameter of 10 mm. To fully reveal their relationship, an NFIR model was identified and is written as

$$R = 0.043r - 0.079d - 0.062 \qquad \textbf{(5-9)}$$

which confirms the relations between R and r, and R and d are approximately linear. The calculated PCC value is 0.965, which suggests an excellent performance of the model. The prediction of h, equivalent to the prediction of d, can be written as

$$h = 3.14 - 37.18R + 1.77r - 1.67R^2 - 0.06r^2 + 1.65Rr \qquad \textbf{(5-10)}$$

with a PCC value of 0.85. To evaluate the performance of the model (5-10), the measured R and size r in Table 5-4 are used to test. Table 5-5 shows the estimated values and the ground truth of h for the nine defects in Sample 4. The averaged percentage error of nine defect is around 5%. The result clearly demonstrates that the measured R value has a potential to estimate the defect thickness for flat-bottom holes through considering the defect diameter.

Table 5-5 The defect thickness comparison of nine studied defect in Sample 4 between the ground truth and estimation using the model (5-10)

Defect ID	Ground Truth (mm)	Prediction (mm)	Error (mm)	Percentage Error (%)
Sample 4-1	7	6.91	0.09	1.29
Sample 4-2	7	7.24	0.24	3.43
Sample 4-3	7	6.17	0.83	11.86
Sample 4-4	6	6.09	0.09	1.50
Sample 4-5	6	5.63	0.37	6.17
Sample 4-6	6	5.96	0.04	0.67
Sample 4-7	5	5.00	0.00	0.00
Sample 4-8	5	5.13	0.13	2.60
Sample 4-9	5	5.87	0.87	17.40

The experimental results in Table 5-3 (block-shaped defect) and Table 5-5 (flat-bottom hole defect) reveal that the performance of defect thickness estimation of flat-bottom hole defect is better than block-shaped defect. When considering the method to create the predictive model, the model of block-shaped defect is established based on the correlated relationship of R-h and R-d, which are a non-linear model and linear model, respectively. The model of flat-bottom hole defect is established based on the correlated relationship of R-d and R-r, which are both linear models. From this observation, it is possible that the model established from the same model type (e.g., linear model & linear model) provides the performance better than the model established from the different model type (e.g., linear model & nonlinear model).

5.5 Summary

Different with most of degradation assessment research focusing on damage/defects detection and depth measurement, this thesis addresses the challenge to estimate the defect thickness based on a single-side inspection of pulsed thermography under the reflection mode. This thesis proposes to use the thermal reflection coefficient (R) and measurable geometrical parameters of the damage, including size and depth, to estimate the thickness using a Nonlinear

Finite Impulse Response (NFIR) model. Applications of the proposed approach on three CFRP laminates show that:

a. The proposed method considerably improves the degradation assessment performance by extending the measurement of damage/defects from two dimensions to three dimensions.

b. For a specific material, the R value is strongly correlated with the defect size, depth and thickness. It has been observed that the relationship of R with the defect depth and the relationship of R with the defect size are approximately linear, while that for R and the defect thickness is approximately exponential. This observation allows deriving an empirical model to establish their independence, which enables the quantification of defect thickness using a single-side pulsed thermographic inspection.

c. The identified NFIR models demonstrated the potential to estimate the defect thickness using R and other measurable physical parameters. The Pearson Correlation Coefficients of the prediction for block defects and flat-bottom holes are 0.75 and 0.85, respectively.

With this developed approach, the interlaminar bond integrity of composite joints can be better evaluated by accurately estimating the thin air-gap in the interface of dissimilar polymer composite materials. The single-side inspection not only reduces the inspection time but also extends the application on components where one side is not accessible.

A potential disadvantage of this approach is that the air-gap thickness is a function of multiple correlated parameters, which may limit its application on irregular air-gap. One potential solution is to use the Principle Component Analysis to select the most important parameter to simplify the model or convert to a function of multiple independent parameters.

6 THREE-DIMENSIONAL DEFECT RECONSTRUCTION

6.1 Introduction

It has been observed that the results of most subsurface defect measurement methods such as Peak Slope Time (PST [73], [109]), Absolute Peak Slope Time (APST [77]), Logarithm Second Derivative (LSD [40]), Nonlinear System Identification (NSI [96]), and Least-Squares Fitting (LSF [76], [80]) methods are usually presented as 2D images. However, 2D visualisation is rather limited in representing and explaining the evolution and progression of a defect. Defects are typically not two-dimensional objects but evolve in 3D space over time. It is of great significance to predict the life of in-service components and to give feedback to design and maintenance [142]. 3D visualisation of inspected parts can provide a better understanding and more details of the defects and reduce operational time and improve quality control of production in the industry. For example, in the area of manufacturing, 3D images from computed tomography (CT) has been widely used to analyse the types of porosity defects occurred in the materials from castings [143], [144], [145], [146]. In the area of nuclear and aerospace industries, 3D visualisation is reconstructed from the digital X-ray images and has been used to view the location, shape and size of the defects like corrosion, delamination and crack, and evaluate the thickness of walls in the object of titanium aerospace investment casting [147], [148]. However, the X-rays technology is comparatively time-consuming [149], comes with potential health risks [150] to the user and is typically limited with respect to the maximum size of the parts to be analysed [137], [147], [151], [152], [153].

Only very few publications have studied the 3D reconstruction and visualisation of subsurface defects by pulsed thermographic inspection. Plotnikov and Winfree [93] visualised a 3D tomogram of the defects by using reversed time of the peak slope masked by the binary contrast image which is constructed by the thermal contrast method. Although this method can visualise the defects in the form of a 3D image, it can visualise only the depth of the defect and cannot visualise the thickness of the defect. Ramirez-Granados *et al.* [92] proposed an approach for 3D reconstruction of subsurface defects by using a finite-difference model. Firstly,

a non-defect nodal network is established with the properties and characteristics of the inspected object for detecting the inner defects. Next, the shape, size, depth, thickness, and location of subsurface defects are computed by means of the minimisation of a cost function and the determination of depth and a thickness function. After that, each non-defect node of the established nodal network is replaced with the computed defect node. This method requires the knowledge of a-priori properties of the defects such as thermal conductivity, density, and specific heat capacity at constant pressure, which are typically unknown in on-site inspections. Elhassnaoui and Sahnoun [91] proposed a method for 3D reconstruction of defect shape located on the inaccessible back of a homogeneous material without the need for thermal properties such as thermal diffusivity. Based on thermal distribution, this method analyses thermal response on the object's surface and computes defect distance (defect depth and sample thickness). It modifies the APST method [77] to evaluate defect distance of the object by dividing arbitrary two points from the sample surface to eliminate the thermal diffusivity. However, this method can only be applied to the characterisation of surface defects.

Three-dimensional visualisation of hidden defects based on PT is promising, attractive but challenging. A direct approach using pulsed thermography could be conducting two inspections from both the front and back of a part. The defect depth for each inspection is calculated based on the aforementioned methods, by which means the defect thickness can be computed by considering the sample thickness. However, the deployment of this approach can be limited because 1) one side of the inspected component could be inaccessible e.g. an aircraft wing or fuselage; 2) the accuracy of measurement could be compromised if the defect thickness is very thin due to extreme closed values of defect depths from two inspections; 3) if the defect is too deep one side, the defect could be missed, and 4) it introduces extra cost of inspection time.

This chapter proposes a new three-dimensional subsurface defect reconstruction and visualisation method [99]. Several of the aforementioned problems can be solved by this proposed method. For instance, in the case of one side of the

component could not be accessible, the proposed method provides a single-side inspection method to evaluate it. For another example, when considering the inspected material, in the case of composite materials such as carbon fibre reinforced polymer (CFRP), it is very difficult to analyse and visualise subsurface defects by using directly general 3D heat transfer theory because it is an inhomogenous material which is compounded with several layers of polymer. The proposed method can also solve this problem by indirectly estimating 3D heat flow from the 1D heat transfer solution to reduce the complexity of 3D heat transfer analysis. In addition, a big amount of cost can be saved by the proposed method. Generally, a 3D subsurface defect could be visualised by using 3D image technology device such as 3D CT scanner which is very expensive, while the proposed method can use a general 2D image device technology which is cheaper to produce and visualise 3D images. The outline of this chapter is illustrated in Figure 6-1.
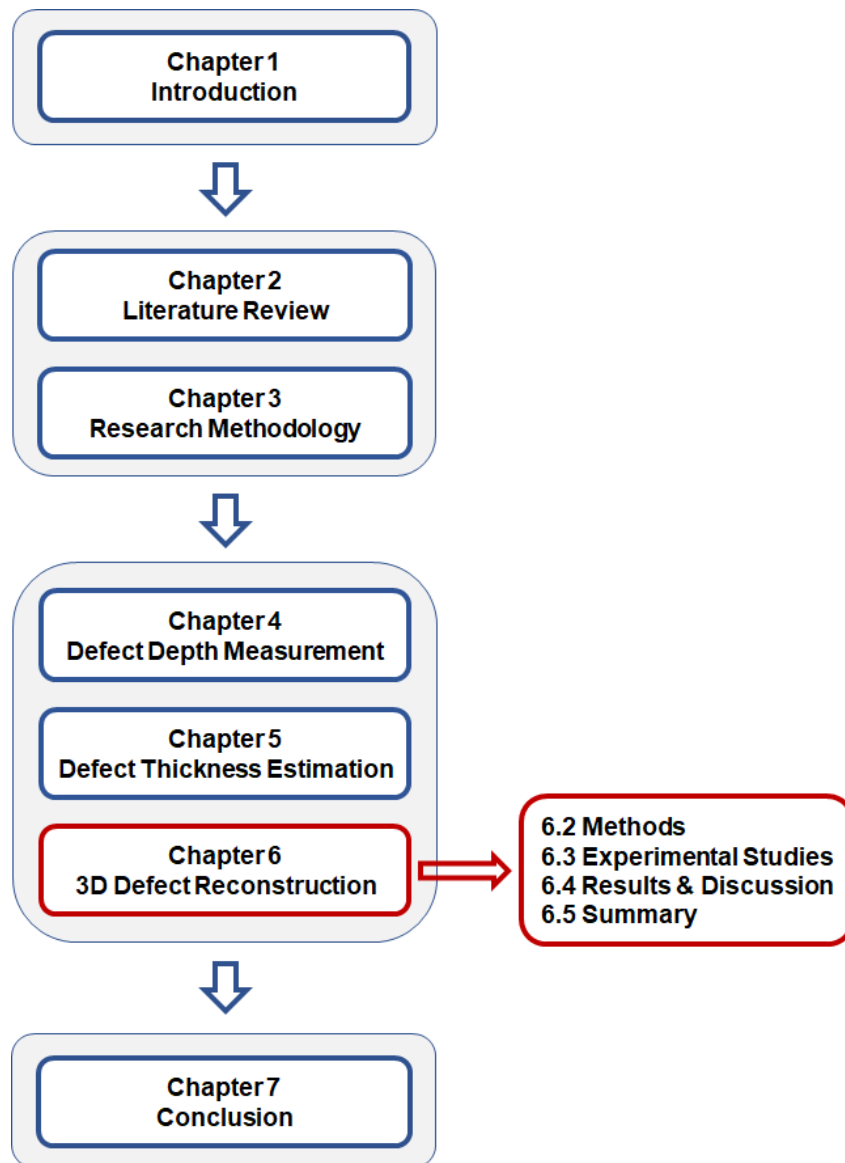
Figure 6-1 The outline of Chapter 6

6.2 Methods

This thesis proposes double-side inspection and single-side inspection methods to reconstruct and visualise 3D subsurface defect.

6.2.1 Double-side Inspection

The method of double-side inspection reconstructs the 3D structure of defects by evaluating the defect depth ($d1$ and $d2$) from both sides of the sample (front and back side). As seen in Figure 6-2 The side view of subsurface defects, the defect thickness (h), at the position of x and y, can be calculated by

$$h(x,y) = L(x,y) - (d1(x,y) + d2(x,y)) \qquad \text{(6-1)}$$

where $h(x,y)$ is the defect thickness, $L(x,y)$ is the thickness of the sample, $d1(x,y)$ is the defect depth from the top surface, and $d2(x,y)$ is defect depth from the bottom surface. The thickness of the sample can be measured by general measurement tools such as a ruler or Vernier callipers. Defect depth can be estimated by methods such as PST [73], [109], LSD [40], APST [77], NSI [96], LSF [76], [80], or NLSF [116] method. In this thesis, the NLSF method is employed to estimate the defect depth due to its fine performance.
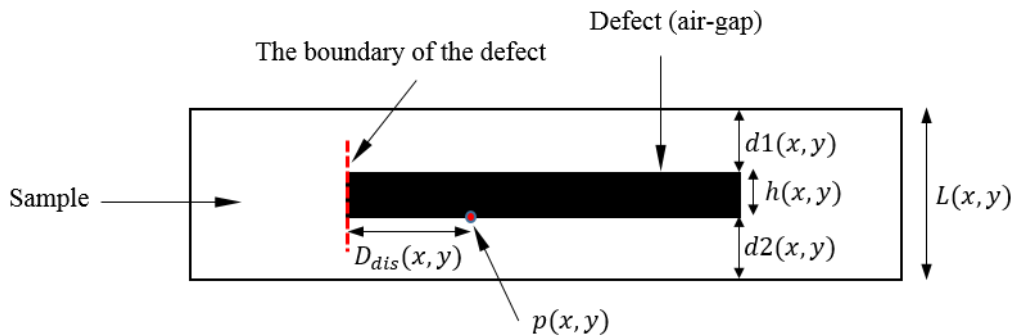
Figure 6-2 The side view of subsurface defects

6.2.2 Single-side Inspection

Although the double-side inspection is straightforward, there are a few limitations. This thesis introduces a novel single-side inspection approach to overcome these limitations. The proposed method estimates the defect thickness $h(x,y)$ by establishing a predictive model between h, the defect depth d (e.g. either $d1$ or $d2$) estimated from a single-side inspection, thermal wave reflection coefficient (R), and shortest distance from the boundary of the defect to the inspected point location $p(x,y)$ (D_{dis}), written as

$$h(x, y) = f(R(x, y), d(x, y), D_{dis}(x, y)) \qquad \textbf{(6-2)}$$

The defect thickness can then be inferred based on this model. The values of $d(x, y)$ and $D_{dis}(x, y)$ are achievable using the existing methods, but the challenge is to measure $R(x, y)$. In this thesis, the developed New Least-Squares Fitting method (NLSF) [116] is applied to estimate R and d simultaneously.

The thermal wave reflection coefficient (R) can be directly computed from the analytical model is written in the Equation (4-1) in Chapter 4.

6.2.3 Inspection Process

The single-side inspection and the double-side inspection can be described in the flowcharts as shown in Figure 6-3. For the single-side inspection, the first step is to select the region of interest (ROI), which aims to select a region for defect estimation and visualisation to reduce overall processing time. The ROI was selected manually in this thesis. The second step is defect measurement to obtain subsurface information of ROI including defect depth (d), the shortest distance from the boundary of the defect to the inspecting point (D_{dis}), and the thermal wave reflection coefficient of the defect (R), which are achieved by the NLSF method. The third step is noise reduction to enhance image quality (R image and d image), which is achieved by the application of a Median Filter [154] in this thesis. The fourth step is to establish the relationship model between h, R, and D_{dis}, shown in Equation (6-2), based on the estimated parameters in the second step. The fifth step is to estimate the defect thickness based on the established model. The last step is to visualise the defect in the form of a 3D image, where the reconstructed defect (size, depth, thickness, and location of the defect) is fused with the dimension (width, length and thickness) of the sample to produce a volume image. This volume image is then rendered and displayed in the form of a 3D image. For the double-side inspection, most steps are similar to the single-side inspection except the second, the fourth, and the fifth step. In the second step, the sample's thickness and defect depth of both side of the sample is required, whilst the defect depth from the single-side inspection requires one

side only. The fourth step is to align the position of the defect region between the front side and the backside and the fifth step is to estimate the defect thickness from Equation (6-1).
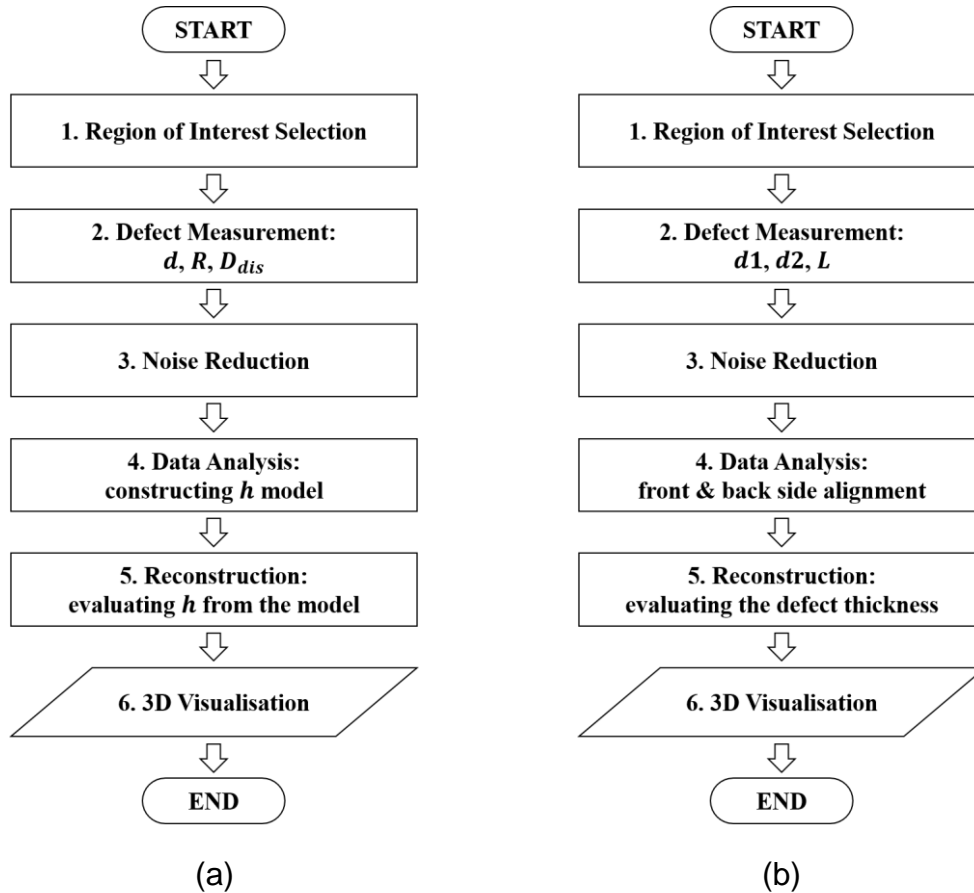
Figure 6-3 Inspection process (a) single-side inspection (b) double-side inspection

6.3 Experimental Studies

6.3.1 Testing Sample 2

Sample 2 in Chapter 5 was used in this study. The dimension of Sample 2 is 75 mm × 230 mm × 8 mm, shown in Figure 5-4(a). It includes five-block defects with a thickness (h) of 0.5 mm, 1.0 mm, 2.0 mm, 3.0 mm, and 4.0 mm, respectively, named Defect 1 to Defect 5. The distance between two adjacent defects is 30 mm. The width (r), length, and depth (d) for all defects are 10 mm, 75 mm, and 2 mm, respectively. The side view of Sample 2 is shown in Figure 5-4(b). This sample is aimed at studying the relationship between the thermal wave reflection

coefficient $R(x,y)$, defect thickness $h(x,y)$, and the shortest distance from the boundary of the defect to the inspected point location $D_{dis}(x,y)$ when the defect depth $d(x,y)$ is fixed.

6.3.2 Testing Sample 5

As a use case, Sample 5 was made from steel with a dimension of 210 mm × 240 mm × 35 mm, as shown in Figure 6-4. There is an 'S' shape triangular air-gap through the sample. By measurement, at the top side of the sample, the defect is estimated to be triangular in shape, which has the base about 25 mm and the maximal thickness about 20 mm, illustrated in Figure 6-4(c). At the bottom side of the sample, the defect is also estimated to be triangular in shape, which has the base about 16 mm and the maximal thickness about 16 mm, illustrated in Figure 6-4(d). The sample was inspected at the flat side using the proposed single-side thermographic inspection, illustrated in Figure 6-4(b).

(a)   (b)

(c)

(d)
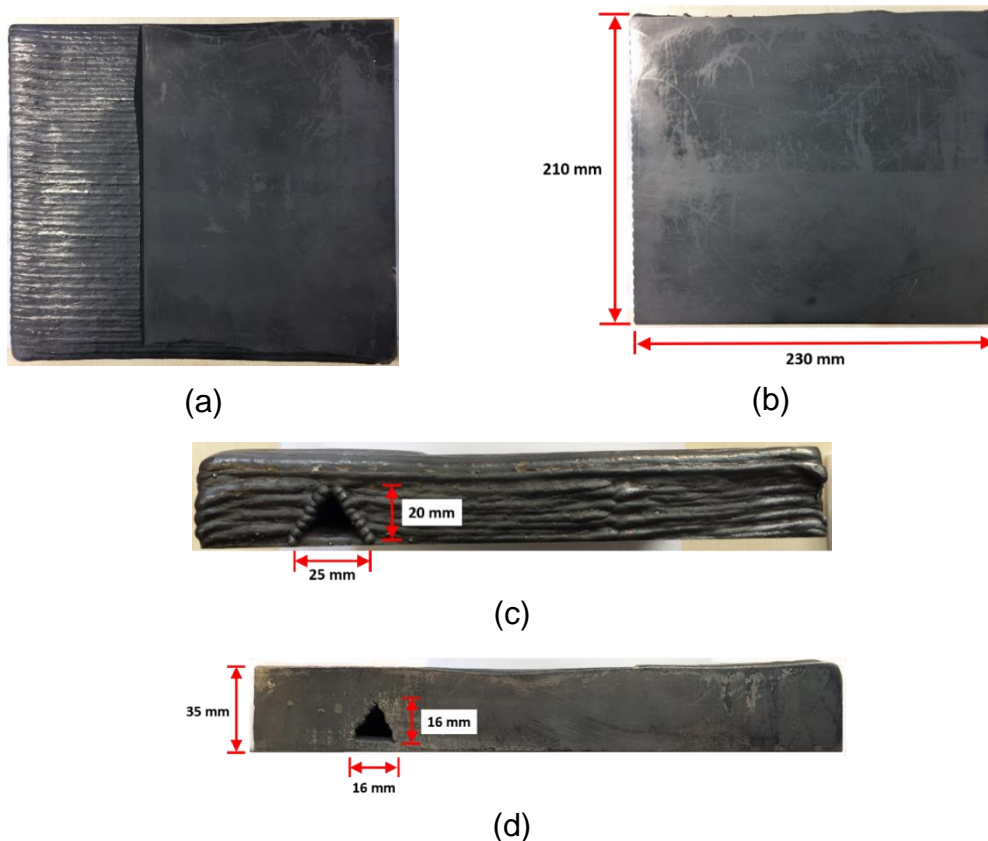
Figure 6-4 Snapshots of Sample 5: a steel plate with triangle air-gap defects (a) the backside of the sample (b) the front side of the sample (c) the top side of the sample (d) the bottom side of the sample

6.3.3 Experimental Setup

The configuration of the experiment is shown in Figure 3-3(a) in Chapter 3. The experiments were conducted using the Thermoscope FLIR SC7600 with two capacitor banks powered Xenon flash lamps mounted in an internally reflective hood, as shown in Figure 3-4 in Chapter 3. Considering the thickness of Sample 2 and the low thermal diffusivity of CFRP, a sampling rate of 10 Hz was used and totally 900 frames (equivalent to 90 s) were captured after the flash. Considering the thickness of Sample 5 and the high thermal diffusivity of steel, a sampling rate of 50 Hz was used and totally 500 frames (equivalent to 10 s) were captured.

6.4 Results and Discussion

6.4.1 Results of Testing Sample 2

6.4.1.1 Double-side Inspection

In this experiment Defect 4 and Defect 5, with a thickness of 3 mm and 4 mm, respectively, were in the focus because they can be detected from both sides of the sample. Defect 1, Defect 2 and Defect 3 were not selected because the defect depth of the back of these defects is too deep (5.5 mm, 5.0 mm, and 4.0 mm, respectively) to measure considering the depth to width ratio of a defect. The NLSF method was applied to the selected regions to estimate the defect depth where the thermal diffusivity (α) was chosen as 0.5×10^{-6} m^2/s. The estimated defect depth after reducing noise from inspection of two sides are shown in Figure 6-5. Observation from the front of the part shows that the measured depths for Defect 4 and Defect 5 is similar. This is expected as both defects have a 2 mm depth, as illustrated in Figure 5-4. The depth map from the back shows that Defect 4 (light blue) is much deeper than Defect 5 (deep blue). In the data analysis process, the defect position at the front and the back of the part was aligned and registered. After that, the defect thickness was calculated by Equation (6-1). The estimated parameters including defect depths and thickness are shown in Table 6-1. It is observed that, on the front, the average of the estimated defect depth of Defect 4 is approximately identical to the design (2 mm)

with an error of 1%, while Defect 5 has about 10% error. For the back of the part, the average error of the estimated defect depth for Defect 4 and Defect 5 are around 18% and 16%, respectively. The computed defect thickness of Defect 4 and Defect 5 are 3.55 mm and 4.50 mm, which have the percentage error of 18.33% and 12.50%, respectively. It is observed that the performance of the double-side inspection method is better when the defect is thicker. Finally, the surface information (dimension of the sample) and subsurface information (defect depth and defect thickness) were used to build the 3D volume image and visualised in the form of a 3D image, as shown in Figure 6-6. It is clearly visible that Defect 5 is thicker than Defect 4, and the estimated 3D volume for both defects is close to the design shown in Figure 5-4. It should be noted that the z-axis is scaled up to better visualise the detail of the defect surface.

(a)

(b)
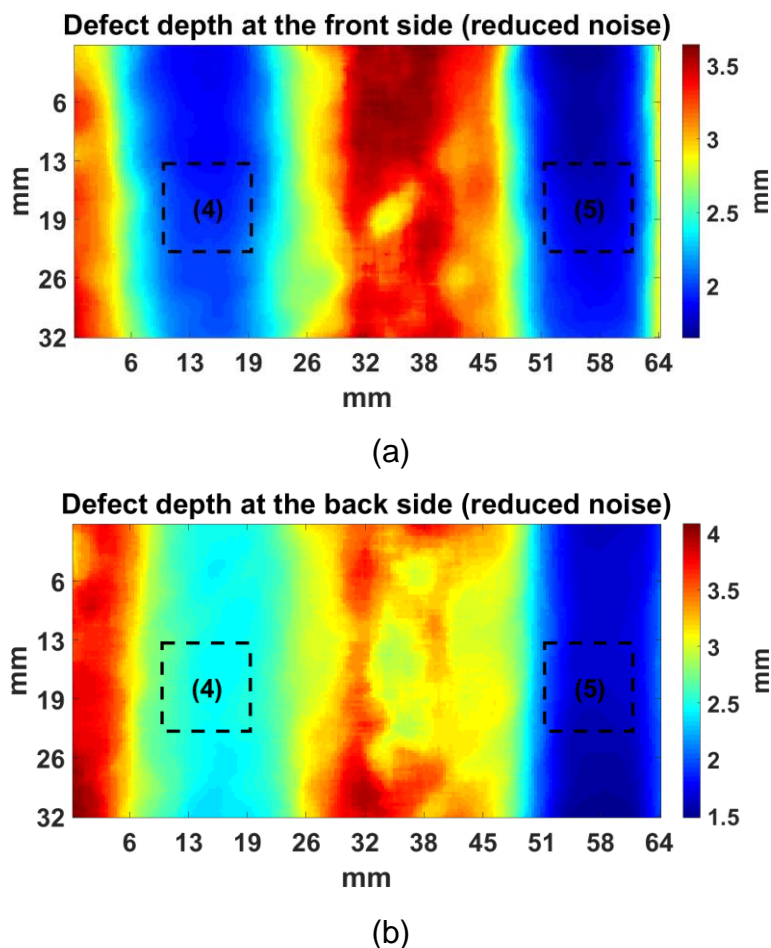
Figure 6-5 The estimated defect depth image of Sample 1 after reducing noise (a) at the front side (b) at the backside, where the left defect is Defect 4 and the right one is Defect 5

150

Table 6-1 Estimated values of Sample 1 from the double-side inspection method

Defect ID	Ground Truth (mm)			Average of The Estimated Value (mm)		
	Defect Depth		Defect Thickness	Defect Depth		Defect Thickness
	Front Side	Back Side		Front Side	Back Side	
	$d1$	$d2$	h	$d1$	$d2$	h
Defect 4	2.00	3.00	3.00	1.98±0.05	2.47±0.05	3.55±0.10
Defect 5	2.00	2.00	4.00	1.82±0.07	1.68±0.06	4.50±0.10
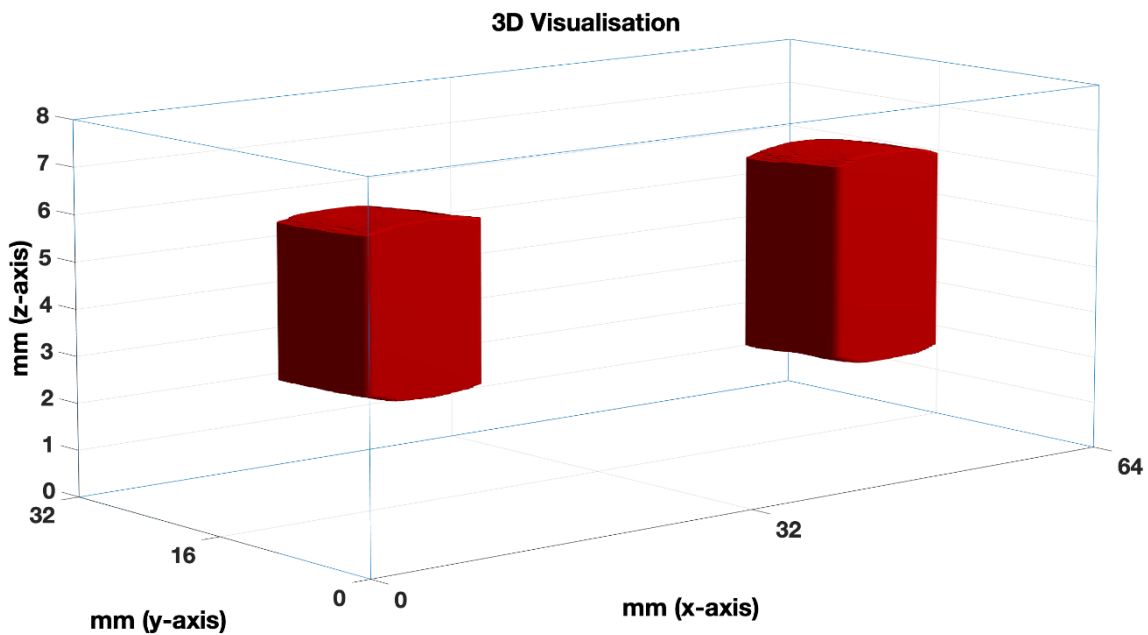
Figure 6-6 The 3D visualisation of Sample 1 from the double-side inspection

6.4.1.2 Single-side Inspection

Due to the large width of Sample 2 (230 mm), the defects of this sample suffer non-uniform heating for a single inspection, described in Section 5.3.2 in Chapter 5, which could lead to unreliable results [140]. To reduce this effect, in this study, the sample has been captured five times, where each defect was placed on the centre of the camera's view once. An area of the centralised defect with the size of 160×120 pixels for five data files was then cropped and merged into one file with a size of 160×600 pixels for easier analysis. Figure 6-7 shows a snapshot of the raw thermal image at time 23 s. The defects are labelled as "(1)", "(2)", "(3)", "(4)", and "(5)" to represent the defect thickness of 0.5 mm, 1.0 mm, 2.0 mm, 3.0

mm, and 4.0 mm, respectively. The ROI of each defect is about 10 mm × 10 mm (around 30×30 pixels), as highlighted in Figure 6-7, which are used for evaluating the performance of the proposed technique. In case of unknown defect, the region of defect which has smooth values of R can be used for extracting data.
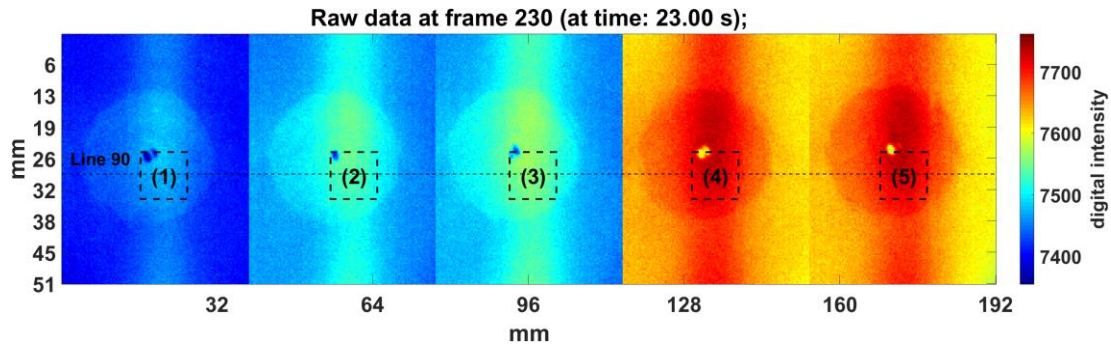
Figure 6-7 The raw thermal image at frame 230 for Sample 2 after combining 5 inspections, where the regions of interest are highlighted

The relationship between defect thickness (h) and thermal wave reflection coefficient (R) requires to be established before the prediction of h. To reduce the influence of the heat leaked to each opened side on the results, only a region of 6×30 pixels on the middle area of each defect were sampled. Measured R values were averaged (R_{ave}) and are shown in Table 6-2.

Table 6-2 The average of estimated R values in the middle area of each defect

Defect ID	The Designed h (mm)	The averaged R (R_{ave}) in the middle area of 6×30 pixels
Defect 1	0.5	0.4765±0.0025
Defect 2	1.0	0.5461±0.0037
Defect 3	2.0	0.5858±0.0071
Defect 4	3.0	0.6004±0.0034
Defect 5	4.0	0.5940±0.0039

The averaged R values, denoted by R_{ave}, in the middle area were used as the representative of R to establish the R_{ave} vs h relationship. It is observed that the averaged value of R increases following the increase of defect thickness. This observation is expected because the heat is more difficult to be leaked through the 3D conduction around air-gap if the defect is thicker. As can be seen from the plot between R_{ave} and h in Figure 6-8, the associate is not linear but

152

approximately exponential. An exponential fitting was applied on them, and the relationship between R_{ave} and h can be written as

$$R_{ave} = -0.2820e^{\frac{-h}{0.5898}} + 0.5974 \qquad \textbf{(6-3)}$$

To estimate the value of h using the measured R_{ave}, the model (6-3) can be reversed as

$$h = -0.5898ln\frac{R_{ave} - 0.5974}{-0.2820} \qquad \textbf{(6-4)}$$
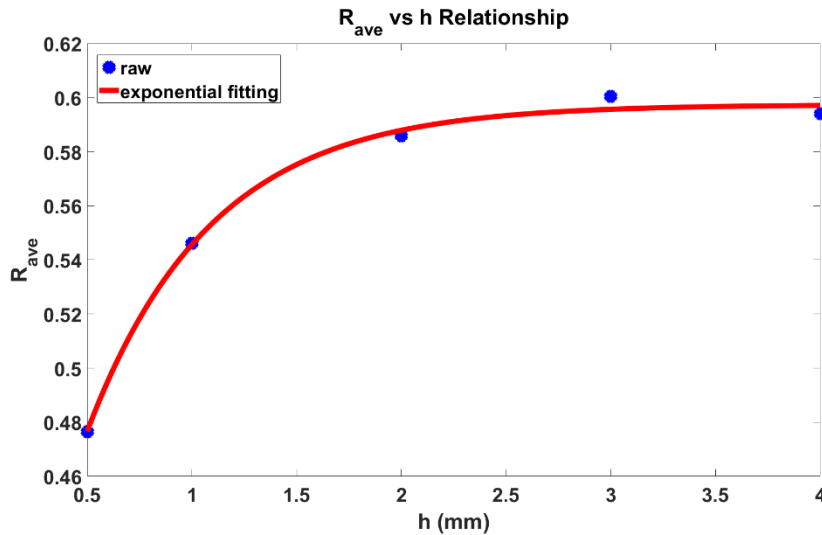
Figure 6-8 The plot of $R_{ave} - h$ curve of Sample 1

It is observed that the curve of R-h in Figure 6-8 is similar to Figure 5-10 in Chapter 5. Nevertheless, the value of R is slightly different due to R in Figure 6-8 is averaged by the area of 6×30 pixels, whilst R in Figure 5-10 is averaged by the area of 1×10 pixels.

Figure 6-10 shows plots of estimated R and d of the cross-section at line 90 (see in Figure 6-9), where it can be clearly seen that the R values are not consistent for one defect even though the five defects have a consistent thickness. It indicates that there are some other factors affected the R value. It is suggested in Figure 6-10 that R value at both sides of the defect's boundary is less than the middle region. This observation could be caused by the fact that the heat around

the middle of the defect is more difficult to leak than that around the boundary of the defect. This issue must be addressed if the identified model from the regions of 6×30 pixels is applied to the ROI of 30×30 pixels.
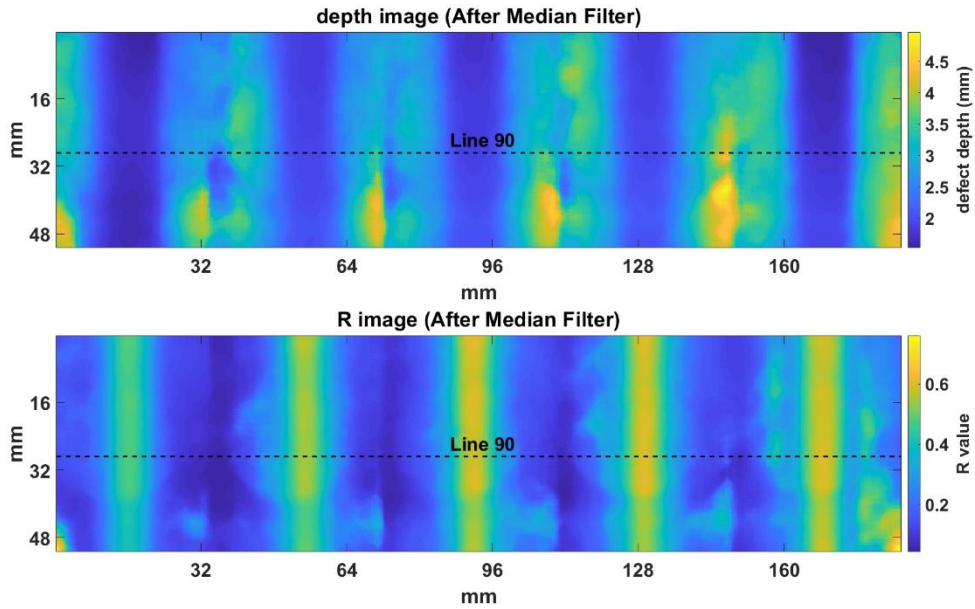
Figure 6-9 Snapshot at line 90 of the depth image and R image after noise filtering
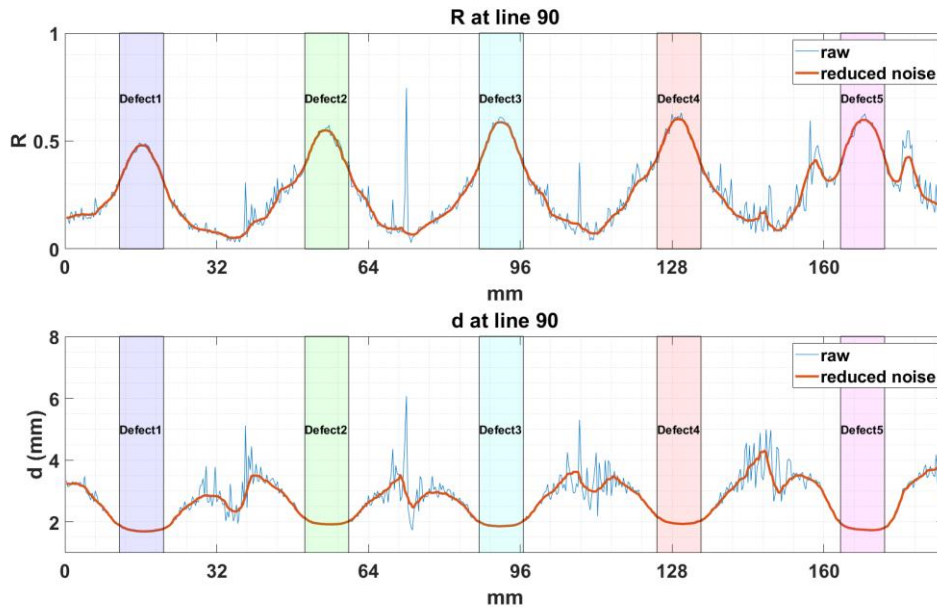
Figure 6-10 Plots of estimated R and d of the cross-section at line 90

To improve the accuracy of R estimation, the shortest distance from the boundary of the defect to the inspected point (D_{dis}), shown in Figure 6-2, is taken into account to correct the R value. The re-calculated R (R_{new}) is a function of R and D_{dis}

$$R_{new} = f(R, D_{dis}) \qquad \text{(6-5)}$$

This function can be approximated by a polynomial model, parameters of which can be estimated based on the known D_{dis}. The estimated model is written as

$$R_{new} = 0.2214 + 0.7413R - 0.0168D_{dis} + 0.6135R^2 + 0.0011D_{dis}{}^2 \\ - 0.0326RD_{dis} \qquad \text{(6-6)}$$

after that, the defect thickness can be reconstructed by

$$h = -0.5898ln\frac{R_{new} - 0.5974}{-0.2820} \qquad \text{(6-7)}$$

The average of the estimated defect thickness of each defect for the regions of 30×30 pixels is shown in Table 6-3. It is suggested that the maximum error of the estimated depth for all defect is less than 13%. For Defect 2 to Defect 4, the error is less than 5%. It is interesting to observe that Defect 1 and Defect 5, which are close to the boundary of the sample, have a larger error than others, which could be caused by the manufacturing error. The average R value increases following the increase of the estimated defect thickness (h). The error of the estimated defect thickness is less than 19%, particularly for Defect 1 to Defect 4, the error is less than 10%. The large error of h for Defect 5 is caused by the saturated R value, which is 0.53, the same as the R value for Defect 4. The reconstructed defects for the regions of 30×30 pixels are visualised in Figure 6-11, which suggests that the proposed technique can effectively reconstruct the 3D structure of simple defects. The estimation of the bottom surface has an increasing error following the increment of defect thickness.

Table 6-3 Estimated values of Sample 1 from the single-side inspection method

Defect ID	Ground Truth (mm)		Average of The Estimated Value			Error (mm)	
	d	*h*	*d* (mm)	*h* (mm)	*R*	*d*	*h*
Defect 1	2.00	0.50	1.74±0.05	0.45±0.01	0.41±0.06	0.26	0.05
Defect 2	2.00	1.00	1.96±0.06	1.02±0.16	0.48±0.06	0.04	0.02
Defect 3	2.00	2.00	1.91±0.05	2.15±0.38	0.51±0.07	0.09	0.15
Defect 4	2.00	3.00	2.00±0.07	2.96±0.50	0.53±0.07	0.00	0.04
Defect 5	2.00	4.00	1.79±0.06	3.25±1.04	0.53±0.06	0.21	0.75
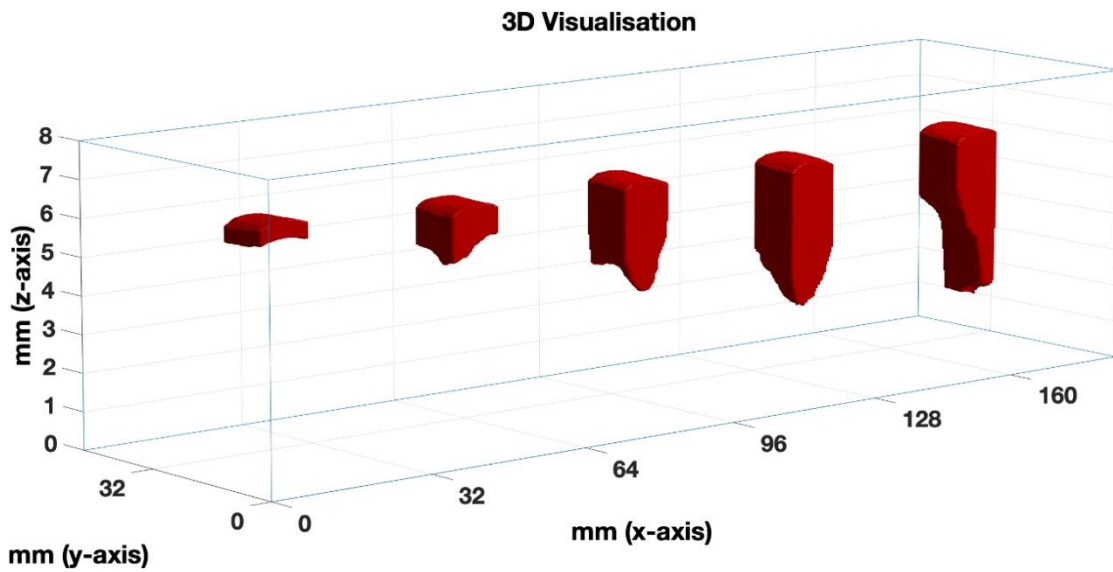
Figure 6-11 The 3D visualisation of the five defects of Sample 2 using the proposed single-side inspection

In terms of the performance of single-side inspection method and double-side inspection method, the experimental results reveal that the double-side inspection method performs better in thicker defects such as Defect 5. The average error of the estimated defect thickness of Defect 5 by double-side inspection method is 12.50% whilst the single-side inspection method is 18.75%. However, in case of thin defect, the single-side inspection method performs better than double-side inspection method. The single-side inspection method can evaluate Defect 1 to Defect 3, which have thinner thickness, while the double-side inspection method cannot evaluate them.

6.4.2 Results of Testing Sample 5

Sample 5 was tested by the single-side inspection because the defect was too deep to measure from the other side. To find the relationship between R and h, R values in three areas with a size of 100×60 pixels were sampled as highlighted in Figure 6-12. It should be pointed out that the R values of 100 vertical pixels were averaged. Figure 6-13 plots the cross-section at line 200 of the estimated R and d, where the three selected areas are highlighted.
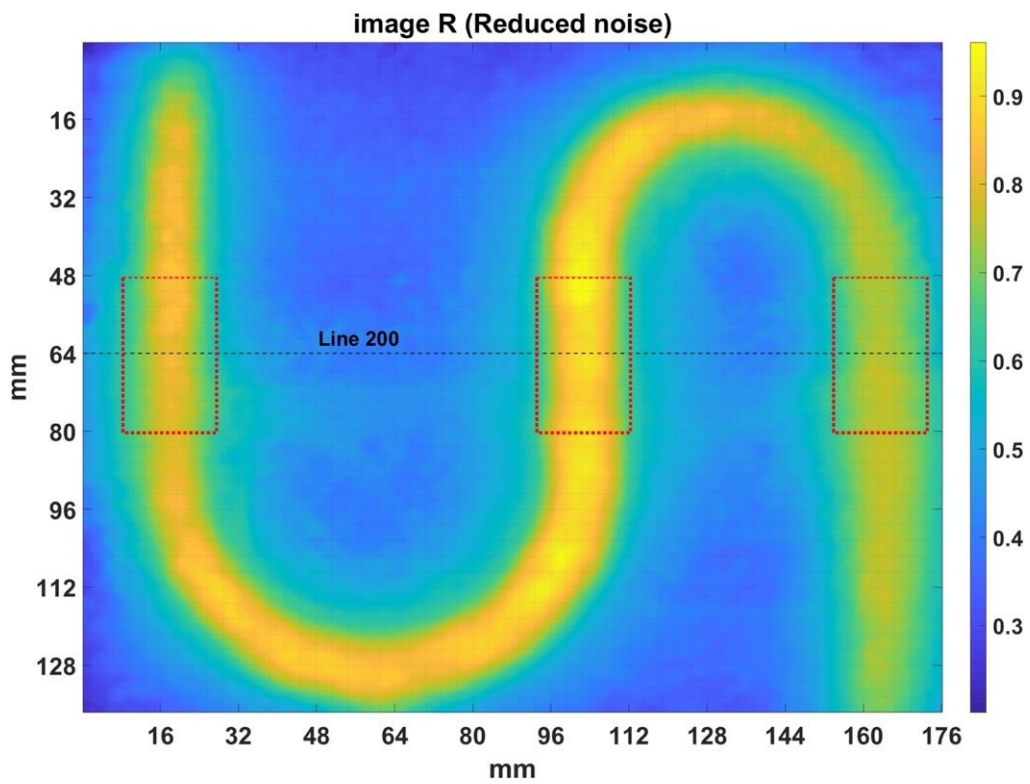
Figure 6-12 The averaged R region over the top side triangle defect area for Sample 5
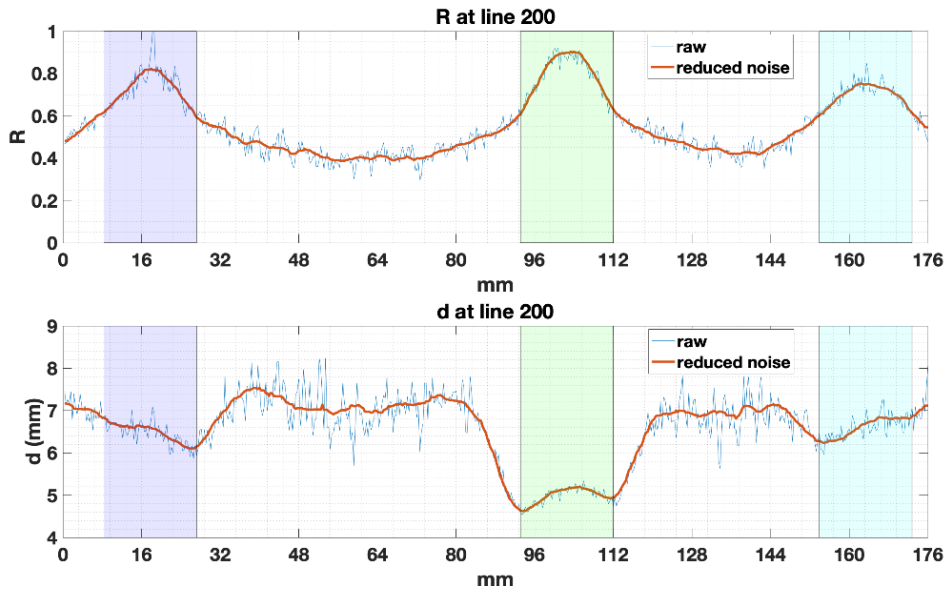
Figure 6-13 Plots of estimated R and d of the cross-section at line 200 of Sample 5

It can be observed that the middle area has the highest value of R, then the left one and the right now. Proven in the experiments of Sample 2, a higher value of R suggests a thicker defect. As illustrated in Figure 6-4, the maximal thickness of the left defect is about 20 mm, and the right one is about 16 mm. Based on the observation of the R values, the maximum thickness of the middle area is assumed to be 24 mm. A numerical model was then established to represent the relationship between R and h, written as

$$h = (1.0698 \cdot 10^6)e^{\frac{R}{0.1050 \cdot 10^6}} - 1.0698 \cdot 10^6 \qquad \textbf{(6-8)}$$

As the last step, the 3D volume image was reconstructed by combing the surface dimension (size and thickness of the sample) and subsurface information (defect depth and defect thickness) and the result is shown in Figure 6-14.
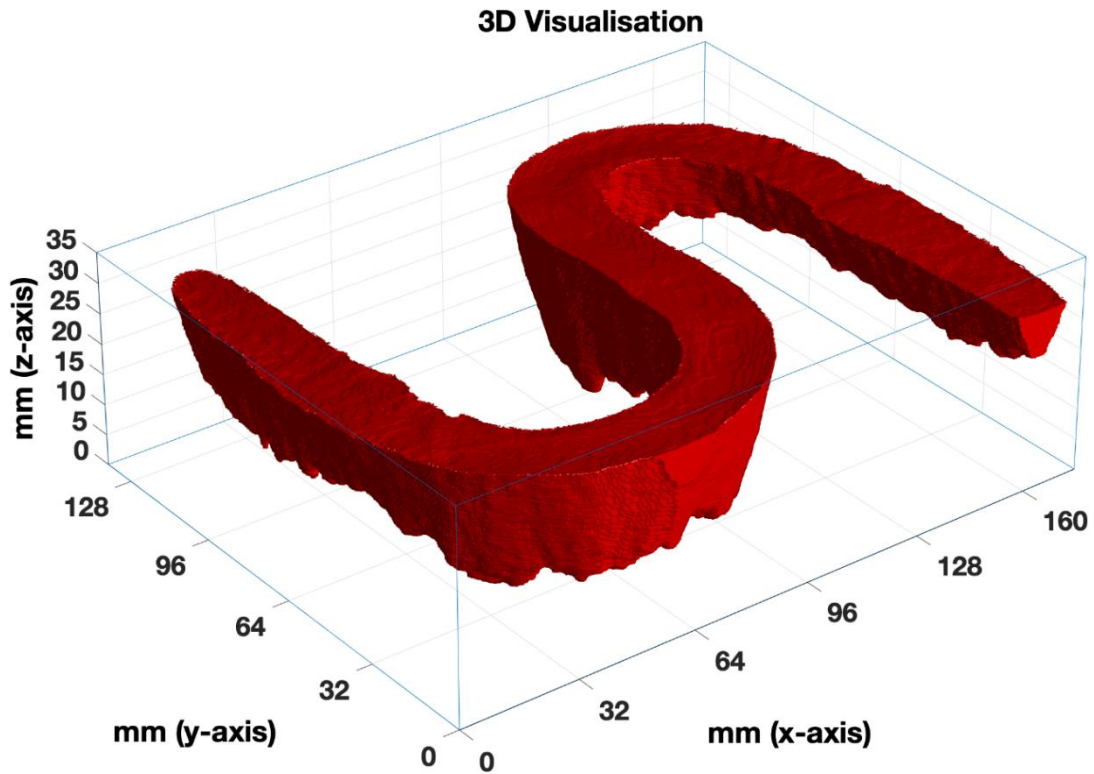
Figure 6-14 3D defect visualisation of Sample 5 using the proposed single-side inspection

The triangular 'S' shape defect can be clearly observed which matches the appearance of the defect shown in Figure 6-4(c) and Figure 6-4(d). To validate the result using other NDT methods, Figure 6-15 shows the comparison of the 2D image of the defect from pulsed thermography and X-ray. It can be seen that the defect shape of both images is similar. A quantitative comparison between these two imaging modalities in terms of 3D defect reconstruction was not conducted in this thesis due to the distortion of thermal images caused by the lens. A further study is required to correct this distortion before conducting a comprehensive comparison.
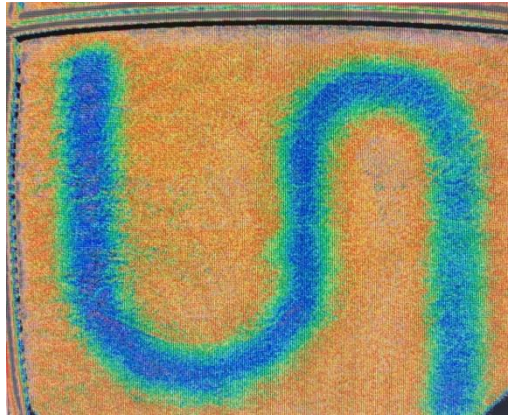
(a)

(b)
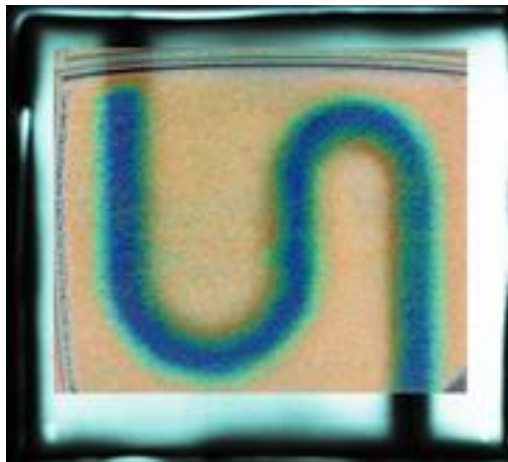
(c)

Figure 6-15 The inspection results in the form of a 2D image for Sample 5 from (a) pulsed thermography (b) X-ray (c) overlay of two modalities

6.5 Summary

This thesis has developed a novel 3D reconstruction and visualisation approach for subsurface defect based on one single-side PT inspection under the reflection mode. The defect thickness, a key parameter to reconstruct defect in a 3D form, was measured through estimating thermal wave reflection coefficient value and establishing its relationship with defect thickness using an empirical model. For the comparison purpose, this thesis also introduces a double-side inspection approach that estimates the defect thickness by measuring the defect depths from both sides of a part. And then the estimated thickness, depth and size of the defect, including the dimension of the part were combined and visualised in the form of a 3D image.

The proposed technique has been tested on two samples with artificial defects on CFRP and steel materials, and the results show that:

a. In comparison with the double-side inspection, the proposed single-side inspection is not only faster but also increases the applicability of 3D defect reconstruction. There are many cases where industrial components can be accessed only on one side, such as an aeroplane wing. Furthermore, some defects are too deep to detect or measure the depth, such as Defect 1-3 in Sample 2 and Sample 5, which limits the applications of the double-side inspection.

b. For Sample 2, the single-side inspection can measure the defect thickness with an error of less than 10% if the thickness is less than 3 mm. The error increases if the thickness increases. For example, the error for the defect with a thickness of 4 mm is 19%.

c. The double-side inspection can produce more accurate thickness measurement if the defect is thick. For defects with a thin thickness, the single-side inspection is more appropriate.

d. The thermal wave reflection coefficient is not only related to the thickness of defect but also related to the shortest distance to the defect boundary.

e. The proposed 3D defect reconstruction solution can effectively assess the defect or damage in CFRP and steel by offering more details of the structure and friendly visualisation.

A drawback of this method is that the defect thickness is a function of multiple correlated parameters, which may constrain its application on irregular shape defects. Based on experiments in this research, it is also discovered that the model to estimate defect thickens is subject to materials. Besides, changing of material properties of tested specimen and defect shape may also have an impact on the precision of the model and then the estimation of defect thickness. To fully explore its potential and improve the applicability of the proposed method, a further study is required by considering different materials with a variety of defect shape, size, depth and thickness.

7 CONCLUSIONS

This thesis has developed a novel three-dimensional subsurface defect reconstruction and visualisation approach with a single-side inspection based on the pulsed thermography method. This chapter describes the accomplishment, explains challenges, highlights major findings, summarises main contributions, discusses limitations, and suggests recommendations of the thesis for the future work.

7.1 Accomplishment of The Research Objectives

This section discusses the challenges and achievement of the research objectives identified in Chapter 1. The description of the corresponding achievement in each objective is discussed below.

7.1.1 Objective 1

The aim of this objective is to identify the most appropriate NDT method for 3D subsurface defect representation. The initial objective was focused on overviewing and understanding the fundamental knowledge of NDT methods such as ultrasonic testing and infrared and thermal testing. To find the best NDT method to achieve the aim of this thesis, the weaknesses and strengths of the classical NDT methods were compared. The factors used for the consideration are the type of materials (e.g. homogeneous or inhomogeneous material, and metallic or non-metallic), the type of defects, location of defects (e.g. inner and outer surface), inspection time, and cost. The main target of this thesis is to advance the inspection of subsurface defect of industrial components. This thesis especially focuses on composite materials, such as carbon fibre-reinforced polymer (CFRP), which is widely used in aerospace, automotive and manufacturing industry. It has been identified that the most suitable and reliable NDT method for this purpose is infrared and thermal testing (IRT).

In order to achieve this objective, the active thermography techniques were reviewed. Based on the properties of the main materials used in this thesis, pulsed thermography, lock-in thermography, and vibro-thermography were reviewed. Summarily, this thesis selected the pulsed thermography under the reflection mode because this technique requires only a short pulse from flash lamps to heat the object's surface which consumes less time of inspection than lock-in thermography. Vibro-thermography is neglected because this technique requires a transducer to excite the object, which needs to contact the object.

After pulsed thermography is selected, a review to find the most appropriate method to represent the subsurface defect in the form of 3D images has been performed. The methods of 3D subsurface defect representation, defect detection, and depth measurement have been reviewed. From the review, there is no method able to directly perform for three-dimensional subsurface defect reconstruction and visualisation. It is found that there are very limited reports on this topic. Even for the published work, most of the studies were conducted in a simulation environment.

7.1.2 Objective 2

This objective aims to determine the best configuration of the acquisition system for the experiments in this thesis. The main equipment of the pulsed thermography configuration consists of infrared camera/video, flash lamps, controller, computer and software. Commonly, limitations of equipment, device, or system can make some issues or make more difficult to experiment. One configuration in this system is the number of frames to be captured for analysis. The number of frames is important to the experiment and data analysis because, if the number of frames is too less or not enough, the analysed result could be incorrect.

The suitable data can help better analyse the data, reduce the complexity of the inspection, increase overall performance, and decrease the operating time. In this thesis, the raw data is defined that raw digital temperature data from the infrared camera. The best quality means that the most suitable data for three-dimensional

subsurface defect reconstruction and visualisation approach. This objective was achieved through heavily and repeatedly experiments. To obtain the best raw thermal data, several experimental parameters have been taken into account, including frame rate, duration time of the capture, the distance between the sample and the camera lens, the amount of excitation energy, and the sample's thickness. The experiments were set up systematically, and variable and factors were controlled precisely. For instance, to test the effects of frame rate, all other factors were fixed and only the frame rate is varied.

In summary, the workpiece was placed in front of the infrared camera's line of sight at a distance of 250 mm from the lens. The applied energy is approximately 2 kJ over the inspection area of approximately 160 mm × 200 mm. The suitable frame rate of the capture for the CFRP specimen is 10 Hz or 25 Hz and for the metallic specimen is 25 Hz or 50 Hz. The length of data capture depends on the sample's thickness and defect depth.

7.1.3 Objective 3

This objective is to estimate essential parameters of defect for later 3D reconstruction. In order to achieve this objective, first of all, the state-of-the-art methods relative to defect detection and depth measurement were studied. It was found that there is no method that can directly be used for this thesis because most of them can perform depth measurement but not thickness measurement. Thus, a new method to perform for defect thickness measurement is needed. The performance of the state-of-the-art methods was compared under a numerical simulation environment. From the comparison, it has been identified that the least-squares fitting method (LSF) provided the high accuracy of depth measurement and robustness to noise. This method is based on a modification of the heat transfer function. From the analysis of the LSF method, it is found that the estimation of the thermal wave reflection coefficient can not only improve the accuracy of depth measurement but also estimate the defect thickness. However, the LSF method sets the thermal wave reflection coefficient with a constant value of one. From the theory, this value can vary from zero to one depending on

several factors such as the size of the air-gap defect and materials inside the defect. Consequently, the hypothesis is that the thermal wave reflection coefficient value has some relations with the defect depth and thickness. To test this hypothesis, the new least-squares fitting (NLSF) method established on the LSF method has been developed. The experimental results support the hypothesis. It is concluded that the improvement of the accuracy of depth measurement and the thickness estimation can be achieved by the developed NLSF method.

In addition, it was found that most defect depth measurement methods based on polynomial fitting have an over-fitting issue. Thus, a nonlinear system identification method (NSI) method to measure the depth was developed to tackle this issue. This method can improve the reliability and confidence level of defect depth measurement in a more automatic and flexible manner.

7.1.4 Objective 4

This objective is to develop a method to represent the subsurface defect in the form of 3D images. Most defect depth measurement methods can measure defect size with only one side inspection. However, for measuring defect thickness, they can calculate the defect thickness from defect depth based on double-side inspection. In some situations, access to both sides of the sample could be impossible due to the limitation of space. To solve this limitation, estimating the defect thickness with a single-side inspection is a solution.

This objective was fulfilled by using the developed novel defect depth measurement method, named new least-squares fitting (NLSF) method. Based on the assumption that the defect thickness is related to the thermal wave reflection coefficient, a systematic experiment was set up. The specimens for the experiment were made from carbon fibre-reinforced polymer. The artificial defects were designed in different defect thickness and depth, both of semi-close air-gap (block defect) and open air-gap (flat bottom defect). From the experimental results, the relationship between the defect thickness and thermal wave reflection coefficient was established and represented by a mathematic

model. The reconstructed defect thickness, the defect depth, the defect size, and the sample dimension were then merged and converted to a volume image to represent the 3D subsurface defect images.

7.1.5 Objective 5

This objective was achieved through three processes of validation: model simulation, experimental studies, and a use case. In the first stage, experiments in numerical simulation environment were taken action to study and test the characteristics and capability of each state-of-the-art defect depth measurement method (PST, LSD, APST, and LSF) and the developed novel method (NLSF). In such an environment, variables are adjusted and controlled easily such as noise adjustment (real experiment environment are much more difficult to adjust and control noise level and thermal wave reflection coefficient value). Several noise levels and thermal wave reflection coefficient values were simulated to compare the performance, accuracy, and precision of each defect depth measurement method. The comparison results in numerical simulation can imply the overall performance of each method. In term of principle, the results from the comparison from numerical simulation can indicate that the developed method has the overall highest performance.

Results from numerical simulation can be different from the real environment. In order to validate the results, the real experiment environment was co-operated. A sample with artificial defects was created to test the performance of the developed defect depth measurement method. The LSF method, which is the best existing method from the overall tested results and based on the same concept of a heat transfer solution, was chosen to compare the results. The experimental results confirm that the developed NLSF method has the highest accuracy of depth measurement against the ground truth. Collectively, the results from both numerical simulation environment and real experiment environment support that the developed defect depth measurement method is superior to existing methods.

The developed method was also tested for defect thickness estimation. To test the thickness estimation of the subsurface defect, samples which compound with different defect depth and thickness were created. The relationship between the thermal wave reflection coefficient and the defect thickness was examined, plotted, and established a model. The Pearson correlation coefficient (PCC) was used as a tool to validate the examined relationship. After the proposed algorithm was ensured, it then was applied to test with a use case. The method was used to inspect a steel sample with triangular air-gap defect inside. The tested results successfully demonstrated that the proposed solution can detect and visualise the hidden triangular shape of the defect. It is noted that the models for different materials and types of defect are different, but the method to examine the relationship is the same.

7.2 Conclusions

The overall conclusions of this thesis can be highlighted below:

(1) This thesis proposed a new method to reconstruct a three-dimensional subsurface defect by using thermal wave reflection coefficient value based on optical pulsed thermography with a single-side inspection.

(2) The three-dimensional subsurface defect reconstruction is achieved through three main steps: defect depth measurement, defect thickness estimation, and 3D defect reconstruction.

(3) The proposed method is tested and validated by model simulations, experimental studies, and a use case.

(4) The used samples in this thesis consist of four carbon fibre reinforced polymer (CFRP) samples with different artificial defect size, defect depth, and defect thickness, and a steel sample with a 's' shape triangular air-gap inside.

(5) Under the model simulations, even with the noise level of 25 dB, the averaged percentage error of the proposed defect depth measurement method is less than 0.25%.

(6) Under the experimental studies, the averaged percentage error of defect thickness estimation is less than 10% when the defect thickness is no more than 3 mm.

7.3 Major Findings

The major findings of this thesis can be highlighted below:

(1) The determination of thermal wave reflection coefficient value can improve the overall performance of defect depth measurement.

(2) In case of semi-close defect and open defect, there are some relationship between thermal wave reflection coefficient, defect size, defect depth, and defect thickness.

(3) At the same size and depth of block air-gap defect, thermal wave reflection coefficient has a trend to increase following the increase of defect thickness. The value of thermal wave reflection coefficient of thicker defect is more than thinner defect.

(4) The relationship between thermal wave reflection coefficient, defect size, defect depth, and defect thickness can be applied to reconstruct subsurface defect in the form of 3D image.

7.4 Contributions to Knowledge

The main contributions of this thesis can be summarised below:

(1) The over-fitting problem can be solved. A polynomial model with too low order cannot sufficiently fit the observed data, and consequently, depth estimation maybe not sufficiently accurate. While a model with too high order may fit the observed data too well to model the noise rather than the underlying relationship. The NSI method provides the optimal order for model fitting automatically, which significantly deskills the data analysis process. In addition, the performance of depth measurement against heavy noise is improved dramatically.

(2) The accuracy of defect depth measurement can be improved. The NLSF method is established through introducing a new heat transfer model that includes multiple physical parameters to better describe the observed thermal behaviour in pulsed thermography inspection. A modified analytical modelling with five parameters is introduced to better fit the observed temperature curve using a nonlinear optimisation technique. This method is not only able to estimate the defect depth more accurately but also able to estimate the thermal wave reflection coefficient (R) directly at the same time. The thermal wave reflection coefficient is an important parameter to build the 3D subsurface images.

(3) The defect thickness can be quantified by a single-side inspection. The introduced single-side inspection method not only reduces the inspection time but also extends the application on component where one side is not accessible.

(4) The hidden defect inside both homogeneous material and inhomogeneous material can be reconstructed and visualised in the form of 3D images. In general, three-dimensional heat transfer solution is used to analyse the 3D heat flow for homogeneous material (e.g. steel). It is very difficult and complex to apply it on inhomogeneous material (e.g. CFRP). The developed method reduced the complexity by introducing a modified one-dimensional heat transfer function to approximate the three-dimensional heat transfer function.

To produce the 3D image of subsurface defect, the 3D imaging technology device (expensive price) is usually used to scan the object such as 3D CT scan. The proposed technique in this thesis can use the 2D imaging device technology (relatively low cost) to produce and visualise the 3D image of defects.

7.5 Research Limitations

The aim and objectives of the thesis were achieved completely, however, there are some limitations relating to the research, which are described below:

(1) The proposed defect depth measurement method has been modified from an equation which commonly used for homogenous materials. To test with

inhomogeneous materials or porous materials, there are some potential error due to the heat may not be spread consistently in these materials.

(2) The accuracy of defect depth measurement of the NLSF method depends on data length. The time when maximal temperature contrast between the considered defect pixel and the reference pixel from the non-defective area was used to determine the data length. The depth measurement in the non-defective area needs more data than the defective area. Measurement of deep defect needs more data length than shallow defect. Furthermore, the efficiency of the NLSF method is affected by the selection of parameters bounds before applying the optimisation technique. Setting the parameter bounds and the initial values far from the ground truth could be a solution to increase the computational time.

(3) The defect thickness is a function of multiple correlated parameters, which may constrain its application on irregular shape of defects. The model to estimate the defect thickness is subject to materials. Besides, changing of material properties of tested sample and defect shape may also have an impact on the precision of the used model and then the estimation of defect thickness.

(4) The performance of the identified models of the defect thickness estimation using the NLSF method is limited to the produced specimens. The change of materials or defect shape may have an influence on the results. To fully explore its potential and improve the versatility of the identified model, further study is required by considering different materials with a variety of defect shape, size, depth, and thickness.

(5) The CFRP samples were produced from local manufacturing in the university. The preciseness of production could be slightly less than the high standard of manufacturing.

(6) The visualised 3D images, which is in the form of a volume image, was reconstructed from the defect size, defect depth, defect thickness, and sample's dimension. This process consumes a lot of computer memory if the tested sample is large.

7.6 Recommendation for Future Work

This thesis shows outcomes of using pulsed thermography with single-side inspection method to reconstruct the subsurface defect in the form of 3D image. However, there are some issues need to be further addressed. Recommendations for future work are suggested below:

(1) Quality improvement of the testing samples:

Samples quality can be improved to meet the high standard of manufacturing. High quality of sample can further refine the validation of the proposed technique.

(2) Testing Addition of material samples and artificial defects:

More CFRP sample and new material sample (e.g., steel) with different defect types, defect size, defect thickness, and defect shape can be tested and evaluated to make a more comprehensive assessment of the proposed technique. In this thesis, basic defect shape (rectangle and triangle) were tested and visualised in the form of 3D images. More complex defect shape can be experimented to test the flexibility and reliability of the proposed method. Including, more validation of their visualisation is recommended.

(3) More inspection technique comparison:

The experimental results can be validated and compared quantitatively with other NDT methods such as ultrasonic testing or radiographic testing. The experiments in this thesis were only tested by pulsed thermography under the reflection mode, other infrared thermographic inspection technique such as long pulse thermography, lock-in thermography, and eddy current pulsed thermography, can be experimented.

(4) Visualisation Improvement of the reconstructed three-dimensional defect:

The reconstructed 3D defect in this thesis is visualised in the form of a 3D box view without any outer surface texture. The visualisation of the outer surface can be improved. For example, the 3D subsurface defect can merge with real 3D sample's surface image such as using 3D scanner or 3D camera to make more beautiful.

REFERENCES

[1] N. H. Xiao, *New Technologies and Technical Standards for Modern Non-Destructive Testing Technology and Application*. Beijing: Beijing Silver Sound Audiovisual Press, 2004.

[2] D. M. McCann and M. C. Forde, "Review of NDT methods in the assessment of concrete and masonry structures," *NDT E Int.*, vol. 34, no. 2, pp. 71–84, 2001, doi: 10.1016/S0963-8695(00)00032-3.

[3] G. Shen, "Review of non-destructive testing in China," *Insight*, vol. 48, no. 7, pp. 398–401, 2006.

[4] A. Manohar, "Quantitative Nondestructive Testing using Infrared Thermography," University of California, 2012.

[5] A. Sophian, G. Tian, D. Taylor, and J. Rudlin, "A feature extraction technique based on principal component analysis for pulsed Eddy current NDT," *NDT E Int.*, vol. 36, pp. 37–41, 2003, [Online]. Available: http://www.csa.com/partners/viewrecord.php?requester=gs&collection=TRD&recid=AN139545AN.

[6] G. Simpson and J. Blitz, "Ultrasonic Methods of Nondestructive Testing," *Springer*, vol. 2, 1995.

[7] R. K. Miller and P. McIntire, "Acoustic emission testing," in *Nondestructive Testing Handbook Vol.5*, American Society for Nondestructive Testing, 1987.

[8] G. Wang and T. W. Liao, "Automatic identification of different types of welding defects in radiographic images," *NDT E Int.*, vol. 35, no. 8, pp. 519–528, 2002, doi: 10.1016/S0963-8695(02)00025-7.

[9] P. J. Shull, *Nondestructive Evaluation: Theory, Techniques, and Applications*. CRC, 2002.

[10] J. Blitz, *Electrical and Magnetic Methods of Non-Destructive Testing*. Springer, 1997.

[11] X. P. V. Maldague, *Infrared Methodology and Technology*. Gordon and Breach Science, 1994.

[12] S. Sfarra *et al.*, "Square Pulse Thermography (SPT) and Digital Speckle Photography (DSP): Non- Destructive Testing (NDT) Techniques Applied to the Defects Detection in Aerospace Materials," *2nd Int. Symp. NDT Aerosp.*, pp. 1–8, 2010.

[13] V. P. Vavilov and D. D. Burleigh, "Review of pulsed thermal NDT: Physical principles, theory and data processing," *NDT E Int.*, vol. 73, pp. 28–52, 2015, doi: 10.1016/j.ndteint.2015.03.003.

[14] X. P. V. Maldague, *Theory and Practice of Infrared Technology for Nondestructive Testing*. New York: John Wiley & Sons, 2001.

[15] C. Ibarra-Castanedo, "Quantitative subsurface defect evaluation by pulsed phase thermography: depth retrieval with the phase," University of Laval, 2005.

[16] C. Meola and G. M. Carlomagno, "Recent advances in the use of infrared thermography," *Meas. Sci. Technol.*, vol. 15, no. 9, 2004, doi: 10.1088/0957-0233/15/9/R01.

[17] F. C. Sham, C. Nelson, and L. Long, "Surface Crack Detection by Flash Thermography in Concrete Surface," *J. Insight Winst. Northampt.*, vol. 50, no. 5, pp. 240–243, 2008.

[18] J. S. F. Chu, "Studies of Using Infrared Flash Thermography (FT) for Detection of Surface Cracks, Subsurface Defects and Water-paths in Building Concrete Structures," *Evaluation*, 2008.

[19] H. Nayeb-Hashemi, D. Swet, and A. Vaziri, "New electrical potential method for measuring crack growth in nonconductive materials," *Meas. J. Int. Meas. Confed.*, vol. 36, no. 2, pp. 121–129, 2004, doi: 10.1016/j.measurement.2004.05.002.

[20] M. A. Omar, Y. Zhou, R. Parvataneni, and E. Planting, "Calibrated pulse-

thermography procedure for inspecting HDPE," *Adv. Mater. Sci. Eng.*, vol. 2008, 2008, doi: 10.1155/2008/186427.

[21] K. T. Wan and C. K. Y. Leung, "Fiber optic sensor for the monitoring of mixed mode cracks in structures," *Sensors Actuators, A Phys.*, vol. 135, no. 2, pp. 370–380, 2007, doi: 10.1016/j.sna.2006.08.002.

[22] C. Ibarra-Castanedo, M. Genest, P. Servais, X. P. V. Maldague, and A. Bendada, "Qualitative and quantitative assessment of aerospace structures by pulsed thermography," *Nondestruct. Test. Eval.*, vol. 22, pp. 199–215, 2007, doi: 10.1080/10589750701448548.

[23] P. Meinlschmidt, "Thermographic detection of defects in wood and wood-based materials," in *14th International Symposium on Nondestructive Testing of Wood*, 2005, pp. 39–45.

[24] M. Y. Y. Hung, Y. S. Chen, S. P. Ng, S. M. Shepard, Y. Hou, and J. R. Lhota, "Review and comparison of shearography and pulsed thermography for adhesive bond evaluation," *Opt. Eng.*, vol. 46, no. 5, p. 051007, 2007, doi: 10.1117/1.2741277.

[25] J. a. Schroeder, T. Ahmed, B. Chaudhry, and S. Shepard, "Non-destructive testing of structural composites and adhesively bonded composite joints: pulsed thermography," *Compos. Part A Appl. Sci. Manuf.*, vol. 33, no. 11, pp. 1511–1517, 2002, doi: 10.1016/S1359-835X(02)00139-2.

[26] Y. Zhao *et al.*, "A confidence map based damage assessment approach using pulsed thermographic inspection," *NDT E Int.*, vol. 93, pp. 86–97, Jan. 2018, doi: 10.1016/j.ndteint.2017.10.001.

[27] P. O. Moore, Ed., *Nondestructive Testing Overview*, 3rd ed. The American Society for Nonstructive Testing, 2012.

[28] P. J. Tikalsky, "Overview of non-destructive testing (NDT) methods of materials evaluation," in *In-Situ Evaluation of Historic Wood and Masonry Structures*, 2006, pp. 31–35.

[29] P. O. Moore and N. A. Tracy, Eds., *Liquid Penetrant Testing*, 3rd ed. American Society for Nondestructive Testing.

[30] "Penetrant Testing Materials," *NDT Resource Center*. https://www.nde-ed.org/EducationResources/CommunityCollege/PenetrantTest/PTMaterials/ptmaterials.htm (accessed Jul. 01, 2019).

[31] M. Willcox and G. Downes, "A Brief Description of NDT Techniques," *Insight NDT Equip. Ltd.*, no. 771, pp. 1–22, 2000, doi: 10.1016/S1365-1609(03)00027-3.

[32] P. W. Bennett, "Infrared Moisture Detection, Jersey Shore Leak Detection, Hidden Roof and Window Leaks," *A Full House Inspection Co. LLC.* http://www.afullhouseinspection.com/node/38 (accessed Jul. 01, 2019).

[33] C. Ibarra-Castanedo *et al.*, "Active Infrared Thermography Techniques for the Nondestructive Testing of Materials," in *Ultrasonic and Advanced Methods for Nondestructive Testing and Material Characterization*, 2007, pp. 325–348.

[34] X. P. V. Maldague, T. S. Jones, H. Kaplan, S. Marinetti, and M. Prystay, "Fundamentals of Infrared and Thermal Testing," in *Nondestructive Handbook*, 3rd ed., Ohio: ASNT, 2001.

[35] K.-P. Möllmann, D. Karstädt, F. Pinno, and M. Vollmer, "Selected Critical Applications for Thermography: Convections in Fluids, Selective Emitters and Highly Reflecting Materials," in *Proceedings of the Infrared Camera Calibration Conference*, pp. 161–174.

[36] H. A. Thajeel, "Numerical modeling of infrared thermography techniques via ANSYS," Missouri University of Science and Technology, 2013.

[37] C. Meola, "Origin and Theory of Infrared Thermography," in *Infrared Thermography: Recent Advances and Future Trends*, Science Ed., C. Meola, Ed. New York: Bentham Science, 2012, pp. 3–28.

[38] X. P. V Maldague, "Introduction to NDT by active infrared thermography,"

Mater. Eval., vol. 60, no. 9, pp. 1060–1073, 2002, [Online]. Available: http://w3.gel.ulaval.ca/~maldagx/r_1221t.pdf.

[39] C. Ibarra-Castanedo *et al.*, "Comparative Study of Active Thermography Techniques for the Nondestructive Evaluation of Honeycomb Structures," *Res. Nondestruct. Eval.*, vol. 20, no. 1, pp. 1–31, 2009, doi: 10.1080/09349840802366617.

[40] S. M. Shepard, J. R. Lhota, B. a. Rubadeux, D. Wang, and T. Ahmed, "Reconstruction and enhancement of active thermographic image sequences," *Opt. Eng.*, vol. 42, no. 5, pp. 1337–1342, 2003, doi: 10.1117/1.1566969.

[41] J. M. Spicer and R. Osiander, "Active Thermography," *Int. J. Occup. Saf. Ergon.*, vol. 15, no. 4, pp. 363–371, 2002.

[42] B. Liu, H. Zhang, H. Fernandes, and X. Maldague, "Quantitative evaluation of pulsed thermography, lock-in thermography and vibrothermography on foreign object defect (FOD) in CFRP," *Sensors (Switzerland)*, vol. 16, no. 5, 2016, doi: 10.3390/s16050743.

[43] G. Busse, D. Wu, and W. Karpen, "Thermal wave imaging with phase sensitive modulated thermography," *J. Appl. Phys.*, vol. 71, pp. 3962–3965, 1992.

[44] S. Shepard, "Understanding Flash Thermography," *Mater. Eval.*, vol. 64, no. 5, pp. 460–464, 2006.

[45] D. P. Almond, S. L. Angioni, and S. G. Pickering, "Long pulse excitation thermographic non-destructive evaluation," *NDT E Int.*, vol. 87, no. December 2016, pp. 7–14, 2017, doi: 10.1016/j.ndteint.2017.01.003.

[46] Z. Wang, G. Y. Tian, M. Meo, and F. Ciampa, "Image processing based quantitative damage evaluation in composites with long pulse thermography," *NDT E Int.*, vol. 99, no. April, pp. 93–104, 2018, doi: 10.1016/j.ndteint.2018.07.004.

[47] D. Sharath, M. Menaka, and B. Venkatraman, "Defect characterization using pulsed thermography," *J. Nondestruct. Eval.*, vol. 32, no. 2, pp. 134–141, 2013, doi: 10.1007/s10921-012-0166-4.

[48] H. S. Carslaw and J. C. Jaeger, *Conduction of Heat in Solid*, 2nd ed. Oxford: Clarendon Press, 1986.

[49] G. Giorleo and C. Meola, "Comparison between pulsed and modulated thermography in glass-epoxy laminates," *NDT E Int.*, vol. 35, no. 5, pp. 287–292, 2002, doi: 10.1016/S0963-8695(01)00062-7.

[50] C. Ibarra-Castanedo, N. P. Avdelidis, M. Grenier, X. Maldague, and A. Bendada, "Active thermography signal processing techniques for defect detection and characterization on composite materials," *Thermosense XXXII*, vol. 7661, p. 76610O, 2010, doi: 10.1117/12.850733.

[51] L. D. Favro and X. Han, "Thermal Wave Materials Characterization and Thermal Wave Imaging," in *Sensing for Materials Characterization, Processing, and Manufacturing*, G. Birnbaum and B. A. Auld, Eds. ASNT TONES, 1998, pp. 399–415.

[52] J. Liu, J. Gong, L. Qin, and Y. Wang, "Study on Lock-in Thermography Defect Detectability for Carbon-Fiber-Reinforced Polymer (CFRP) Sheet with Subsurface Defects," *Int. J. Thermophys.*, vol. 36, no. 5–6, pp. 1259–1265, 2015, doi: 10.1007/s10765-015-1874-7.

[53] C. Meola, G. M. Carlomagno, and L. Giorleo, "The use of infrared thermography for materials characterization," *J. Mater. Process. Technol.*, vol. 155–156, no. 1–3, pp. 1132–1137, 2004, doi: 10.1016/j.jmatprotec.2004.04.268.

[54] W. Bai and B. S. Wong, "Evaluation of defects in composite plates under convective environments using lock-in thermography," *Meas. Sci. Technol.*, vol. 12, no. 2, pp. 142–150, 2001, doi: 10.1088/0957-0233/12/2/303.

[55] A. Dillenz, T. Zweschper, and G. Busse, "Progress in ultrasound phase thermography," in *Processings of SPIE, The International Society for*

Optical Engineering, Thermosense XXIII, 2001, vol. 4360, pp. 574–579, doi: 10.1117/12.421042.

[56] L. D. Favro, R. L. Thomas, H. Sui, X. Han, G. Sun, and Z. Ouyang, "Infrared imaging of defects heated by a sonic pulse," *Rev. Sci. Instrum.*, vol. 71, no. 6, pp. 2418–2421, 2000, doi: 10.1063/1.1150630.

[57] Y. He, G. Y. Tian, M. Pan, and D. Chen, "Eddy current pulsed phase thermography and feature extraction," *Appl. Phys. Lett.*, vol. 103, no. 8, pp. 1–4, May 2013.

[58] G. Y. Tian, J. Wilson, L. Cheng, D. P. Almond, E. Kostson, and B. Weekes, "Pulsed eddy current thermography and applications," *Lect. Notes Electr. Eng.*, vol. 96, pp. 205–231, 2011, doi: 10.1007/978-3-642-21099-0_10.

[59] J. Wilson, G. Tian, I. Mukriz, and D. Almond, "PEC thermography for imaging multiple cracks from rolling contact fatigue," *NDT E Int.*, vol. 44, no. 6, pp. 505–512, 2011, doi: 10.1016/j.ndteint.2011.05.004.

[60] U. Netzelmann, G. Walle, S. Lugin, A. Ehlen, S. Bessert, and B. Valeske, "Induction thermography: principle, applications and first steps towards standardisation," *Quant. Infrared Thermogr. J.*, vol. 13, no. 2, pp. 170–181, 2016, doi: 10.1080/17686733.2016.1145842.

[61] W. Ren, J. Liu, G. Y. Tian, B. Gao, L. Cheng, and H. Yang, "Quantitative non-destructive evaluation method for impact damage using eddy current pulsed thermography," *Compos. Part B Eng.*, vol. 54, no. 1, pp. 169–179, 2013, doi: 10.1016/j.compositesb.2013.05.004.

[62] G. Y. Tian, Y. Gao, K. Li, Y. Wang, B. Gao, and Y. He, "Eddy current pulsed thermography with different excitation configurations for metallic material and defect characterization," *Sensors (Switzerland)*, vol. 16, no. 6, 2016, doi: 10.3390/s16060843.

[63] H. Zhang, R. Yang, Y. He, A. Foudazi, L. Cheng, and G. Tian, "A Review of Microwave Thermography Nondestructive Testing and Evaluation," *Sensors*, vol. 17, no. 5, p. 1123, May 2017, doi: 10.3390/s17051123.

[64]   H. I. Ringermacher, R. J. Archacki, and W. A. Veronesi, "Nondestructive testing: Transient depth thermography," US Patent no. 5,711,603, 1998.

[65]   Y. Wang *et al.*, "Thermal pattern contrast diagnostic of microcracks with induction thermography for aircraft braking components," *IEEE Trans. Ind. Informatics*, vol. 14, no. 12, pp. 5563–5574, 2018, doi: 10.1109/TII.2018.2802046.

[66]   X. Li *et al.*, "Periodic Pulsed Thermography for Inner Defects Detection of Lead-Steel Bonded Structure," *IEEE Sens. J.*, vol. 18, no. 11, pp. 4679–4688, 2018, doi: 10.1109/JSEN.2018.2822290.

[67]   L. Cheng and G. Y. Tian, "Transient thermal behavior of eddy-current pulsed thermography for nondestructive evaluation of composites," *IEEE Trans. Instrum. Meas.*, vol. 62, no. 5, pp. 1215–1222, 2013, doi: 10.1109/TIM.2013.2243505.

[68]   N. P. Avdelidis and D. P. Almond, "Transient thermography as a through skin imaging technique for aircraft assembly: Modelling and experimental results," *Infrared Phys. Technol.*, vol. 45, no. 2, pp. 103–114, 2004, doi: 10.1016/j.infrared.2003.07.002.

[69]   L. Bai, S. Tian, Y. Cheng, G. Y. Tian, Y. Chen, and K. Chen, "Reducing the effect of surface emissivity variation in eddy current pulsed thermography," *IEEE Sens. J.*, vol. 14, no. 4, pp. 1137–1142, 2014, doi: 10.1109/JSEN.2013.2294195.

[70]   M. Kasemann, B. Walter, C. Meinhardt, J. Ebser, W. Kwapil, and W. Warta, "Emissivity-corrected power loss calibration for lock-in thermography measurements on silicon solar cells," *J. Appl. Phys.*, vol. 103, no. 11, 2008, doi: 10.1063/1.2930880.

[71]   T. Schmugge, A. French, J. C. Ritchie, A. Rango, and H. Pelgrum, "Temperature and emissivity separation from multispectral thermal infrared observations," *Remote Sens. Environ.*, vol. 79, no. 2–3, pp. 189–198, 2002, doi: 10.1016/S0034-4257(01)00272-3.

[72] Y. Gao and G. Y. Tian, "Emissivity correction using spectrum correlation of infrared and visible images," *Sensors Actuators, A Phys.*, vol. 270, pp. 8–17, 2018, doi: 10.1016/j.sna.2017.12.027.

[73] L. D. Favro, X. Han, P. K. Kuo, and R. L. Thomas, "Imaging the early time behavior of reflected thermal wave pulses," in *SPIE -The International Society for Optical Engineering*, 1995, vol. 2473, pp. 162–166.

[74] S. K. Lau, D. P. Almond, and J. M. Milne, "A quantitative analysis of pulsed video thermography," *NDT E Int.*, vol. 24, no. 4, pp. 195–202, 1991, doi: 10.1016/0963-8695(91)90267-7.

[75] S. M. Shepard, "Temporal Noise Reduction, Compression and Analysis of Thermographic Image Data Sequences," US Patent no. 6,516,084 B2, 2003.

[76] J. G. Sun, "Analysis of Pulsed Thermography Methods for Defect Depth Prediction," *J. Heat Transfer*, vol. 128, no. 4, pp. 329–338, 2006, doi: 10.1115/1.2165211.

[77] Z. Zeng, J. Zhou, N. Tao, L. Feng, and C. Zhang, "Absolute peak slope time based thickness measurement using pulsed thermography," *Infrared Phys. Technol.*, vol. 55, no. 2–3, pp. 200–204, 2012, doi: 10.1016/j.infrared.2012.01.005.

[78] X. P. V. Maldague, *Nondestructive Evaluation of Materials by Infrared Thermography*, 1st ed. London: Springer, 1993.

[79] D. P. Almond and S. K. Lau, "Defect Sizing by Transient Thermography .1. An Analytical Treatment," *J. Phys. D-Applied Phys.*, vol. 27, pp. 1063–1069, 1994, doi: Doi 10.1088/0022-3727/27/5/027.

[80] J. G. Sun, "Method for Determining Defect Depth using Thermal Imaging," US 6,542,849 B2, 2003.

[81] H. Liu, C. Pei, S. Xie, Y. Li, Y. Zhao, and Z. Chen, "Inversion Technique for Quantitative Infrared Thermography Evaluation of Delamination Defects in

Multilayered Structures," *IEEE Trans. Ind. Informatics*, vol. 16, no. 7, pp. 4592–4602, 2020, doi: 10.1109/tii.2019.2950808.

[82]   S. Xie, Z. Chen, T. Takagi, and T. Uchimoto, "Quantitative non-destructive evaluation of wall thinning defect in double-layer pipe of nuclear power plants using pulsed ECT method," *NDT E Int.*, vol. 75, pp. 87–95, 2015, doi: 10.1016/j.ndteint.2015.06.002.

[83]   T. Aujeszky, G. Korres, and M. Eid, "Measurement-based thermal modeling using laser thermography," *IEEE Trans. Instrum. Meas.*, vol. 67, no. 6, pp. 1359–1369, 2018, doi: 10.1109/TIM.2017.2785138.

[84]   G. Jinlong, L. Junyan, W. Fei, and W. Yang, "Inverse heat transfer approach for nondestructive estimation the size and depth of subsurface defects of CFRP composite using lock-in thermography," *Infrared Phys. Technol.*, vol. 71, pp. 439–447, 2015, doi: 10.1016/j.infrared.2015.06.005.

[85]   R. Richter, C. Maierhofer, and M. Kreutzbruck, "Numerical method of active thermography for the reconstruction of back wall geometry," *NDT E Int.*, vol. 54, pp. 189–197, 2013, doi: 10.1016/j.ndteint.2012.10.010.

[86]   S. Lugin and U. Netzelmann, "A defect shape reconstruction algorithm for pulsed thermography," *NDT E Int.*, vol. 40, no. 3, pp. 220–228, 2007, doi: 10.1016/j.ndteint.2006.11.001.

[87]   B. Kaltenbacher, A. Neubauer, and O. Scherzer, *Iterative Regularization Methods for Nonlinear Ill-Posed Problems*. De Gruyter, 2008.

[88]   F. L. Rodríguez and V. De Paulo Nicolau, "Inverse heat transfer approach for IR image reconstruction: Application to thermal non-destructive evaluation," *Appl. Therm. Eng.*, vol. 33–34, no. 1, pp. 109–118, 2012, doi: 10.1016/j.applthermaleng.2011.09.019.

[89]   M. Hanke, *Conjugate gradient type methods for ill-posed problems*. New York: John Wiley & Sons, 1995.

[90]   C. H. Cheng and C. Y. Wu, "An approach combining body-fitted grid

generation and conjugate gradient methods for shape design in heat conduction problems," *Numer. Heat Transf. Part B Fundam. Int. J. Comput. Methodol.*, vol. 37, no. 1, pp. 69–83, 2000, doi: 10.1080/104077900275558.

[91] A. Elhassnaoui and S. Sahnoun, "A three-dimensional reconstruction algorithm for pulsed thermography," *J. Mater. Environ. Sci.*, vol. 5, no. 4, pp. 983–988, 2014.

[92] J. C. Ramirez-Granados, G. Paez, and M. Strojnik, "Three-dimensional reconstruction of subsurface defects using finite-difference modeling on pulsed thermography," *Appl. Opt.*, vol. 51, no. 16, pp. 3153–3161, 2012, doi: 10.1364/AO.51.003153.

[93] Y. A. Plotnikov and W. P. Winfree, "Advanced image processing for defect visualization in infrared thermography," in *Thermosense XX*, 1998, vol. 3361, pp. 331–338, doi: 10.1117/12.304745.

[94] S. Soldan, D. Ouellet, P. Hedayati, A. Bendada, D. Laurendeau, and A. Kroll, "Mapping Non-Destructive Testing Data on the 3D Geometry of Objects with Complex Shapes," *QIRT2014 Conférence*.

[95] M. A. Akhloufi, Y. Guyon, A. Bendada, and C.-I. Castenado, "Three-dimensional non-destructive testing (NDT) in the infrared spectrum," in *Thermosense: Thermal Infrared Applications XXXVII*, 2015, vol. 9485, pp. 1–10, doi: 10.1117/12.2087047.

[96] Y. Zhao, J. Mehnen, A. Sirikham, and R. Roy, "A novel defect depth measurement method based on Nonlinear System Identification for pulsed thermographic inspection," *Mech. Syst. Signal Process.*, vol. 85, pp. 382–395, 2017, doi: 10.1016/j.ymssp.2016.08.033.

[97] P. Cotic, D. Kolaric, V. B. Bosiljkov, V. Bosiljkov, and Z. Jaglicic, "Determination of the applicability and limits of void and delamination detection in concrete structures using infrared thermography," *NDT E Int.*, vol. 74, pp. 87–93, 2015, doi: 10.1016/j.ndteint.2015.05.003.

[98] A. Sirikham, Y. Zhao, H. Y. Nezhad, W. Du, and R. Roy, "Estimation of Damage Thickness in Fiber-Reinforced Composites using Pulsed Thermography," *IEEE Trans. Ind. Informatics*, vol. 15, no. 1, pp. 445–453, 2019, doi: 10.1109/TII.2018.2878758.

[99] A. Sirikham, Y. Zhao, H. Liu, Y. Xu, S. Williams, and J. Mehnen, "Three-dimensional subsurface defect shape reconstruction and visualisation by pulsed thermography," *Infrared Phys. Technol.*, vol. 104, no. December 2019, 2020, doi: 10.1016/j.infrared.2019.103151.

[100] J. Mehnen, L. Tinsley, and R. Roy, "Automated in-service damage identification," *CIRP Ann. - Manuf. Technol.*, vol. 63, no. 1, pp. 33–36, 2014, doi: 10.1016/j.cirp.2014.03.016.

[101] Y. Zhao, J. Mehnen, W. Xu, M. Alrashed, S. Abineri, and R. Roy, "Degradation Assessment of Industrial Composites Using Thermography," *Procedia CIRP*, vol. 38, pp. 147–152, 2015, doi: 10.1016/j.procir.2015.07.045.

[102] M. B. Saintey and D. P. Almond, "Defect sizing by transient thermography. II. A numerical treatment," *J. Phys. D. Appl. Phys.*, vol. 28, no. 12, p. 2539, 1995, doi: 10.1088/0022-3727/28/12/023.

[103] P. H. Vahid, S. Hesabi, and X. Maldague, "The Effect of Pre-processing Techniques in Detecting Defects of Thermal Images," in *Proceedings of the VIIth International Workshop on Advances in Signal Processing for Non Destructive Evaluation of Materials*, 2013, pp. 53–54.

[104] W. Y. Jeong, C. J. Earls, W. D. Philpot, and A. T. Zehnder, "Inverse thermographic characterization of optically unresolvable through cracks in thin metal plates," *Mech. Syst. Signal Process.*, vol. 27, pp. 634–650, 2012, doi: 10.1016/j.ymssp.2011.09.021.

[105] K. Philipp *et al.,* "Multi-sensor system for in situ shape monitoring and damage identification of high-speed composite rotors," *Mech. Syst. Signal Process.*, vol. 76–77, pp. 187–200, 2015, doi:

10.1016/j.ymssp.2016.02.009.

[106] C. J. Earls, "Stochastic inverse thermographic characterization of sub-pixel sized through cracks," *Mech. Syst. Signal Process.*, vol. 30, pp. 146–156, 2012, doi: 10.1016/j.ymssp.2012.01.016.

[107] X. Maldague and S. Marinetti, "Pulse phase infrared thermography.," *J. Appl. Phys.*, vol. 79, no. 5, p. 2694, 1996, doi: 10.1016/S0963-8695(97)87728-6.

[108] C. Ibarra-Castanedo and X. P. V. Maldague, "Defect Depth Retrieval from Pulsed Phase Thermographic Data on Plexiglas and Aluminum Samples," *Proc. SPIE, Thermosense XXVI*, vol. 5405, pp. 348–356, 2004, doi: 10.1117/12.540855.

[109] X. Han, L. D. Favro, P. K. Kuo, and R. L. Thomas, "Early-Time Pulse-Echo Thermal Wave Imaging," in *Review of Progress in Quantitative Nondestructive Evaluation*, vol. 15, D. O. Thompson and D. E. Chimenti, Eds. Plenum Press, New York, 1996, pp. 519–524.

[110] P. K. Kuo and R. L. Thomas, "IR Thermal Wave Tomographic Studies of Structural Composites," pp. 447–451, 1992.

[111] L. D. Favro, X. Han, Y. Wang, P. K. Kuo, and R. L. Thomas, "Pulse-Echo Thermal Wave Imaging," vol. 14, no. 1, pp. 425–429, 1995.

[112] Z. Zeng, C. Li, N. Tao, L. Feng, and C. Zhang, "Depth prediction of non-air interface defect using pulsed thermography," *NDT E Int.*, vol. 48, pp. 39–45, 2012, doi: 10.1016/j.ndteint.2012.02.008.

[113] M. Pilla, M. Klein, X. Maldague, and A. Salerno, "New Absolute Contrast for pulsed thermography," vol. 1, no. 1, pp. 53–58, 2002.

[114] D. Palumbo and U. Galietti, "Damage Investigation in Composite Materials by Means of New Thermal Data Processing Procedures," *Strain*, vol. 52, no. 4, pp. 276–285, Aug. 2016, doi: 10.1111/str.12179.

[115] F. Lopez, C. Ibarra-Castanedo, V. De Paulo Nicolau, and X. Maldague,

"Optimization of pulsed thermography inspection by partial least-squares regression," *NDT E Int.*, vol. 66, 2014, doi: 10.1016/j.ndteint.2014.06.003.

[116] A. Sirikham, Y. Zhao, and J. Mehnen, "Determination of thermal wave reflection coefficient to better estimate defect depth using pulsed thermography," *Infrared Phys. Technol.*, vol. 86, pp. 1–10, 2017, doi: 10.1016/j.infrared.2017.08.012.

[117] C. Spiessberger, A. Dillenz, and T. Zweschper, "Active Thermography for Quantitative NDT of CFRP Components," in *2nd International Symposium on NDT in Aerospace 2010*, 2010, pp. 1–7.

[118] D. Almond and P. Patel, *Photothermal science and techniques*. London: Chapman & Hall, 1996.

[119] A. K. Boyat and B. K. Joshi, "A Review Paper: Noise Models in Digital Image Processing," no. May, 2015, doi: 10.5121/sipij.2015.6206.

[120] M. Welvaert and Y. Rosseel, "On the definition of signal-to-noise ratio and contrast-to-noise ratio for fMRI data," *PLoS One*, vol. 8, no. 11, 2013, doi: 10.1371/journal.pone.0077089.

[121] R. Kieser, P. Reynisson, and T. J. Mulligan, "Definition of signal-to-noise ratio and its critical role in split-beam measurements," *ICES J. Mar. Sci.*, vol. 62, no. 1, pp. 123–130, 2005, doi: 10.1016/j.icesjms.2004.09.006.

[122] W. Minkina and S. Dudzik, "Errors of Measurements in Infrared Thermography," in *Infrared Thermography*, Chichester, UK: John Wiley & Sons, 2009, pp. 61–80.

[123] K. Y. Chan, C. K. Kwong, T. S. Dillon, and Y. C. Tsim, "Reducing overfitting in manufacturing process modeling using a backward elimination based genetic programming," *Appl. Soft Comput.*, vol. 11, no. 2, pp. 1648–1656, Mar. 2011, doi: 10.1016/j.asoc.2010.04.022.

[124] S. Chen and S. A. Billings, "Representations of non-linear systems: the NARMAX model," *Int. J. Control*, vol. 49, no. 3, pp. 1013–1032, Mar. 1989,

doi: 10.1080/00207178908559683.

[125] H. L. Wei and S. A. Billings, "Model structure selection using an integrated forward orthogonal search algorithm assisted by squared correlation and mutual information," *Int. J. Model. Identif. Control*, vol. 3, no. 4, p. 341, 2008, doi: 10.1504/IJMIC.2008.020543.

[126] S. A. Billings and H. L. Wei, "An adaptive orthogonal search algorithm for model subset selection and non-linear system identification," *Int. J. Control*, vol. 81, no. 5, pp. 714–724, May 2008, doi: 10.1080/00207170701216311.

[127] S. L. Kukreja, H. L. Galiana, and R. E. Kearney, "Structure detection of NARMAX models using bootstrap methods," in *Proceedings of the 38th IEEE Conference on Decision and Control (Cat. No.99CH36304)*, vol. 1, pp. 1071–1076, doi: 10.1109/CDC.1999.832938.

[128] S. A. Billings and H. Wei, "Sparse Model Identification Using a Forward Orthogonal Regression Algorithm Aided by Mutual Information," *IEEE Trans. Neural Networks*, vol. 18, no. 1, pp. 306–310, Jan. 2007, doi: 10.1109/TNN.2006.886356.

[129] Y. Zhao, H. L. Wei, and S. A. Billings, "A new adaptive fast cellular automaton neighborhood detection and rule identification algorithm," *IEEE Trans. Syst. Man, Cybern. Part B Cybern.*, vol. 42, no. 4, pp. 1283–1287, 2012, doi: 10.1109/TSMCB.2012.2185790.

[130] Y. Zhao, S. A. Billings, H. Wei, F. He, and P. G. Sarrigiannis, "A new NARX-based Granger linear and nonlinear casual influence detection method with applications to EEG data," *J. Neurosci. Methods*, vol. 212, no. 1, pp. 79–86, Jan. 2013, doi: 10.1016/j.jneumeth.2012.09.019.

[131] Y. Zhao, S. A. Billings, H. Wei, and P. G. Sarrigiannis, "Tracking time-varying causality and directionality of information flow using an error reduction ratio test with applications to electroencephalography data," *Phys. Rev. E*, vol. 86, no. 5, p. 051919, Nov. 2012, doi: 10.1103/PhysRevE.86.051919.

[132] Y. Zhao, L. Tinsley, S. Addepalli, J. J. Mehnen, and R. Roy, "A coefficient clustering analysis for damage assessment of composites based on pulsed thermographic inspection," *NDT E Int.*, vol. 83, pp. 59–67, 2016, doi: 10.1016/j.ndteint.2016.06.003.

[133] D. Pieper, K. M. Donnell, M. T. Ghasr, and E. C. Kinzel, "Integration of microwave and thermographic NDT methods for corrosion detection," 2014, pp. 1560–1567, doi: 10.1063/1.4865009.

[134] P. Wang, Z. Li, L. Zhou, and Y. Pei, "Microwave nondestructive detection and quantitative evaluation of kissing defects in GFRP laminates," *Compos. Sci. Technol.*, vol. 162, pp. 117–122, Jul. 2018, doi: 10.1016/j.compscitech.2018.04.029.

[135] G. Singh, H. M. Bapat, B. P. Singh, M. Bandyopadhyay, R. K. Puri, and D. N. Badodkar, "Thickness Evaluation of Aluminium Plate Using Pulsed Eddy Current Technique," *J. Inst. Eng. Ser. D*, vol. 94, no. 2, pp. 89–93, Oct. 2013, doi: 10.1007/s40033-013-0028-y.

[136] S. Dixon, P. A. Petcher, Y. Fan, D. Maisey, and P. Nickolds, "Ultrasonic metal sheet thickness measurement without prior wave speed calibration," *J. Phys. D. Appl. Phys.*, vol. 46, no. 44, p. 445502, Nov. 2013, doi: 10.1088/0022-3727/46/44/445502.

[137] S. C. Garcea, Y. Wang, and P. J. Withers, "X-ray computed tomography of polymer composites," *Compos. Sci. Technol.*, vol. 156, pp. 305–319, 2018, doi: 10.1016/j.compscitech.2017.10.023.

[138] S. M. Shepard, M. Frendberg, and Y. L. Hou, "Characterization of Full-Range Time Evolution in Active Thermography," in *12th International Conference on Quantitative Infrared Thermography (QIRT)*, 2014, doi: 10.21611/qirt.2014.178.

[139] S. A. Billings, *Nonlinear System Identification*. Chichester, UK: John Wiley & Sons, Ltd, 2013.

[140] S. Dudzik, "A simple method for defect area detection using active

thermography," *Opto-electronics Rev.*, vol. 17, no. 4, pp. 338–344, 2009, doi: 10.2478/s11772-009-0016-9.

[141] M. F. Beemer and S. M. Shepard, "Aspect ratio considerations for flat bottom hole defects in active thermography," *Quant. Infrared Thermogr. J.*, vol. 6733, no. September, pp. 1–16, 2017, doi: 10.1080/17686733.2017.1328642.

[142] T. J. Marrow, "New Techniques for In-situ Observations of Crack Growth Behaviour," *17th Eur. Conf. Fract.*, pp. 408–420, 2008.

[143] G. Vosniakos, S. Michael, and A. Vasileiou, "Digital Manufacturing Process Chain for One-Off Replacement Parts: A Precision Casting Case Study," *J. Manuf. Mater. Process.*, vol. 1, no. 2, pp. 1–18, 2017, doi: 10.3390/jmmp1020017.

[144] F. Peti and L. Grama, "Analyze of the possible causes of porosity type deffects in aluminium high pressure diecast parts," *Scientific Bulletin of the Petru Maior University of Târgu Mureş*, no. December, pp. 41–44, 2011.

[145] J. L. Malisano, S. Kumar, C. M. A. Lui, and K. A. Q. O'Reilly, "X-Ray Computed Tomography versus Metallography for Porosity Analysis in Aluminium RPT Castings," in *Proceedings of the 5th Decennial International Conferences on Solidification Processing*, 2017, vol. 3, pp. 3–6, [Online]. Available: https://ora.ox.ac.uk/objects/uuid:c8b5cd60-c6ae-40b5-85ce-755779c2fe20.

[146] A. du Plessis, B. J. Olawuyi, W. P. Boshoff, and S. G. le Roux, "Simple and fast porosity analysis of concrete using X-ray computed tomography," *Mater. Struct. Constr.*, vol. 49, no. 1–2, pp. 553–562, 2016, doi: 10.1617/s11527-014-0519-9.

[147] A. Du Plessis and P. Rossouw, "X-ray computed tomography of a titanium aerospace investment casting," *Case Stud. Nondestruct. Test. Eval.*, vol. 3, pp. 21–26, 2015, doi: 10.1016/j.csndt.2015.03.001.

[148] U. Ewert *et al.*, "Mobile Computed Tomography for Inspection of Large

Stationary Components in Nuclear and Aerospace Industries," vol. 53, no. 2, pp. 308–310, 2012.

[149] A. du Plessis, S. G. le Roux, and A. Guelpa, "Comparison of medical and industrial X-ray computed tomography for non-destructive testing," *Case Stud. Nondestruct. Test. Eval.*, vol. 6, pp. 17–25, 2016, doi: 10.1016/j.csndt.2016.07.001.

[150] B. F. Wall, G. M. Kendall, A. A. Edwards, S. Bouffler, C. R. Muirhead, and J. R. Meara, "What are the risks from medical X-rays and other low dose radiation?," *Br. J. Radiol.*, vol. 79, no. 940, pp. 285–294, 2006, doi: 10.1259/bjr/55733882.

[151] J. P. Kruth, M. Bartscher, S. Carmignato, R. Schmitt, L. De Chiffre, and A. Weckenmann, "Computed tomography for dimensional metrology," *CIRP Ann. - Manuf. Technol.*, vol. 60, no. 2, pp. 821–842, 2011, doi: 10.1016/j.cirp.2011.05.006.

[152] G. A. Jones and P. Huthwaite, "Limited view X-ray tomography for dimensional measurements," *NDT E Int.*, vol. 93, pp. 98–109, 2018, doi: 10.1016/j.ndteint.2017.09.002.

[153] M. Kageyama *et al.*, "X-ray phase-imaging scanner with tiled bent gratings for large-field-of-view nondestructive testing," *NDT E Int.*, vol. 105, pp. 19–24, 2019, doi: 10.1016/j.ndteint.2019.04.007.

[154] S. H. Teoh and H. Ibrahim, "Median Filtering Frameworks for Reducing Impulse Noise from Grayscale Digital Images: A Literature Survey," *Int. J. Futur. Comput. Commun.*, vol. 1, no. 4, pp. 323–326, 2013, doi: 10.7763/ijfcc.2012.v1.87.